An evaluation of the effects of idealized ice nuclei on the apportionment of upper tropospheric w...
Harkey, Monica K.
ProQuest Dissertations and Theses; 2009; Dissertations & Theses @ University of Wisconsin at Madison
pg. n/a

AN EVALUATION OF THE EFFECTS OF IDEALIZED ICE NUCELI ON THE APPORTIONMENT OF UPPER TROPOSPHERIC WATER VAPOR IN THE UWNMS

by

Monica K. Harkey

A dissertation submitted in partial fulfullment of
the requirements for the degree of

Doctor of Philosophy
(Atmospheric and Oceanic Sciences)

at the
UNIVERSITY OF WISCONSIN-MADISON
2009

Committee's Page. This page is not to be hand-written except for the signatures

A dissertation entitled

An Evaluation of the Effects of Idealized Ice Nuclei
on the Apportionment of Upper Tropospheric Water in the UWNMS

submitted to the Graduate School of the
University of Wisconsin-Madison
in partial fulfillment of the requirements for the
degree of Doctor of Philosophy

by
Monica Kateri Harkey

Date of Final Oral Examination: August 10, 2009

Month & Year Degree to be awarded: **December** 2009 **May** **August**

****

Approval Signatures of Dissertation Committee

Matthew H. Hitchman

John A. Young

Signature, Dean of Graduate School

Martin Cadwallader

Committee's Page. This page is not to be hand-written except for the signatures

Thank you to Marcus Buker, Will Lewis, and Professor Greg Tripoli for all their help and patience with my questions about the NMS.

Thank you to my committee members (Professors Jim Burt, Matt Hitchman, Grant Petty, Pao Wang, and John Young) for their willingness to listen and talk with me about this topic, modeling nuances, and lots of other sciencey things.

Thank you to Marcus Buker, Beth Klusinske, Amihan Huesmann, Andrew Parker, Marek Rogal, and Nick Zachar for keeping me company in the office. Dudes, you rock.

Most thanks go to the friends and family whose gentle, always positive support has allowed for some modicum of stubbornness to see this project through. Because that's what got me to finish.

M&D, JMH, NMG, T&P, je vous aime!

Table of Contents

List of Tables

List of Figures

Abstract

The spatial coincidence of aerosol loading from biomass burning, a high frequency of cirrus, and circulations tending to bring air into the stratosphere suggests that biomass burning-derived IN are likely to have some impact on tropical cirrus, which could then impact the transport of vapor into the lower stratosphere. Unfortunately our knowledge of cloud-aerosol interactions is still lacking. Most studies of cloud-aerosol interaction, have focused on the microphysical changes of water droplets in the presence of aerosol. Aerosol-*ice* particle interaction is a relatively new research topic. Some measurements exist of the composition of some species of organic IN, but not enough to explain their structure, nucleating behavior, and concentration. As an exploratory study, eight experiments to explore the effects of populations of idealized ice nuclei have been conducted with a mesoscale model in three categories—the effect of concentration, the effect of activation temperature, and the effect of the location and extent of the initial IN population. The sensitivity of the environment to these scenarios was seen by horizontally averaging changes in ice and vapor over gridpoints influenced by IN activation, and plotting those changes as a function of time and height. These simulations, over the Amazon Basin, span a 60-hour period from the 26th - 28th of September, 1992, coincident with frontal and mesoscale convective activity.

With the exceptions of IN introduced near the surface, substantial effects on ice and vapor as a result of IN activity (at least 0.001 g/kg, or 1 ppmv) were found to be concentrated in the latter part of the experiments, after about 35 hours. This is near the beginning of convective activity along a stalled stationary front. One pattern was that more gridpoints experienced negative changes in both vapor and ice than positive changes over the course of the 60 hours modeled for each experiment. With the onset of convection in the last half of the model runs, a second pattern emerged in several experiments, above 10 km: a dipole in vapor change that persists for several hours, with positive changes below and negative changes above an inflection point that varies between about 11 and 12 km. The prime factor in the creation of both of these patterns is vertical velocity. Rising air with smaller and more numerous crystals leads to evaporative moistening of upper levels—the expected result from the hypothesis that initiated this work, seen in the creation of the positive portion of the dipoles. Most of the air that has been

influenced by IN activation tends to experience negative vertical velocites, and negative changes in vapor and ice via precipitation. The many degrees of freedom in cloud processes make this a much more nuanced story than the generalizations we can make based on the sign of vertical velocity. For example, noisy changes in vertical velocity are what produce the upper, negative portion of the dipole feature. Understanding this, and knowing how little is known about the behavior and concentration of IN in the real world, these modeled studies are a good first-order estimate of the effects of IN, and guidance for future studies when more information about IN is available.

Chapter 1: Introduction and Background

An important objective in atmospheric science is to understand more thoroughly the role clouds play in the Earth's changing climate. The intricate interactions between cloud properties and the local environment makes this a challenging goal. One straightforward avenue of investigation involves the study of varying cloud particle sizes. The research proposed in this document involves such a study-how will changing cloud particle sizes affect the local and downstream environments? Specifically, how might changing properties of ice clouds near the tropopause affect the lower stratosphere? It is proposed that decreasing particle sizes in cirrus near the tropopause may elucidate some of the changes in the environment of the upper troposphere/lower stratosphere, via changes in the phase and distribution of water.

In recent years, satellite and balloon-borne instruments have detected a decreasing trend in stratospheric temperatures. Ozone loss and increases in greenhouse gas concentrations would be logical causes of stratospheric cooling, but they may not be the only causes. De F. Forster and Shine (1999) found a strong correlation between the decrease in stratospheric temperatures and a positive trend in stratospheric water vapor. In fact, their model studies showed that the water vapor trend in the lower stratosphere (below 30 km in height) has more influence on stratospheric temperatures than ozone loss or an increase in water vapor concentration throughout the whole stratosphere.

The cause of the increase of water vapor in the stratosphere is not well understood. Data which indicate the trend, coming from radiosondes, satellites, balloons, and aircraft, are sparse (although less so in recent years), with limited spatial or temporal resolution. Still, the trend can be quantified. Using a compilation of 46 years of stratospheric observations, Rosenlof et al. (2001) found a 1% per year increase in the concentration of stratospheric water vapor--a two parts per million volume (2 ppmv) increase-- since 1954. What could account for this increase? To answer this, we first need to understand what controls there are on stratospheric water vapor.

Within the stratosphere, chemical reactions will produce water vapor:

$$CH4 + OH \rightarrow CH3 + H2O\ .$$

De F. Forster and Shine (1999) noted that methane oxidation could account for up to 40% of the increase in stratospheric water vapor. Rosenlof et al. (2001) found that the increase in tropospheric methane would at most produce an increase in stratospheric moisture by about 1.1 ppmv, but that the contribution of moisture by the methane-to-water reaction would not explain the large changes in the concentration of moisture in the lower stratosphere, where the methane oxidation is "far from complete." The controls on vapor in the lower stratosphere are not strictly chemical, and are we must turn our attention to the more nuanced dynamical and microphysical controls on moisture transport into the stratosphere.

Brewer (1949) theorized that the stratospheric water vapor concentration is controlled by temperatures at the tropical tropopause. As air moves slowly upwards into the stratosphere, it would be cooled and dehydrated to the local minimum saturation mixing ratio. Another, quicker way for air to be dehydrated as it enters the stratosphere is by convective overshooting. Especially energetic convection can force air into the stratosphere, where the air would be cooled adiabatically to considerably cooler temperatures. The very cold air in these convective overshoots could dehydrate very effectively. Modeling this process, Sherwood and Dessler (2000) show large-scale, slow (~0.1 K/day) ascent into the stratosphere with moderate dehydration as a result, following Brewer's theory, but punctuated by overshooting convective turrets rapidly detraining more thoroughly dehydrated air at various levels. This resulted in a horizontal "age" spectrum of air, with older air being less dehydrated and younger air coming from the more dehydrated convective overshoots.

Other influences on stratospheric water vapor include periodic motions such as Kelvin and gravity waves. These wave motions act to change local temperatures, promoting saturation and dehydration, either by mixing or adiabatic cooling. For example, gravity waves induced by convection will dehydrate by lifting and cooling air to the local saturation vapor pressure, where ice crystals may form and precipitate (Potter and Holton, 1995). These waves may dehydrate air via the creation of cross-isentropic circulations which drag moisture up from lower levels, which could then precipitate in the wave crest (Pfister et al., 1993).

In an explanation of where the tropopause was cold enough to produce the aridity of the stratosphere, Newell and Gould-Stewart (1981) proposed that a "stratospheric fountain" existed over the western Pacific. Observed saturation mixing ratios of water vapor just above the tropical tropopause range from ~2 to ~6 ppmv (Jensen et al., 1996(a), and Sherwood and Dessler, 2000, respectively). Given temperature data from the 100 mb level, Newell and Gould-Stewart considered the distribution of temperatures cold enough to explain a 3.5 ppmv saturation mixing ratio, which was chosen as the lower limit of stratospheric moisture content. They then theorized that where the tropical tropopause was coldest would indicate where the largest vertical motion into the stratosphere occurred. Noting that the locations of coldest tropopause temperatures were over the tropical western Pacific from November to March, and over the Bay of Bengal and India during the monsoon, they named that region the "stratospheric fountain."

The stratospheric fountain theory was challenged by Dessler (1998) who argued that the average tropical tropopause was sufficiently cold to dehydrate rising parcels of air. Using extratropical measurements of water and methane in the lower and middle stratosphere, Dessler calculated how much of the water could be a result of the oxidation of methane, subtracted that amount from the detected water vapor concentration, and assumed the result equals the water vapor concentration within a latitude band in the tropical stratosphere. This method estimates the amount of water vapor in the tropical stratosphere before its transport to higher latitudes to be about 3.8 ppmv. For air to be dehydrated to this mixing ratio, the tropopause would not need to be as cold as Newell and Gould-Stewart suggested. This also implies that there may not be a preferential location for air to enter the stratosphere.

In fact, since Dessler (1998) was published, researchers have found evidence that there may be a net subsidence in the western Pacific: Sherwood (2000) analyzed radiosonde data to find net subsidence near the tropopause in the western Pacific; and Gettleman et al. (2000) used a global chemical tracer model to find a downward flux of water vapor over the west Pacific. These observations and results may be explained by the presence of wave-generated cirrus overlying cumulonimbus anvils. The adiabatic cooling associated with the formation of cirrus clouds, in addition to the radiative cooling that would take place with an anvil cloud below, would often result in colder air being moved downstream into the subsiding portion of the wave motion, enhancing subsidence (Hartmann et al., 2001).

Not surprisingly, when there are more than one means of vapor transport into the stratosphere, no one method is the only one that occurs in time or space. Using a high-resolution tunable laser absorption spectrometer to measure water isotopes in the upper troposphere during the Cirrus Regional

Study of Tropical Anvils and Cirrus Layers-Florida Area Cirrus Experiment (CRYSTAL-FACE) Webster and Heymsfield (2003) found the amount of water isotopes would be explained by slow ascent of vapor and by convective overshoots. For their particular data, the ratio of influence was calculated to be about 22% transport by convective overshoots and 78% by gradual ascent.

Given that transport mechanisms all dehydrate air via ice formation and sedimentation, it is not surprising that the persistence of high, thin (often subvisible) cirrus in the tropics has been noted (for example, Jensen et al., 1996(a,b); Roumeau et al., 2000; Omar and Gardner, 2001), spurring research to investigate the effects of cirrus cloud particles on stratospheric chemistry. In models of wave-generated cirrus near the tropopause, it was found that longer wave periods and the fewer the ice crystal number densities will allow for large (r ~10 microns) crystal sizes, promoting dehydration by sedimentation (Jensen et al., 1996(b)). The effects of changing cirrus particle size were explored by Rosenfeld et al. (1998), who found that when the tropical tropopause is warm (May-July), smaller cloud particles will offset the dehydration of air as it enters the stratosphere; with smaller particles the removal of water by sedimentation is lessened.

Concurrent with the observed water vapor increases in the stratosphere, water vapor in the deep tropical upper troposphere seems to have increased from 1979 to 2001, while decreasing in the southern hemisphere subtropics, without a corresponding change in upper tropospheric temperatures (Bates and Jackson, 2001). What control mechanism(s) could there be, then, to account for the increase in stratospheric moisture? Perhaps an answer can be found in further exploration of the research described by Jensen et al. (1996(a,b)) and Rosenfeld et al. (1998)--in that the same controls on cirrus microphysics may also affect the dehydration of air as it enters the stratosphere. The question that arises then is, what could affect changes in cirrus microphysics?

Earth's population has grown from about 2.8 billion in 1955 to over 6 billion in 2000. Over those 45 years, the population of developing countries (including all of South America, the maritime continent, and most of sub-Saharan Africa) has increased by 2.9 billion (World Resources Institute, 2004). With a growing population, competition for land and natural resources has become more intense and spatially concentrated. One byproduct of the population growth has been an increase in biomass burning, as it is a cheap and easy method of clearing land. Recently Christopher et al. (2000) estimated that 100 Tg of aerosols are released into the atmosphere by biomass burning, and of that, 80 Tg/year are from tropical regions, such as Brazil, Indonesia, and in sub-Saharan Africa. One estimate of the deforestation rate from burning, using Landsat MSS and thematic mapper (TM) data, was found to be 15,000 km2/year from 1978 to1988 (an increase of 78,000 km2 forested area burned in 1978 to 230,000 km2 in 1988) in the Brazilian Amazon basin alone (Skole and Tucker, 1993). Using data from the Geostationary Operational Environment Satellite (GOES) visible infrared spin scan radiometer atmospheric sounder (VAS) Prins and Menzel (1994) found that the areal extent of biomass burning more than doubled from 1981 to 1993 in South America. Biomass burning in African savannahs accounts for about a third of tropical biomass combustion, with an average of 440 million ha in African savannahs burned annually (Andreae et al., 1996).

Perhaps it is human activity that is affecting water vapor concentrations in the upper troposphere and lower stratosphere, by modification of cloud properties. Hobbs and Locatelli (1969) found significant increases in the number of ice nuclei (IN) downwind of a forest fire in Washington state. This knowledge leads to two questions: how likely is it that part of the ~80 Tg/year of aerosols released by biomass burning are IN that will affect clouds near the tropical tropopause? how could the expected increased IN concentration affect cirrus microphysics? A detailed answer to the first question is currently unavailable—for example, it is still largely unknown exactly how aerosols may act as IN. The second question, on the other hand, is answerable and is a central part of this proposed research. One would expect that, given more aerosols, there will be smaller and more numerous cloud particles: aerosol number and cloud particle number (per unit volume) would be positively correlated; aerosol number and cloud particle effective radius would be anti-correlated. This is not a new idea, and it has been investigated both in the field and with satellite data.

Most studies of aerosol-cloud relationships are mutually reinforcing: Kaufman et al. (1997) used AVHRR data to infer increases in warm cloud reflectivity (from 0.35 to 0.45) and decreases in cloud droplet effective radius (from 14 to 9 µm) when smoke is present; in modeling cloud parcels with data obtained during the Large-Scale Biosphere-Atmpsphere (LBA) experiment in Amazonia in 1998 and 1999, Roberts et al. (2003) found that biomass burning output can increase cloud droplet concentration by up to seven times in the dry season; for clouds over the ocean in middle and high latitudes both

Nakajima et al. (2001) and Suzuki et al. (2004) found a positive correlation between aerosol and cloud particle numbers, assuming that cloud reflectivity is inversely proportional to cloud particle effective diameter (see Figure 1.1); using AVHRR data, Nakajima found that the average effective radius has decreased by 10-15 % for low-cloud droplets in the Amazon basin, where biomass burning is prevalent (ref. in Roberts et al., 2003); Sherwood (2002a) noted a "clear [negative] correspondence" between a TOMS-derived aerosol index and cloud particle effective diameter (Figure 1.2); Jiang et al. (2008) had similar results comparing ice particle effective diameter and CO concentrations as a proxy for biomass-burning-derived aerosols. However, with the exceptions of Sherwood's and Jiang's work, most studies have focused only on the interaction between low (warm) clouds and aerosols. It is interesting that Nakajima et al. (2001) found large aerosol numbers in the tropics, but wrote "low [warm, as detected by satellite] clouds interacting with aerosols are not dominant in this region." This means that the clouds that could interact with tropical aerosols are high clouds, such as cumulonimbus and cirrus. It is also important to note that in the tropics one of the dominant aerosol types is dust, particles of which are effective ice nuclei (IN) but not effective cloud condensation nuclei (CCN). Other aerosols present in the tropics that may be more effective as IN than as CCN include organic aerosols, which are a significant component of smoke plume composition (Crutzen and Andreae, 1990). In fact, in the upper troposphere over half of the dry aerosol mass can be composed of organic materials (Zobrist et al., 2006).

The transport of smoke plumes has been studied (Artaxo et al.. 1998; Clarke et al, 2001; Gregory et al., 1996; Pickering et al., 2001; Trosnikov and Nobre, 1998). Talbot et al. (1999) found that "much of the tropospheric column from 2-10 km altitude [within the study volume of PEM Tropics A] was fumigated with varying degrees of combustion emissions." During the same study, air with high concentrations of combustion emissions was found south of the Southern Pacific Convergence Zone (SPCZ) that had been pumped through deep convection over Africa, and rapidly transported across the Pacific (Clarke et al., 1999). Despite using a model with no vertical diffusion, Trosnikov and Nobre (1998) found that plumes from biomass burning in Amazonia were carried offshore to the Pacific Ocean, below 3 km altitude and between 5°N and 5° S.

The effects of biomass burning may not be limited to the lower and mid-troposphere, however. There are established chemical links between the boundary layer and the stratosphere. For example, Pitari et al. (2002) noted that about 27 percent of stratospheric sulfate comes from the boundary layer, after being pumped upwards by convection. Sherwood and Dessler (2003), in an effort to model the seasonal variation of the concentration of carbon dioxide in the tropical tropopause layer (TTL, at 390K; the TTL ranges from 14 - 18.5 km, or 355 - 425 K, as described by Fueglistaler et al, 2009), found a lack of influence of air from the free troposphere--most of the influence on the state of this layer just below the stratosphere came from the boundary layer via convective updrafts.

The question remains whether or not combustion-derived aerosols will affect tropical cirrus. Sherwood (2002b) studied data retrieved from satellites, and was able infer a connection between biomass burning and cirrus microphysics. Using International Satellite Cloud Climatology Project (ISCCP) cumulonimbus ice crystal "effective diameter" (D_e) data derived from AVHRR measurements and water vapor estimates from Halogen Occultation Experiment (HALOE), Sherwood found that D_e was "tightly correlated" with a ratio of the humidity of an air parcel at a upper bound in the TTL to the humidity of that air parcel at a lower bound in the TTL, before having risen to the higher level (2002b). The anti-correlation between an aerosol index and D_e was found to be conspicuous "over regions of known biomass burning . . . suggesting that agricultural burns are the most important source of . . . influences on [cumulonimbus] ice crystal size" (2002a). Sherwood's papers, however encouraging to this proposed research, still fall short of making quantitative, direct links from biomass burning to cirrus microphysics and effects on stratospheric water vapor.

More recently, Jiang et al. (2008), investigating aerosol relationships to clouds and precipitation in South America, used satellite-derived CO concentrations as a proxy for biomass-burning-derived aerosols, and found a decrease in the effective radius of ice particles in "polluted" clouds ([CO] > 240 ppbv), especially in the dry season, when there is more aerosol loading and less vapor for the aerosol to interact with. They also found that there is less rain from polluted clouds during the dry season, which does not appear to be the result of dynamical differences between clean and polluted clouds. Lin et al. (2006) and Andreae et al. (2004) suggest that while the decrease in cloud droplet size by aerosols may decrease precipitation initially, later results would include an enhanced updraft (with smaller cloud droplets and less precipitation, there would be less drag and entrainment), leading to higher cloud tops. An enhanced updraft may also lead to greater convergence at the surface, increased precipitation, and increased frequency of intense precipitation events. Lin et al. (2006) found empirical evidence of these very interesting concepts, including higher cloud tops with increasing aerosol optical thickness, using various satellite-derived datasets. Still, the relationships described focus on only part of the picture—clouds and precipitation—and not how the distribution of gaseous water may change, over time, in the presence of aerosols.

As first steps towards establishing links between biomass burning output and stratospheric water vapor--what is considered an indirect aerosol effect--the University of Wisconsin Non-hydrostatic Modeling System (UWNMS) has been used to model the transport and activation of an idealized biomass burning-derived IN population, and the changes in water vapor distribution that follow changing cloud properties. In the bulk of pages to follow, we will explore field campaign data (Chapter 2), review the model's treatment of water vapor (Chapter 3), and evaluate model performance (Chapter 4) before turning the discussion to the results (Chapter 5) and discussion of two very interesting commonalities among the varied experiments (Chapters 6 and 7). This research shows how over a relatively short period--60 hours of modeled time--mesoscale effects of IN on water vapor exist, from the unsurprising, reassuring validation of the hypothesis that IN activation will lead to an increase in vapor aloft, to the unexpected amount of area showing *decreases* in vapor not caused by recent IN activation/vapor uptake for ice formation. What we can learn from this work, how the results can add to our understanding of vapor transport into the lower stratosphere, will be the focus of Chapter 8.

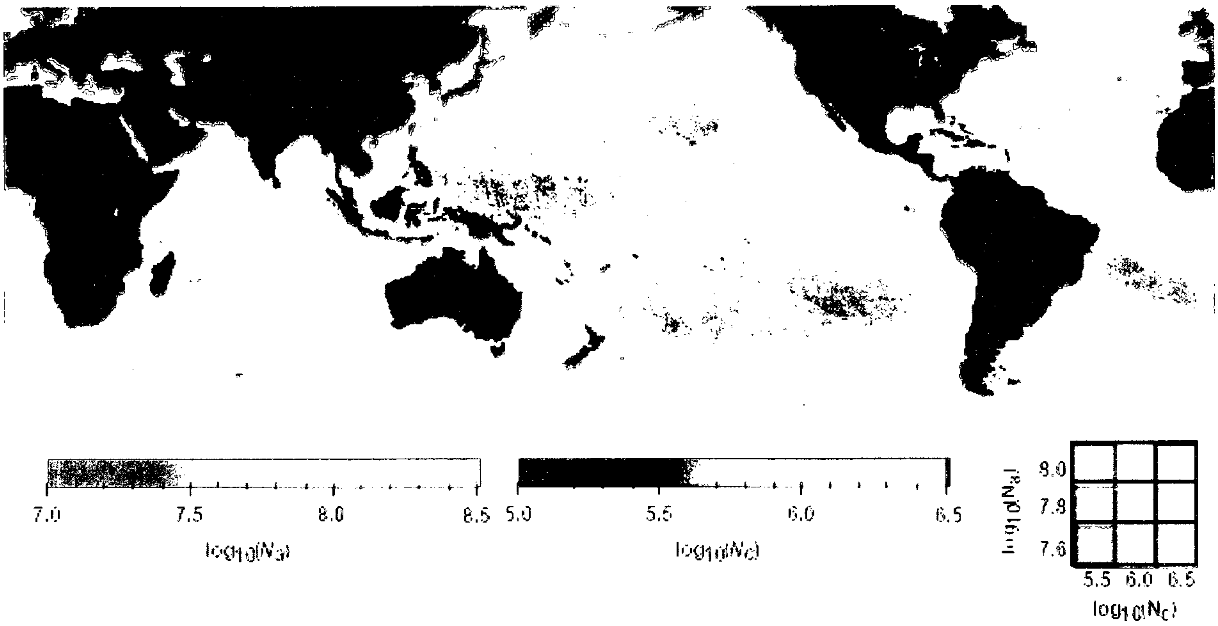

Figure 1.1. (adopted from Nakajima et al., 2001) From a study on low cloud-aerosol interaction over the oceans, the correlation between column aerosol number (red) and cloud particle number (green), both in particles/cm2, is shown for a four-month average of 1990. Bright yellow in this image indicates both aerosol and cloud particle numbers are large. The tropics are dominated by a bright red color, which indicates a large aerosol number but small cloud particle number. Nakajima et al. (2001) explained this by saying that "low clouds interacting with aerosols are not dominant in this region."

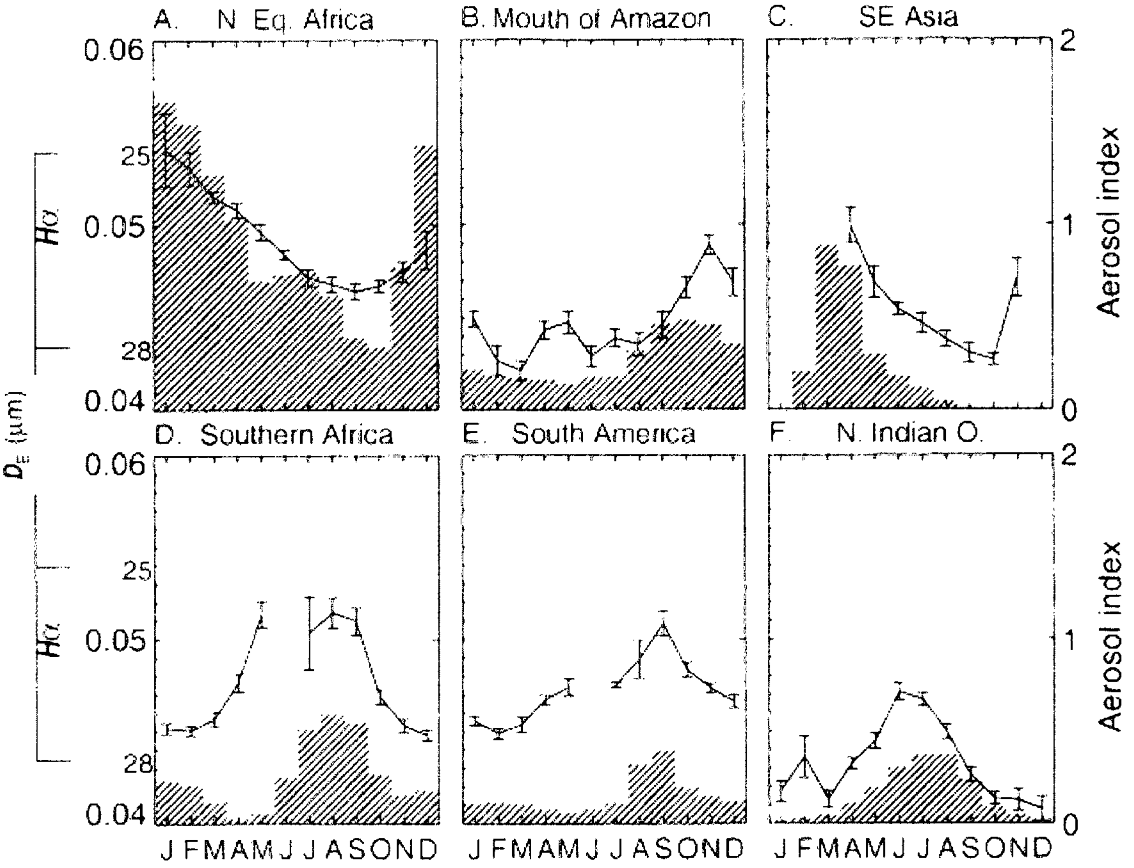

Figure 1.2. (adopted from Sherwood, 2002a) The seasonal relationship between cloud effective diameter (D_e, line plots, scale shown at left with small font) and an index of TOMS column aerosol amount (hatched areas, scale at right). The two are anti-correlated—when aerosol amount increases, D_e is seen to decrease.

Chapter 2: the Study Volume

Realizing that the tropical atmosphere was under-sampled in-situ, in the 1990's NASA organized three large-scale field campaigns with a focus on tropical chemistry: the Transport and Atmospheric Chemistry near the Equator-Atlantic (TRACE-A) experiment from 21 September – 26 October 1992; the Pacific Exploratory Mission-Tropics A (PEM-Tropics A) from 24 August – 6 October 1996; and PEM-Tropics B from 6 March to 18 April 1999. The areal coverage of these campaigns are shown in Figure 2.1. These three field campaigns are investigated in this chapter for their suitability –in terms of location, time, and presence of chemicals indicative of biomass burning-- for further study involving the UWNMS.

Chemical species indicative of biomass burning include monocarboxylic acids such as formic acid (HCOOH) and acetic acid (CH_3COOH), methyl chloride (CH_3Cl), ethane (C_2H_6), and ethyne (C_2H_2) (Gregory et al., 1999; Talbot et al. 1999). Table 2.1 lists compounds indicative of biomass burning that were measured during these three field campaigns. Crutzen and Andreae (1990) found that emissions of non-methyl hydrocarbons (such as ethane and ethyne) peak during smoldering combustion, when the fire temperatures are lower and combustion less efficient. Combustion efficiency varies, and hence predominant emissions vary, with length of burning time as well as fuel type. Often a fire will quickly reach a flaming stage, with rapid combustion and high temperatures, then progress into the smoldering phase, characterized by declining temperatures. Fires occurring in humid airmasses, such as in Southeast Asia, have a dampened flaming stage of combustion, and more time spent in the smoldering stage where combustion efficiency is low (Tang et al., 2003). In the Brazilian Amazon, a significant portion of biomass burning occurs as pasture maintenance and clearing, which includes burning stumps, roots, downed branches and organic material in soil. These materials tend to smolder when burned (Bertschi et al., 2003). During flaming combustion, which takes place at high temperatures, most products are oxidized, unlike smoldering combustion, during which products are emitted directly to the atmosphere without oxidation (Bertschi et al., 2003). The predominant emissions of flaming combustion are carbon dioxide, formed from efficient combustion of carbon-rich plant material, and nitrogen oxides, formed by oxidation of the air within the flame (Crutzen and Andreae, 1990).

DC-8 flight numbers 6, 7, 10, 13, 15, and 16 of the TRACE-A experiment, 6, 8, 12, 17, and 18 of PEM Tropics A, and 5 and 6 of PEM Tropics B were selected for having sampled, at cirrus-like altitudes, high concentrations of chemicals indicative of biomass burning plumes (Table 2.1). Figures 2.2 – 2.4 show concentrations of chemical species associated with some of these plumes detected during TRACE-A flight no. 6 (27 September 1992), PEM Tropics-A flight no. 17 (1-2 October 1996), and PEM Tropics-B flight no. 5 (6-7 March 1999), respectively. Circled time-height sections correspond to plumes included as part of a trajectory study (below). For comparison, mean values of ethane, ethyne, acetic acid, and nitric acid in "aged marine" air (air that has not been influenced by continental emissions for at least 5 days) are given in Figure 2.5. Tropical South Atlantic data (magenta) are derived from air samples taken during TRACE-A, and indicate an aged biomass burning influence in upper levels of the atmosphere (Talbot et al., 1996). The Pacific basin south of the ITCZ is represented in blue, from data collected during PEM Tropics-A (Gregory et al., 1996).

TRACE-A	***PEM Tropics A***	***PEM Tropics B***
CO_2, CO, CH_3Cl (methyl chloride), C_2H_6 (ethane), C_2H_4 (ethene), C_2H_2 (ethyne), H_2O_2, CH_3OOH (methyl hydroperoxide), N_2O, CH_4, HNO_3, HCOOH (formic acid), CH_3COOH (acetic acid), peroxyacetyl nitrate (PAN)	CO_2, CO, CH_3Cl (methyl chloride), C_2H_6 (ethane), C_2H_4 (ethene), C_2H_2 (ethyne), H_2O_2, CH_3OOH (methyl hydroperoxide), N_2O, CH_4, HNO_3, HCOOH (formic acid), CH_3COOH (acetic acid), CH_3ONO_2 (methyl nitrate), peroxyacetyl nitrate (PAN)	CO_2, CO, CH_3Cl (methyl chloride), C_2H_6 (ethane), C_2H_4 (ethene), C_2H_2 (ethyne), H_2O_2, CH_3OOH (methyl hydroperoxide), N_2O, CH_4, HNO_3, CH_3ONO_2 (methyl nitrate), peroxyacetyl nitrate (PAN)
CCN, aerosol number and number density	CCN, unheated and heated fine aerosol, ultrafine aerosol, aerosol size distribution, number density	unheated and heated fine aerosol, ultrafine aerosol, aerosol size distribution, number density

Table 2.1. Atmospheric constituents measured during each experiment on high-altitude DC-8 flights that correlate to biomass burning emissions.

Data from TRACE-A flight no. 6 show a reasonably well fumigated boundary layer. Concentrations of ethane, ethyne, and acetic acid are all high relative to background amounts (Figure

2.5). At the top of the first ascent and just after the start of the second descent, between 8 and 10 km in altitude, concentrations of all three chemical species indicate plume samples along the flight track. PEM Tropics-A flight no. 17 seems to have sampled plumes at the top of the first ascent and during the last descent, as evidenced by relatively high concentrations of the same three chemical species. However, the "high" values seen on the PEM Tropics-A flight are not nearly as high as those for the TRACE-A flight. This may suggest an older plume, which has been diluted over time and distance. Data from PEM Tropics-B flight no. 5 suggest plumes were sampled at the top of the first ascent, just above 10 km at ~70000 seconds, and in the boundary layer at the end of the first descent. Since acetic acid was not detected during the PEM Tropics-B campaign, this "plume" estimation uses ethane, ethyne, and nitric acid. The TRACE-A flight and the PEM Tropics-A flight both appear to have sampled plumes from smoldering combustion, since there are high concentrations of non-methyl hydrocarbons but not high concentrations of carbon dioxide nor nitrogen oxides such as PAN (not shown). The PEM Tropics-B flight, on the other hand, seems to have sampled a mixed plume above the boundary layer—the concentrations of both ethane and ethyne are high, as is nitric acid, which results from nitrogen oxides reacting with water vapor.

But where did the plumes come from? Isentropic trajectories (Figures 2.6 – 2.8) for these three flights were calculated to find out, though we need to view these results with some caution since the trajectory method, which does not account for cloud radiative heating or cooling, is ill-suited for use in cloudy areas (Fuelberg et al., 1996). 10-day backward trajectories ending along $\theta = 340$ - 350 K (300 – 200 hPa) portions of the flight track of TRACE-A no. 6 traveled northwestward in the flow of the South Atlantic high, which suggests that the biomass burning chemicals detected on this flight (plumes 1 and 2) were produced locally. These trajectories seem more than reasonable given the average meteorological conditions during the TRACE-A experiment (Bachmeier and Fuelberg, 1996). Air arriving along $\theta = 340$ - 350 K (again, 300 – 200 hPa) portions of the flight track of PEM Tropics-A flight no. 17 put on quite a show. About two-thirds of the trajectories track the ITCZ, moving westward towards the flight track. The remainder, which includes likely smoke plume materials, undertook various journeys to the flight track, sweeping along a mid-latitude system off the coast of New Zealand and into the realm of the South

Pacific Convergence Zone (SPCZ), which angles southeastward between these two trajectory "regimes" (Fuelberg et al., 1999). Given the relative cleanliness of South Pacific air, it is unclear what the source is of the combustion-derived chemicals sampled on this flight, though kinematic trajectory studies show southern Africa and South America to be potential sources (Board et al., 1999). The ten-day backward trajectories ending on $\theta = 320 - 360$ K (600 – 200 hPa) portions of the track of PEM Tropics-B flight no. 5 show air that has curved around the North Pacific high, having passed southward from Alaska and eastward from northern Asia. Fuelberg et al. (2001) also calculated trajectories for this flight, with some trajectories suggesting travel over Alaska, similar to those shown here, but most of their trajectories traveled from Japan, southern China, Southeast Asia, even northern Africa. The difference in these trajectories is likely the technique; the clouds associated with the Aleutian Low hinders the isentropic calculations shown in Figure 2.8. This implies that combustion-derived chemicals sampled on this flight (plume 5) may have "industrial" sources such as vehicle combustion and cooking fires (China and Japan) as well as biomass burning sources (Southeast Asia).

How likely is it that these sampled plumes would interact with cirrus? Again, we will look at isentropic trajectories, though forward five days in time, and compare trajectory paths to satellite images to gauge potential smoke-cirrus interaction. Figures 2.9 – 2.11 show those portions of trajectories on and between the 340 K and 360 K isosurfaces, or approximately 500 to 200 hPa. At first glance the forward trajectories from TRACE-A flight no. 6 appear to be erroneous, since there is very little horizontal movement (Figure 2.9). However, knowing that copious convection, including mesoscale convective complexes (MCSs), occurred ahead of a cold front that was slowly moving through the region (Bachmeier and Fuelberg, 1996), and given how poorly the isentropic assumption fares in areas of cloudy convection, the trajectories seem reasonable. The satellite image in Figure 2.9 shows widespread convection roughly halfway through the forward trajectory calculation time. It seems extremely likely then that the biomass burning emissions detected during TRACE-A flight no. 6 would interact with cirrus.

The potential for cirrus interaction with combustion material sampled during PEM Tropics-A flight no. 17 is also likely. Figure 2.10 shows how the trajectories initialized along that flight track propagate northwestward towards the Maritime Continent, along the SPCZ line and towards the SPCZ-ITCZ confluence (Fuelberg et al., 1999), where they become stagnant. We can safely assume then that biomass burning emissions and cirrus would likely interact in this region. Air sampled along upper portions of the PEM Tropics-B flight track (Figure 2.11), covering about 6 to 11 km in altitude, has varying pathways forward in time. Some trajectories move with the circulation of the North Pacific High, moving southwestward to join the trade winds. Others move northeastward ahead of a mid-latitude trough (Fuelberg et al., 2001). Infrared satellite images (such as the one in Figure 2.11) covering the forward trajectory time period indicate the trajectory swath had little influence or interaction with high clouds. Though the biomass burning emissions detected on PEM Tropics-B flight no. 5 may eventually advect to a region with cirrus formation, it appears unlikely during this time frame, making the PEM Tropics-B campaign unattractive for further study with the UWNMS.

This leaves the TRACE-A and PEM Tropics-A time periods as candidates for study with the UWNMS. TRACE-A trajectories suggest emissions from local sources, which is supported by a satellite fire count (Figure 2.12), and near-certain biomass burning chemical-interaction with ice particle formation in clouds, evidenced by both meteorological analysis (Bachmeier and Fuelberg, 1996) and satellite imagery (Figure 2.9). PEM Tropics-A trajectories may have a biomass burning source (Board et al., 1999), which seems reasonable given fire counts over Australia and Africa in the days preceding flight no. 17 (Figure 2.13), and emissions are transported to a region where intense convection and lofting may occur. Either field campaign would be suitable for investigation with the UWNMS, however, given the strong spatial concurrence of biomass burning –we've seen there's a lot more biomass burning-derived chemicals in the air over Brazil, which means a greater potential for some of that "gunk" to be ice nuclei—and potential cirrus interaction during TRACE-A, that time period appears more attractive and was selected for study. The general circulation over this area in boreal autumn is such that the atmosphere is fairly well-fumigated with biomass burning emissions—most of the area's biomass burning takes place late in the dry season (August through October) and is mixed by diurnal convection (Chapter 4). The one disadvantage to this choice is that convection (hence biomass burning emission transport and cirrus formation) may not reach the high altitudes over South America as it can over the

Maritime Continent. Though not part of the "stratospheric fountain," the region above northern South America may still be important for vapor entering the stratosphere (Dessler, 1998). In the next chapters, we will explore how well the UWNMS represents conditions present before, during, and after TRACE-A flight no. 6, and how varying IN concentrations and properties affect the local distribution of water vapor.

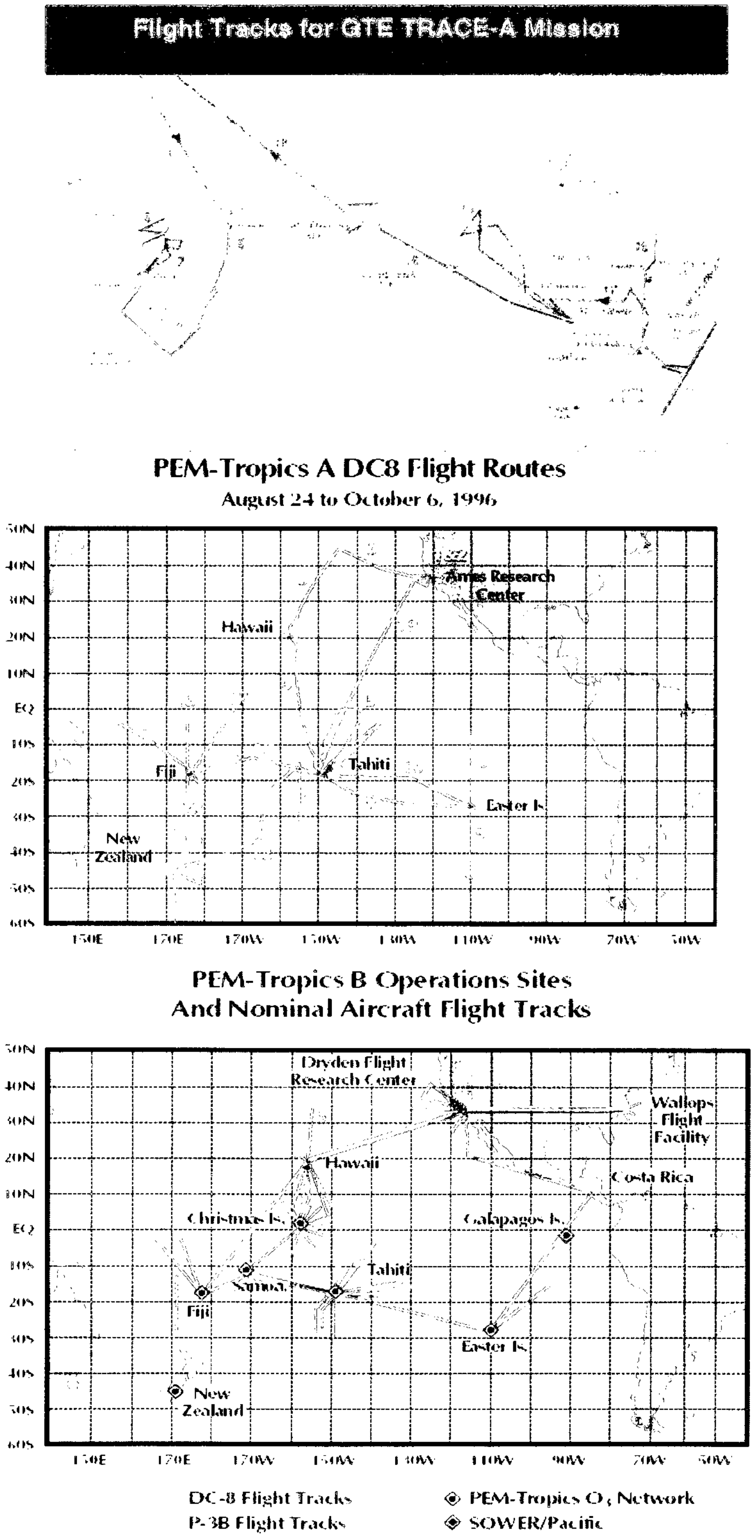

Figure 2.1. Flight tracks of three NASA Global Tropospheric Experiment (GTE) field campaigns, TRACE-A, PEM-Tropics A, and PEM-Tropics B.

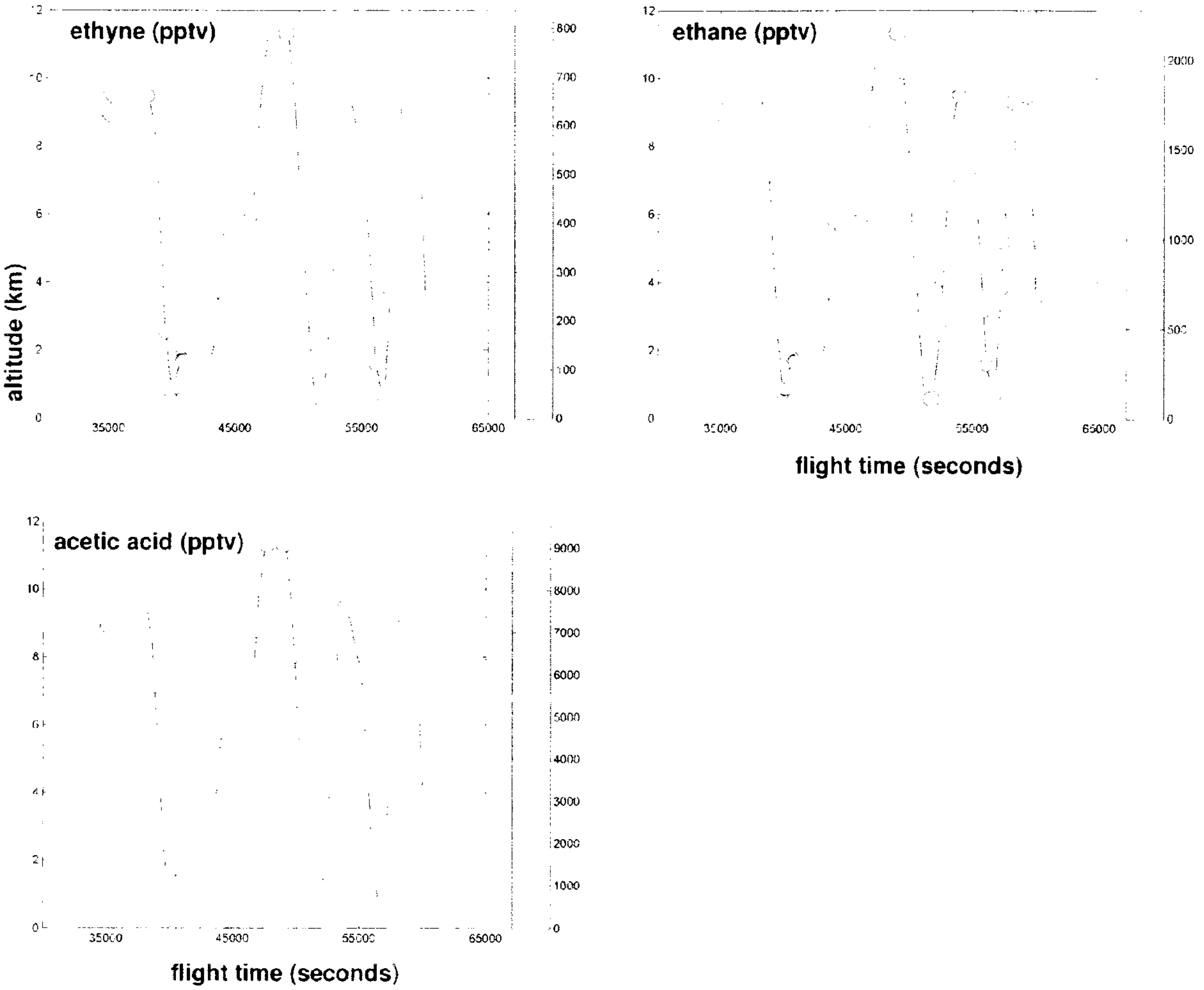

Figure 2.2. Concentrations of ethyne (upper left), ethane (above), and acetic acid (lower left) detected along TRACE-A flight number 6, which took place September 27th, 1992 over northeastern Brazil. Concentrations are color coded; blue indicates missing data. The concentrations of all three are high during the first peak, the first two descents into the boundary layer, indicating likely smoke plume (or pall) samples. The concentrations of ethyne and ethane are also elevated between 8 and 10 km of the descent from the second peak, which could indicate a plume that experienced some loss of acetic acid through dry or moist scavenging.

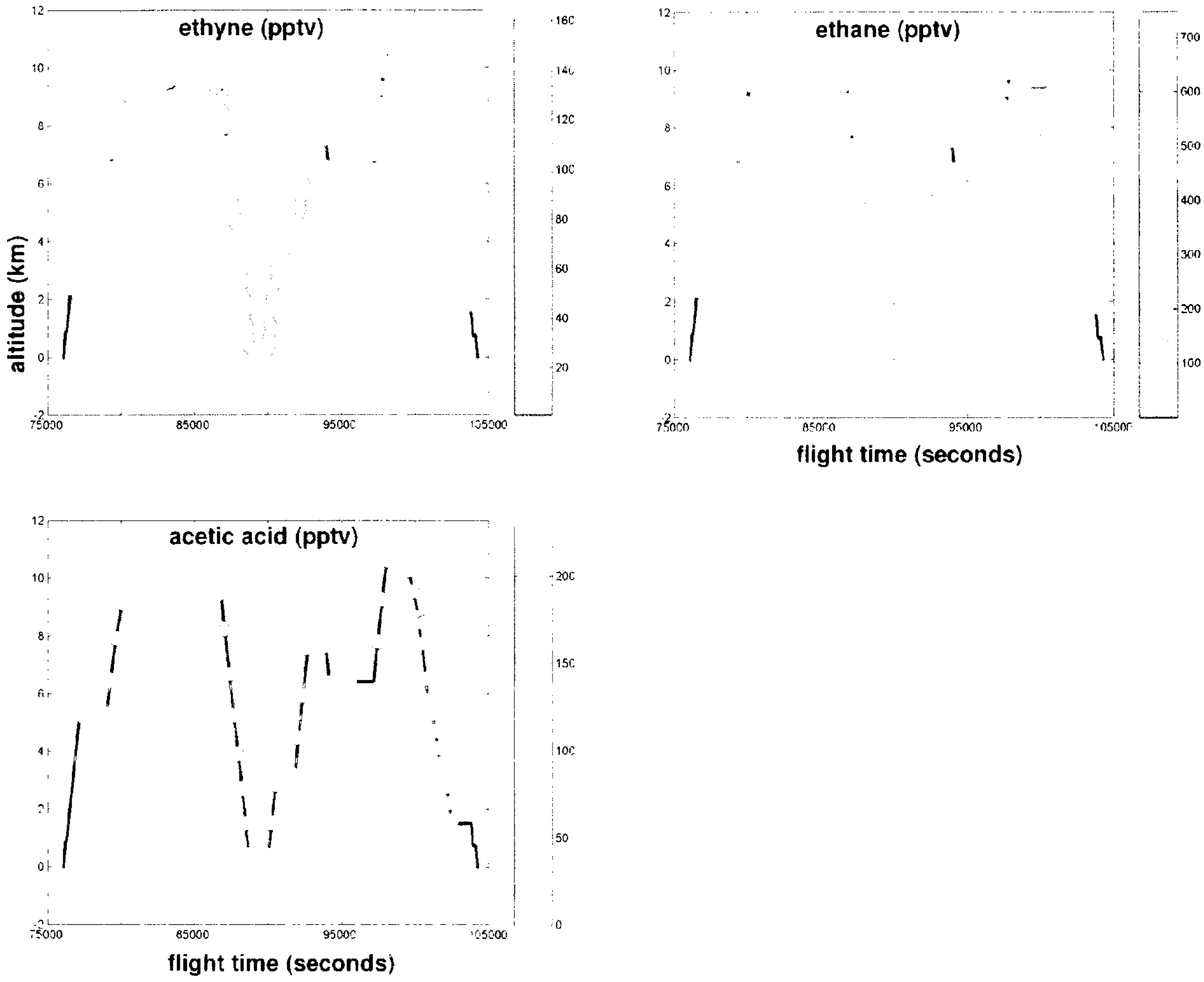

Figure 2.3. Concentrations of ethyne (upper left), ethane (above), and acetic acid (lower left) detected along PEM Tropics-A flight number 17, which took place the 1st and 2nd of October 1992 from Fiji northeastward to the equator and back. Concentrations are color coded; blue indicates missing data. The concentrations of all three are high just after 80000 seconds and during the last decent, indicating likely smoke plume (or pall) samples.

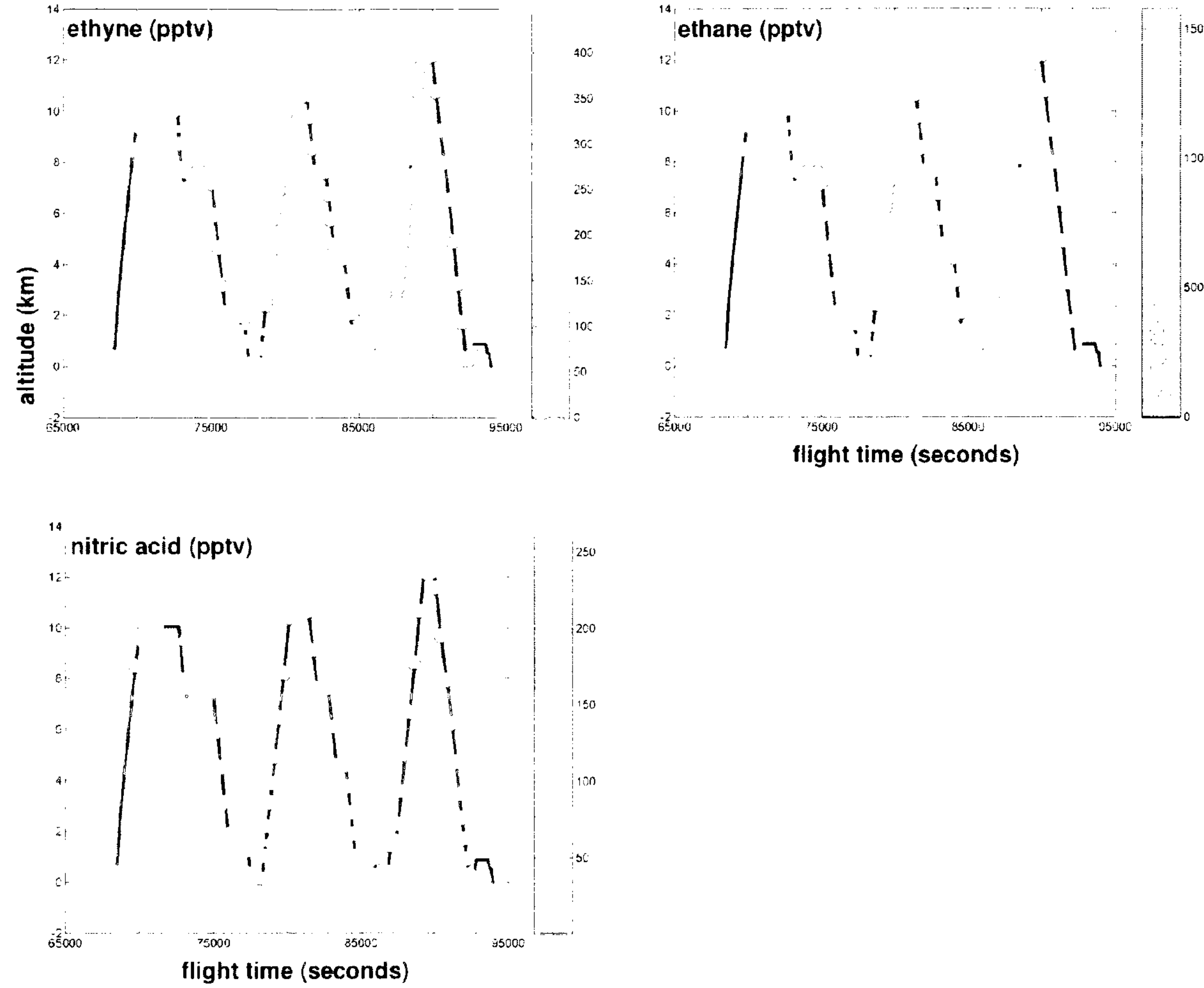

Figure 2.4. Concentrations of ethyne (upper left), ethane (above), and nitric acid (lower left) detected along PEM Tropics-B flight number 5, which took place the 6th and 7th of March 1999 from the Dryden Flight Research Center in California to Hawaii. Concentrations are color coded; blue indicates missing data. The concentrations of all three are high just after 72000 seconds and in the first descent into the boundary layer, indicating a likely smoke plume (or pall) samples.

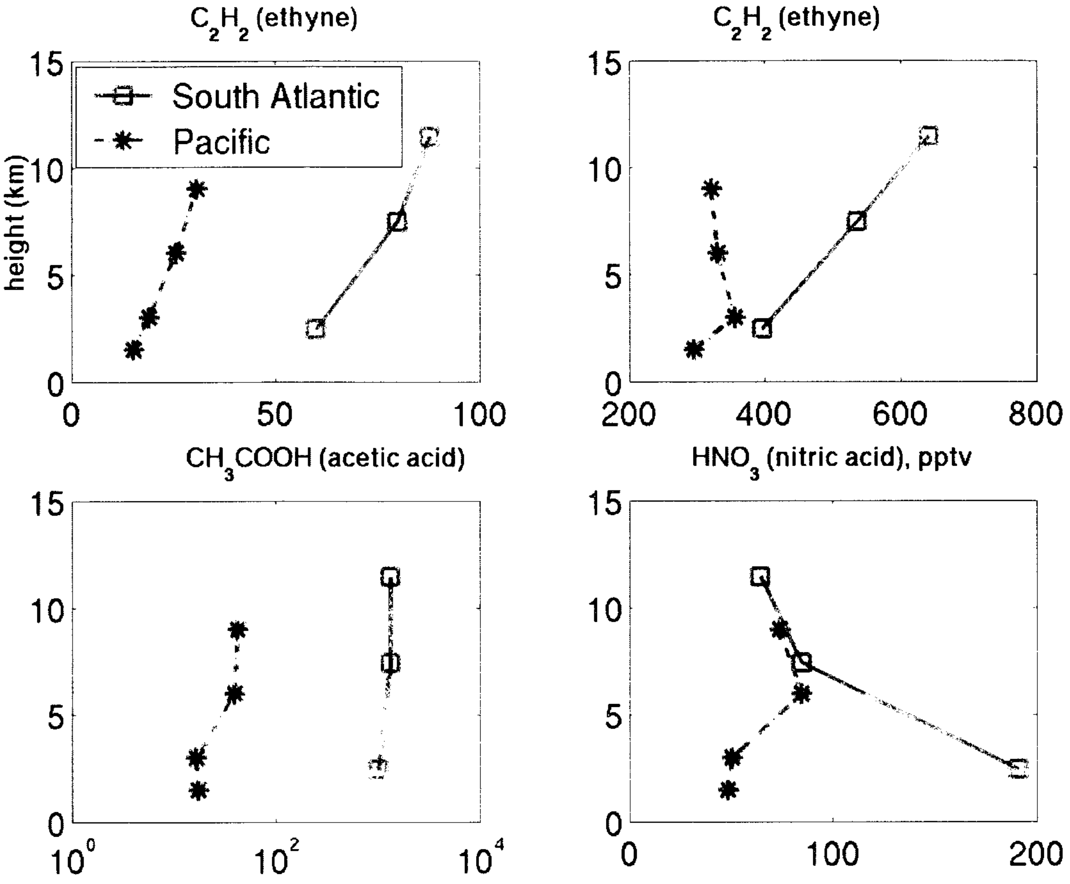

Figure 2.5. Average concentrations (pptv) in aged marine air over the tropical South Atlantic, in magenta, adapted from Talbot et al., 1996, as well as median concentrations (pptv) sampled south of the ITCZ in the Pacific basin during PEM Tropics-A, in blue, adapted from Gregory et al., 1999.

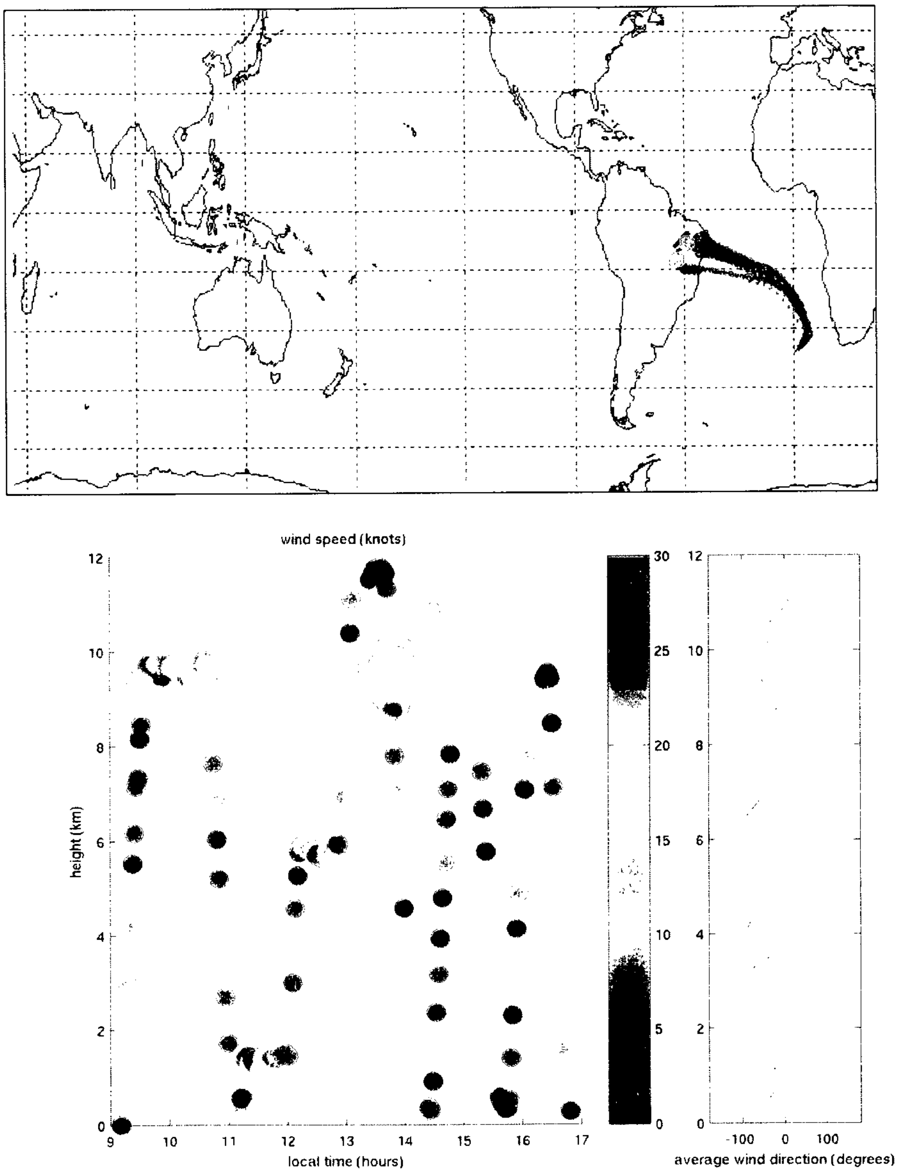

Figure 2.6. The age of 10-day backward trajectories ending on θ = 340 - 350 K portions of the flight track of TRACE-A flight no. 6, 27 September 1992 (top), with *in-situ* wind measurements (bottom). The trajectories are shown with positions every 12 hours, color coded such that the oldest are orange and yellow. Green dots on the trajectory plot indicate those portions of the flight track that appeared to sample a plume above the boundary layer, between 8 and 10 km (see Figure 2.2), the times/heights of which are circled on the wind plot. Both plumes were found in areas with north-northwesterly winds averaging about 10 knots.

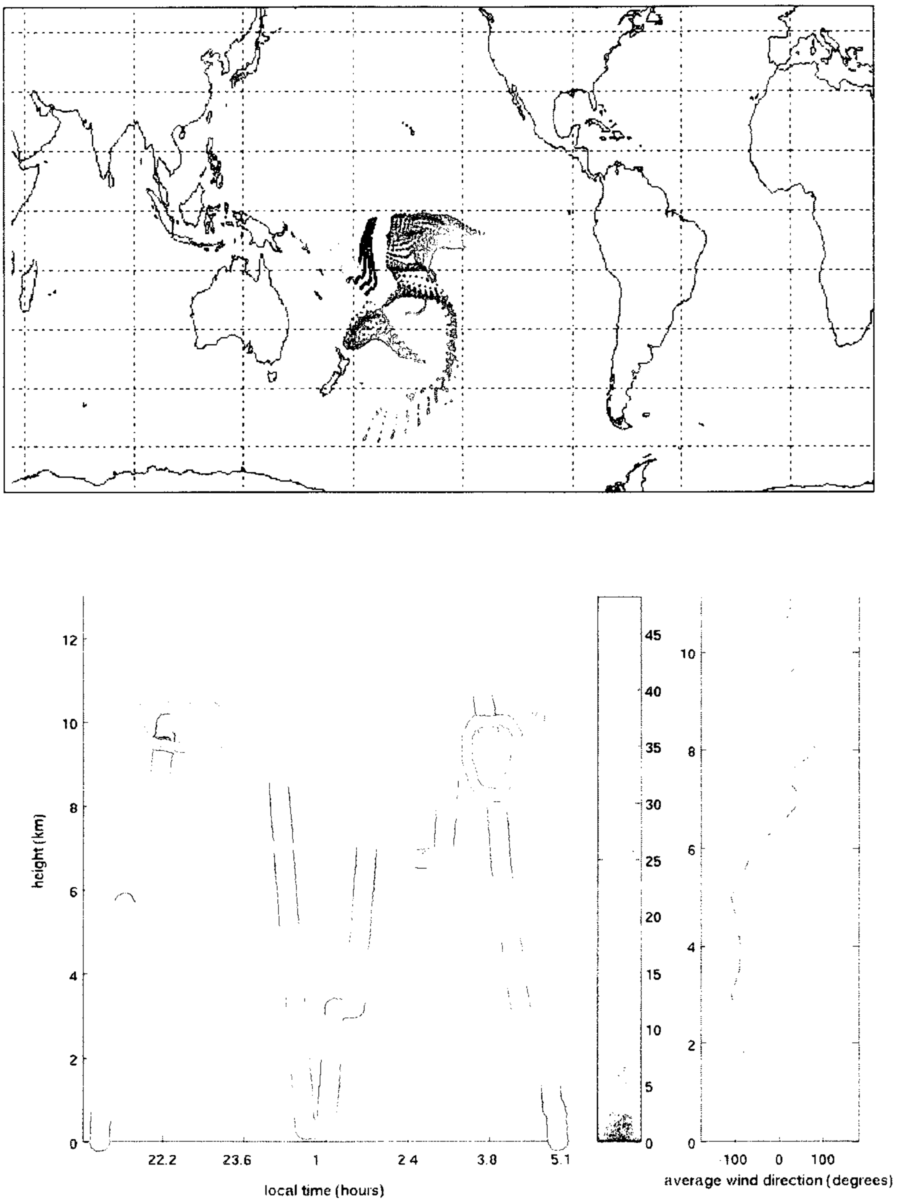

Figure 2.7. The age of 10-day backward trajectories ending on θ = 340 - 350 K portions of the flight track of PEM Tropics-A flight no. 17, 1-2 October 1996 (top), with *in-situ* wind measurements (bottom). The trajectories are shown with positions every 12 hours, color coded such that the oldest are orange and yellow. The green dot on the trajectory plot indicates the portion of the flight track that appeared to sample fumigated layers between 8 - 10 km (see Figure 2.3). Because this flight left from and returned to Fiji, it appears that the same plume may have been sampled twice. Both periods of potential plume-detection occurred where winds were northeasterly, between 25 – 50 knots.

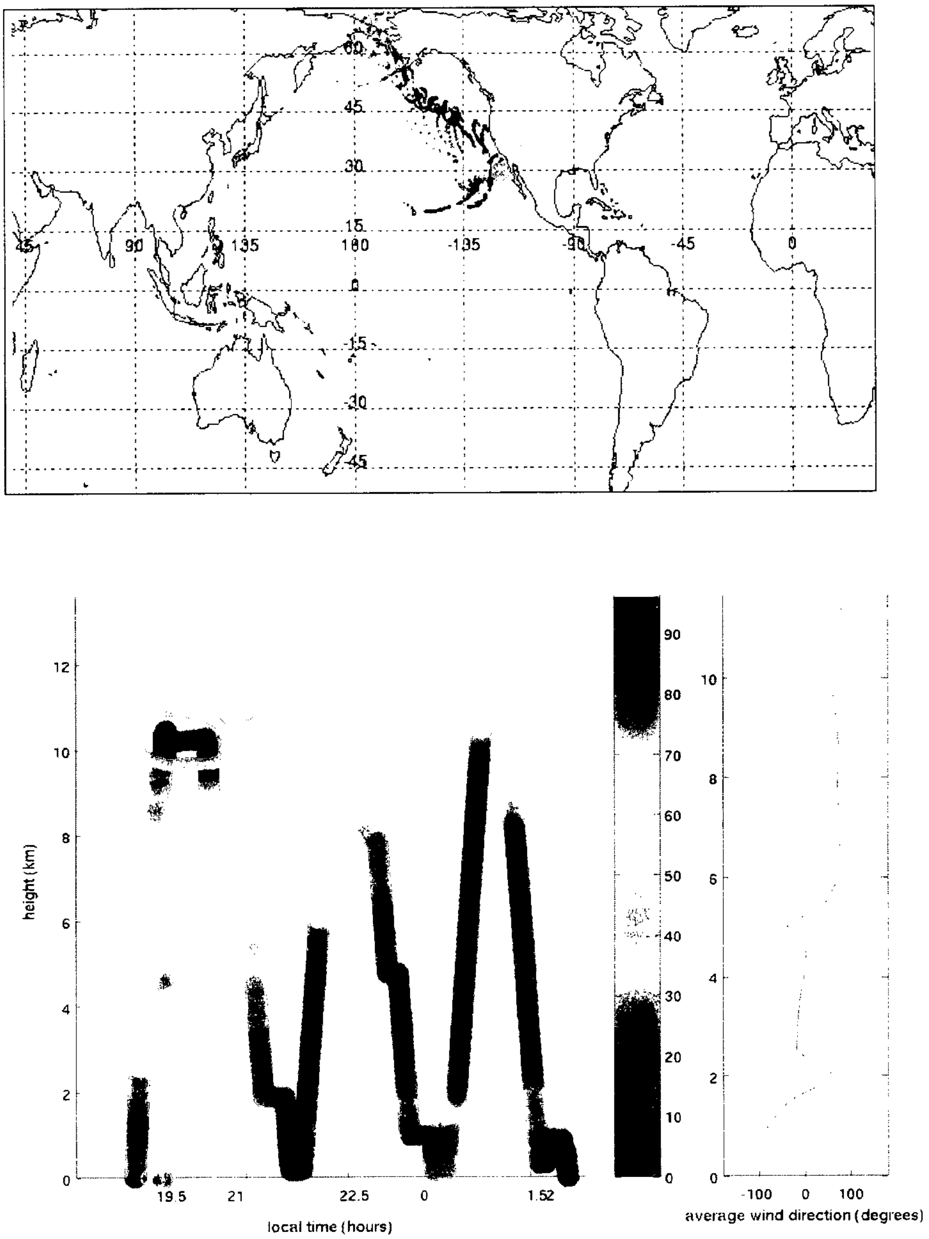

Figure 2.8. The age of 10-day backward trajectories ending on θ = 320 - 360 K portions of the flight track of PEM Tropics-B flight no. 5, 6-7 March 1999 (top), with *in-situ* wind measurements (bottom). The trajectories are shown with positions every 12 hours, color coded such that the oldest are orange and yellow. The green dot on the trajectory plot indicates the portion of the flight track that appeared to sample a plume just above 10 km (see Figure 2.4), which was found in an environment with northeasterly winds of 80 – 90 knots.

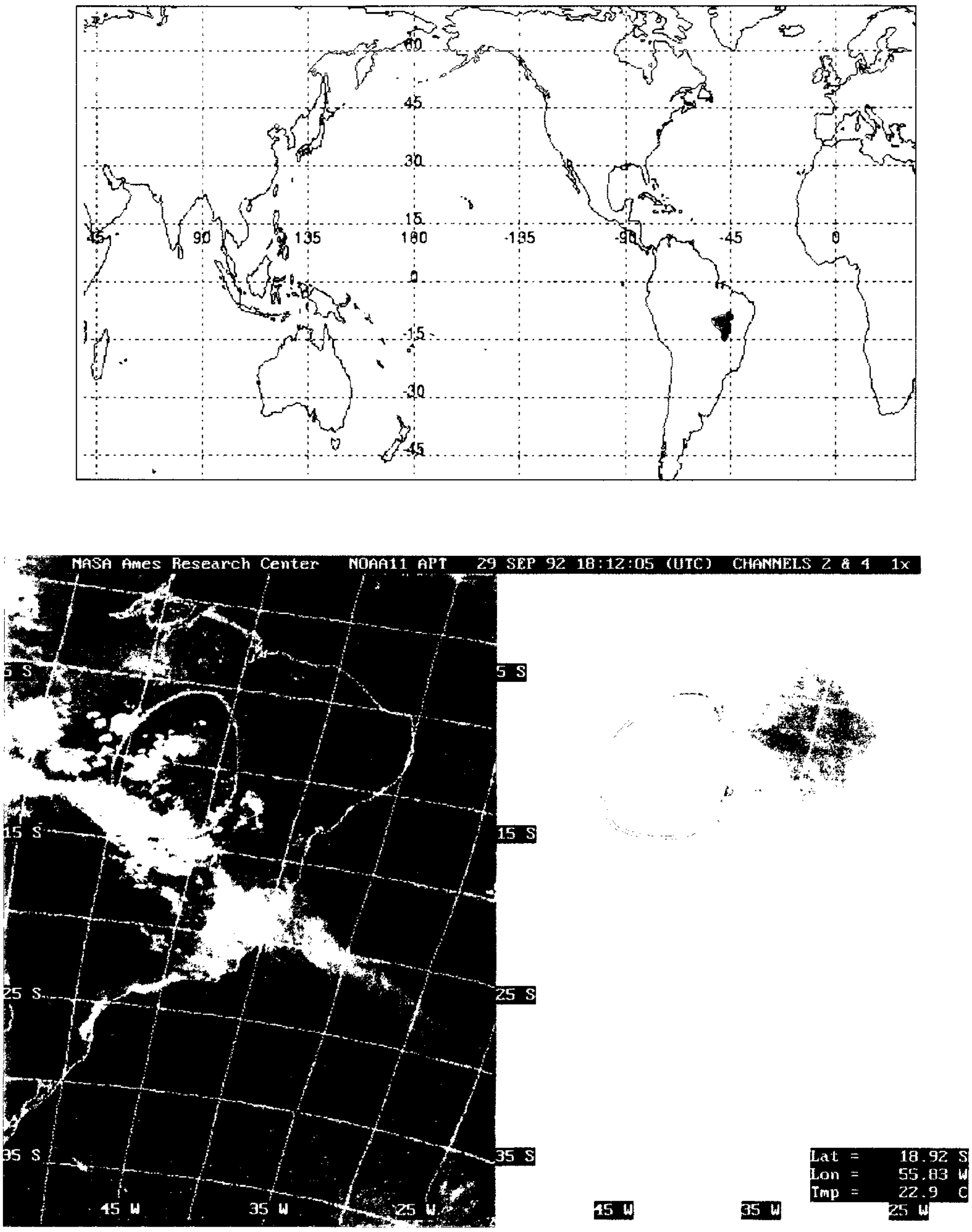

Figure 2.9. The age of 5-day forward trajectories starting on the flight track of TRACE-A flight no. 6 (top), covering 27 September 1992 at 12Z to 3 October 1992 at 0Z. The trajectories, initialized along all flight altitudes (~0.5 to 11.5 km), are shown with positions every 12 hours, color coded such that the oldest are black and blue. Also shown are visible and infrared satellite images from the AVHRR instrument onboard NOAA-11 corresponding to 18:12Z on 29 September, with the flight's study volume circled in red.

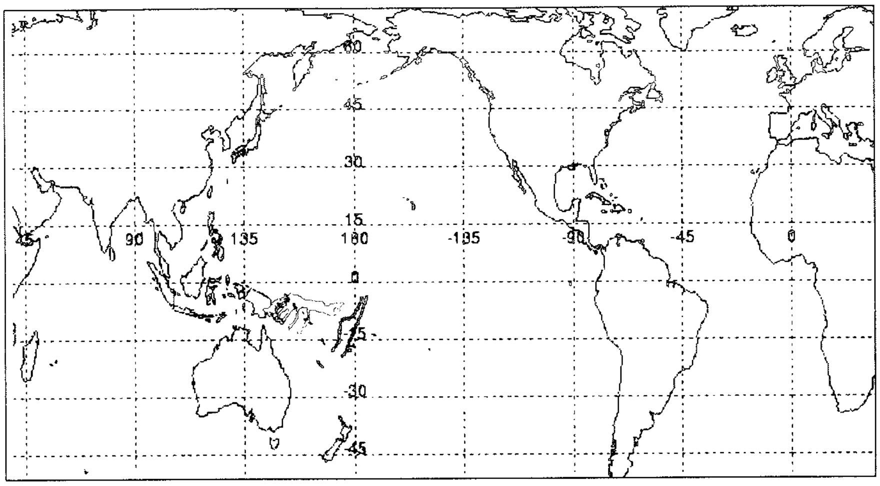

Figure 2.10. The age of 5-day forward trajectories starting on the flight track of PEM Tropics-A flight no. 17 (top), covering 2 October 1996 at 0Z to 7 October 1996 at 12Z. The trajectories are shown with positions every 12 hours, color coded such that the oldest are black and blue. The flight volume is indicated on an infrared satellite image from NOAA's GOES-9 corresponding to 7 October at 0Z.

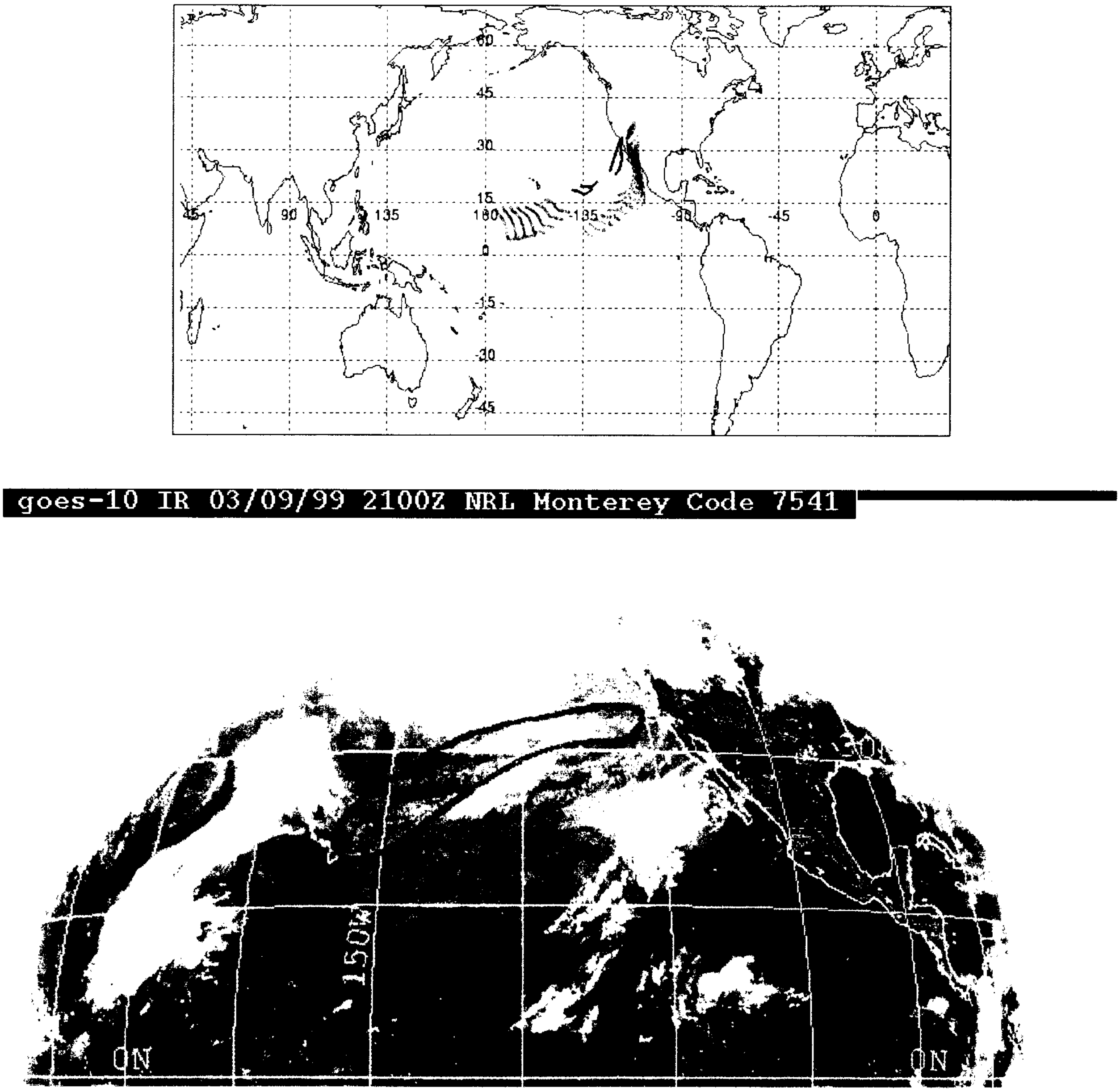

Figure 2.11. The age of 5-day forward trajectories starting on the flight track of PEM Tropics-B flight no. 5 (top), covering 7 March 1999 at 0Z to 12 March 1999 at 0Z, with an infrared satellite image from NOAA's GOES-10 corresponding to 21Z on 9 March. The trajectories are shown with positions every 12 hours, color coded such that the oldest are black and blue. Some trajectories move with the circulation of the North Pacific High, others move northeastward ahead of a mid-latitude trough.

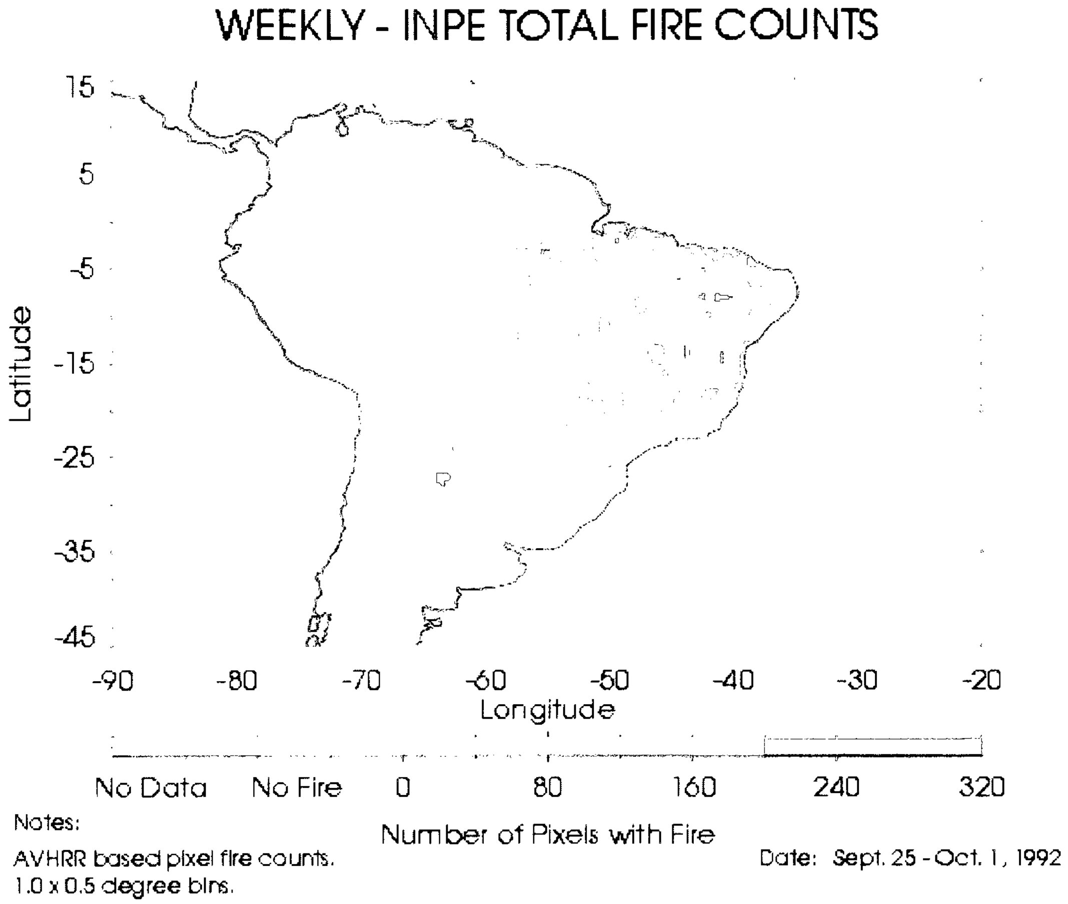

Figure 2.12. From the Instituto Nacional de Pesquisas Espaciais (INPE), or National Institute for Space Research, of Brazil: the total number of fire pixels detected using NOAA's AVHRR data over five days, bracketing the duration of TRACE-A flight no. 6 on 27 September 1992.

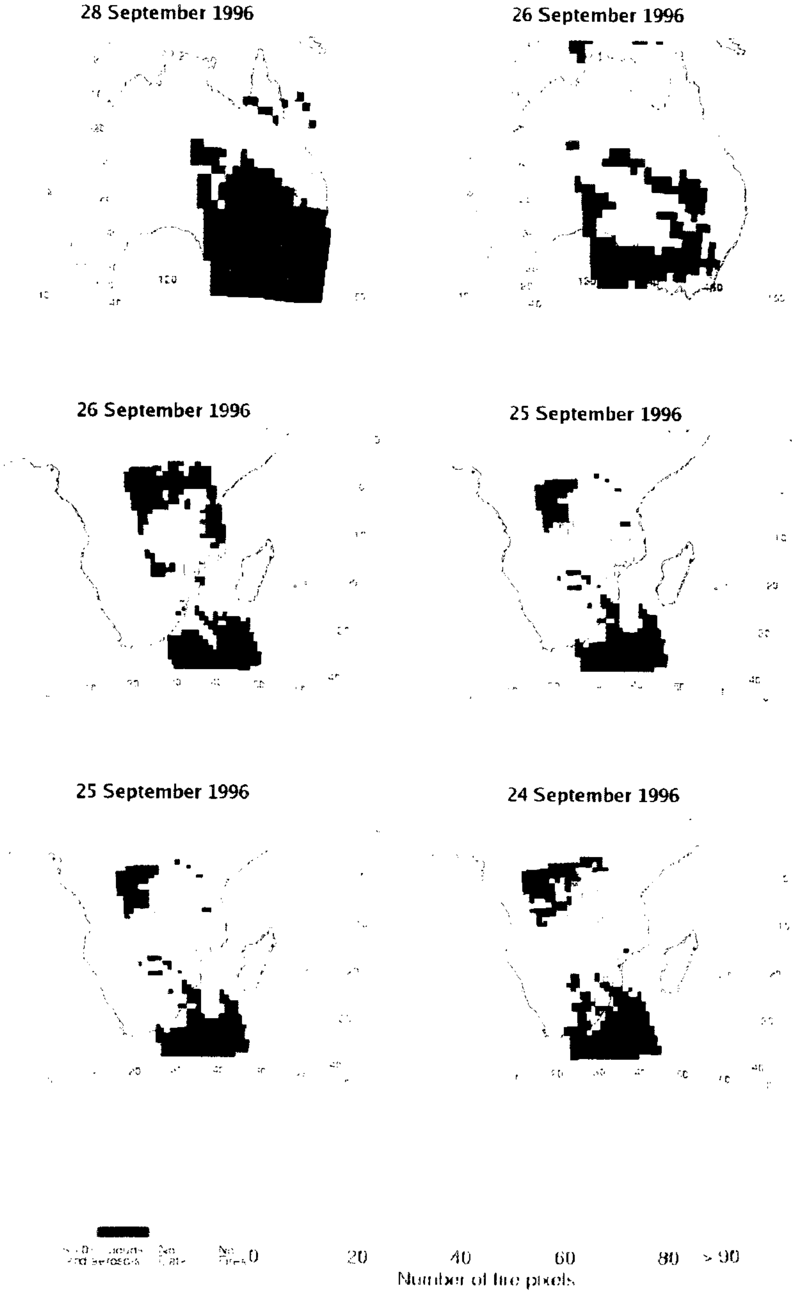

28 September 1996

26 September 1996

26 September 1996

25 September 1996

25 September 1996

24 September 1996

Figure 2.13. AVHRR-derived daily total fire counts for portions of Australia (top row) and Africa (middle and bottom rows). Reading left to right and top to bottom, days correspond to the trajectories calculated backwards in time starting 2 October, at the end of PEM Tropics-A flight no. 17.

Chapter 3: the UWNMS

Tropical regions, with frequent convective activity, are best represented by a non-hydrostatic model such as the UWNMS. This study is composed of several UWNMS model runs for varying concentrations of our idealized heterogeneous ice nucleus. The UWNMS is initialized with two datasets, ECMWF meteorological analyses and HALOE water vapor. The initial state of the model is set by these datasets. Once past the initial state (at zero seconds), the model diagnoses meteorological variables itself, now using the datasets only as boundary conditions. In this section, the ECMWF and HALOE datasets will be described, followed by a discussion of the overall structure of the UWNMS as well as specific information on its treatment of water vapor.

the ECMWF analyses

The ECMWF operational analyses used for this research comprise of 2.5 x 2.5 degree gridded global surface and upper air data. Variable data such as temperature, relative humidity, pressure, geopotential height, and meridional, zonal, and vertical winds are compiled twice daily (at 0Z and 12Z) to make each monthly file. The vertical resolution (i.e., the number of standard pressure levels) depends on the year—before April of 1999 analyses used 15 levels, and afterwards 21, with levels being added at 20, 7, 5, 3, 2, and 1 hPa. Detailed information about the ECMWF operational dataset and the Integrated Forecast System (IFS) can be found online (http://badc.nerc.ac.uk/data/ecmwf-op/ and http://www.ecmwf.int/research/ifsdocs/) as well as in a paper by Trenberth (1992).

the HALOE dataset

A reasonable representation of the water vapor distribution, for use as both starting and boundary conditions by the UWNMS is extremely important for this research. Though it does account for the production of water vapor by methane oxidation in the mid-stratosphere, ECMWF data do not include any assimilated observations of stratospheric water vapor. This may explain the too-rapid movement of the water vapor "tape-recorder" as well as the dry bias above 250 hPa in ECMWF analyses (Lahoz et al., 2004, and Jensen et al., 1999, respectively). In order to more accurately represent the vertical profile of water vapor, HALOE data were put in to the model.

As the instrument uses solar occultation to obtain data, HALOE volume mixing ratio data are composed of about 15 sunset and 15 sunrise measurements made daily, at differing latitudes, with the entire range of ~60°S to 60°N sampled, on average, monthly (Russell et al, 1993). Because of the lack of more frequent measurements, data binning and averaging were performed to create monthly files of mass mixing ratio data to use as UWNMS input.

For the experiments described in Chapters 5 – 7, both sunrise and sunset HALOE data were obtained, averaged over a calendar month, and binned by both pressure and latitude (see Table 3.1). Gaps in data, which evidenced themselves as bins having a value of zero, were filled using a polynomial fit to any existing data. For example, if all pressure bins for a particular latitude bin were filled except one, the non-zero data were used in the interpolation of a value for the empty bin. A polynomial fit was necessary since the data for a given latitude are not linear over the pressure range (Figure 3.1). Figure 3.2 shows the binned and averaged data for the month of September 1992. Figure 3.3 illustrates the difference HALOE data makes in the vertical distribution of water vapor in the UWNMS.

pressure bins	200 hPa	150 hPa	100 hPa	70 hPa	50 hPa	30 hPa	10 hPa
latitude bins	30°S	20°S	10°S	0°	10°N	20°N	30°N

Table 3.1. Latitude and pressure bins created for HALOE monthly compilations.

the UWNMS

For all model runs described in the following sections, the UWNMS was set up with a domain of 140 and 90 gridpoints in the x and y planes, respectively, and 100 in the vertical, with a horizontal spacing of 30 km and vertical spacing of 200 m. The altitude of the domain stretches from the surface up to and including 20 km. The vertical gridpoint spacing was chosen to allow for the resolution of any convectively-generated gravity waves (Joan Alexander, personal communication). With this resolution the maximum model timestep allowed, and hence what was used, is twenty seconds. The model grid was centered at 5° N and -55° E, in the Brazilian state of Para, seen in Figure 3.4. Please see Appendix A for a copy of the file used to set these parameters, the NMSTASK. All experiments began at 0 UTC on the 26th of September, 1992, and ran for 60 hours (2.5 days).

The UWNMS uses a spherically transformed coordinate system, with pressure as the vertical coordinate. As mentioned earlier, the model does not assume hydrostatic balance. Assumptions and other non-assumptions that were made in the model formulation include: using a quasi-compressible closure, in order to accommodate larger grid sizes; not using the Boussinesq approximation since density differences are not always small enough to be neglected; and not allowing supersaturation with respect to liquid water, such that any water vapor in excess of saturation immediately forms condensate. The model predicts ice-liquid potential temperature (θ_{il}), which is conserved over any phase changes, and uses it to diagnose virtual potential temperature and cloud water (or cloud ice).

A reasonably accurate radiation scheme is an important component of modeling cirrus. Liu et al. (2003a) found that when radiative processes (such as heating) were not included in a cirrus model, the lifetime of the cloud was noticeably shorter. The UWNMS is well able to account for radiative feedbacks on local dynamics (Tripoli, 1992). The radiation scheme is split into two parts, one each for shortwave and longwave calculations. Shortwave parameters of backscatter fraction and single scatter albedo are calculated using a two-stream model per Stevens et al. (1978). Longwave parameterization is also calculated using a two-stream model, treating each layer as homogeneous, per Chen and Cotton (1983).

The horizontal resolution used for these case studies is too coarse for the UWNMS to predict convection explicitly; with explicit convection updrafts and downdrafts would displace mass over a wider area than is reasonable, and would also be weaker than the average observations. The model is therefore set up to use the convective parameterization scheme by Emanuel (1991). This scheme accounts for saturated and unsaturated updrafts and downdrafts, with discrete mixing resulting in a buoyancy sorting of air. The resulting upward and downward mass fluxes, including information on the amount and phase of liquid involved in each, is then passed, in turn, to the model's dynamics, advection, and thermodynamics routines, which in turn affect the distribution of and potential for activation conditions for the ice nucleus populations modeled in this study. As such, the IN population is not directly affected by the cumulus parameterization, but indirectly, which is reasonable given they are initialized (with two exceptions which will be discussed in Chapter 5) well above the level at which convection originates (Tripoli, personal communication). Explicit convection, the result of inbalances such as buoyancy acting on vertical motions, can occur alongside parameterized convection, since the activation of parameterized convection at a gridpoint depends on a variety of factors: the amount of instability, the amount of turbulence, the strength of the cap on potential convection, the presence of convective activity in the area, etc (Tripoli, personal communication). The difference between explicit and parameterized convection that we must keep in mind is how tracers are treated. In parameterized convection, for tracers (such as IN) to be affected they must be present at the originating level of convection. If they are, they will be lofted to the cloud top in one timestep. This is a fault in the parameterization, Tripoli explains—it assumes equilibration occurs in one timestep, which is not realistic. Tracers affected by explicit convective motions will be moved with vertical (and horizontal) motions—a more realistic, and slower transport towards the cloud top.

Water vapor information in the UWNMS is expressed as a mass mixing ratio. In the thermodynamics portion of the model, the number of gridpoints with condensate are counted, flagged, and gathered together into a separate 1-D array for microphysical processing. The microphysics routine is comprehensive, with creation and conversion among pristine crystal, aggregate, snow, hail, and rain categories. These are calculated as *tendencies*, or the mass mixing ratio of water (in liquid, ice, or vapor form, depending on conversion type) per timestep. Below, the parts pertaining to pristine crystal production and loss are discussed in detail.

The three pre-existing mechanisms for pristine ice crystal formation are: phoretic contact nucleation, splintering, and sorption/deposition. Phoretic contact nucleation accounts for ice forming as Brownian motion, small-scale vapor fluxes or kinetic energy gradients cause an aerosol to impact onto a cloud droplet, which then freezes. For the phoretic nucleation process to occur, cloud condensate and an ambient temperature below 270.16 K is required; an aerosol population is assumed to be mixed upward from a surface-source. The sorption/deposition category accounts for ice crystals forming homogeneously via sublimation when the temperature is below freezing and the air has a humidity above ice saturation. Finally, if the ambient temperature is between 270.16 and 265.16 K, and riming is occuring, existing ice crystals are allowed to splinter apart, impacting supercooled water droplets that freeze on contact. Each of these tendencies forms new ice crystals of a user-specifed size (called PMAS in the model). For the studies described here PMAS was set to be 4.8 x 10^{-10} grams, equivalent to a solid ice sphere with a radius of 5 microns. (Note—PMAS is set in the NMSTASK, but there it's called "AMI0.") An idealized heterogeneous ice nucleation scheme was added as another ice formation mechanism after much investigation of the properties of IN, and in particular, chemical species from biomass burning that are suspected to act as IN.

The knowledge of ice nuclei is still limited. There are several mechanisms by which IN can influence ice formation (by contact nucleation, deposition nucleation, immersion freezing, etc., see Figure 3.5). A gross sense of *typical* IN properties exists; measurements have been made of the chemical composition of aerosols within ice crystals--despite all these "pieces," a complete model of IN activity has not been formulated. For example, we may know what elements made up an IN (Kojima et al, 2004, Cziczo et al., 2004), but by measuring the chemical composition the IN has been destroyed, and it can only be classified according to its ingredients, and not its structure, behavior, or concentration. Some promising laboratory experiments with oxalic acid, found in biomass burning plumes, which most likely acts as immersion nuclei, have been recently conducted by Zobrist et al. (2006). Prenni et al. (2001) found that other organic acids require higher relative humidities to activate than most IN, suggesting that some organics may actually inhibit ice formation. Field experiments have yet to catch up to these lab-based discoveries; we do not have measurements, for example, of oxalic acid in any of the three campaigns discussed in Chapter 2.

The number of IN is somewhat better known than which chemical species make up the various modes of ice nucleation. The general trend is such that the number of aerosol particles that can act as IN increases with decreasing temperature and with increasing saturation. Figure 3.6 shows an example of IN (all nucleation modes) measurements in several locations. Between -10 and -20 °C the IN concentrations vary between ~10 and 1000 per liter. As a comparison, Andreae et al. (2004) note the concentration of condensation nuclei in a smoky Amazonian boundary layer is 2000-8000 per *cubic centimeter*! Pruppacher and Klett (1997) point out that measurement techniques require "considerable caution" when interpreting IN concentrations given in literature. They note that the filter technique used to gather the data in Figure 3.6 may underestimate the number of IN by as much as an order of magnitude. Given this information, the fact that the data may represent background IN concentrations, heavy IN loading, and/or middling concentrations, and that only a fraction of those IN may be of biomass burning origin, the concentrations modeled in this work were chosen to cover a wide range of admittedly arbitrary, though reasonably possible IN numbers—from 30 to 120 IN per liter.

These teases of IN information, with some descriptions more complete than others, are only the beginnings of a thorough account of IN. Our goal then is to model a simple, generalized IN population that can be modified and tailored to different chemical species in the future. Here, several assumptions were made to model IN activity, while also taking into account model limitations:

(1) one property of ice nuclei is that they are often hydrophobic. Hence, our IN will not be affected by liquid water processes, such as wet depositional scavenging. This is obviously a simplification--wet deposition is something that can normally occur--but those effects will be ignored in order to focus on the effects of IN on ice crystals, since we know there are potential IN at and above freezing levels.

(2) according to Tripoli (personal communication), depositional nucleation is the most likely ice formation mechanism in layered clouds such as cirrus, as the likelihood of conditions existing for other mechanisms to act is low. For example, contact freezing, condensation freezing, and immersion freezing all require the presence or formation of a cloud droplet. However, tropical cirrus, unless generated by vigorous convective updrafts, generally do not occur in temperature regimes that support the existence of an unfrozen cloud droplet. With this in mind, our IN are modeled as depositional ice nuclei. This means that in convectively generated cloud ice, and at lower altitudes with higher humidities, our IN will compete for vapor to form ice along with other ice nucleation mechanisms. In synoptically-forced cirrus or in cirrus formed in gravity waves, where the humidity is lower, our IN population's influence will be more strongly felt.

(3) the criteria for homogeneous depositional nucleation is that the temperature be at or below 0° C and that the environment is supersaturated with respect to ice. Since our IN are assumed to use the deposition mechanism for ice formation, the conditions for IN activation are assumed to be the conditions for depositional nucleation, albeit with varying temperature conditions. In order to focus on the effect of IN on high clouds, most of the experiments use an activation temperature of 238.16 K. For three experiments the activation temperature is raised to 273.15 K as sensitivity studies of activation temperature.

(4) organics are a primary component of biomass burning emissions, so it seems plausible that smoke-derived organic ice nuclei exist. It would be appropriate, then, to give our idealized IN population characteristics of organic species that may act as IN. Observations during the FIRE-CRYSTAL FACE campaign indicate the average size of an organic particle in an ice crystal is ~0.45 microns (Kojima et al., 2004). I originally intended for the initial crystal size of IN-formed ice to reflect this average size. However, difficulties arose in interpreting the differences between cases with and without IN present—since the model uses a bulk microphysics scheme, with ice represented as a mass concentration, it was impossible to discern whether differences were due to different sizes or different number concentrations of ice particles. With this in mind, we use PMAS as the starting size for all crystals formed.

(5) the IN are assumed to be massless and have no direct radiative properties.

(6) once activated, the IN are assumed lost; if a crystal formed with an IN evaporates, the IN does not remain. This assumption was made because the model calculates microphysics in bulk—since individual IN-formed crystals can not be tracked we have no way of knowing when and where an IN-formed crystal evaporates—and because there is no empirical knowledge of how many IN are released/remain intact after ice evaporates.

(7) in preliminary studies, the introduction of the IN population to the model was done in one timestep, at the start of the model run. This appeared to cause a shock to the model in that a lot of noise was generated that obscured any potential effects of IN activation. Model output suggested that the model stabilizes at around 4.5 hours into a run. In order to reduce the shock

and the resulting noisiness, the IN concentration is instead "ramped up" using a hyperbolic tangent function, starting at 4.5 hours into the model run and with a halfway point at 6 hours. Examples of this function are shown in Figure 3.7.

the heterogeneous ice nucleation process

For every gridpoint with condensate, when the temperature is less than or equal to the activation temperature (238 or 273 K), the air is saturated with respect to ice, and at least one IN is present, the IN will activate. Per model gridpoint, the mass mixing ratio of pristine crystals that result from IN activation depends on the growth of the ice crystals, the number of IN activated, and the timestep, such that:

$$\frac{\left(\frac{dm_{ice}}{dt}\cdot\left(\mathit{model\ timestep}\right)\cdot\left(\mathit{number\ of\ ice\ nuclei\ at\ gridpoint}\right)\right)}{\left(\rho_{dry}\cdot V_{gridpoint}\right)},$$

where (dm_{ice}/dt) is the equation for unventilated crystal growth given in Pruppacher and Klett (1997):

$$\left(\frac{dm_{ice}}{dt}\right)_0 \approx \frac{4\cdot\pi\cdot C\cdot s_{v,i}}{\left(\frac{R\cdot T_{env}}{\left(e_{sat,i}\left(T_{env}\right)\cdot D_v^*\cdot M_w\right)}+\frac{L_s}{\left(k_a^*\cdot T_{env}\right)}\left(\frac{L_s\cdot M_w}{R\cdot T_{env}}-1\right)\right)},$$

and where C is the capacitance of the crystal, $s_{v,i}$ is the saturation ratio with respect to ice, D^*_v is the vapor diffusivity, M_w is the molecular weight of water, L_s is the latent heat of sublimation, and k^*_a is the thermal conductivity. For the capacitance derivation, please see Appendix B. For a gridpoint with an IN concentration of 60 /L, if all those IN activate at 200 hPa, a temperature of 238 K, and a 0.1% supersaturation, we can expect to see a 8.44×10^{-8} g/kg change in the vapor and pristine ice categories per second, or 1.69×10^{-6} g/kg change in vapor per timestep (20 seconds). For reference, the average vapor mixing ratio near 5° S and 200 hPa is 7.56×10^{-6} g/kg (Figure 3.2).

Once an ice crystal population is created by this method, it is added to the populations of ice crystals created by homogeneous sorption/deposition, splintering, and phoretic nucleation to form an array of the total mass mixing ratio conversion of vapor to pristine ice. If needed, the mass is repaired so that the conversion tendencies among all condensate categories (and vapor) are non-negative. Once the terminal velocities are calculated for each condensate the mixing ratios are returned to the thermodynamics subroutine, where potential temperature and the mixing ratios of vapor and condensate are distributed back from the 1-D array of points with condensate to the whole 3-D grid and precipitation tendencies are diagnosed. Now the ice crystals are free to act radiatively, and convert to other categories in subsequent timesteps: to vapor by evaporation, to rain by melting, to aggregates by aggregation, and to snow by aggregation. Pristine crystals are also allowed to grow by riming (cloud droplet mass converted to crystal mass). The effects that various IN populations have on the amount (mass, not number) and location of pristine crystals in the model, and the relationships among the resulting dynamical feedbacks, are discussed in the following chapters.

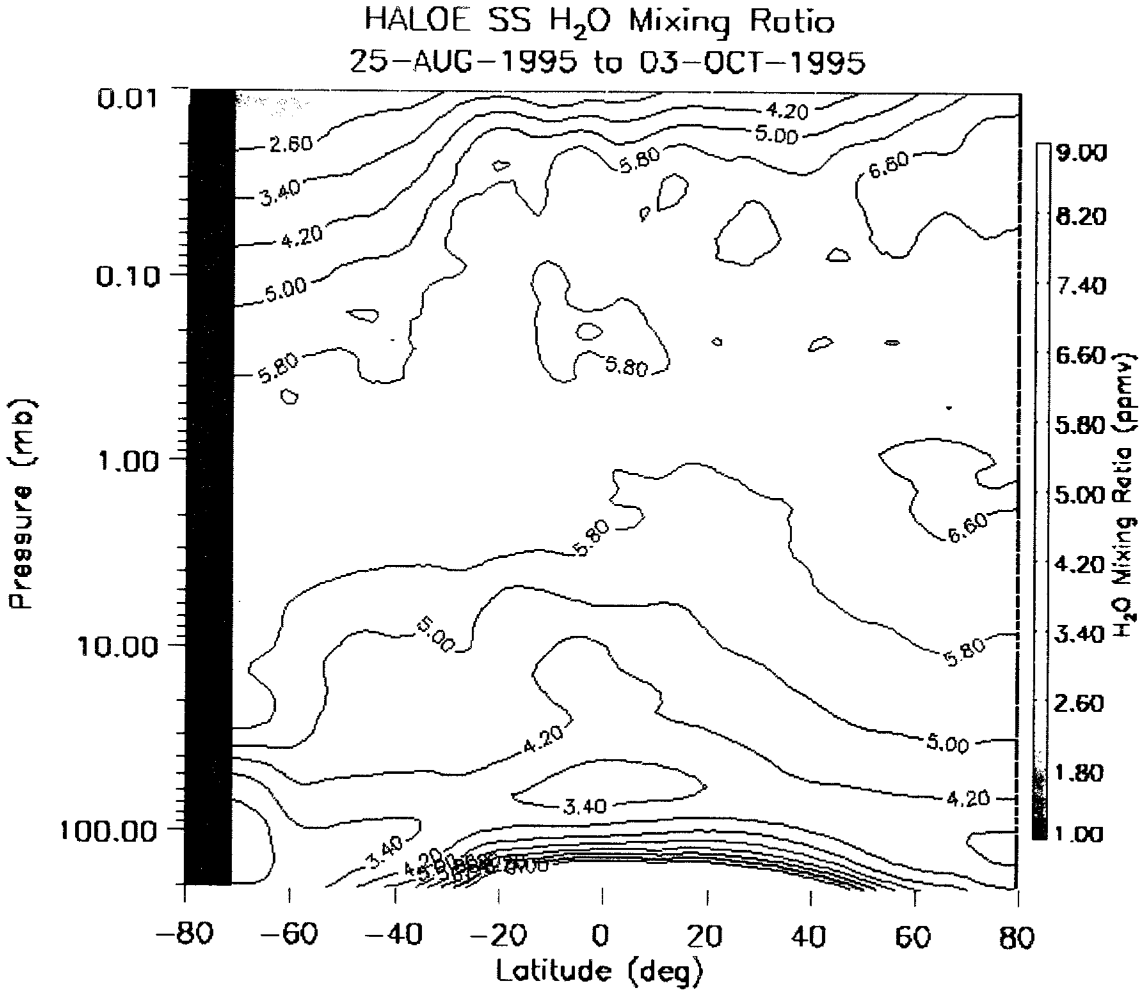

Figure 3.1. HALOE sunset ("SS") data for early boreal autumn (1995). Note the water vapor concentration for any latitude is non-linear with pressure.

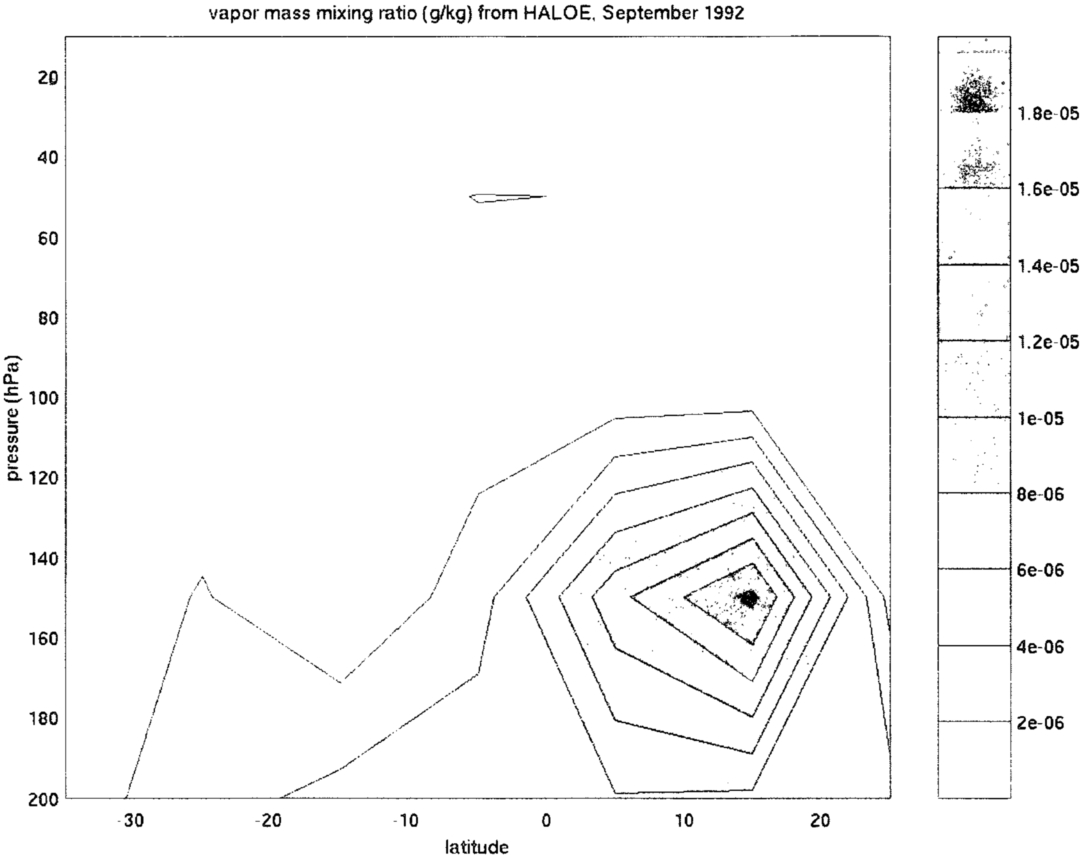

Figure 3.2. The result of binning and averaging HALOE data over the month of September 1992. For each latitude and pressure range given in Table 3.1. there is an amount of vapor which is used as input to the UWNMS for initial conditions and boundary updates. Since the UWNMS works with mass mixing ratio, the data here are seen in those units, converted from the data's original volume mixing ratio (as seen in Figure 3.1).

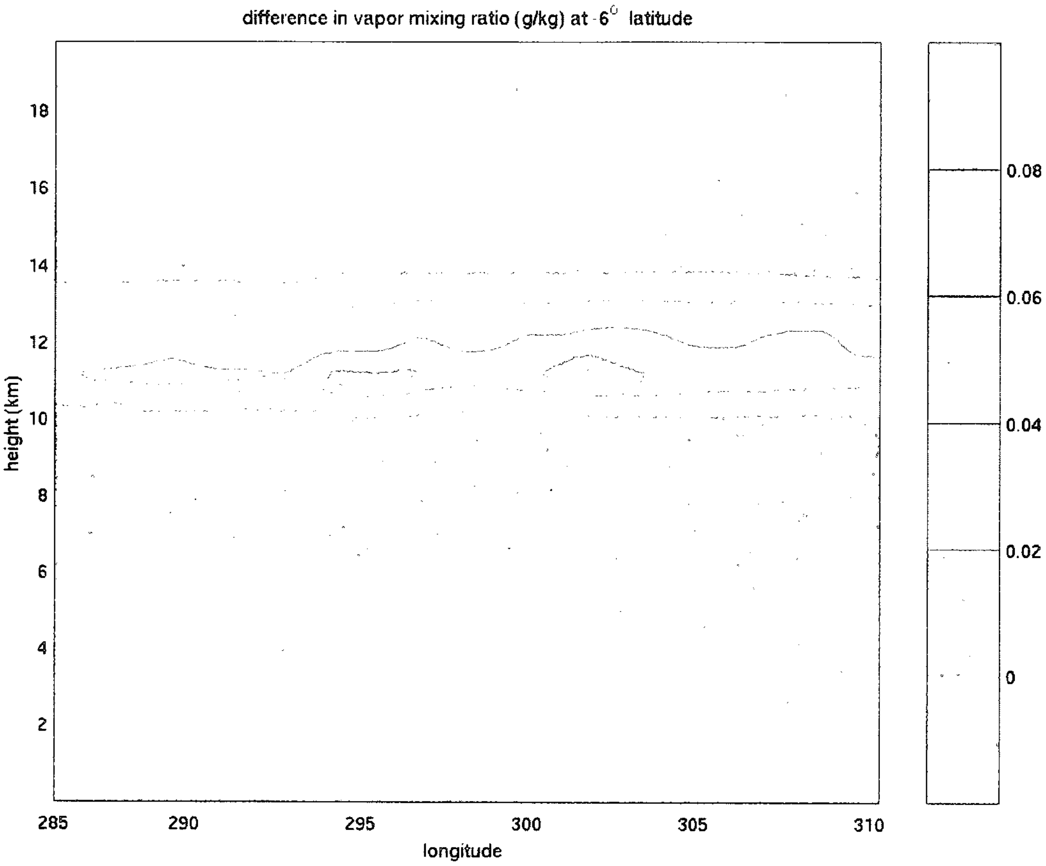

Figure 3.3. The difference in water vapor at 6° S, for a UWNMS model run with HALOE data minus a run without HALOE data, 90 minutes into model run time. At and above 250 hPa (approximately 11 km) binned HALOE data are linearly averaged with ECMWF humidity for UWNMS initial and updated boundary conditions. The inclusion of HALOE data results in slightly more moist layer (up to 0.08 g/kg of vapor) between about 10.4 and 13.8 km.

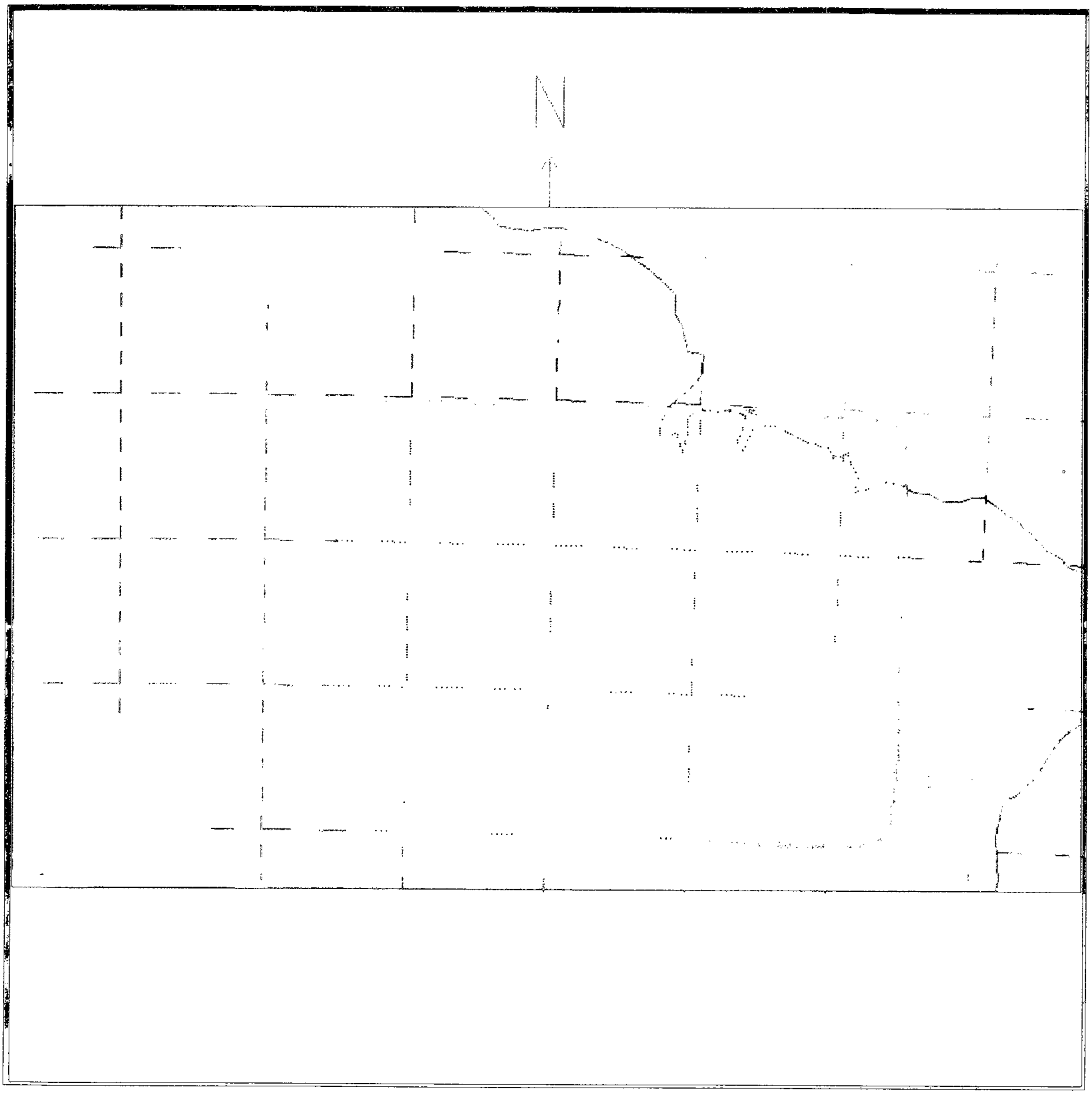

Figure 3.4. The UWNMS model domain, a section of northern South America. The grey shaded rectangle shows the initial latitude/longitude of the ice nucleus populations modeled.

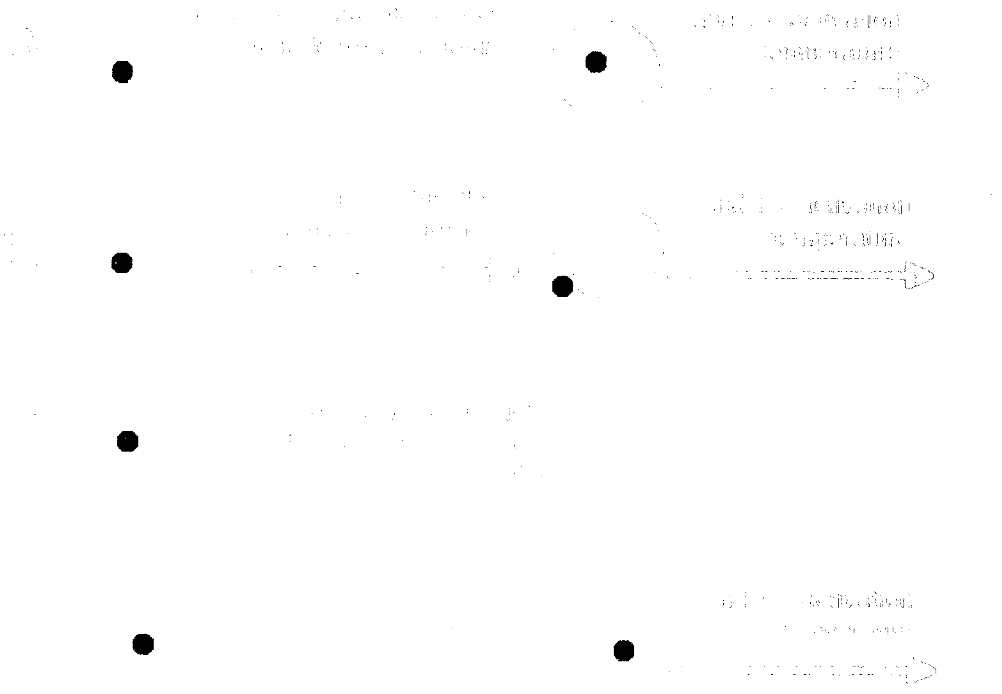

Figure 3.5. With time increasing from left to right, each black dot represents an ice nucleus and illustrates four modes of heterogeneous ice nuclei activation: (a) condensation freezing, (b) contact freezing, (c) depositional freezing, and (d) immersion freezing.

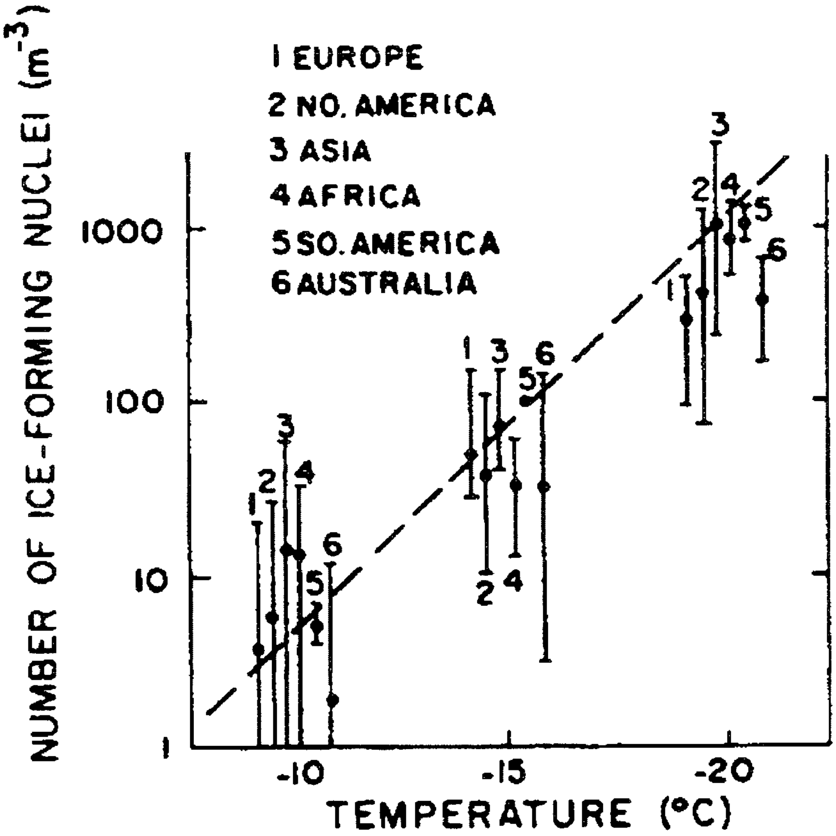

Figure 3.6. (adopted from Pruppacher and Klett, 1997) The median IN number concentration as a function of temperature, from 44 various locations using a filter method. The dashed line represents N_{IN} (L^{-1}) = 10^{-5} * exp(0.6 Δ T).

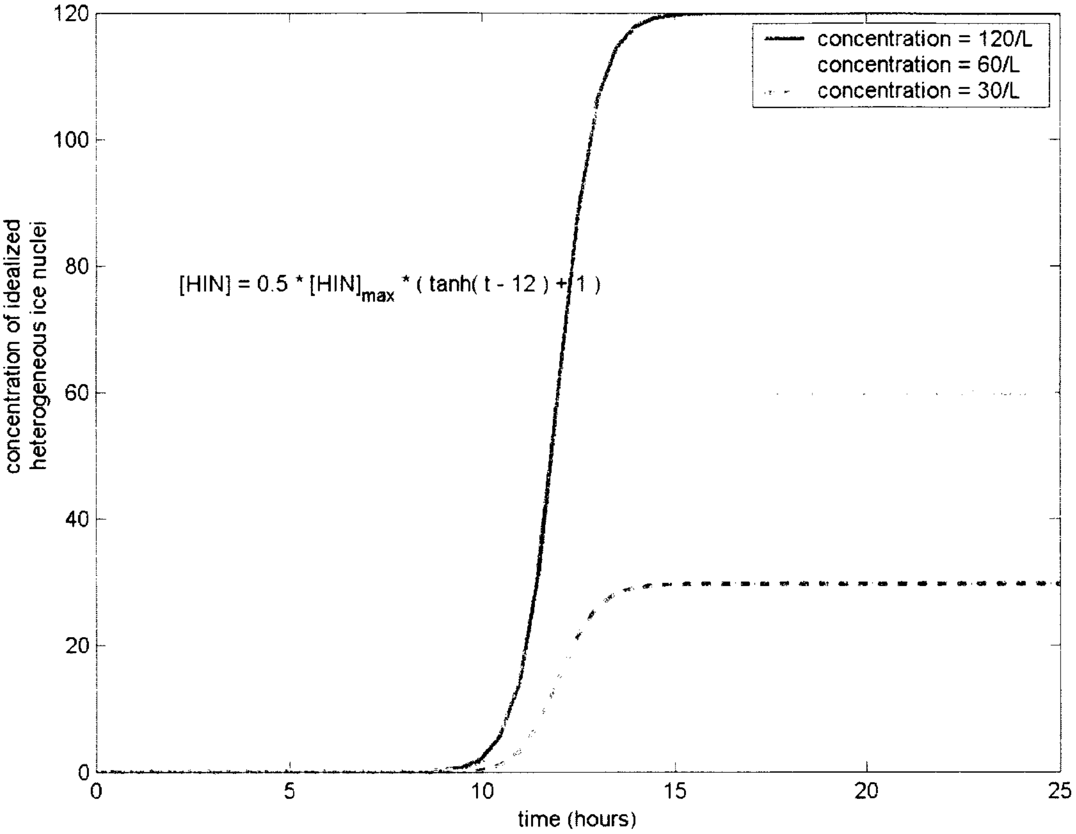

Figure 3.7. Three examples of how the IN concentration is slowly increased over several timesteps in order to avoid shock to and noise in the model. These examples show the IN concentration "ramp up" centered at 12 hours into the run, and do not show any activation, which decreases the IN concentration. In the model, the ramp up of IN concentration is less any activation that occurs.

Chapter 4: Meteorological Overview

Before any discussion of the effects of the idealized ice nuclei in the UWNMS, we should first validate and assess the model's performance. How well does the model represent reality? We will see in this chapter comparisons between model output and TRACE-A flight data, satellite images, and the ECMWF data used as boundary conditions. In this chapter too we will gain an understanding of the representativeness of the modeled time period to the area's climate, as well as the overall weather patterns, as they frame any evaluation of the effects of IN in the four following chapters.

The TRACE-A flight we found most suitable for study with the UWNMS (Chapter 2) was flight number 6, which took place over northeastern Brazil the 27th of September 1992, from roughly 09:15 to 16:50 UTC. For northeastern Brazil, this time of year is characterized by increasing cloudiness in a transition to austral summer, when the Amazon convection center dominates (Figures 4.1i and 4.1j, Hastenrath, 1997). During this transition an upper tropospheric high forms over the western Amazon, with an axis along approximately 10°S. Winds at the 500 hPa level are correspondingly easterly north of this axis and westerly on the poleward side. At 200 hPa the flow is zonal on average, though downstream of the northern Andes the flow tends slightly equatorward. Closer to the surface, the South Atlantic High ensures on-shore flow north of, and westerly flow south of about 20° S.

These patterns are evident during the months of September and October 1992. Though the TRACE-A experiment took place during a particularly long-lasting ENSO event, tropical convection and the strength of the upper tropospheric high over the western Amazon had very little anomalies (Chelliah, 1994). Figure 4.2 shows circulation patterns averaged over 13 September – 11 October 1992 at 850, 500, and 200 hPa. Data shown come from ECMWF twice-daily global analyses. At 850 hPa the most prominent feature is the anticyclone centered near the Brazilian coastline at 20°S. The northern portion of South America experienced easterly winds at this altitude (approximately 1.5 km above sea level), with wind strength diminishing with increased distance from the Atlantic coast. The center of anticyclonic circulation shifts northward to 15° S at 500 hPa (about 5.9 km), with strong westerly flow on the poleward side, and weak easterlies equatorward. Winds at the center of the anticyclone are weak, corresponding perfectly to the location and lack of notable horizontal displacement of the forward trajectories calculated for TRACE-A flight no. 6 (Figure 2.9). At 200 hPa (about 12.5 km) the anticyclone can still be seen, with strong zonal flow south of 20°S and weak easterlies north of 10° S. At both 500 and 200 hPa a cyclonic curvature exists near 65°W and an anticyclonic curvature near 40°W (Figures 4.2a and 4.2b).

Flight 6 sampled altitudes ranging from within the boundary layer (at about 1.5 km) to around 11.5 km. Figure 4.3 shows the circulation averaged over 26 September at 0Z to 28 September 1992 at 12Z, exactly the time period modeled in the UWNMS experiments. Over these 60 hours, winds are generally follow the average, though they appear to be weaker over the northern part of South America, north and west of the anticyclone, than in the four-week averaged winds. The cyclonic and anticyclonic curvatures present in Figures 4.2a and 4.2b are lacking during this shorter time period. This jibes with the stalled cold front that angled along a line from about 10° S in the western mountains to 20° S, north of Rio, seen in Figure 4.4 (Bachmeier and Fuelberg, 1996). Combustion materials from the fires at this time (Figure 2.12) would not travel far—ideal conditions for investigating the effects of combustion materials on clouds with the UWNMS. But how accurate is the UWNMS?

We can assess the accuracy of the UWNMS using three parameters: potential temperature, water vapor mixing ratio, and approximate cloud cover. We can qualitatively estimate the accuracy of the UWNMS' convection parameterization scheme by comparing a time series of model output –modeled without any heterogeneous ice nuclei– to satellite data,. Clouds are represented by the presence of condensate in the UWNMS, so the altitude of condensate is shown here, instead of amount, in order to approximate near-infrared satellite images. Note that the horizontal scale used in the model is too coarse to resolve individual clouds, hence, I use the term "clouds" as shorthand for "areas with condensate." The modeled region experiences two main types of convection: local, diurnal convection, which peaks near 2 pm local time, and mesoscale systems, which peak a couple of hours later (Betts and Jakob, 2002, Greco et al., 1990).

As a reference, the tropopause in the UWNMS is at about 16.5 km or 100 hPa, where the average temperature is near 200K (Figure 4.5). The domain-averaged vapor mixing ratio is also shown, in Figure

4.6. The domain-averaged temperatures at IN-injection levels of 200 hPa (12.5 km), 250 hPa (11 km), and 300 hPa (9.7 km) are 218, 230, and 242K, respectively, and the average temperatures at 500 and 850 hPa (5.9 and 1.5 km) are 267 and 290K (Figure 4.5).

For the 26th of September: UWNMS results show clouds associated with the stalled front in the south and southwestern parts of the model domain, with some convection in the center of the domain (at 6 UTC, or 3 am local time, see Figure 4.7) that dissipates near daybreak. Convection associated with the front appears to intensify over the course of the day, as cloud height increases around 298 degrees east, 10 degrees south—compare Figures 4.7 to 4.8. A satellite image for this day (Figure 4.9) shows that the UWNMS represents the cloudy frontal boundary well, but not a line of afternoon convection along 5-7 degrees south, equatorward of the front. In Figure 4.10, ISCCP's cloud top pressure product (Rossow et al., 1996) implies that the UWNMS may be compensating for the lack of cloudy convection in the center of the domain with more vigorous convection in the southern part of the domain—cloud tops are modeled to be near 11 km rather than the ISCCP-derived "real" cloud top heights of 5.9 - 9.7 km (approx. 500 -300 hPa). Also, Figure 4.10 somewhat validates the cloudiness in the northwestern part of the UWNMS domain. Unfortunately, satellite coverage is insufficient during this time period for this cloud information to be available regularly. Over the next hour and a half, one area of cloudiness extends further upward, with cloud tops reaching just above 12 km (where the average temperature is slightly warmer than 220K) near 300 degrees east, 10 degrees south (Figure 4.11).

By the 27th the frontal boundary has moved a bit equatorward in the western portion of the model domain and the UWNMS cloud positions reflect this shift well (Figures 4.12 and 4.14). The satellite images for this day (Figures 4.13 and 4.15) again validate UWNMS clouds along the front. At 6 UTC the UWNMS misses the widespread clouds equatorward of the front (Figures 4.12 and 4.13), which are likely "pops" of small-scale, diurnal convection. Around 18 UTC (4 pm local time) the UWNMS indicates growing convective clouds slightly north of 10 degrees south (Figure 4.12), which better approximates the widespread pops of convection in central Brazil. For the 28th, the field of clouds associated with the stalled front appear to be dissipating in the UWNMS (Figure 4.16). Areas of convective cloudiness exists in the center of the domain, with five areas with cloud tops above 12 km.

ISCCP cloud top pressure corresponding to the end of the modeled time period (Figure 4.17) suggests that the UWNMS is representing convective strength (as estimated by cloud top height) fairly well. The next available satellite image, for 18:12 UTC on the 29th (Figure 4.18), shows a similar distribution of convective clouds.

Overall the UWNMS represents cloudy areas associated with the stationary front fairly well during the modeled time period. Unfortunately, convection equatorward of the front is not as well represented, especially on the 26th and early hours of the 27th. This is likely caused by two things. A convection parameterization had to be used here because the horizontal grid spacing (30 km by 30 km) is too large to account for small-scale "pops" of convection, especially without a triggering mechanism as large as a frontal boundary. There are some differences in cloud top height between model simulations with and without cumulus parameterization—with cumulus parameterization the energy of convection appears to be spread out, so that cloud tops are lower and the cloudy areas are larger (the red in Figure 4.19) while convection without parameterization is more focused on smaller scales and with higher cloud tops (the scattered blue areas in Figure 4.19).

Both TRACE-A *in-situ* measurements and ECMWF data are used to gauge temperature and moisture fields in the UWNMS. In order to compare these datasets, some conversions had to be performed. First, the UWNMS calculates and outputs virtual potential temperature, θ_v. This was converted to potential temperature (θ) using

$$\theta = \frac{\theta_v}{1 + 0.61 \cdot w_v} .$$

ECMWF relative humidity (RH) was converted to a mass mixing ratio (g/kg) using:

$$w_v = RH \cdot 0.622 \cdot \left(\frac{e_{sat}}{p - e_{sat}} \right) \cdot 1000,$$

where p is pressure, and

$$e_{sat} = 6.112 \cdot \exp\left(\frac{L_{lv}}{R_v} \cdot \left(\frac{1}{T_{tr}} - \frac{1}{T}\right)\right) \qquad \text{and} \qquad T = \frac{\theta}{\left(\frac{1000}{p}\right)^{0.286}} \; .$$

Figures (4.20 – 4.23) show how well TRACE-A measurements of potential temperature and water vapor compare to UWNMS output at noon local time. TRACE-A measurements included ambient temperature, saturation vapor pressure with respect to water, and relative humidity with altitude measured in meters, determined by aircraft radar. For comparison to UWNMS data, TRACE-A temperature data were converted to potential temperature and both relative humidity and saturation vapor pressure were used to calculate a vapor mass mixing ratio in g/kg using the equations above. Because the aircraft data do not exist on the same vertical scale as the UWNMS, Figures 4.20 – 4.23 include flight data 0.15 km above and below the UWNMS comparison level. In plotting data for a small range of heights, we can be sure there are data to compare to the UWNMS output. It also accounts for any variability or error in the radar-estimated heights of the TRACE-A data. The converted TRACE-A flight data and UWNMS output agree favorably at 5.9 and 9.7 km (Figures 4.22 and 4.23 show that the moisture fields compare very favorably, and the temperature differences are less than two degrees), but at the lower levels UWNMS output are notably drier than TRACE-A measurements, with small differences in temperature. Figure 4.20 shows that the UWNMS is drier at 0.8 km by up to 5 or 6 g/kg—half of what is observed in some places, only the southernmost point sampled by the TRACE-A flight in the figure shows a temperature difference with the UWNMS greater than 5K. At 1.5 km (Figure 4.21), the UWNMS is similarly 50% drier than flight measurements indicate, and again the greatest difference in temperature between the model and flight measurements is at the southernmost part of the domain, where the temperature difference is near 8K. This may be the result of comparing UWNMS output at one level to measurements on and *near* that level, it may be the result of the surface parameterization of the UWNMS (Tripoli, personal communication), or that the UWNMS is initialized with ECMWF data.

Figures 4.24 – 4.31 give a side-by-side comparison of UWNMS output to ECMWF data at two times and four altitudes. Please refer to Figure 4.5 for the relationships between geometric height, pressure, and temperature from UWNMS output at ECMWF pressure levels. For both times and all heights, the UWNMS represents water vapor fairly well, though with a finer resolution and topography (30 by 30 km in the UWNMS compared to 2.5 by 2.5 degrees in the ECMWF model), more structure can be seen in the UWNMS' output than in the plots of ECMWF water vapor. Potential temperature is 1-5 K cooler in the UWNMS than the ECMWF data, the difference is largest at lower levels (925 and 850 hPa, or approximately 0.8 and 1.5 km, respectively), as seen in Figures 4.24 – 4.27. The differences are likely due to differences in surface parameterization between the models—for example, the UWNMS domain was set to have 95% of land cover as a uniform forest with a roughness length of 1 meter (after Campbell and Norman, 1998, Table 5.1). Since neither the UWNMS nor the ECMWF data compare well to the *in-situ* measurements of water vapor at the two lower levels, it is possible (and likely!) that surface parameterizations in both the UWNMS and ECMWF model were not as detailed as they could be.

Figures 4.28 – 4.31 show temperature and moisture data at the two upper levels (500 and 300 hPa, or approximately 5.9 and 9.7 km). Here, too, potential temperature is cooler in the UWNMS than in the ECMWF data, though by only 1-2 K. The UWNMS – ECMWF moisture comparison does not have the same consistency. At 500 hPa the UWNMS is slightly more moist than ECMWF data, and at 300 hPa the UWNMS is drier than ECMWF data. This suggests that convective transport of water vapor in the UWNMS may not be as rigorous as represented by the ECMWF model; convection may be reaching and moistening the 500 hPa in the UWNMS, for example, where the ECMWF modeled convective transport of water vapor to higher levels.

The apparent coolness and dryness of the UWNMS at lower levels compared to *in-situ* measurements, as well as the model resolution and use of cumulus parameterization are each likely contributors to differences in the vigor and distribution of convection, especially in the first 30-40 hours of the UWNMS experiment. Fortunately there are clouds in the model, the lifting along the frontal boundary is very well modeled by the UWNMS, as is the deep convection equatorward of the front late in the modeled time period (on the 28th). Some of that convection reaches at least 12 km, which is plenty high enough to interact with the sheets of idealized ice nuclei. To this interaction we now turn our attention in the remaining chapters.

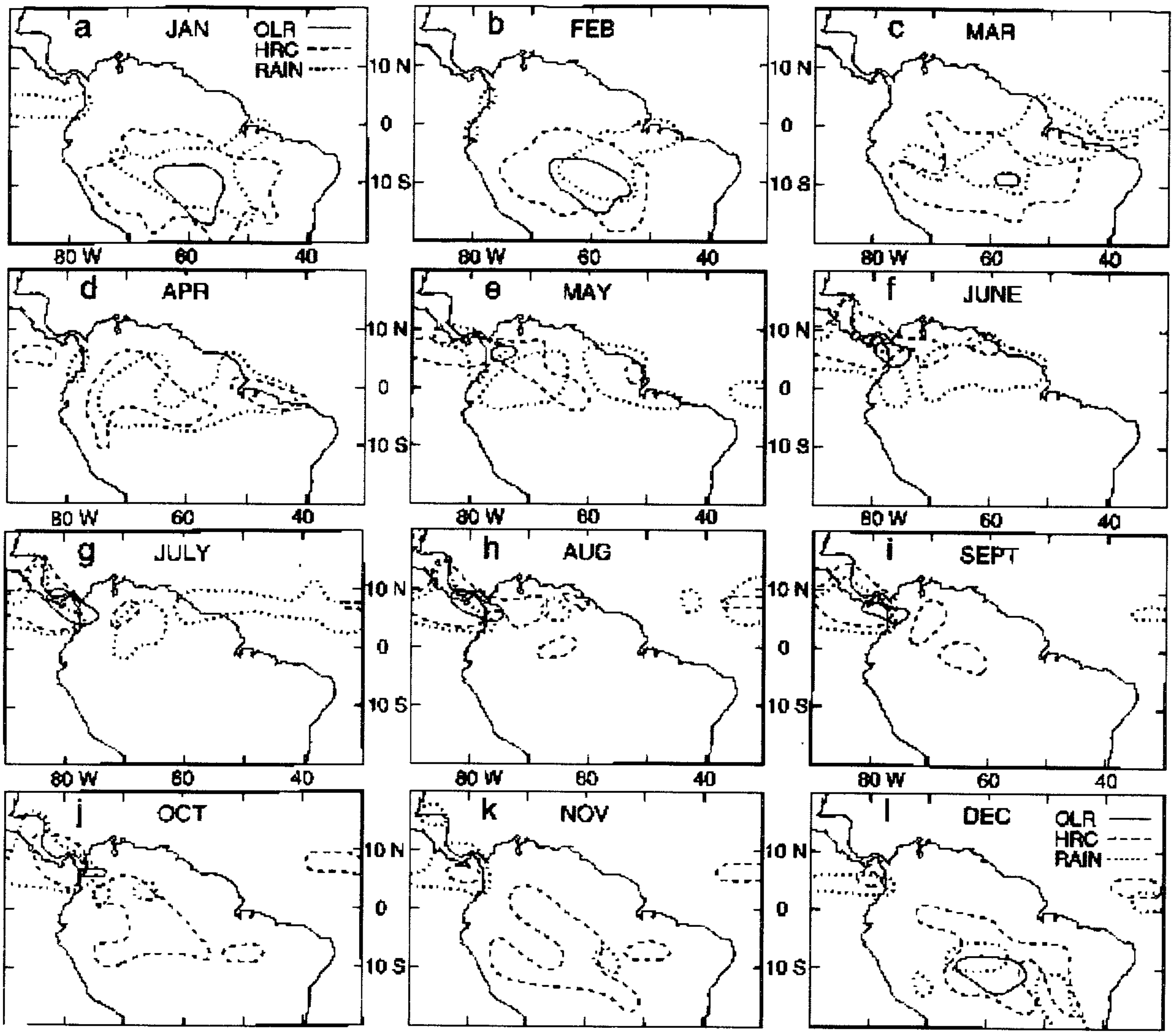

Figure 4.1. (adopted from Hastenrath, 1997) Areas with outgoing longwave radiation (OLR) less than 200 W/m^2 are enclosed by solid lines (indicating deep convection present), areas with highly reflective clouds more than 5 days per month are enclosed by dashed lines (the frequency of deep convection), and dotted lines enclose areas with more than 300 mm rain per month. With these data, shown in monthly increments above, we get a sense of the annual cycle of convection over the Amazon basin.

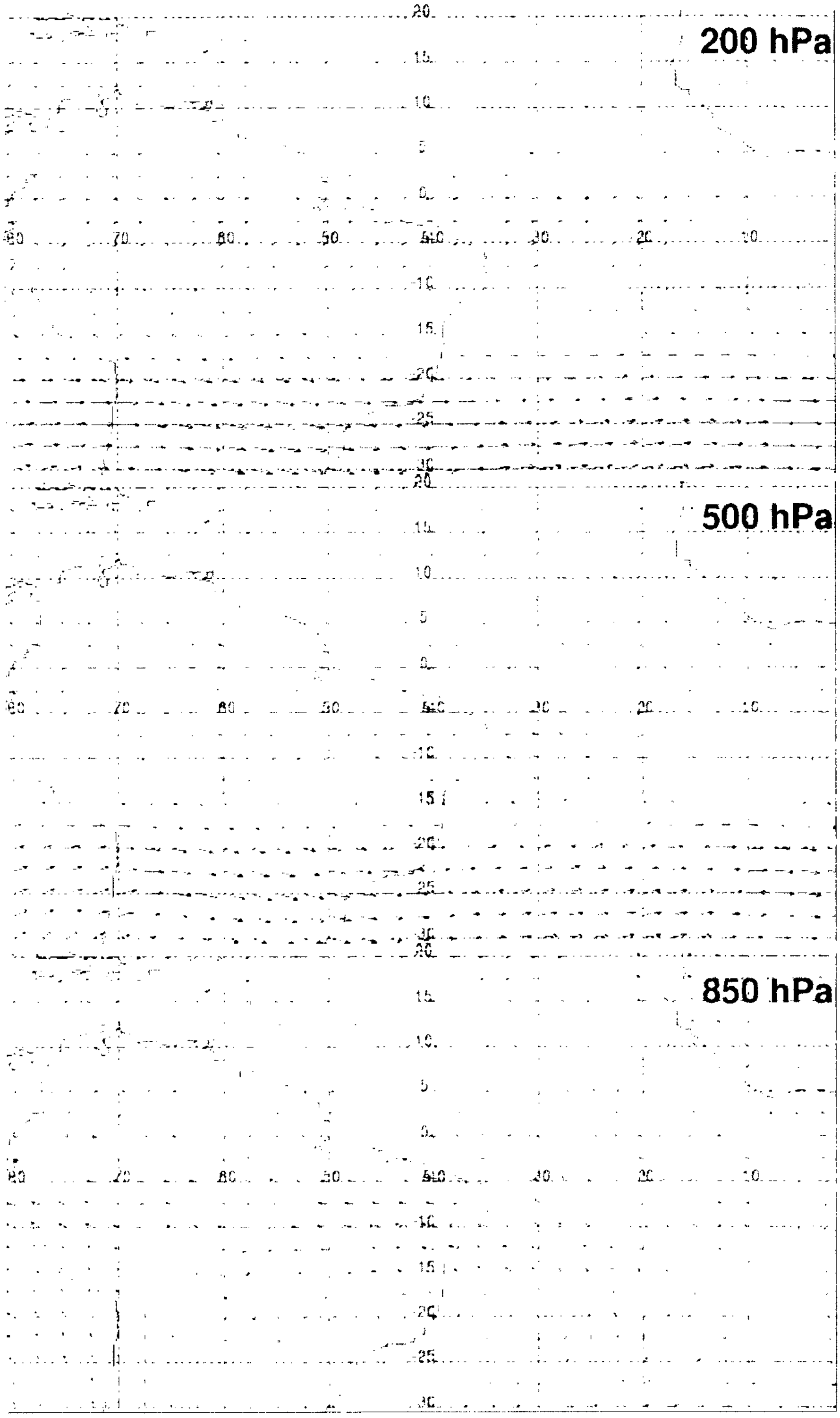

Figure 4.2. Winds from twice-daily ECMWF analyses, averaged over the period from 13 September 1992 at 12 Z to 11 October 1992 at 12 Z, corresponding to two weeks before and after TRACE-A flight no. 6. The u-component of the wind is contoured in blue, and the UWNMS model domain used in this research is outlined by the green box.

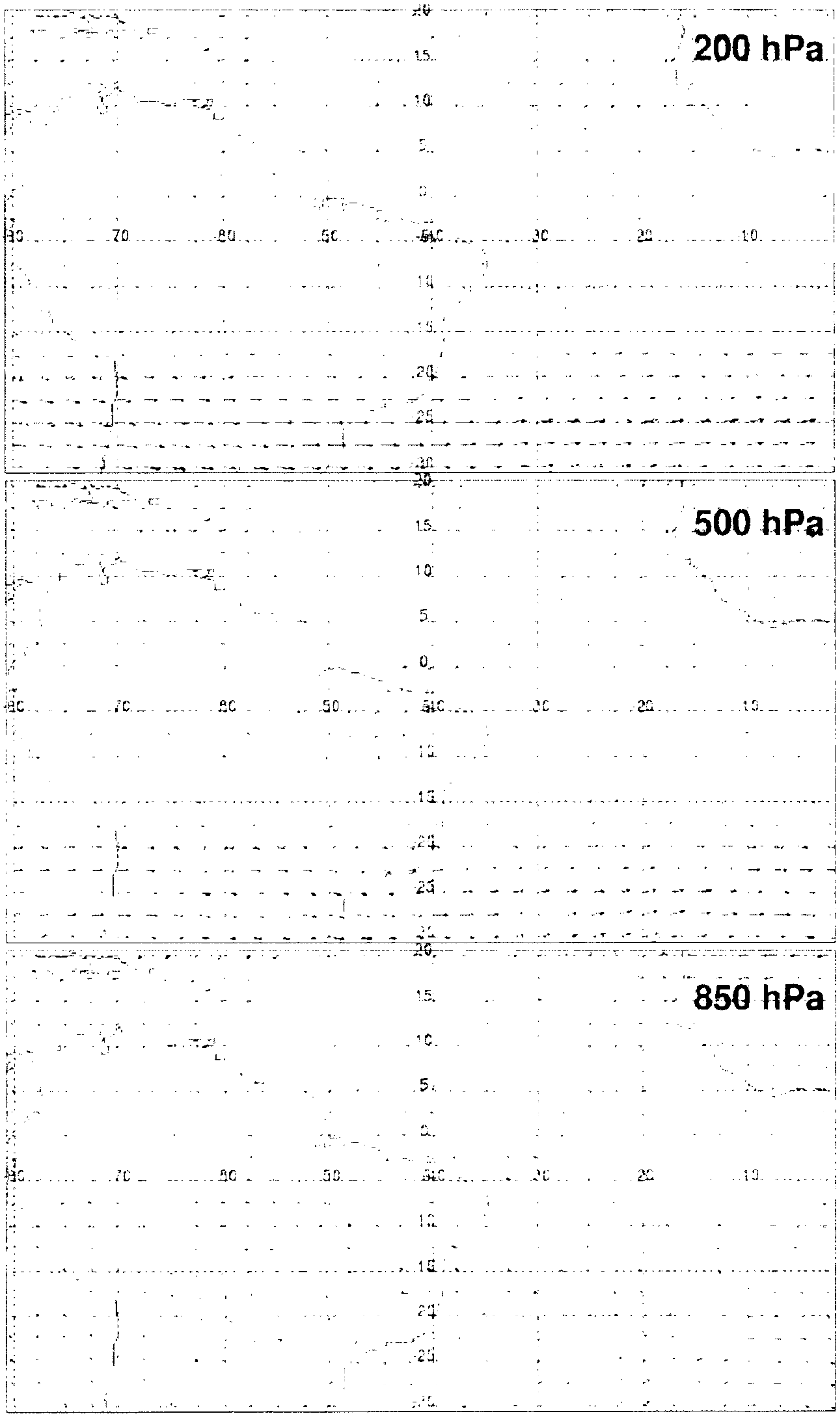

Figure 4.3. Winds from twice-daily ECMWF analyses, averaged over the period modeled with the UWNMS, from 26 September 1992 at 0 Z to 28 September 1992 at 12 Z. The u-component of the wind is contoured in blue, and the UWNMS model domain used in this research is outlined by the green box.

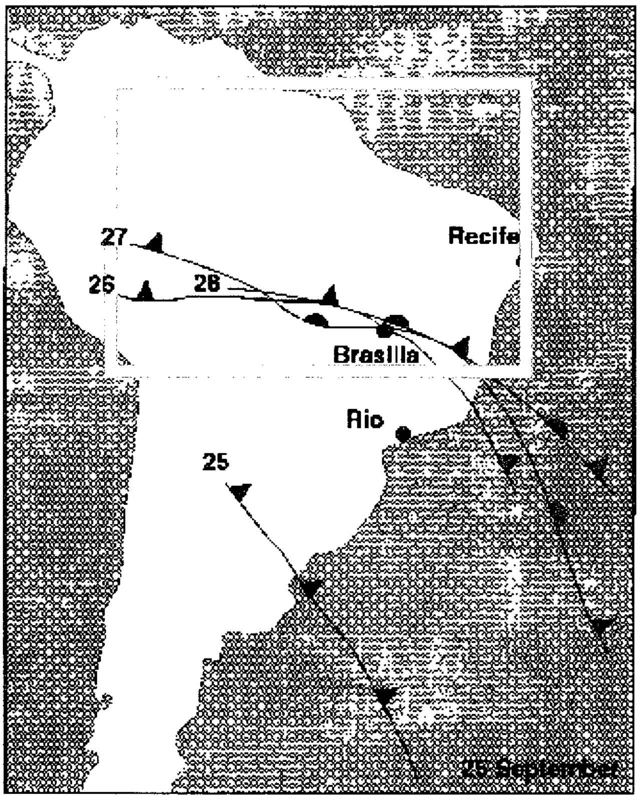

Figure 4.4. (adopted from Bachmeier and Fuelberg, 1996) The surface cold front position at 12 UTC, 25-28 September 1992. The *approximate* boundaries of the UWNMS domain are shown in green.

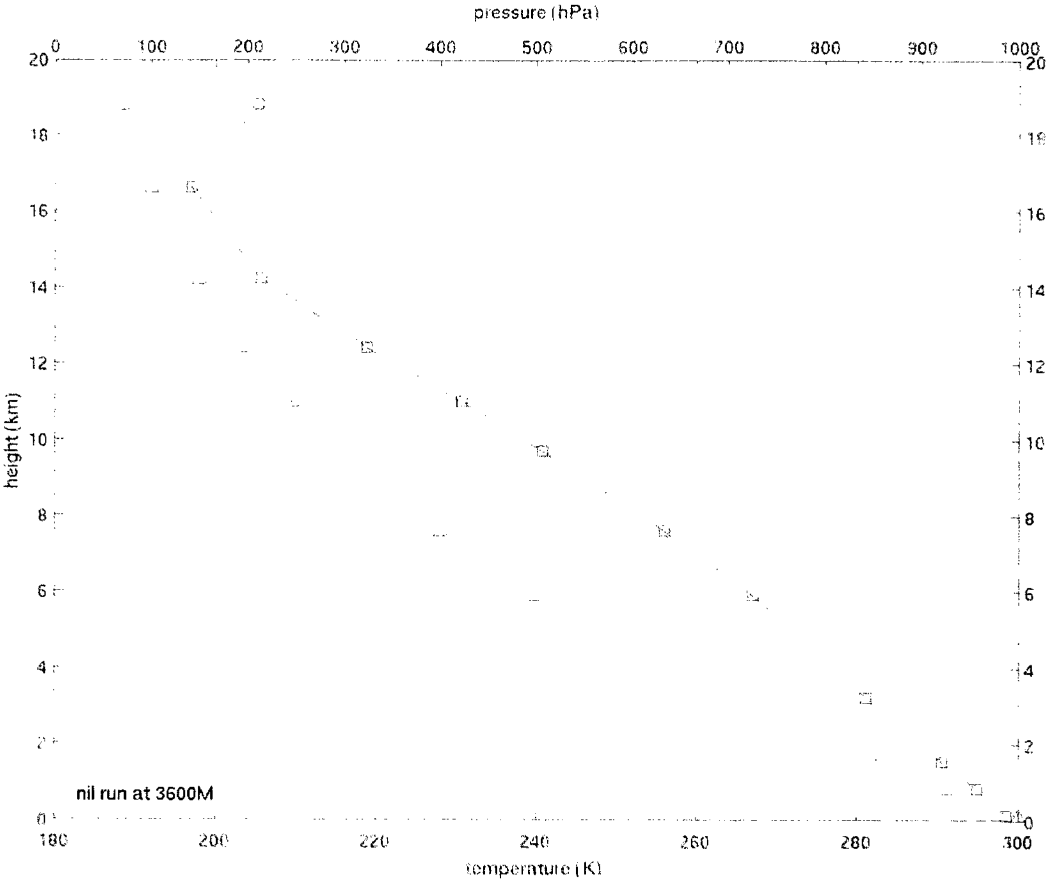

Figure 4.5. Domain-averaged temperature as a function of height (blue squares) at the end of the control run of the UWNMS (with no ice nuclei), 9 am local time (12 UTC) on September 28th. Also plotted for comparison (red triangles) is the relationship between geometric height and ECMWF pressure levels.

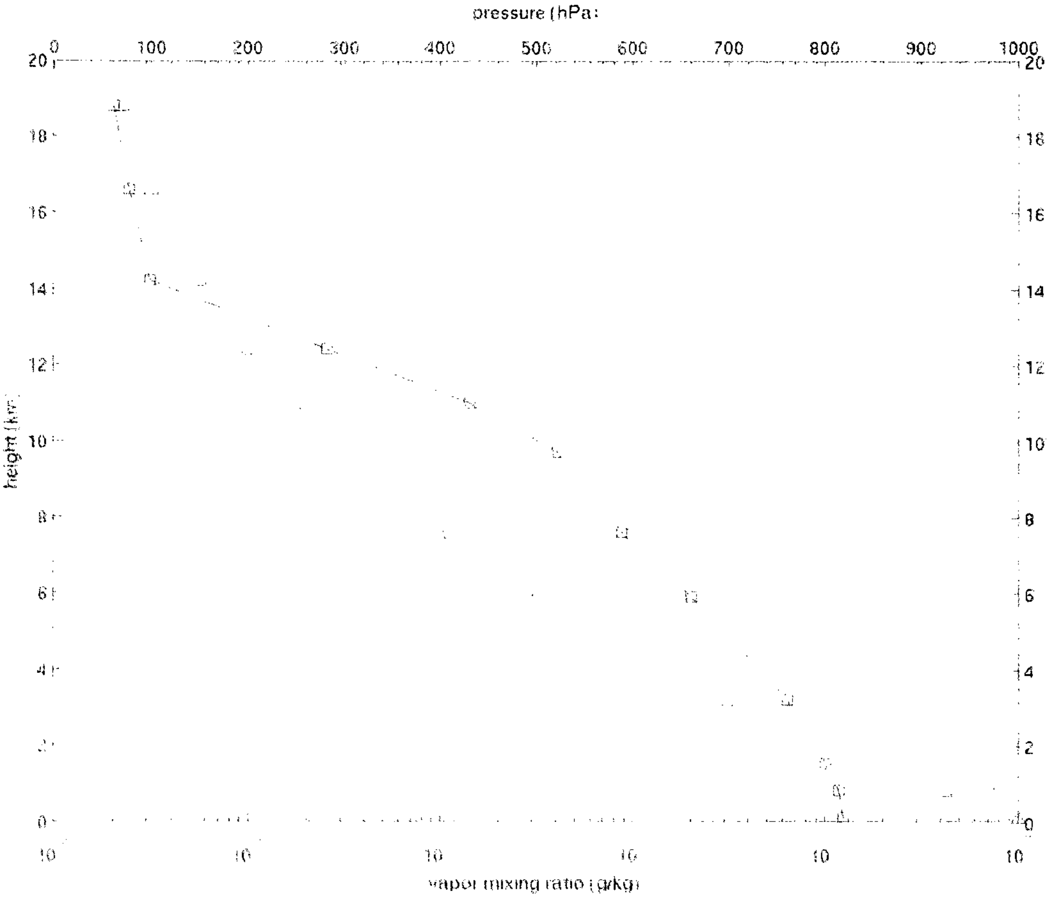

Figure 4.6. Domain-averaged vapor mixing ratio as a function of height (blue squares) at the end of the control run of the UWNMS (with no ice nuclei), 9 am local time (12 UTC) on September 28th. Also plotted for comparison (red triangles) is the relationship between geometric height and ECMWF pressure levels.

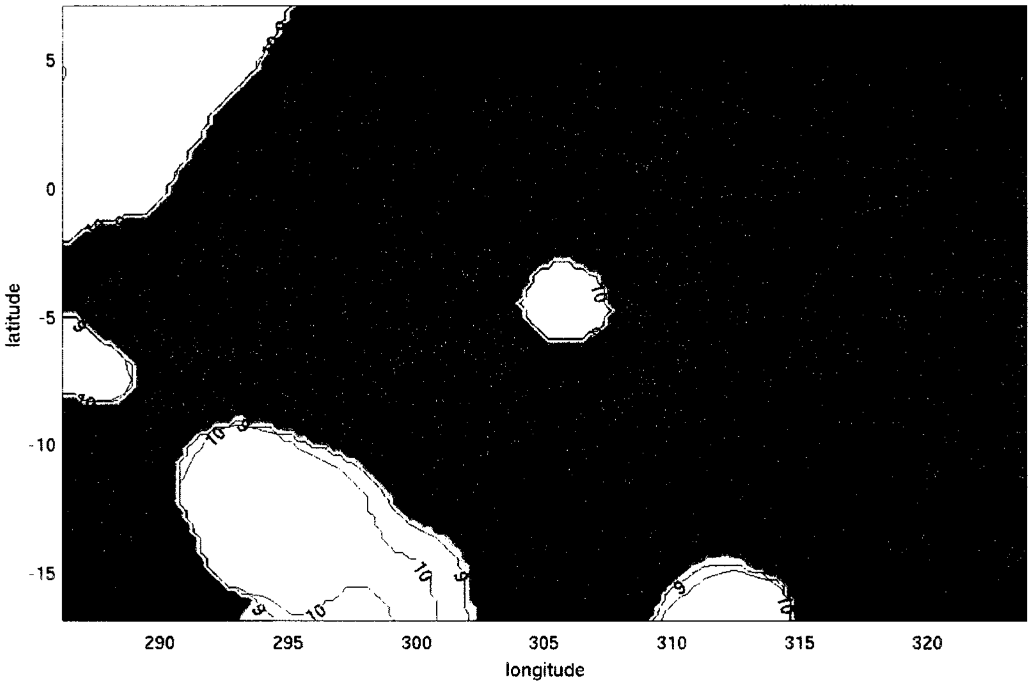

Figure 4.7. The maximum altitude of condensate in the UWNMS at 6 hours into the control run (with no idealized ice nuclei), at 3 am local time (6 UTC) on September 26th.

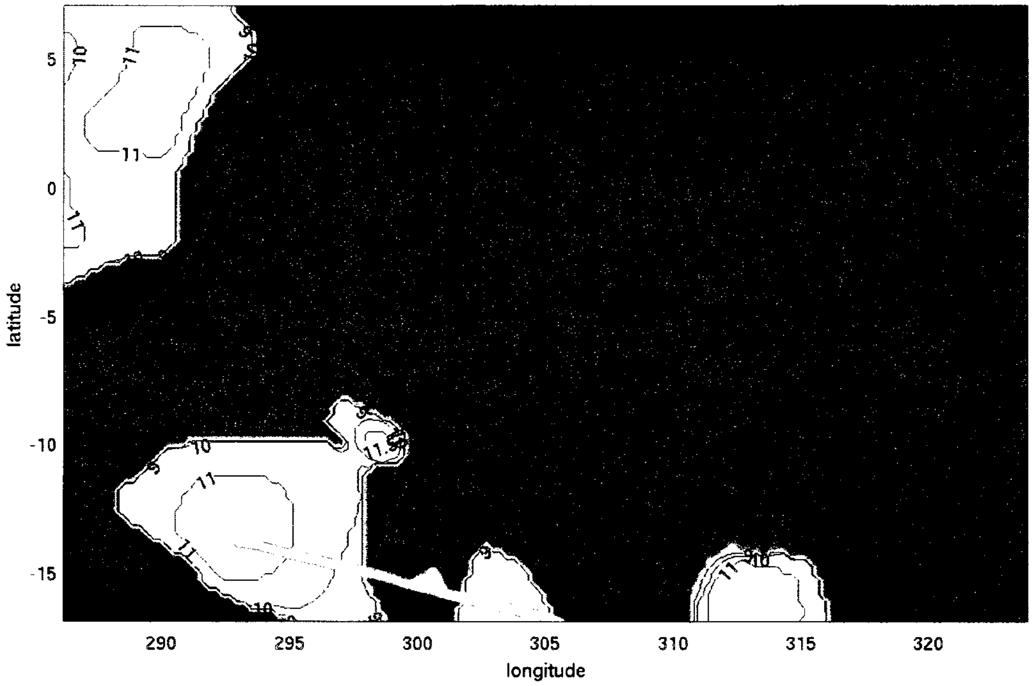

Figure 4.8. The maximum altitude of condensate in the UWNMS at 18 hours into the control run (with no idealized ice nuclei), at 3 pm local time (18 UTC) on September 26th. The position of the surface cold front (in blue) is shown as well—drawn to match the estimated position of the front in Figure 4.8.

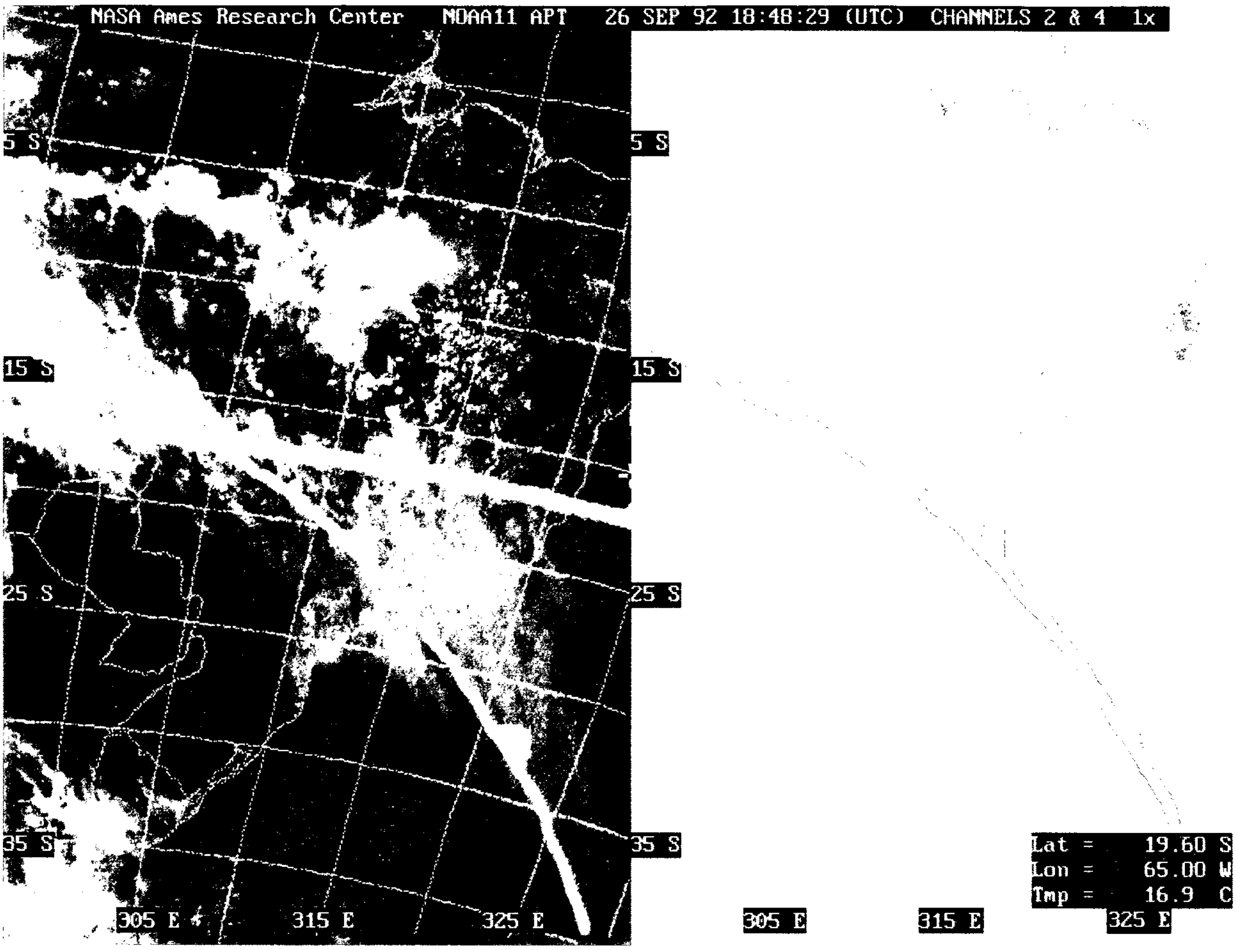

Figure 4.9. Visible (left) and infrared (right) satellite images from the AVHRR instrument onboard NOAA-11 corresponding to 18:48 UTC (3:48 pm local time) on September 26th. A broad swath of clouds associated with the position of a stalled front (in blue) extends southeastward from near 295° E, 15° S to 325° E, 35° S. The thick green line indicates the southern boundary of the UWNMS model domain used in this research.

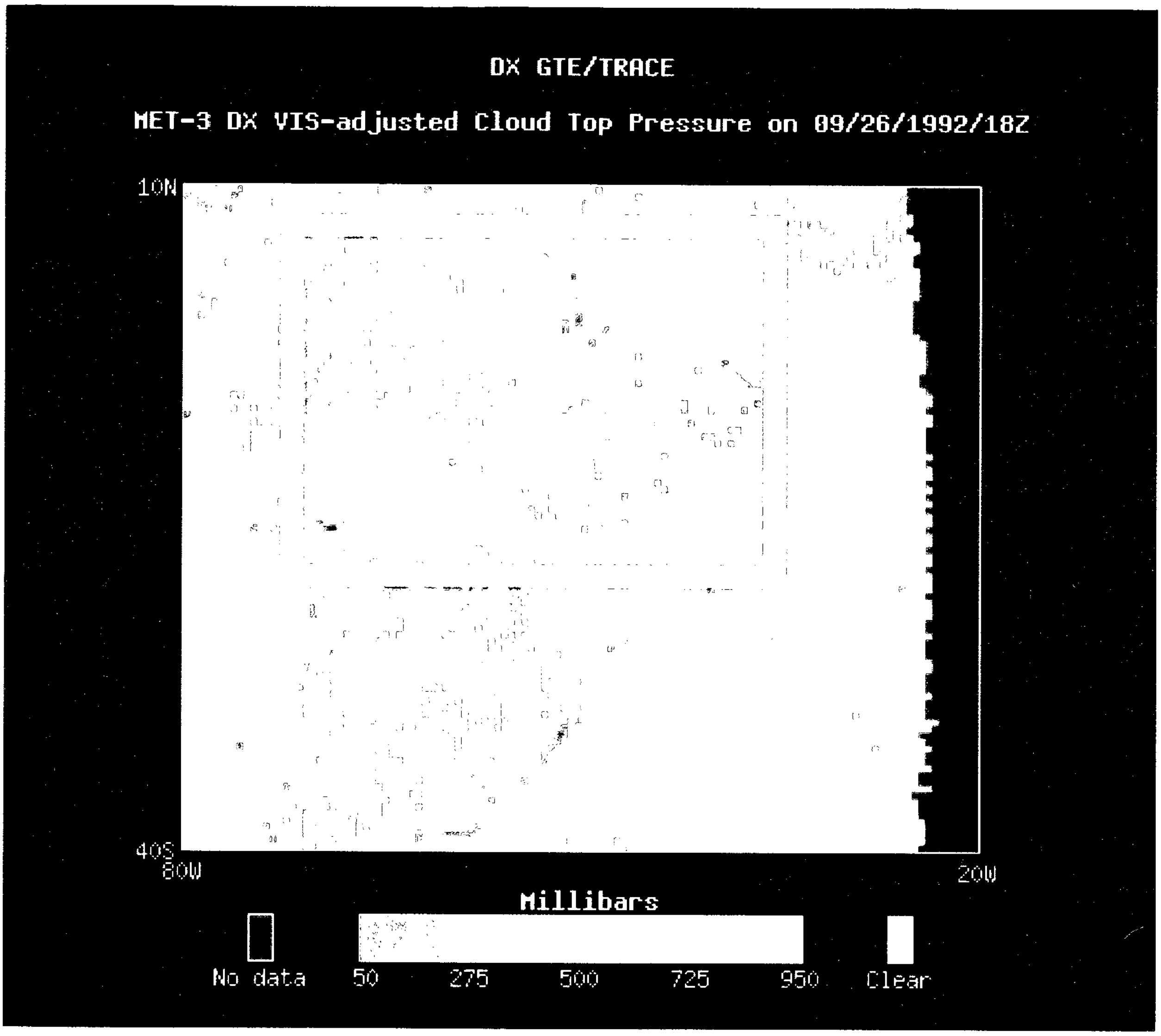

Figure 4.10. ISCCP's cloud-top pressure at 18 UTC on September 26th. The UWNMS model domain is outlined in red. Cloud-top pressures range from near 500 hPa to 300 hPa (approx. 5.9 to 9.7 km) in the southern part of the model domain, the line of convection across the center of the model domain has cloud tops at or above 250 hPa (approx. 11 km).

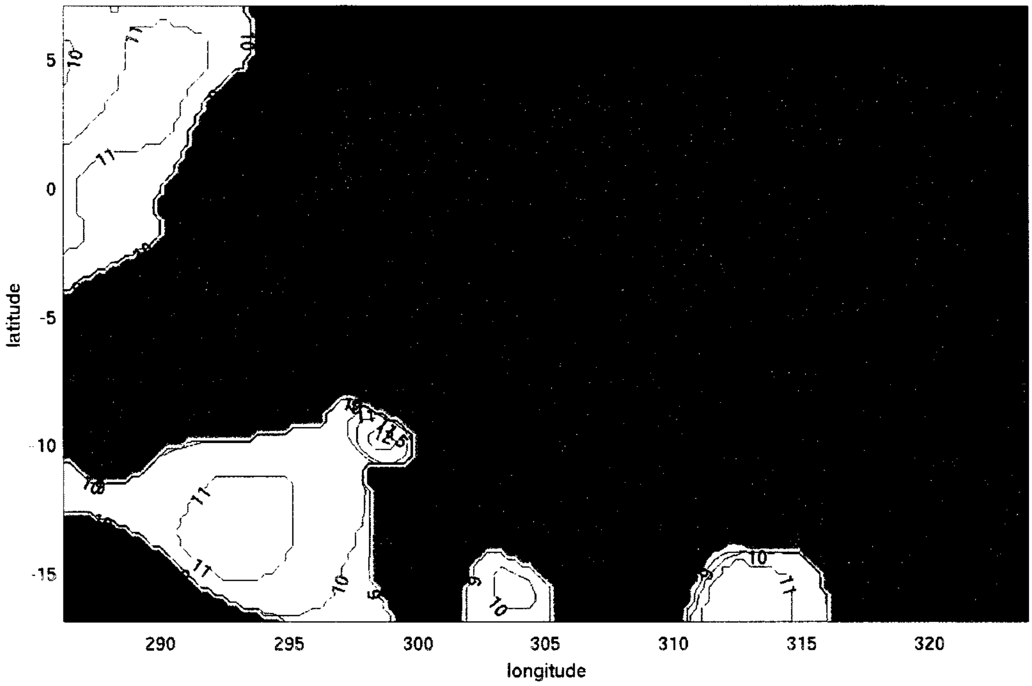

Figure 4.11. The maximum altitude of condensate in the UWNMS at 19.5 hours into the control run (with no idealized ice nuclei), at 4:30 pm local time (19:30 UTC) on September 26th.

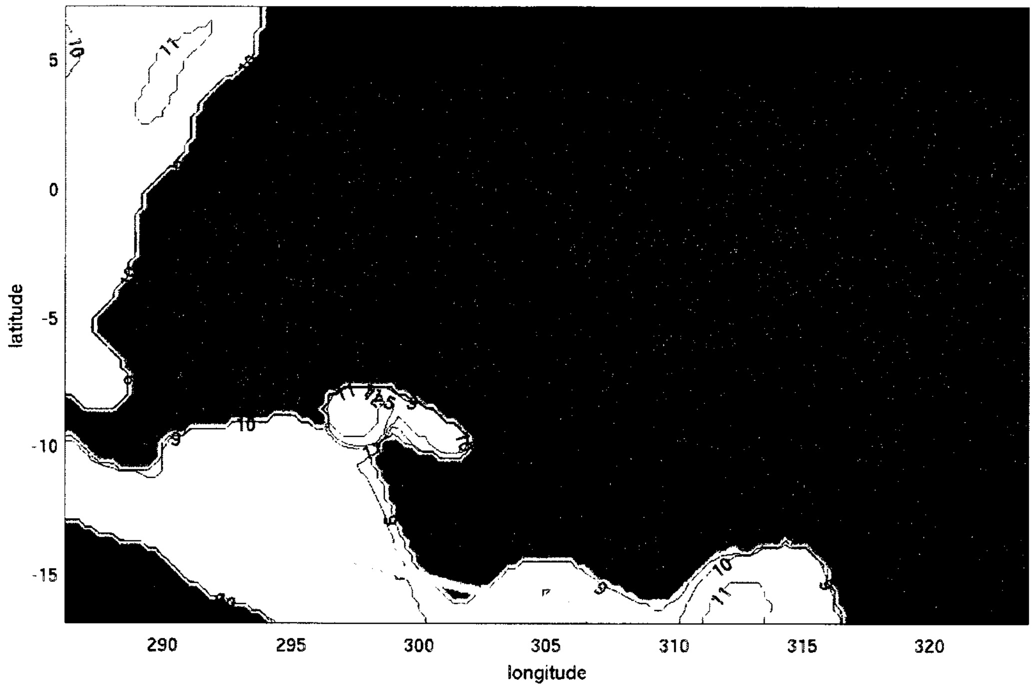

Figure 4.12. The maximum altitude of condensate in the UWNMS at 30 hours into the control run (with no idealized ice nuclei), at 3 am local time (6 UTC) on September 27th. The position of the surface cold front (in blue) is shown as well—drawn to match the estimated position of the front in Figure 4.12.

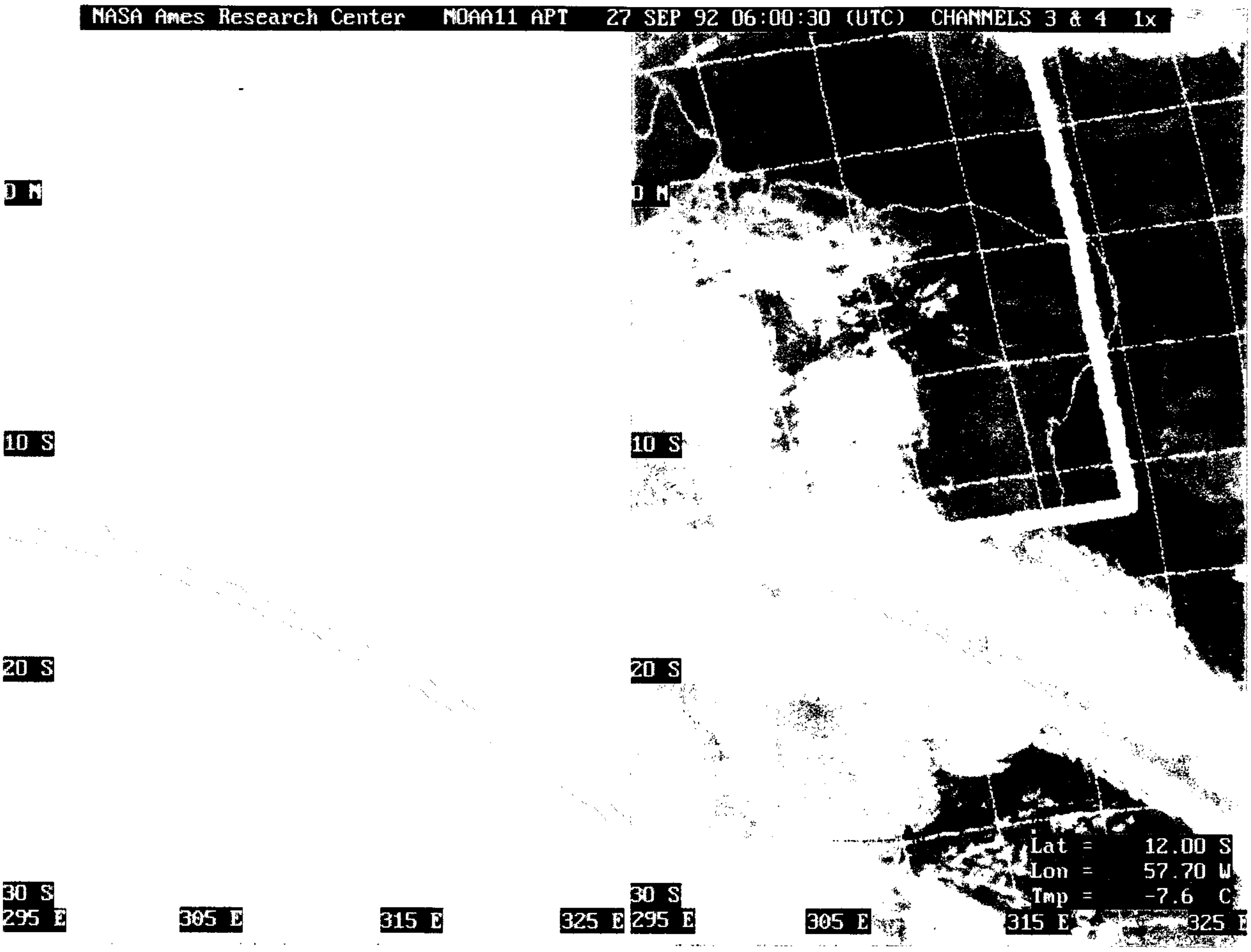

Figure 4.13. Two infrared satellite images from the AVHRR instrument onboard NOAA-11 corresponding to 6 UTC (3 am local time) on September 27th. A broad swath of clouds associated with the position of a stalled front (blue) extends southeastward from near 295° E, 15° S to 325° E, 30° S. The thick green lines indicate the southern and eastern boundaries of the UWNMS model domain used in this research.

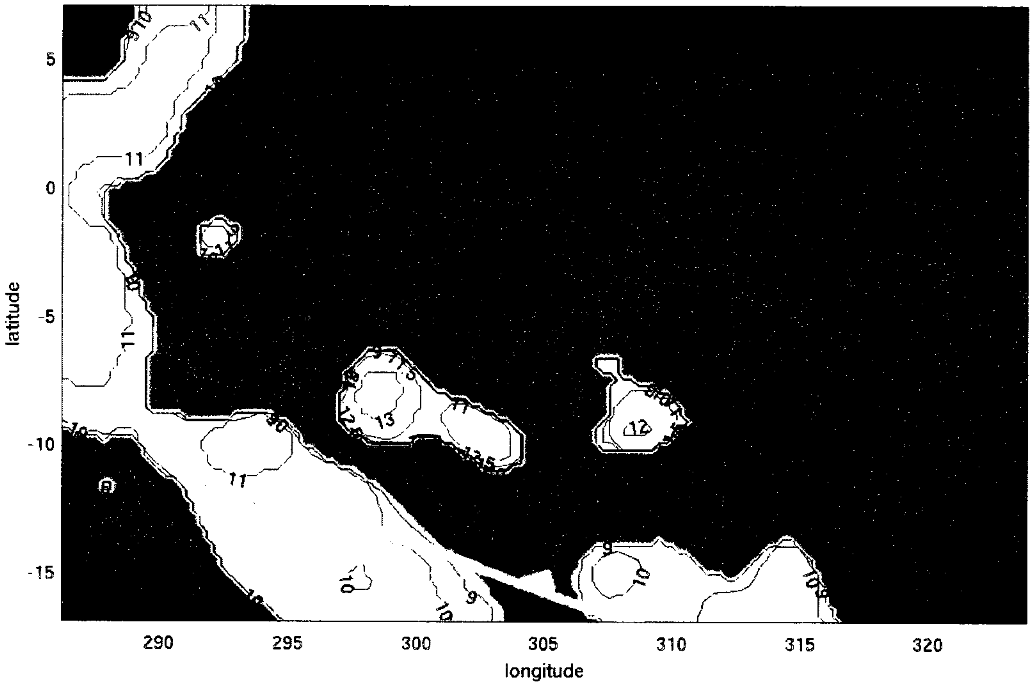

Figure 4.14. The maximum altitude of condensate in the UWNMS at 42 hours into the control run (with no idealized ice nuclei), at 3 pm local time (18 UTC) on September 27th. The position of the surface cold front is shown (in blue)—drawn to match the estimated position of the front in Figure 4.14.

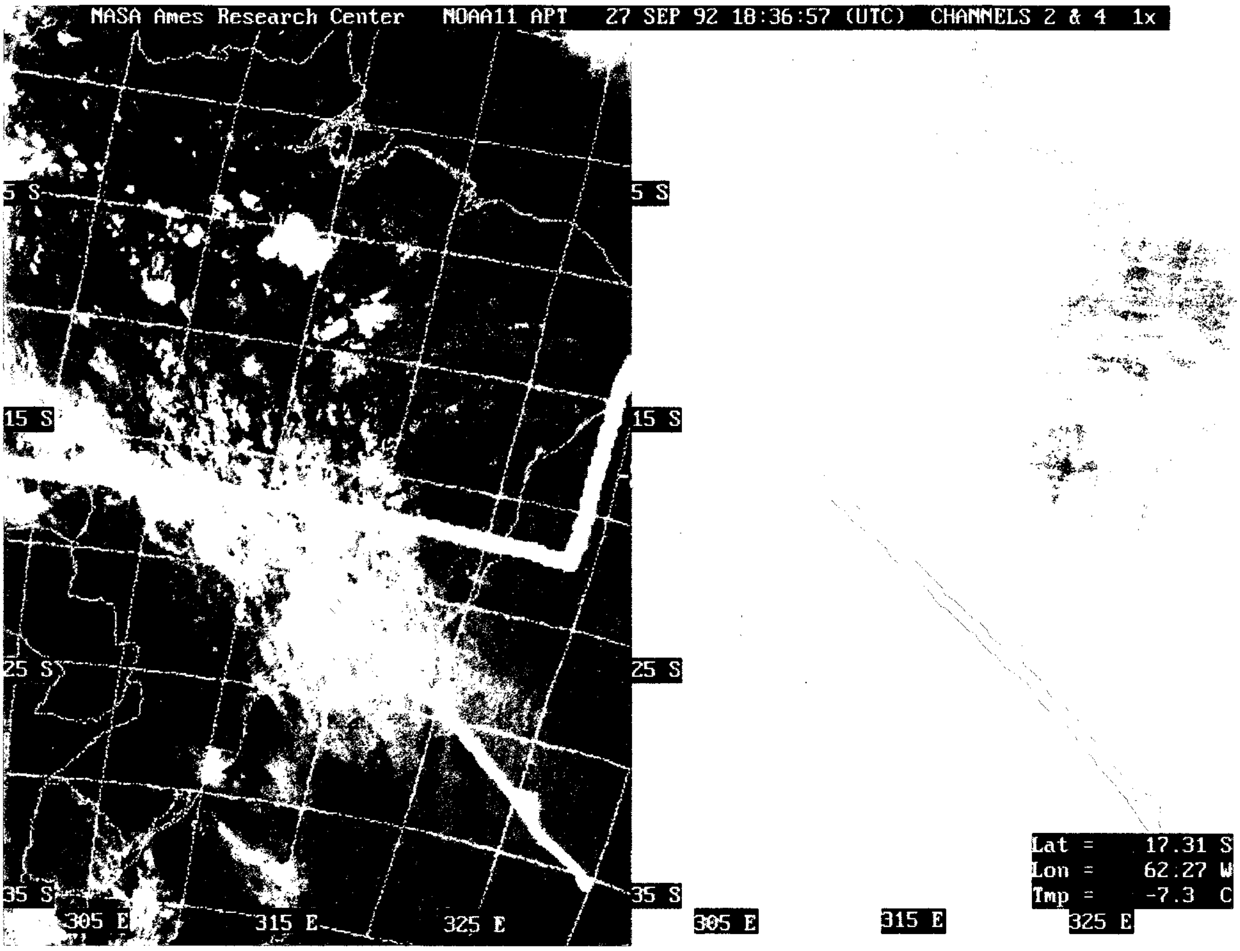

Figure 4.15. Visible and infrared satellite images from the AVHRR instrument onboard NOAA-11 corresponding to 18:36 UTC (3:36 pm local time) on September 27th. A broad swath of clouds associated with the position of a stalled front (blue) extends southeastward from near 305° E, 15° S to 325° E, 30° S. The thick green lines indicate the southern and eastern boundaries of the UWNMS model domain used in this research.

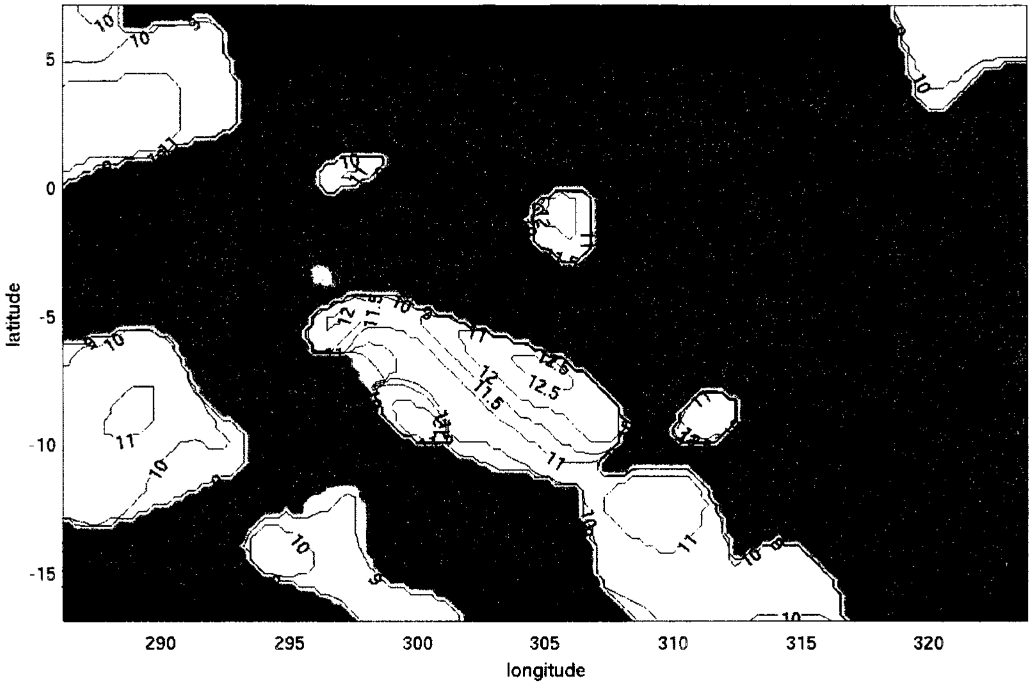

Figure 4.16. The maximum altitude of condensate in the UWNMS at 60 hours into the control run (with no idealized ice nuclei), at 9 am local time (12 UTC) on September 28th.

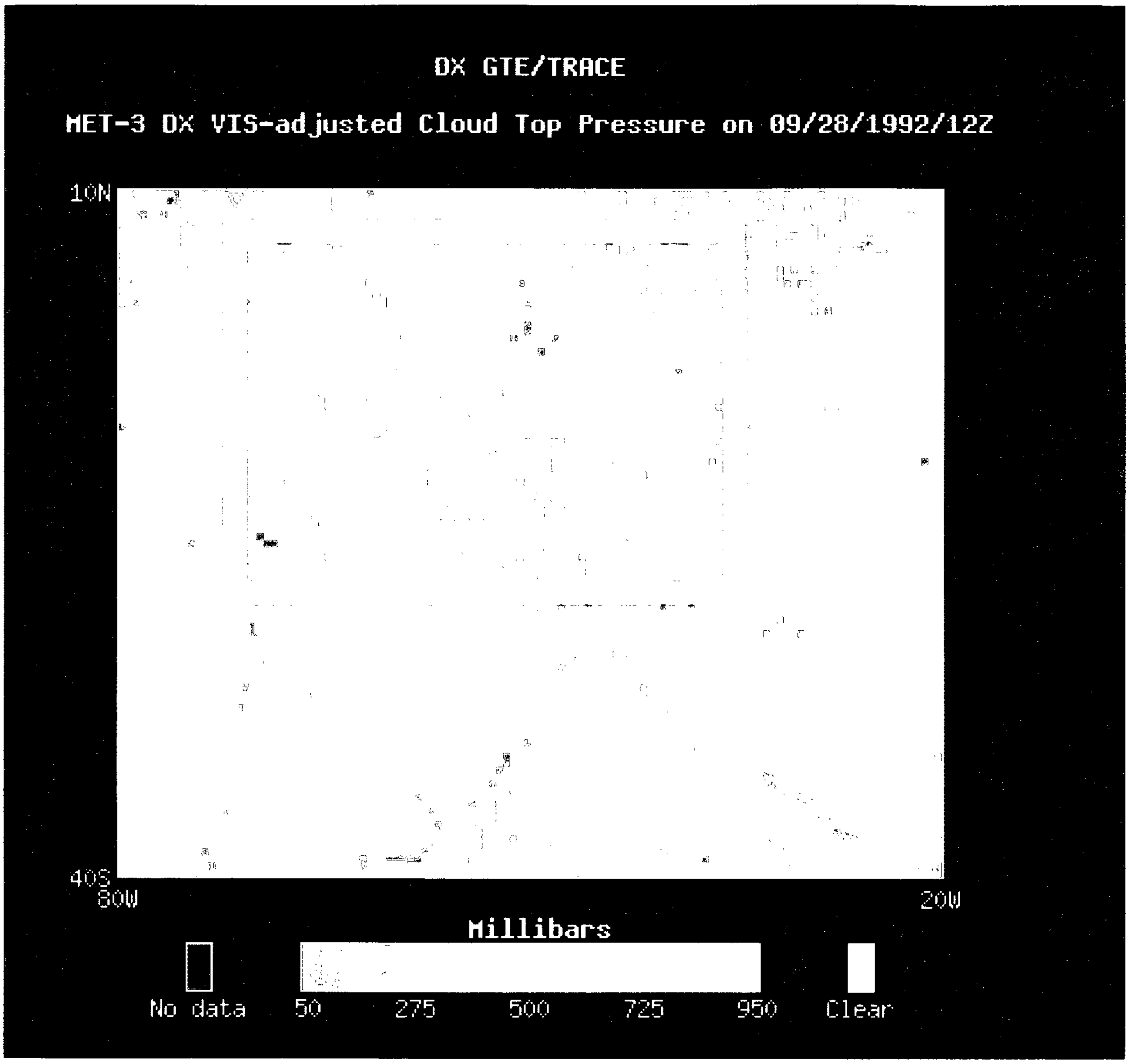

Figure 4.17. ISCCP's cloud-top pressure at 12 UTC on September 28th. The UWNMS model domain is outlined in red. The northwest-southeast swath of clouds have cloud-top pressures ranging from near 250 hPa (11 km)--mostly in the northwestern portion of the model domain, to closer to 300 hPa (approximately 9.7 km) in the mid and southern parts of the domain. Equatorward of this high clouds, there are also scattered low clouds with cloud top pressures below 700 hPa (3 km).

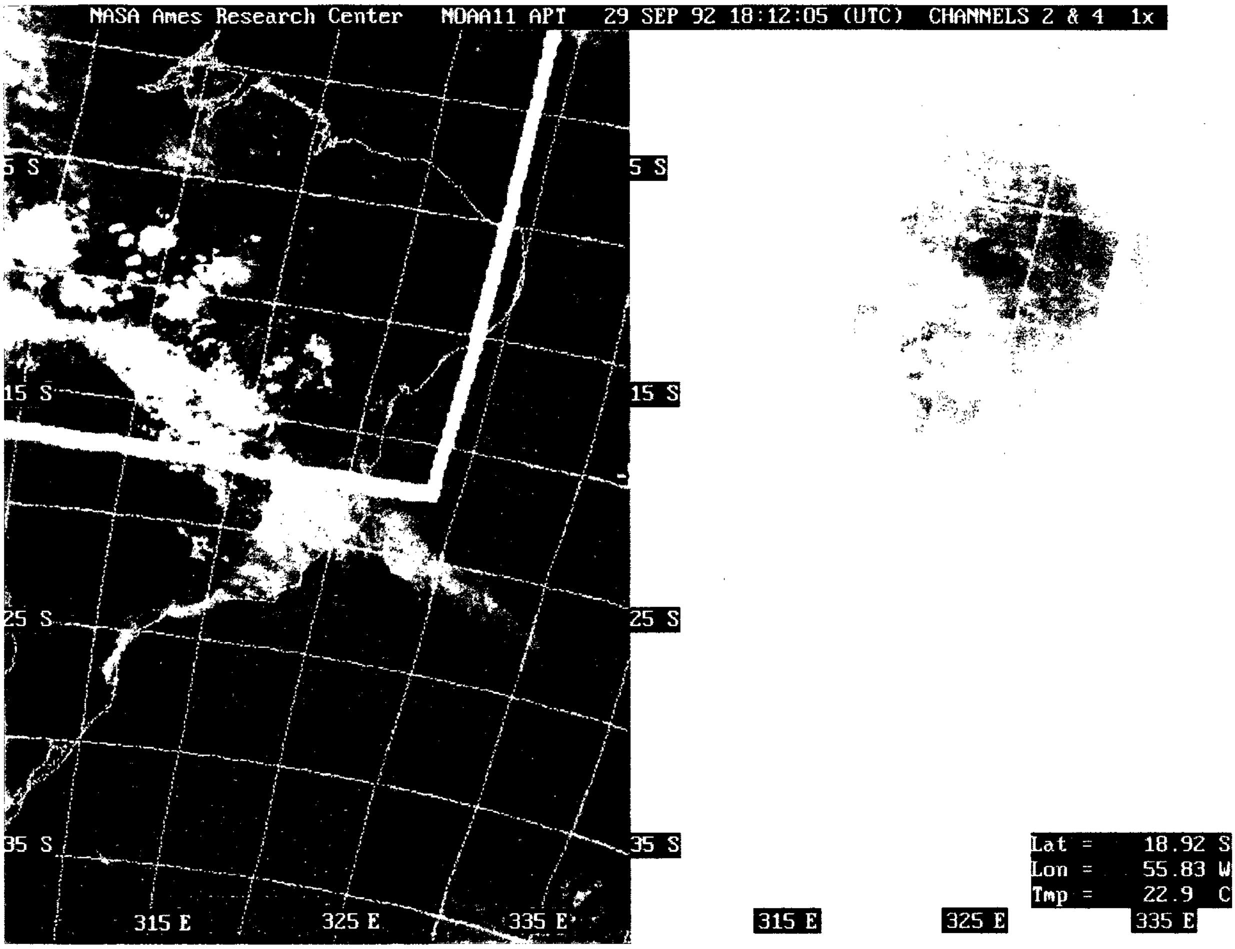

Figure 4.18. Visible and infrared satellite images from the AVHRR instrument onboard NOAA-11 corresponding to 18:12 UTC (3:12 pm local time) on September 29th. The thick green line indicates the southern boundary of the UWNMS model domain used in this research.

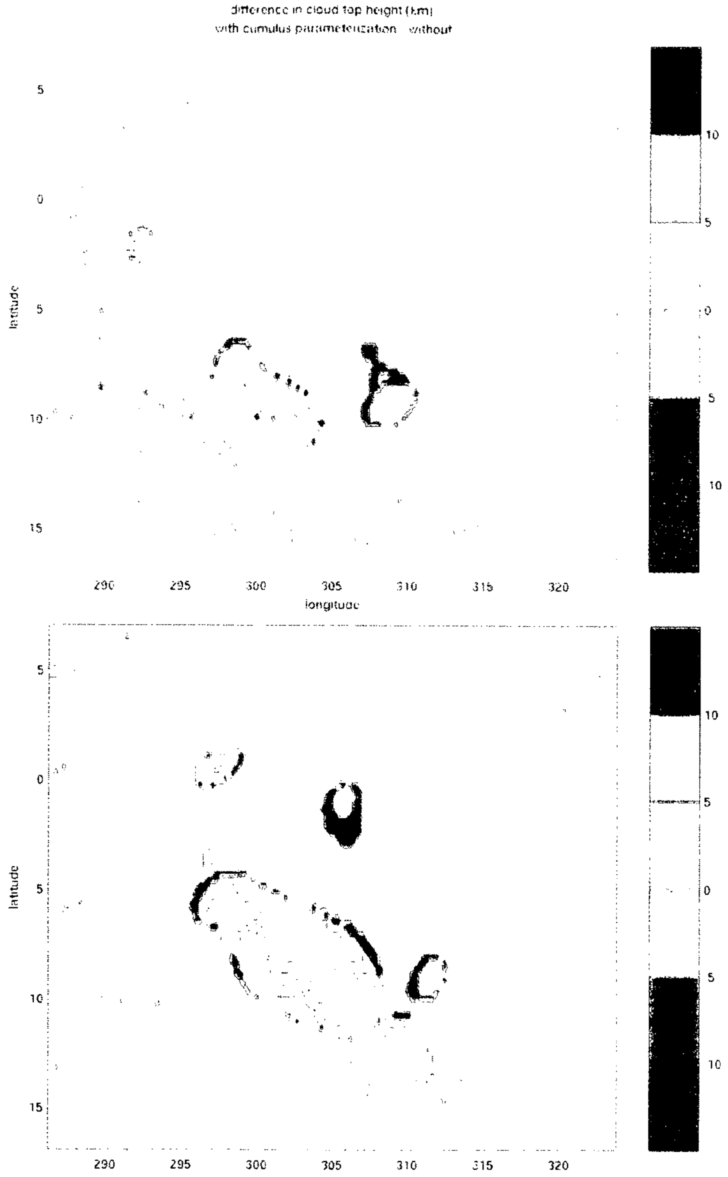

Figure 4.19. There are some differences in cloud top height between model simulations with and without cumulus parameterization, shown here for two different times, at 42 hours, corresponding to 3 pm local time (18 UTC) on September 27th (top) and 60 hours, corresponding to 9 am local time (12 UTC) on September 28th (bottom) into the model runs. Red and orange areas indicate higher cloud tops when there is cumulus parameterization. With cumulus parameterization the energy of convection appears to spread out, so that cloud tops are lower and the cloudy areas are more spread out (the red) while convection without parameterization is more focused on smaller scales and with higher cloud tops (the scattered blue areas)—compare these images to the areas of cloudiness for the same time periods (Figures 4.13 and 4.15).

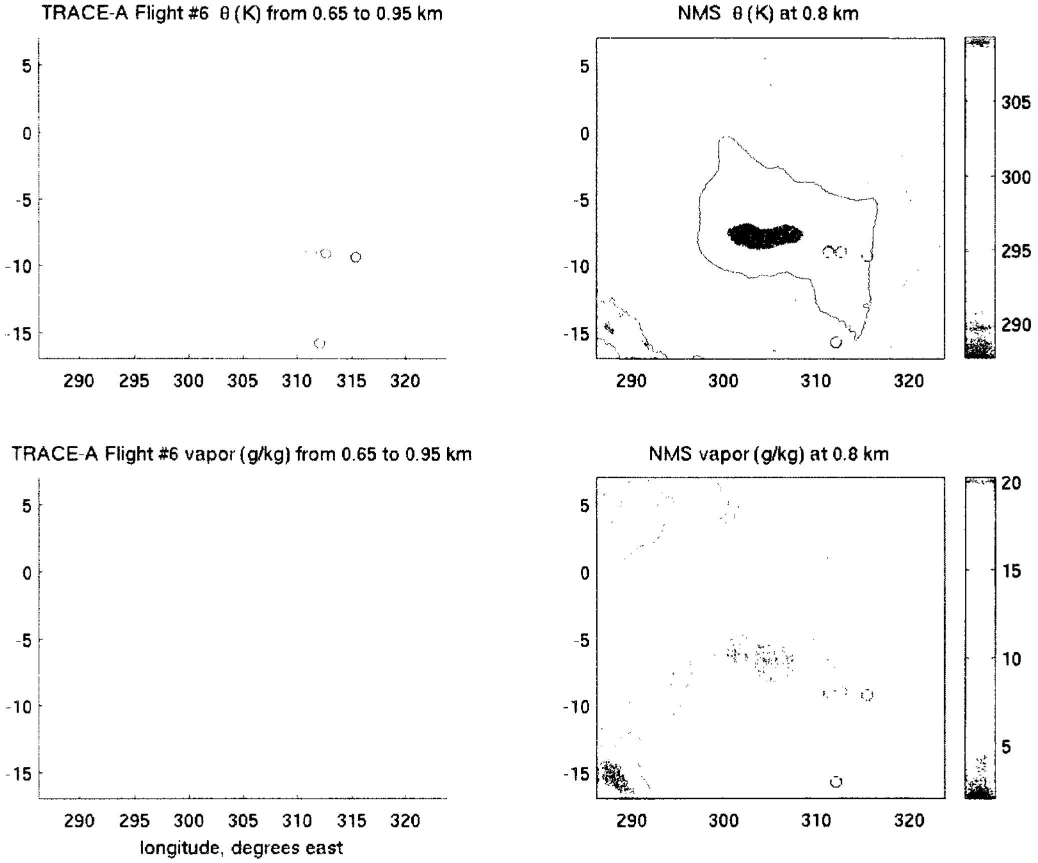

TRACE-A Flight #6 θ (K) from 0.65 to 0.95 km

NMS θ (K) at 0.8 km

TRACE-A Flight #6 vapor (g/kg) from 0.65 to 0.95 km

NMS vapor (g/kg) at 0.8 km

Figure 4.20. At 0.8 km, a comparison of TRACE-A flight number 6 in-situ measurements (left) of temperature (top) and humidity (bottom), converted to potential temperature and vapor mixing ratio, to UWNMS potential temperature and vapor mixing ratio (right). TRACE-A flight number 6 took place on the 26th of September 1992, from approximately 09:15 to 16:50 UTC. Flight data are shown for a small range of altitudes (0.8 +/- 0.15 km) to ensure that there are data to compare to the UWNMS output at 0.8 km, 15:00 UTC. Near the center of the domain the model is drier. This is likely a result of the land surface parameterization of the UWNMS.

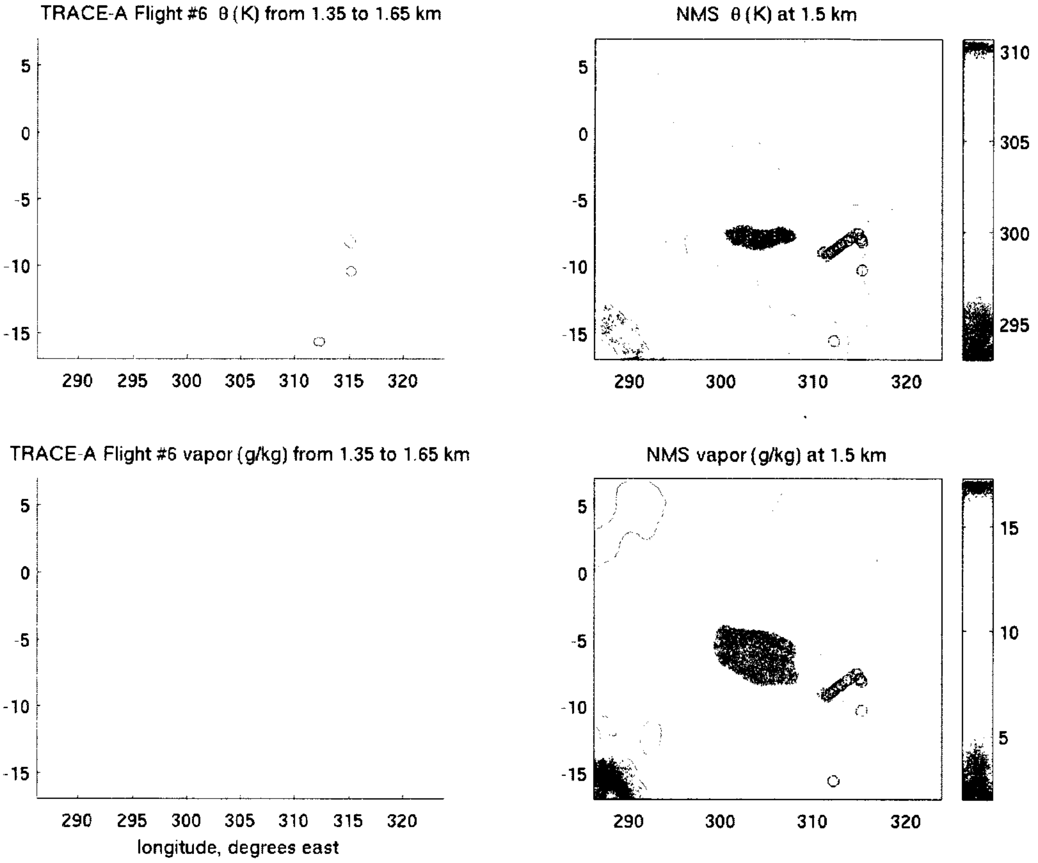

Figure 4.21. At 1.5 km, a comparison of TRACE-A flight number 6 in-situ measurements (left) of temperature (top) and humidity (bottom), converted to potential temperature and vapor mixing ratio, to UWNMS output of potential temperature and vapor mixing ratio (right). TRACE-A flight number 6 took place on the 26th of September 1992, from approximately 09:15 to 16:50 UTC. Flight data are shown for a small range of altitudes (1.5 +/- 0.15 km) to ensure that there are data to compare to the UWNMS output at 1.5 km, 15:00 UTC. The UWNMS output at this level is slightly warmer, except at the southern domain boundary where it is cooler than flight measurements. At the southern domain boundary, the UWNMS is more moist than flight measurements indicate, and near the center of the domain the model is drier. This is likely a result of the land surface parameterization of the UWNMS.

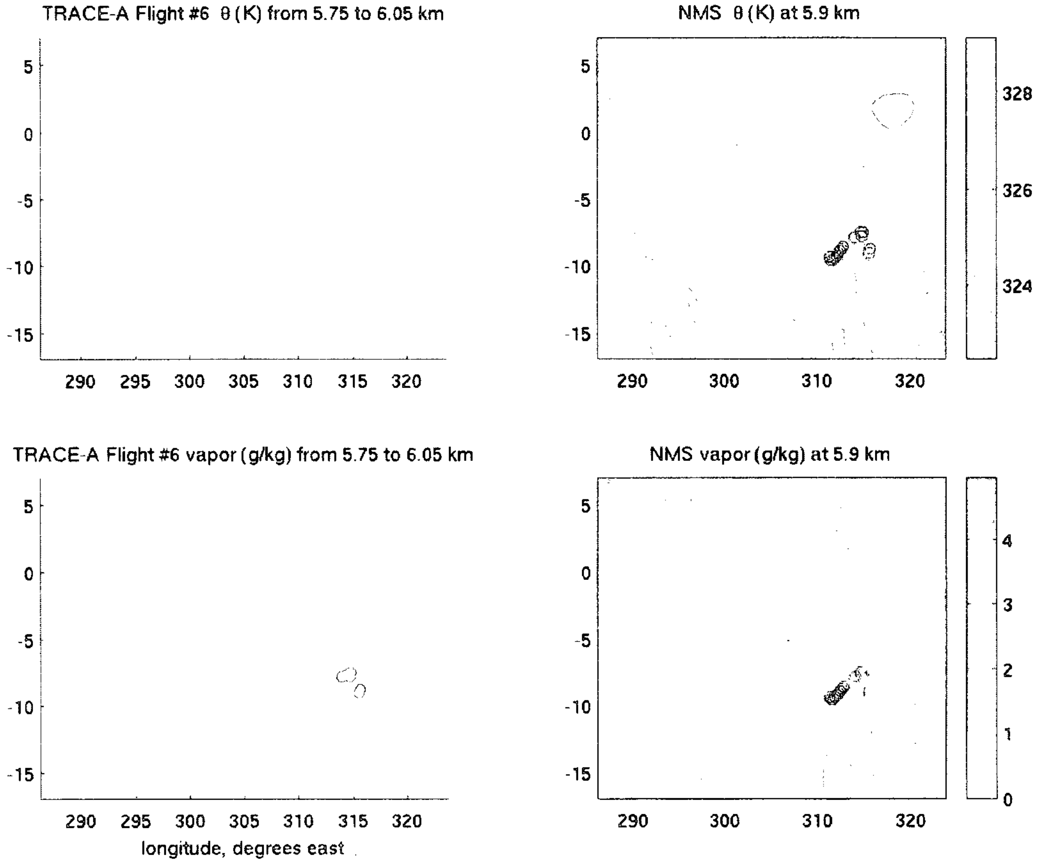

Figure 4.22. At 5.9 km, a comparison of TRACE-A flight number 6 in-situ measurements (left) of temperature (top) and humidity (bottom), converted to potential temperature and vapor mixing ratio, to UWNMS output of potential temperature and vapor mixing ratio (right). TRACE-A flight number 6 took place on the 26th of September 1992, from approximately 09:15 to 16:50 UTC. Flight data are shown for a small range of altitudes (5.9 +/- 0.15 km) to ensure that there are data to compare to the UWNMS output at 5.9 km, 15:00 UTC. At this level the UWNMS output compares favorably to flight measurements.

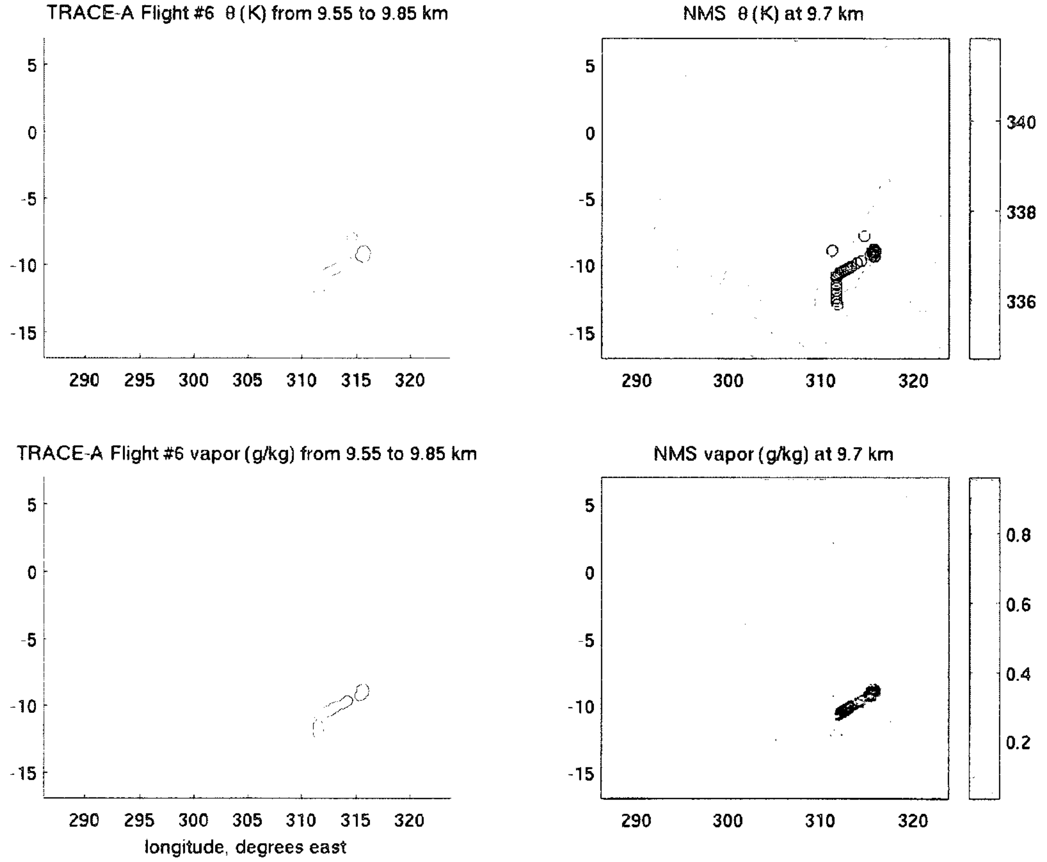

Figure 4.23. At 9.7km, a comparison of TRACE-A flight number 6 in-situ measurements (left) of temperature (top) and humidity (bottom), converted to potential temperature and vapor mixing ratio, to UWNMS output of potential temperature and vapor mixing ratio (right). TRACE-A flight number 6 took place on the 26th of September 1992, from approximately 09:15 to 16:50 UTC. Flight data are shown for a small range of altitudes (9.7 +/- 0.15 km) to ensure that there are data to compare to the UWNMS output at 9.7 km, 15:00 UTC. At this level the UWNMS output compares favorably to flight measurements.

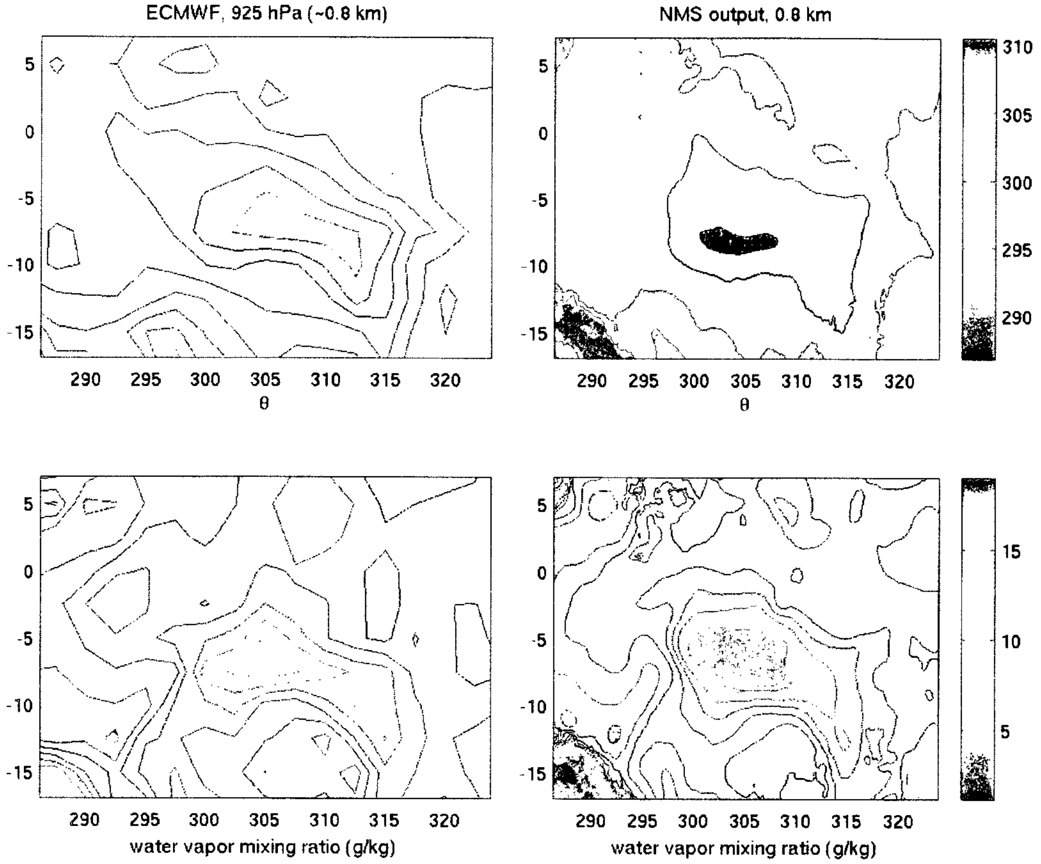

Figure 4.24. A comparison of ECMWF data (left) to UWNMS output (right) at 12 UTC on September 26th, at approximately the same height—the average geometric height of the 925 hPa layer is 0.8003 km. The UWNMS potential temperature field (top right) has a lot less structure than the ECMWF potential temperature at this level. The UWNMS fares better in representing water vapor, though a bit drier in the center of the model domain. These differences are most likely because of differing surface parameterizations between models.

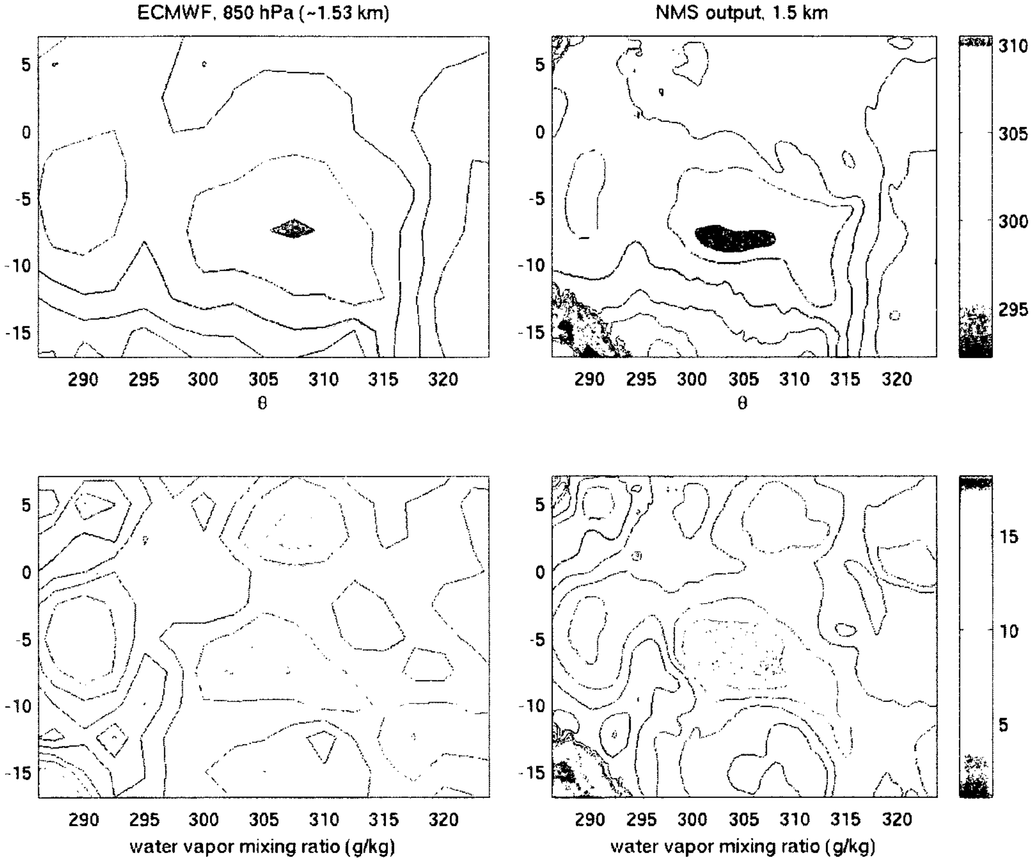

Figure 4.25. A comparison of ECMWF data (left) to UWNMS output (right) at 12 UTC on September 26th—the average geometric height of the 850 hPa layer is 1.53 km, so for this comparison UWNMS data from 1.4 and 1.6 km were averaged. The UWNMS potential temperature field (top right) is a bit cooler than the ECMWF potential temperature at this level, and the effects of topography (southwestern corner of the model domain) are much more obvious. The UWNMS is again a bit drier in the center of the model domain (bottom row).

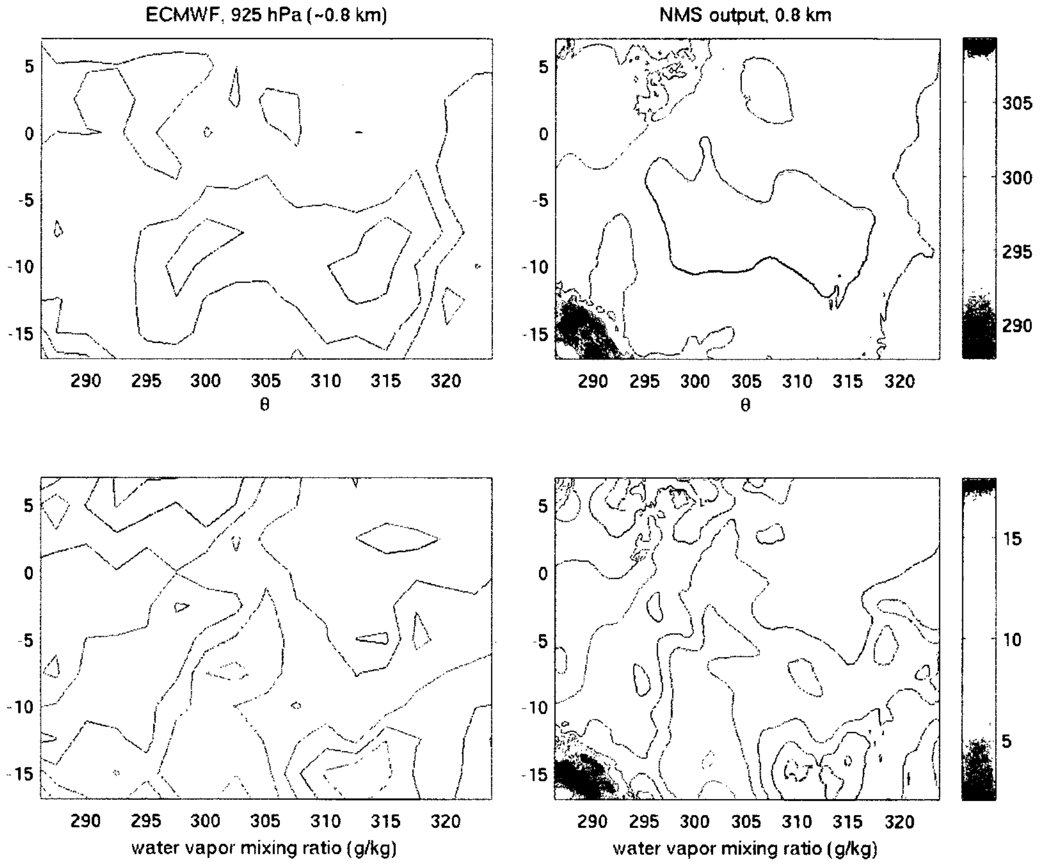

Figure 4.26. A comparison of ECMWF data (left) to UWNMS output (right) at 12 UTC on September 28th, at approximately the same height—the average geometric height of the 925 hPa layer is 0.8003 km. This comparison is very similar to Figure 4.7, 48 hours earlier. The UWNMS potential temperature field (top right) has a lot less structure than the ECMWF potential temperature at this level. The UWNMS fares better in representing water vapor, though a bit drier in the center of the model domain. These differences are most likely because of differing surface parameterizations between models.

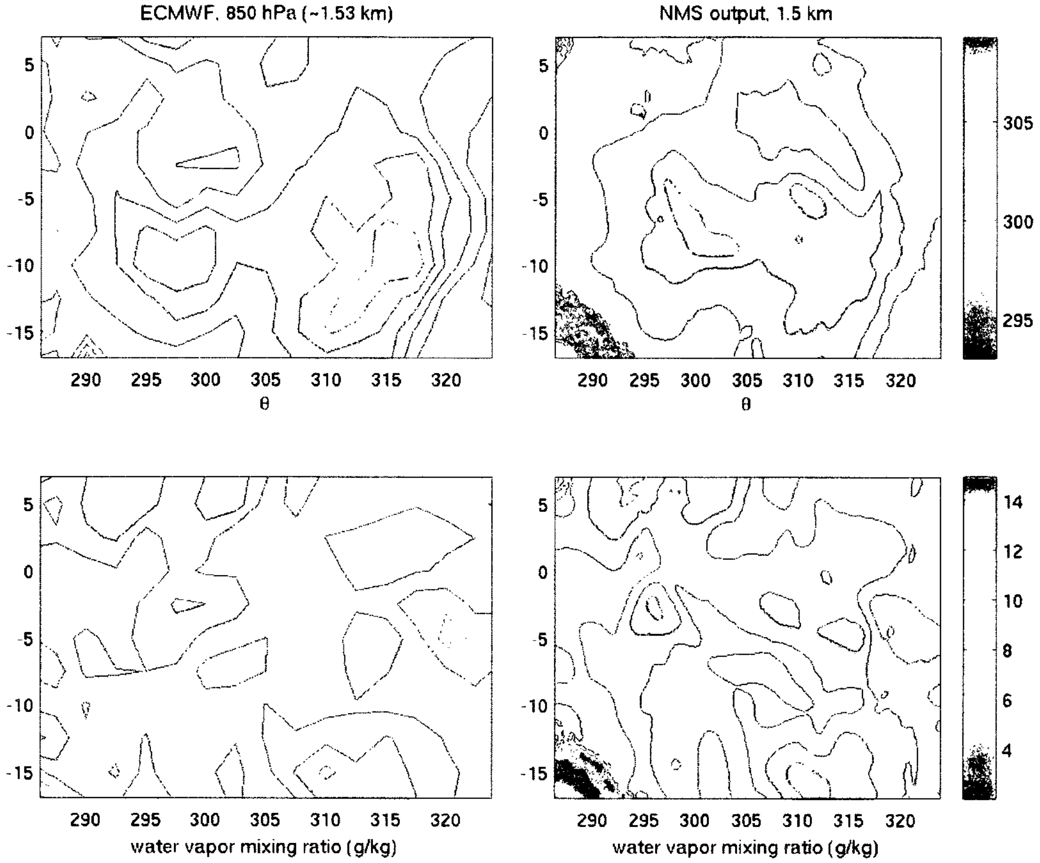

Figure 4.27. A comparison of ECMWF data (left) to UWNMS output (right) at 12 UTC on September 28th—the average geometric height of the 850 hPa layer is 1.53 km, so for this comparison UWNMS data from 1.4 and 1.6 km were averaged. The UWNMS potential temperature field (top right) is a bit cooler than the ECMWF potential temperature at this level, and the effects of topography (southwestern corner of the model domain) are much more obvious. The UWNMS is slightly more moist than the ECMWF datset (bottom row), mountainous topography excluded.

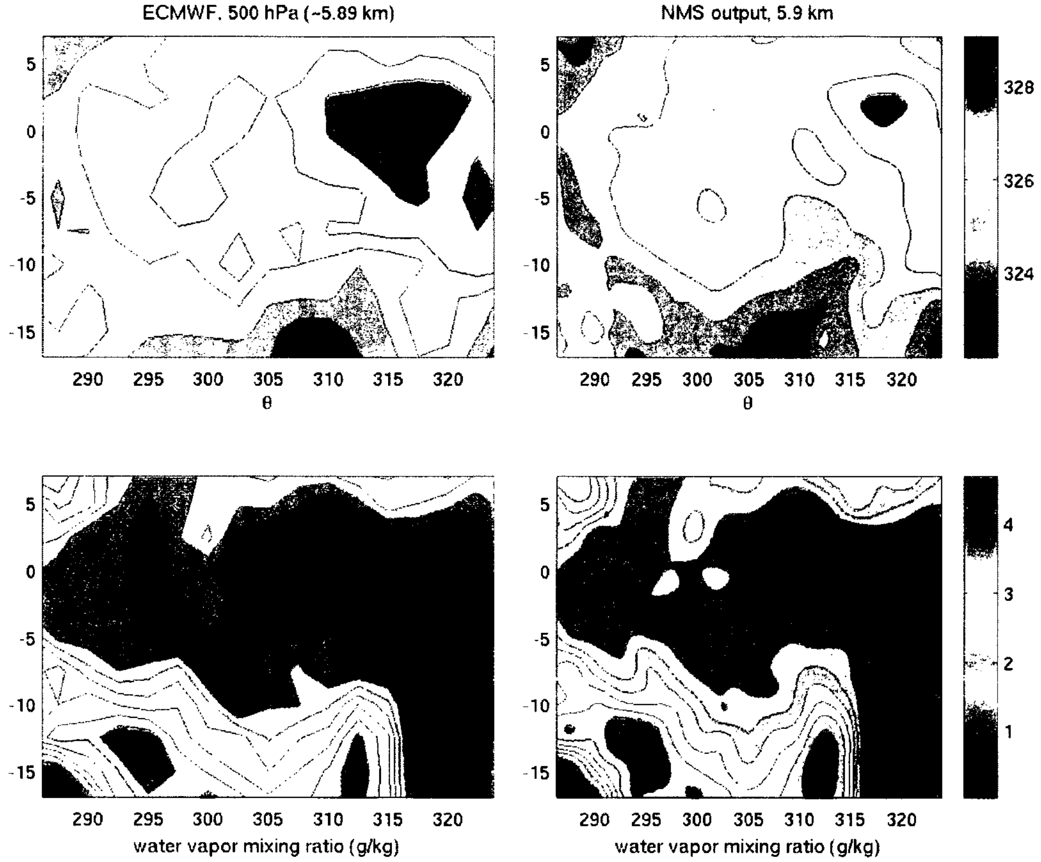

Figure 4.28. A comparison of ECMWF data (left) to UWNMS output (right) at 12 UTC on September 26th—the average geometric height of the 500 hPa layer is 5.8885 km, so for this comparison UWNMS data from 5.8 and 6.0 km were averaged. The UWNMS potential temperature field (top right) is a bit cooler than the ECMWF potential temperature at this level. The UWNMS represents water vapor (bottom row) fairly well, though it is a bit more moist in the west-central part of the domain, compared to the ECMWF vapor field.

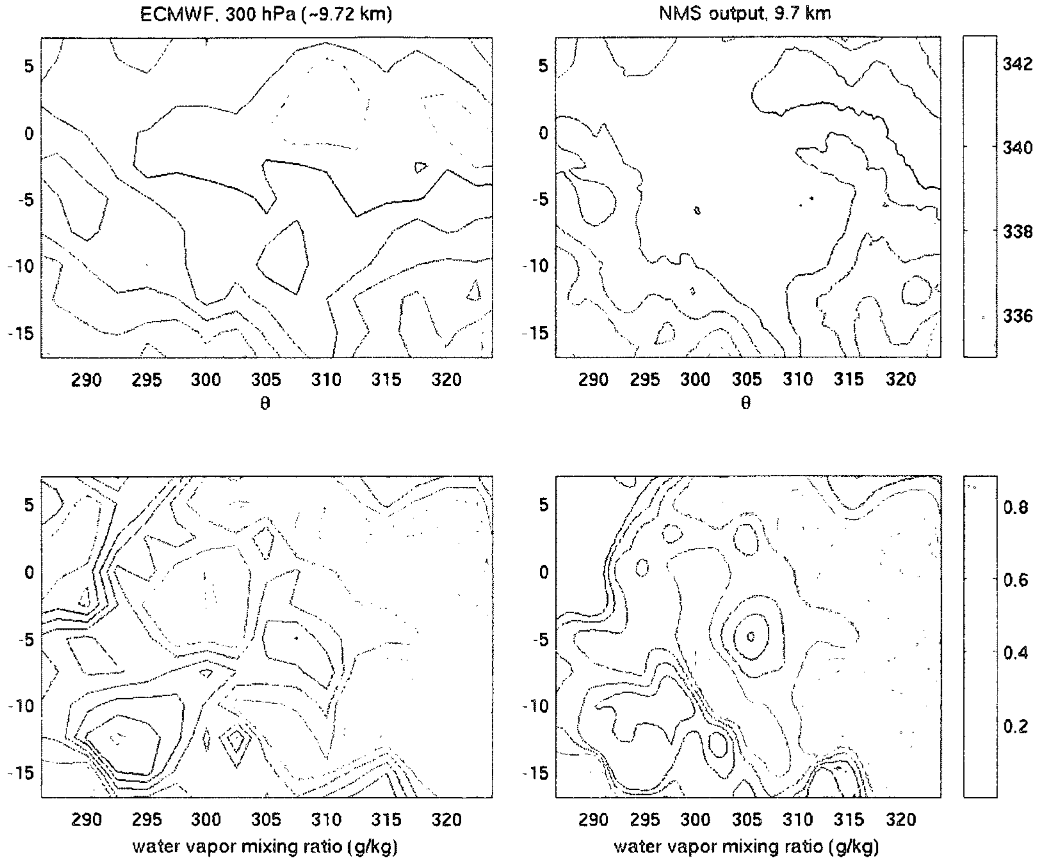

Figure 4.29. A comparison of ECMWF data (left) to UWNMS output (right) at 12 UTC on September 26th—the average geometric height of the 300 hPa layer is 9.7176 km, so for this comparison UWNMS data from 9.6 and 9.8 km were averaged. The UWNMS potential temperature field (top right) is again slightly cooler (~1 K) than the ECMWF potential temperature at this level. The UWNMS is slightly more moist in the eastern half of the domain and notably drier in the western half (bottom row).

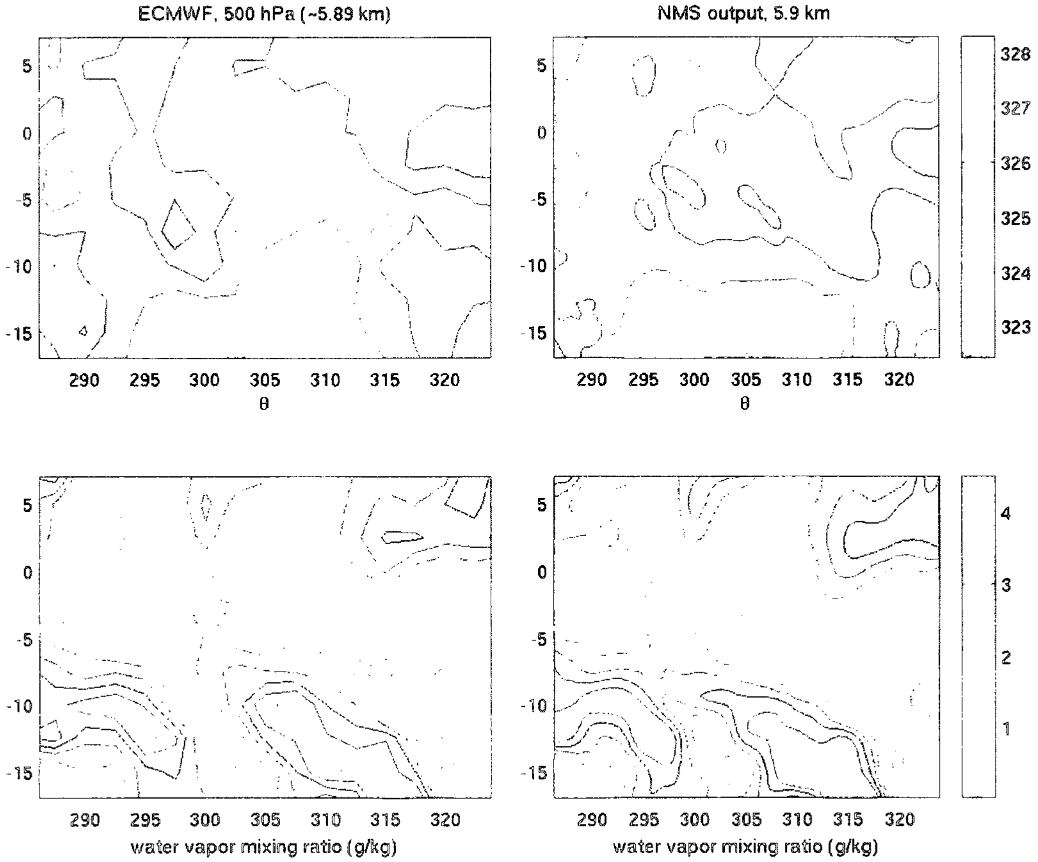

Figure 4.30. A comparison of ECMWF data (left) to UWNMS output (right) at 12 UTC on September 28th—the average geometric height of the 500 hPa layer is 5.8885 km, so for this comparison UWNMS data from 5.8 and 6.0 km were averaged. The comparison between potential temperature fields is mixed (top row), with the UWNMS slightly warmer (~1 K) in the center of the domain. Though slightly more moist, UWNMS represents water vapor well (bottom row).

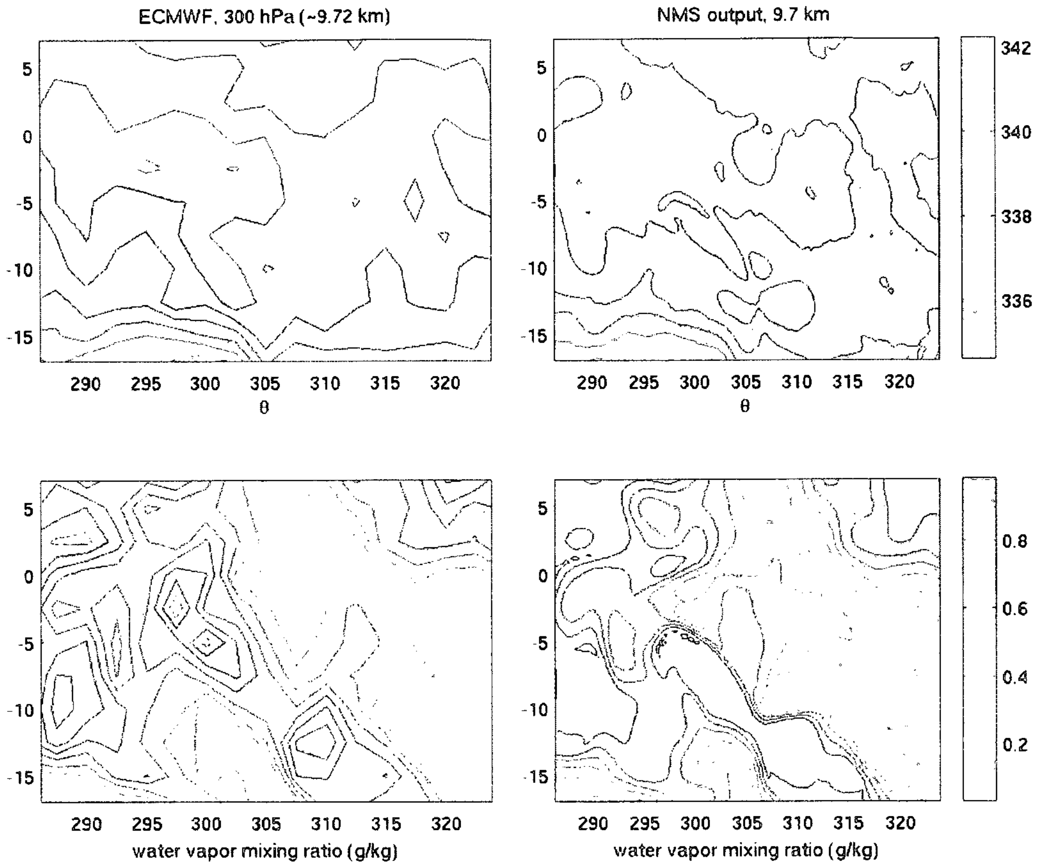

Figure 4.31. A comparison of ECMWF data (left) to UWNMS output (right) at 12 UTC on September 28th—the average geometric height of the 300 hPa layer is 9.7176 km, so for this comparison UWNMS data from 9.6 and 9.8 km were averaged. The UWNMS potential temperature field (top right) is again slightly cooler (~1 K) than the ECMWF potential temperature at this level. The UWNMS is slightly drier than ECMWF (bottom row). It is possible that convection in the UWNMS does not reach this level with the intensity modeled by the ECMWF, or that the timing of UWNMS convection differs.

Chapter 5: Results Overview

Given that we don't know very much about IN (Chapter 3), such as how many there are and where, or about their activation behavior, four categories of experiments were conceived to explore how sensitive the environment is to varying IN properties, and vice versa. In this chapter we will look at data from eight experiments that form four categories: the effect of concentration, the effect of the height of the IN layer, the effect of changing the activation temperature, and the effect of changing a combination of all three variables. How is the location and timing of IN activation affected by these different scenarios? What is the overall effect on the distribution of water, both in phase and height? Here we will investigate the general trends of results, in preparation for more specific, case-study discussion of larger differences in the next two chapters.

At any particular time and location where an IN activated, a passive tracer was also activated to trace the movement of the air in which the IN-induced pristine ice crystal had formed. Since the model microphysics is calculated en masse, we can not follow the individual IN-formed crystals, but we can track the properties of the air in which that ice crystal resides and how that air changes with time. Then, this passive tracer field allows us to see the envelope of IN-influenced air. Besides learning where and when air influenced by IN activation exists, we can also look at the tracer concentrations within the envelopes to get a general sense of the *degree* of influence.

The effect of concentration.

To explore the effects of changing IN concentration, three of the experiments were set up with IN initialized as a "sheet" at 250 hPa (approximately 11 km), with concentrations of 30, 60, or 120 IN/L. Since most tropical deep convection detrains near 200 hPa (Fueglistaler et al., 2009), 250 hPa seems a reasonable initial IN height, assuming IN were convectively transported and allowing for slightly weaker convection (Chapter 4). The IN were allowed to activate when the temperature was at or below 238K and the relative humidity with respect to ice was greater than 100%. On average, temperatures at and below this activation temperature are present above 10 km (Figure 4.5). Figure 5.1 shows a time series of activation tracers, horizontally averaged, for the three different initial concentrations. As time increases, the IN-influenced air is mixed upward and downward away from 11 km. The most striking feature of these three images is that there is so little difference between the envelopes and number of tracers for the 30, 60, and 120 IN/L runs. This seems counterintuitive, for a greater number of IN should result in a greater number of activation events. The reason this may not be the case is because IN nucleation removes water from the vapor stage, and since the amount of vapor is the same when each model experiment is initialized, having a higher IN concentration means that some IN will go unactivated, the vapor being fixed in previous activation events at other times and gridpoints (see Figure 5.2 for a pictoral explanation). This will be especially true at the beginning of the experiments and at the start of each burst of activation (with the onset of convective activity, for example). With time however, these "leftover" IN can activate, though it appears they may do so in small numbers, and not in large enough quantities to affect the time-height average of activation-event tracers in Figure 5.1.

If changes in IN concentration have little to no effect on where and when activation takes place, are there any differences in how the phase of water vapor is apportioned? Figures 5.3 – 5.5 show the first order effect of IN in the same envelope of IN-influenced air, the effect on ice crystal formation, as a difference of mass mixing ratio (perturbed run mixing ratio – clean run mixing ratio). Two patterns are evident in these images. First, as initial IN concentration increases, the number of gridpoints with positive changes in ice decreases with increasing concentration: the percent of the envelope that shows a negative (positive) change is 35.5 (55.5) for 30 IN/L, 42.5 (48.9) for 60 IN/L, and 44.2 (47.2) for 120 IN/L. Secondly, with 30 IN/L there are two areas of positive absolute change in pristine crystal mass worth noting (the brighter pink in Figure 5.3). The first is along the lower edge of the envelope near 55 hours, where increases in ice mass are up to 0.004 g/kg, or 4 ppmv. This is actually quite a small change, as 4 ppmv is less than 2.5% of pristine crystals at that altitude (6-7 km). The second area is near the upper edge of the envelope, during 40-55 hours of model time, corresponding to 1 pm local time on the 27th through 4 am local time on the 28th. Here the increase in crystal mass ranges from 1-3 ppmv. These are small numbers to be sure, but account for 5-25% of the total ice mass at that altitude (12-13 km). Experiments with IN concentrations above 30/L have a negative change in crystal mass in the upper part of the envelope, which will be explored in detail in Chapter 7.

Figures 5.6 – 5.8 show the change in water vapor averaged over IN-influenced gridpoints. Like the change in crystal mass, the number of gridpoints with negative changes in vapor increases with increasing concentration. There is also an interesting feature that develops with higher concentrations in the upper portion of the envelopes from 40 hours onward and above 11 km. For a concentration of 30 IN/L, the positive change in vapor occurs just above and after positive changes in crystal mass. With increasing IN concentration (Figures 5.7 and 5.8), the change in vapor becomes a dipole across 12 km, with positive change below, negative change above, and changes on either side greater than 1%. This dipole in vapor occurs at a time with a corresponding dipole in pristine ice (Figures 5.4 and 5.5), with negative changes above (up to -25% negative changes in ice) and positive below (an increase in ice up to 5%) an axis that angles upward from about 11 km. The tilt of the axis for this dipole in ice suggests that rising air is likely a strong influence in both dipole features.

Another interesting feature, in Figure 5.6, is the (relatively) high change in vapor (~3 ppmv) at the top of the envelope of the 30 IN/L experiment, between 30 and 35 hours, around 3 am local time, when most of the cloudiness in the model domain corresponds to the position of a surface cold front (Figure 4.11). This appears to be the result of a small area of IN activation that takes place at 11.8 km in an area of high water vapor (at around 0.12 g/kg, the RH_i at this location is greater than 100%, see Figure 4.6). It appears that activation conditions existed for a very short period of time—between 1579 and 1580 minutes into model run time. Across three model timesteps then, pristine ice seems to have formed and evaporated (not shown). A second question comes out of this, though—why does this bit of activation take place in the 30 IN/L experiment but not the others? It is because in the 30 IN/L experiment, vertical velocity is slightly higher in this area, which transported just enough moisture upward that activation conditions occur. The change in vertical velocity is small, on the order of a couple millimeters per second (Figure 5.9) and is not in a volume of IN-activation influenced air. Though it is possible to find where and when these differences in vertical velocity and vapor appear (between 11 and 11.6 km around 1265 minutes into modeled time, not shown), it appears to be a "butterfly effect" of how energy is distributed differently in experiments with varying amounts and locations of IN activation, and impossible to tease out exactly *why* the change in vertical velocity across these two experiments occurs. The small area of IN-influence that results in the 30 IN/L experiment here, near 30 hours, has a butterfly effect of its own—as the activation tracers spread from this area, the area of IN-influence grows. Interestingly, as we will see in Chapter 7, the amount of area influenced by IN feeds back on the average changes in environmental humidity.

A common pattern among these three IN-laden runs is that the lower portion of the envelopes (below about 11 km) show very small percent differences in both vapor and pristine ice. This is because of the amount of vapor and ice present, the extent of IN-influenced air, and the relative importance of IN. At lower altitudes, there is more vapor and ice present, so IN-induced changes will be a smaller percent of the total ice or vapor. Changes in vapor and ice will appear to be smaller when averaged over a larger area of IN-influence, even if the changes are, per gridpoint, the same magnitude as changes at higher levels. Changes in vapor and ice can also be small when there isn't a lot of activation relative to other ice production mechanisms. At lower altitudes, IN may nucleate ice as often as the other nucleation mechanisms in the model (homogeneous sorption/deposition, splintering, and phoretic nucleation)—as long as the temperature is at or below the activation temperature. But at the upper portion of the envelope these other three methods are inhibited: it may be too cold for production via splintering; there is likely less condensate for contact nucleation to act on; the air is drier (for the IN to nucleate, ice saturation is required, but not supersaturation, as it is for homogeneous deposition.) These variations in the conditions under which ice forms may has an impact on which nucleation mechanism dominates. It is possible, then, that at the upper edge of the envelope IN activation is the predominant nucleation mechanism, with homogeneous deposition being a close second in importance. At lower altitudes, the effects will be mixed, as IN ice-production would compete with the other three more equally. In these three experiments, the influence of IN wanes the further from the initial height of the IN layer. More gridpoints are influenced by IN activation within 2 km of the initial layer height (not shown). Even within those 4 km about the initial layer height, however, changes are larger at upper altitudes, most likely because IN-formed ice is a larger fraction of all ice formed.

The effect of initial IN-layer height.

How does changing the height of the initial IN layer affect water distribution? Figure 5.10 shows the tracer of activation-influenced air for 60 IN/L initialized at 200, 250, and 300 hPa (approximately 12.4, 11, and 9.7 km, respectively). Again these IN are allowed to activate at temperatures less than or equal to 238.16 K. The envelope shapes are unsurprisingly different given the different initial heights of the IN sheets, but two differences require explanation. First is the difference of the onset of the activation-tracer in space and time. There are only small dynamical differences (in updraft location and strength, for example) between IN-laden experiments, and the envelopes of the two lower-sheeted experiments span the same altitude range at the start. This suggests robust dynamical conditions in the first few hours of the model run that discourage descent of IN initialized at 200 hPa, as the IN are allowed to be advected within the model for 4.5 hours before they can activate. This is unsurprising since the model run starts at 9 pm local time, when any convective activity would be diminishing. When the IN are initialized at 200 hPa, it takes 12 hours for activation to occur. It appears that the IN needed to be advected to when and where there was enough moisture to activate—for example, Figure 5.11 shows that the conditions at varying times and altitudes are too dry for IN activation. The second difference of note is the *number* of activation tracers. After 40 hours, the tracer appears in higher concentrations for the higher-altitude IN-sheet experiment than for the lower altitude experiments. This is not because there is less activation in the lower-altitude experiment, but because the activation-event tracer is more widespread in the low-altitude (300 hPa) experiment than in the higher-altitude (250 and 200 hPa) experiments. Initialized at a lower, more moist altitude, the IN initialized at 300 hPa activate earlier and more often, resulting in more activation-event tracers and more time for those tracers to be re-distributed than the tracers in the higher-altitude experiments. Figure 5.12 shows an expanded area influenced by IN activation, 51 hours into model time at 10 km, for lower initial IN sheet heights. The increased area does *not* appear to be a result of having fewer IN present the further away 10 km is from the initial altitude, since at 12 km the area influenced by IN-activation appears similar for each of the three experiments (if distance from the initial layer of IN was a factor there would be a larger area influenced by IN-activation at 12 km in the high-altitude experiment), as shown in Figure 5.13.

Similar to the effect of increasing concentration, as IN are introduced at progressively lower altitudes, the percent of envelope area showing a negative change in pristine crystal mass grows and becomes the majority—the percent area that is negative (positive) is 35.4 (56.8) for IN initialized at 200 hPa (Figure 5.14), 42.5 (48.9) for IN initialized at 250 hPa (Figure 5.5), and 50.2 (41.2) for IN initialized at 300 hPa (Figure 5.15). We can see the same trend in the envelope of water vapor change (Figures 5.16, 5.8, 5.17). Reasons for the increased number of gridpoints with a negative change in ice and vapor will be explored in Chapter 7. Again, the largest changes in vapor and ice are seen above 11 km, though in the experiments with IN introduced at 250 and 300 hPa, positive crystal mass changes occur near the lower edge of the envelope (below 8 km).

In the IN at 300 hPa experiment the reason for the increase of crystal mass is straightforward—where there is a 20 ppmv increase in crystal mass there is a 20 ppmv decrease in vapor, a clear indication of crystal formation. For this lower-altitude envelope portion of the IN at 250 hPa experiment, the reason for the crystal mass increase is not as simple: an area of IN-influenced air has both an increase in crystal mass *and* vapor, seen 57 hours into model run time in Figure 5.8. The area comprising those IN-influenced gridpoints, shown in Figure 5.18, is very small, at a cloud edge in the southernmost part of the model domain. Let's focus on the range of heights encompassing the positive change in crystal mass covers (6.2 to 8 km). One helpful tool we have is the evaluation of air movement. Figure 5.18 shows that with a negative vertical velocity between 6.9 and 8 km, descending crystals evaporate and moisten lower levels, which instigates new pristine ice formation and a "dent" in vapor around 6.8 km.

When IN are initialized at 200 hPa, the strongest decrease in vapor with IN present is seen along the upper edge of the envelope after 45 hours. Crystal formation (Figure 5.14) would explain part of this, but there is then about 2.5 ppmv of vapor "loss" when IN are present that seems unaccounted for. Across all three experiments there is a strong dipole signature in the change in water vapor, with changes of at least 1%, above 11 km and after about 35 hours—between 11 and 12 km the change is positive and above 12 km the change is negative, sometimes strongly so—which also appears in the experiments with varying concentration. The reasons for this structure will be the subject of Chapter 6.

The effect of activation temperature.

The effects of ice nucleiare highly dependent on the activation conditions. In this collection of sensitivity studies using idealized ice nuclei, it makes sense to investigate how sensitive nucleation is to changes in activation conditions. Here, the activation temperature for the IN is raised to 273 K. On average, temperatures at and below this activation temperature are present above 5 km (Figure 4.5). We can expect that more activation will take place, especially at lower altitudes, even with the same initial concentration of 60 IN/L. This is exactly the result seen in Figure 5.19. With a higher activation temperature the envelope is much larger, since IN at the lower edge of the envelope have a greater chance of activating, and the activation-influenced air can be mixed downward. The magnitude of influence is also greater with a warmer activation condition. Putting these two ideas together, when IN activate at a colder temperature the bulk of activation influence (i.e., the area enclosed by the 6 tracers per liter contour) is above 10 km, but when IN activate at a warmer temperature this area spans 7 to 12 km. How does the distribution of IN influence affect pristine crystal mass and vapor? Oddly, the area with negative changes in both pristine crystal mass *and* vapor becomes greater when IN activate at a warmer temperature (Figures 5.20 and 5.21). That there is more area with negative vapor changes in the warmer-activation experiment is not unexpected—since there is more IN activation (evidenced by the activation tracer counts) there will be more vapor uptake. A 15% increase in area with a negative change in crystal mass between the "regular" and warm-activation experiments is unexpected. In order to diagnose the cause of this, we will need more information. For example, at the earliest time in Figures 5.17 and 5.19, around 10.5 km in altitude, changes in both pristine crystal mass and vapor are negative. This may be the result of crystals having formed (the decrease in vapor) but falling into layers below (the decrease in crystals). The reason the warm experiment shows negative changes in both vapor and pristine ice, and not just compared to the "cold" activation experiment but also overall, is likely comprised of many subtleties such as this one. We investigate this in detail in Chapter 7.

The effects of concentration, initial IN-layer height, and activation temperature.

In order to focus on the impact of ice nuclei on high clouds, sheets of IN have been introduced high in the troposphere at and above 9.7 km (300 hPa), emulating the palls of smokey materials found in flight campaigns such as TRACE-A and the PEM Tropics experiments. However, other realistic geometries exist for the introduction of an IN population. Since smoke is created by fires at the surface, one geometry to explore is a sheet of IN initialized in the boundary layer (below 1 km). Another, a "fumigation" geometry, assumes an idealized meteorology: that IN accumulate over several days and are thoroughly mixed by convective motions. In both of these scenarios, the effects of IN will be most pronounced in the mid-troposphere where vapor is most readily available to form ice.

Figure 5.22 shows the envelope and degree of IN-influence for three experiments, each with IN allowed to activate at 273K: 120 IN/L are initialized at 925 hPa (middle), 60 IN/L are initialized everywhere in the domain (bottom), along with, for comparison, the envelope and degree of IN-influence when 60 IN/L were initialized at 250 hPa (top). When IN are introduced as a sheet at 925 hPa (about 0.8 km), there is no activation until the IN are transported to colder altitudes. As a result, the lower bound of the envelope is effectively the melting level (though it also reflects the lower bound of IN-influenced air transport, as seen near 60 hours). This obviously delays the appearance of the IN-activation tracer by about 7 hours (Figure 5.22), and understandably keeps the bulk of IN-influenced air lower in the atmosphere, especially with a "warm" activation temperature. Convective and other motions transport IN-influenced air to just above 8 km near 30 and 47 hours, coinciding with vertical growth of clouds (Chapter 4). The highest concentration of IN-influenced air exists below 6 km and after 45 hours—this is likely where the bulk of activation occurs, since IN are transported from below and will activate readily in these lower altitudes (higher humidities). In the fumigation experiment, there is no delay in activation, and predictably, the influence is less focused as IN activation is more widespread (compare the concentration of activation-event tracers between this fumigation experiment and the 60 IN/L at 250 hPa experiment in Figure 5.22).

With cloud tops often at and above 10 km, it is surprising that the extent of IN-influence doesn't range to 10 km and above when IN are initialized near the surface. The extent of IN-influence will depend on both transport and the location of activation. Both effects are at work here. In Figure 5.23 we see an example of large numbers of IN activating at a relatively low altitude (between 4.4 and 4.6 km), this activation decreases the number of IN available to influence higher levels. The means of transport, such as whether IN are transported via explicit or parameterized convection, is also important. The average number of gridpoints with parameterization between 25 - 30 and 44 - 48 hours (the first and second periods of peak heights of IN-influence) is 20 and 55 points respectively, out of 1,260,000 gridpoints in the study volume. For comparison, at 25.5 hours into the experiment 53,477 gridpoints have condensate, implying that the majority of condensate ("cloud") is not associated with convective parameterization. The majority of convectively-generated cloudy areas are then most likely to be explicitly generated, with ice nuclei and activation-event tracers mixed upward by vertical motions more slowly than they would with parameterized convection—IN have a chance to activate well before they would reach the cloud top. The location of ice nuclei and activation-event tracers in the model domain is also a factor. Both peaks of maximum height of IN-influenced air occur along the southern boundary of the model domain (Figure 5.24), and the range of heights of both IN and activation-event tracers are subject to an average northwesterly flow (Figure 4.3). It is possible that IN and activation-event tracers are being blown out of bounds, and more importantly, away from the stronger upward motions in the area (Figure 5.24).

Figures 5.25 and 5.26 show the change in pristine ice and vapor mixing ratios, respectively, for the 120 IN/L at 925 hPa experiment. The percent changes in both categories are small given the large amounts of vapor and ice present at these lower altitudes. The magnitude of absolute change in each category are on par with the other experiments, and similar to the experiments with 60 IN/L initialized at 300 hPa with "cold" activation and 60 IN/L initialized at 250 hPa with "warm" activation there are no discernable spatial or temporal patterns in the amount of change. It is interesting that more gridpoints experience a negative change in ice and a positive change in vapor—something to explore in Chapter 7. The largest changes in ice are seen at the start of the experiment, while the largest changes in vapor are positive and at the end (along the bottom edge of the envelope). Air influenced by IN-activation at the start of the experiment is influenced by (on average) rising motions. As IN rise, and activate to form much more pristine ice than there would be otherwise, vapor is reduced above (because the crystal formation below "used" so much vapor) and hence ice is reduced above. As moisture and IN are transported upward by rising air, waves of these positive and negative changes in ice propagate upward (Figure 5.27). The accompanying changes in vapor are not as sensitive to IN activity, most likely because of the high humidities present at these altitudes. The effects on pristine ice are diminished after 21 hours, when air influenced by IN-activation experiences an average downward velocity (Figure 5.27). Near the end of the experiment, the lower bound of envelope decreases in height and there, the change in vapor is notably positive. It appears that the positive change in vapor is caused by areas with increased ice descending, with the ice evaporating and moistening lower levels, shown in Figure 5.28. Once the change in pristine ice declines and becomes negative, the change in vapor below decreases—note the decreased positive change in vapor below 3 km and the increasingly negative change in vapor above 3 km at 58.5 hours (top right of Figure 5.28).

Though the effects of activation in the fumigation experiment are widespread and lessened by averaging over larger areas (not shown), they are still remarkable. Figures 5.29 and 5.30 show, respectively, changes in ice and vapor between this experiment and an IN-free one. Most of the changes are small (less than 25%), with vapor changes less than ice changes—as always, vapor is less sensitive to change as there is more of it than ice. Notable changes in both ice and vapor manifest just before 10 hours into the experiment, below 8 km, summarized below in Table 5.1. It appears that vapor (and ice) are moved upward and downward, out of the layer between 4 and 6 km.

7 to 8 km	△ ice slightly negative	△ vapor slightly positive
6 to 7 km	△ ice positive	△ vapor positive
4.5 to 6 km	△ ice negative	△ vapor negative
4 to 4.5 km	△ ice negative	△ vapor positive until 15 hours, then negative
below 4 km	△ ice small, mixed	△ vapor negative until 15 hours, then positive

Table 5.1. Changes in ice and vapor per Figures 5.29 and 5.30.

Figure 5.31 shows the vertical velocity and amount of condensate at 4 and 6 km. In this layer, air influenced by IN activation includes areas of "clouds" and their surroundings. There are large areas of rising air within the bounds of air influenced by IN activation. Perhaps the patterns seen in Table 5.1 are the result of lofting of numerous small ice crystals, which has two effects—crystals may evaporate and moisten air above 6 km, and secondly, as Andreae et al (2004) note, smaller more numerous crystals can affect vertical motions and enhance precipitation, which then adds moisture to lower levels. Figures 5.32 and 5.33 show the changes in ice, vapor, and vertical velocity at 5 and 7 km respectively. Areas of increased ice and decreased vapor near the center of the southwestern "cloud" in Figure 5.32 suggest IN activation underway. Surrounding that nucleus of activity, there is increased vapor and decreased ice—where increased precipitation efficiency and evaporation are likely. Changes in vertical velocity (top left of Fig. 5.32) appear mostly noisy throughout the domain *except* at the nucleus of likely activation, where there is an enhanced updraft. Surrounding the enhanced updraft is a region of slightly suppressed updraft, coinciding with the area with increased vapor and decreased ice. At 6 km, vapor and ice have coincident negative changes (presumably as a result of increased precipitation efficiency), and at 7 km (Figure 5.33) increases in both vapor and ice dominate the edge of the cloudy area, possibly as air is detrained, since vertical velocities decrease above this altitude (not shown). The decreases in ice seen at 7 km (and above) would result from increased precipitation efficiency at lower levels. These patterns jibe with the findings of Andreae et al (2004): with smaller cloud droplets, updrafts are not diminished as much by precipitation, and convection can intensify, along with precipitation. For example, hail was more often associated with smoke-affected clouds over the Amazon Basin. In this experiment, it is likely that we are seeing both the enhanced updraft and enhanced precipitation at the same time and closely situated in space. The effects are strongest below 7 km, above this height the positive anomaly in vertical velocity decreases in magnitude rapidly to about 9.5 km. Unfortunately, the best we can do is note the strong spatial correlation between changes in vertical velocity and the changes in ice and vapor, we can not prove causation, and so it is possible these effects are the result of noise (Appendix C). The activation of so many IN in a fumigated environment, even if the IN are introduced gradually (Chapter 3) may be a shock to the system. It is interesting that when IN are introduced as a sheet, no matter what the height and activation temperature, there are no such correlations among changes in ice, vapor and vertical velocity where the vertical velocity changes do not appear to be noisy.

Indeed, the shockwave of what appears to be effects of changing particle size on vertical velocity persists to nearly the end of the 60 hours modeled. Near the end of the experiment there is one more feature that stands out: at about 50 hours, a layer of air centered on12.6 km shows a large negative change in ice (up to -25%, Figure 5.29). Figure 5.34 shows changes in ice and vapor at 49.5 and 51 hours, spanning the creation of this feature. Near 13 km at 49.5 hours, there is a decrease in vapor and an increase in ice, suggesting ice formation, possibly from IN activation. At 51 hours, the decrease in vapor is still present near 13 km (the ice hasn't evaporated at this height), but now there is a large decrease in ice at the same altitude—with an increase in ice below to about 11 km. The evolution in time and height implies that the ice formed at 49.5 hours has enhanced a slow descent of ice to lower altitudes. In Figure 5.35, we see that the negative changes in ice at 51 hours and 12.6 km are confined to small areas within clouds that are in descending air. The remainder of the domain at this time/height shows no change in ice. These figures and Figure 5.9--it is interesting how such small areas can affect a big-picture average, and this is definitely something we need to be aware of!

Across the first six experiments (with IN introduced as a sheet above 9 km), the largest changes in both vapor and pristine ice are always in the last half of model run time. As the number of gridpoints under the influence of IN activation, and as the *degree* of IN influence grows (mostly in the upper portion of the envelopes, as seen in the plots of the average activation tracer concentration) the amount of influence and change increases. This is a result of increasingly wider mixing of IN into the study volume, and as we saw in Chapter 4, convection triggered along and ahead of a frontal boundary, starting near 42 hours into the experiments, provided more opportunities for IN to activate.

Also, for these six experiments, the average change in vapor and pristine ice in the presence of IN is within a fairly constant range of -2 to 2 ppmv. This is relatively insignificant at lower altitudes where there is more moisture and potential for ice formation, but much more significant at higher altitudes (above 11 km), where a 2 ppmv change can be 10% or more of the background, or "clean" value. In the course of case study investigation we may see variations that don't show on the horizontally-averaged plots we've looked at here, these smaller-scale variations will provide a basis for determining what conditions the IN themselves are most sensitive to. The next two chapters cover a case study each, discussing patterns and trends identified above.

(1) Why is there a dipole feature in the water vapor difference plots and sometimes in the plots of pristine ice differences? The majority of experiments with IN introduced as a sheet above 9 km (60 IN/L, 120 IN/L, 60 IN/L at 200 hPa, and 60 IN/L at 300 hPa) have this structure in the upper part of the envelope after hour 40, with a negative change above about 12 km and a positive change below to 11 km. It's probable that air influenced by IN activation in these experiments has similar trajectories and histories. How are the histories different from the experiments that do not show this dipole pattern? Two key differences come from the number of IN initialized and from small dynamical differences. The timing of the dipole feature –late afternoon, local time— is when convective activity is likely (Figures 4.12 and 4.13), so we can expect that vertical velocity differences are important. In the next chapter I will explain why this structure exists, as well as why there are differences in its strength and position for the experiments listed above. A similar feature –but at low altitudes—appears in the plots of vapor and ice changes in the experiment with 60 IN/L fumigated throughout the domain with a warm activation temperature. The formation of *this* structure has been explained (above)—we will see in the next chapter how the conditions for the dipole feature are very different.

(2) There is an issue of surprising negativity in both the location of changes in ice and vapor and the number of gridpoints experiencing a negative change in either ice or vapor. First: when considering what kind of results we should see, a positive/negative combination of vapor/pristine ice would not have been surprising. For example, if crystals grow and exist when IN are present where they wouldn't otherwise exist (positive change in pristine ice) vapor will be depleted, or if in the presence of IN, small and numerous ice crystals formed but evaporate more readily (negative change in pristine ice) vapor would be added to the environment. A positive/positive combination is also possible when IN-formed crystals exist where in a clean environment they

wouldn't, and they are evaporating. However, a few experiments show an unexpected negative/negative combination: 120 IN/L, 60 IN/L, and 60 IN/L with warm activation. What conditions create this scenario?

Also, why does the envelope area show an increasingly, and sometimes overall negative change in four categories of experiments? To answer these questions we will have to look at the history and dynamics of air influenced by IN activation. Is the overall negativity a result of progressively more IN added or activating? How are vertical motions influenced by the varying experiments and vice versa?

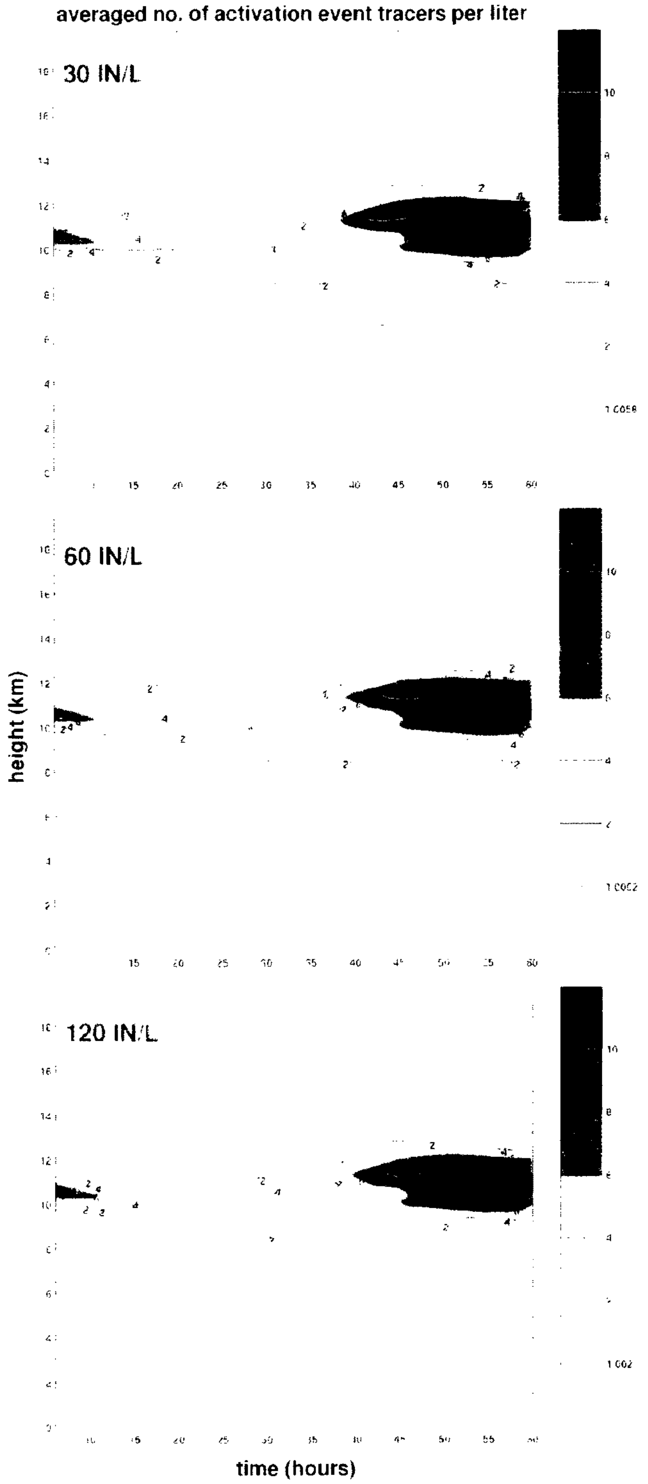

Figure 5.1. With each IN activation, a tracer activates. The tracer concentration is horizontally averaged over time to show where and when air influenced by IN-activation is, for three experiments: 30 IN/L (top), 60 IN/L (middle) and 120 IN/L (bottom). There are no changes in *where* these tracers are (the envelopes are the same), though there are small differences in how *many* tracers there are per liter.

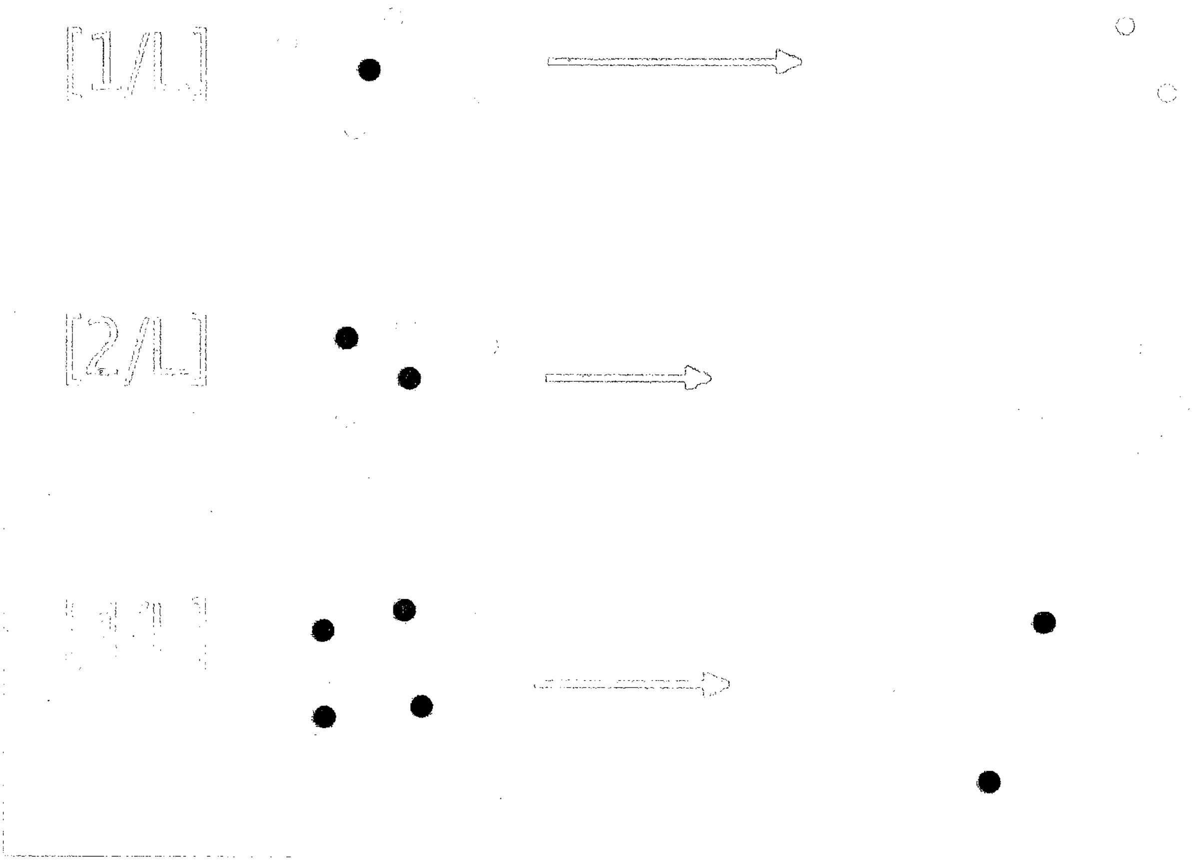

Figure 5.2. The effect of varying IN concentration (black dots) in the same environment—blue dots indicate water vapor. At a high enough IN concentration, water vapor may already be "tied up" in ice formed by IN activation, leaving unactivated IN. Therefore a greater number of IN will not necessarily result in a higher number of activation events, or even larger effects on water vapor and pristine ice.

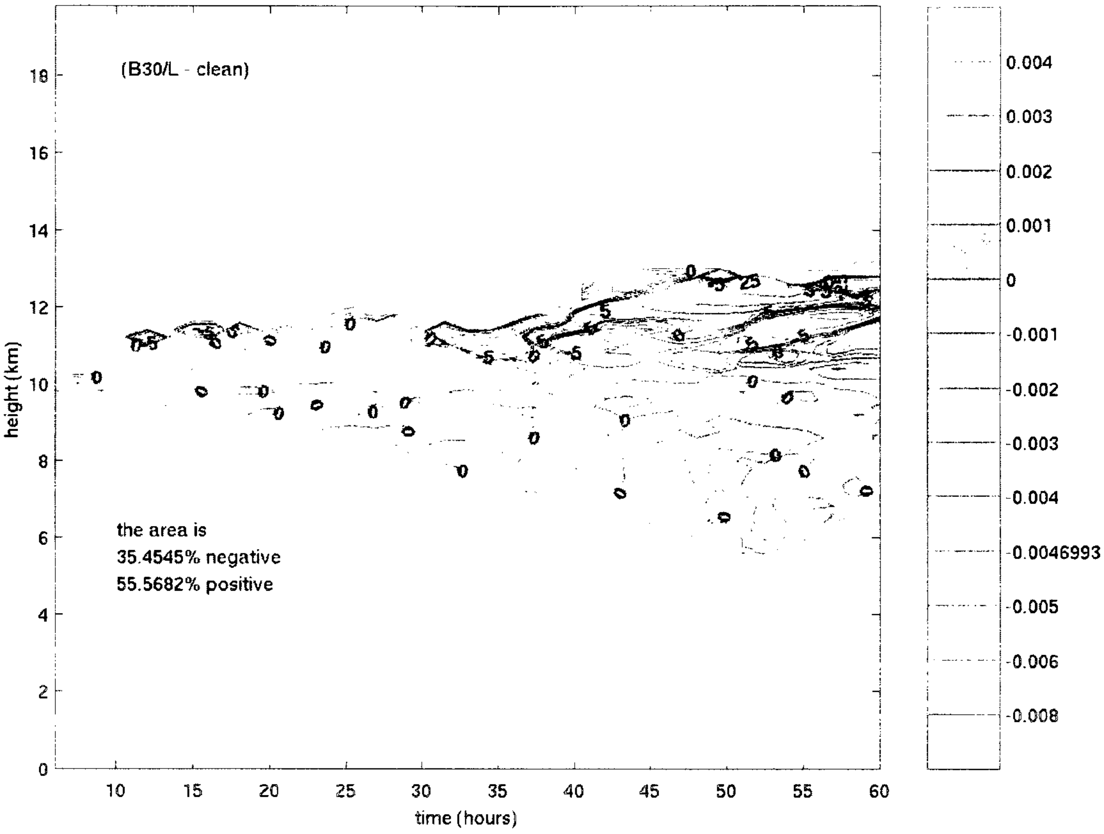

Figure 5.3. The change in pristine crystal mixing ratio when 30 IN/L are introduced as a sheet at 250 hPa, shown as an absolute difference (color, g/kg) and percent difference (contoured at -25, -10, -5, -2, -1, 0, 1, 2, 5, 10, and 25%).

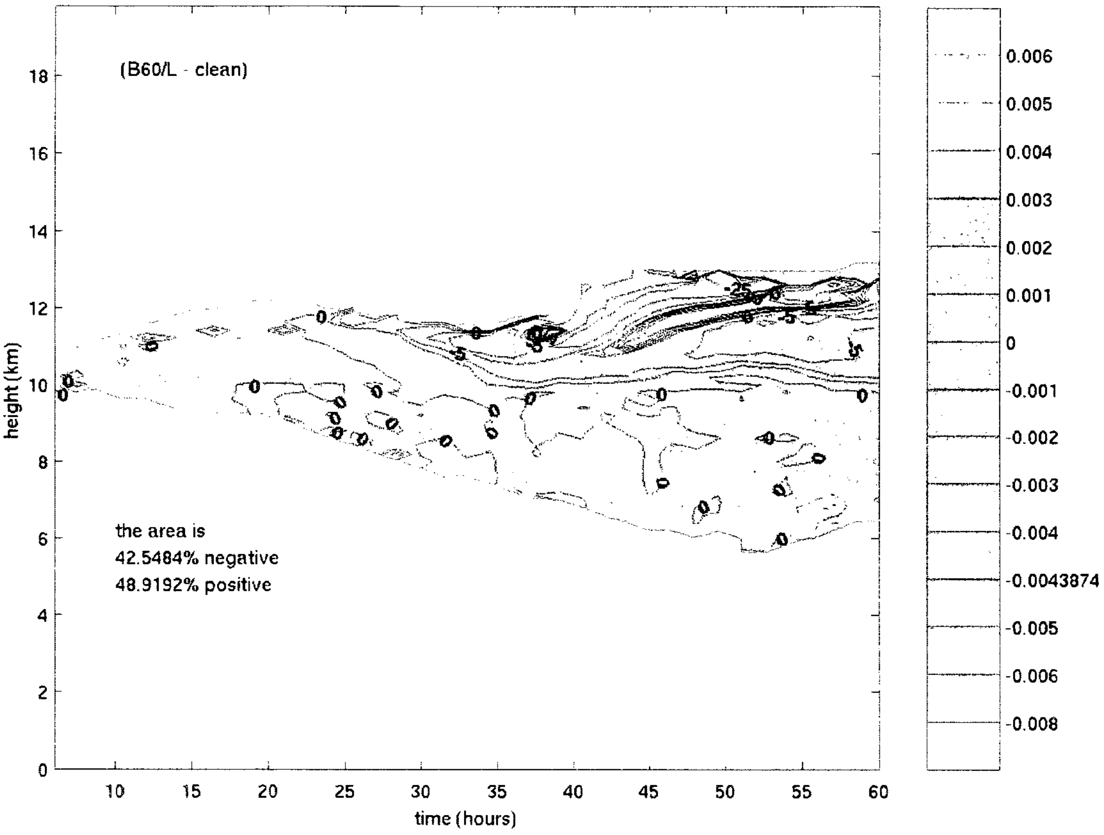

Figure 5.4. The change in pristine crystal mixing ratio when 60 IN/L are introduced as a sheet at 250 hPa, shown as an absolute difference (color, g/kg) and percent difference (contoured at -25, -10, -5, -2, -1, 0, 1, 2, 5, 10, and 25%).

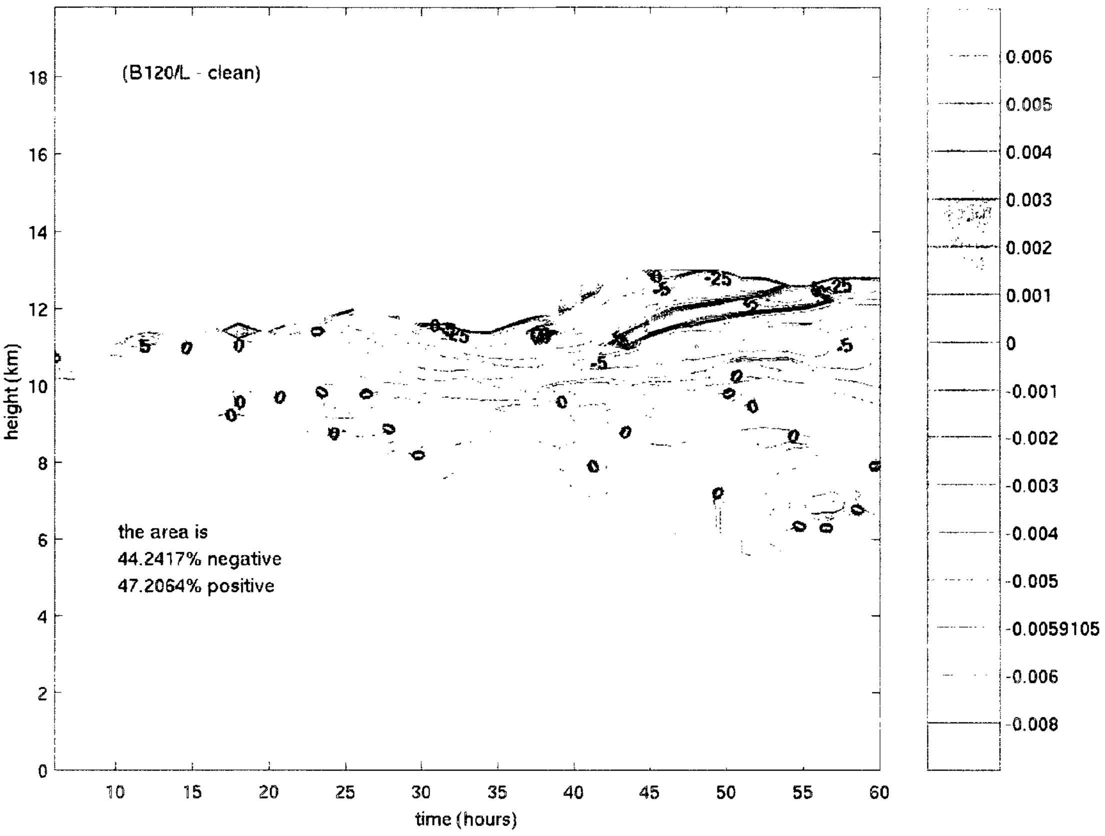

Figure 5.5. The change in pristine crystal mixing ratio when 120 IN/L are introduced as a sheet at 250 hPa, shown as an absolute difference (color, g/kg) and percent difference (contoured at -25, -10, -5, -2, -1, 0, 1, 2, 5, 10, and 25%).

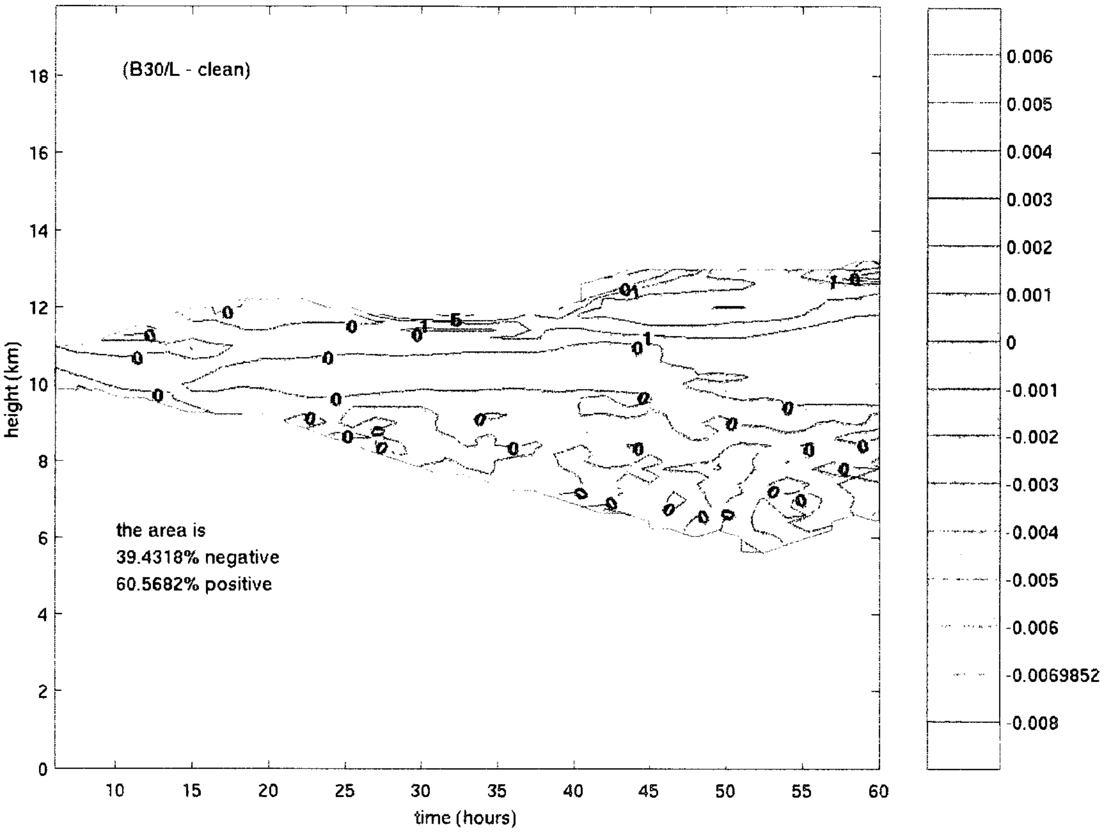

the area is
39.4318% negative
60.5682% positive

Figure 5.6. The change in vapor mixing ratio when 30 IN/L are introduced as a sheet at 250 hPa, shown as an absolute difference (color, g/kg) and percent difference (contoured at -25, -10, -5, -2, -1, 0, 1, 2, 5, 10, and 25%).

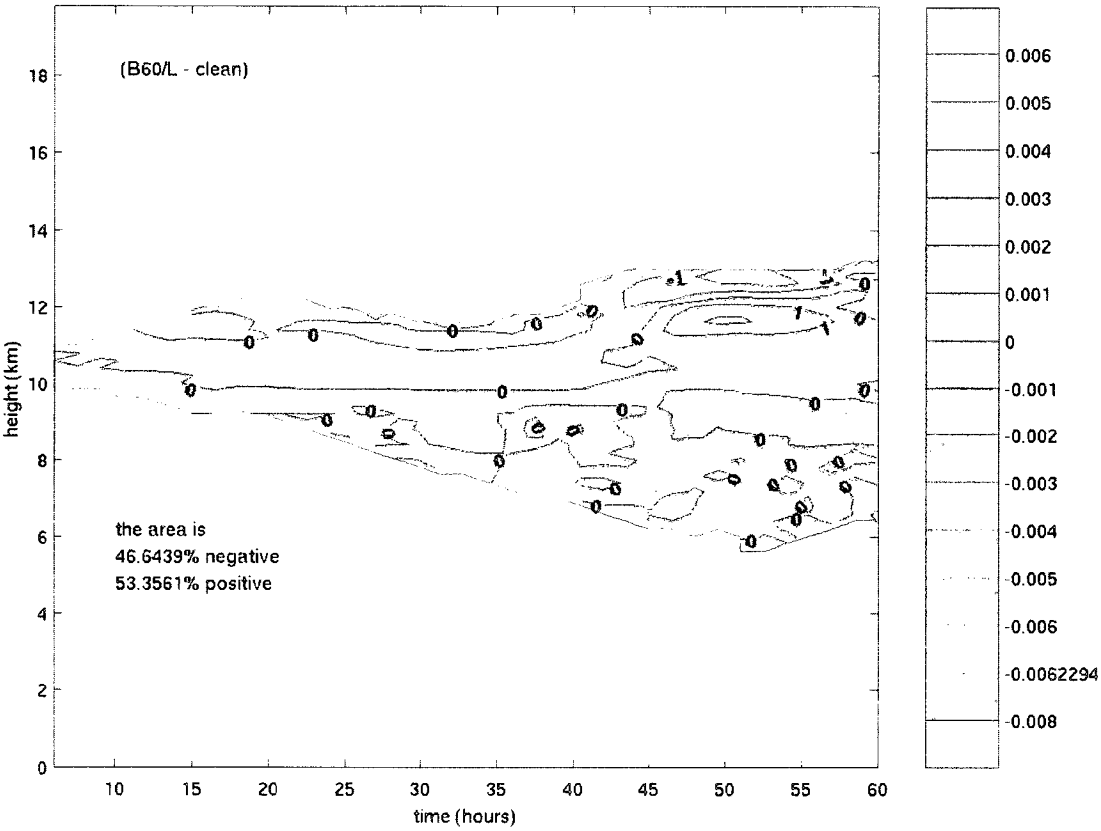

Figure 5.7. The change in vapor mixing ratio when 60 IN/L are introduced as a sheet at 250 hPa, shown as an absolute difference (color, g/kg) and percent difference (contoured at -25, -10, -5, -2, -1, 0, 1, 2, 5, 10, and 25%).

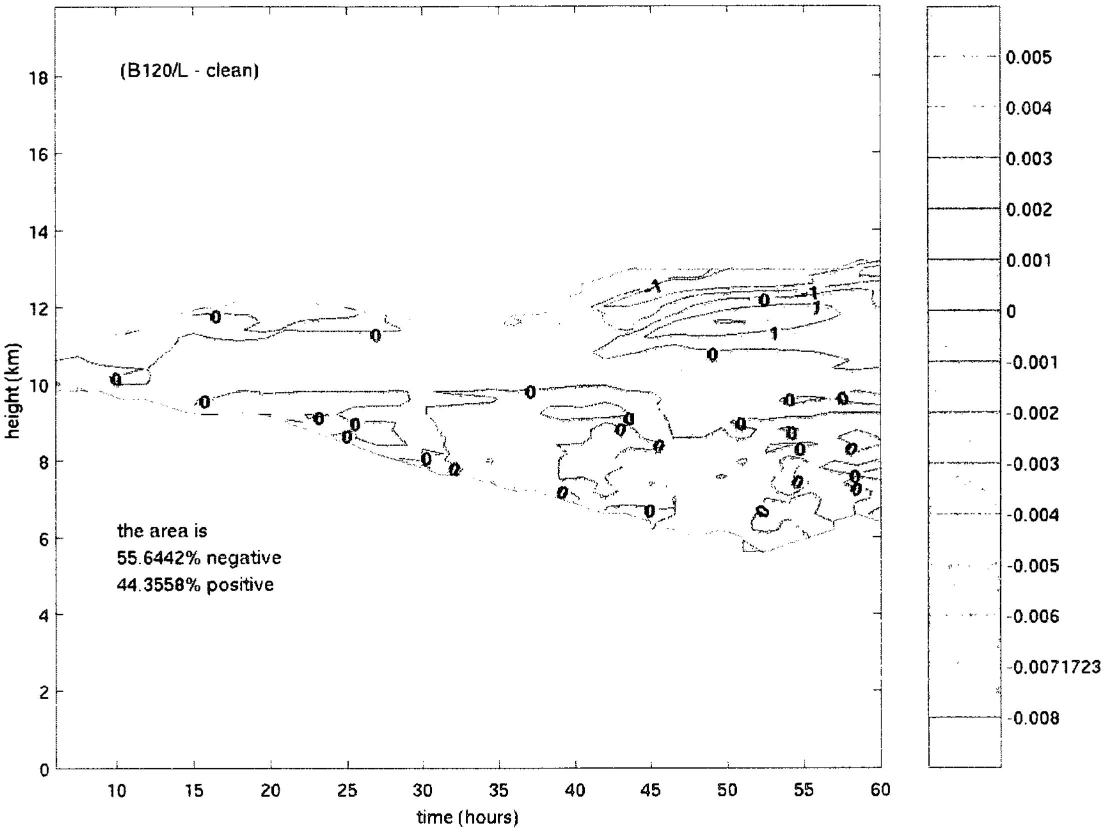

Figure 5.8. The change in vapor mixing ratio when 120 IN/L are introduced as a sheet at 250 hPa, shown as an absolute difference (color, g/kg) and percent difference (contoured at -25, -10, -5, -2, -1, 0, 1, 2, 5, 10, and 25%).

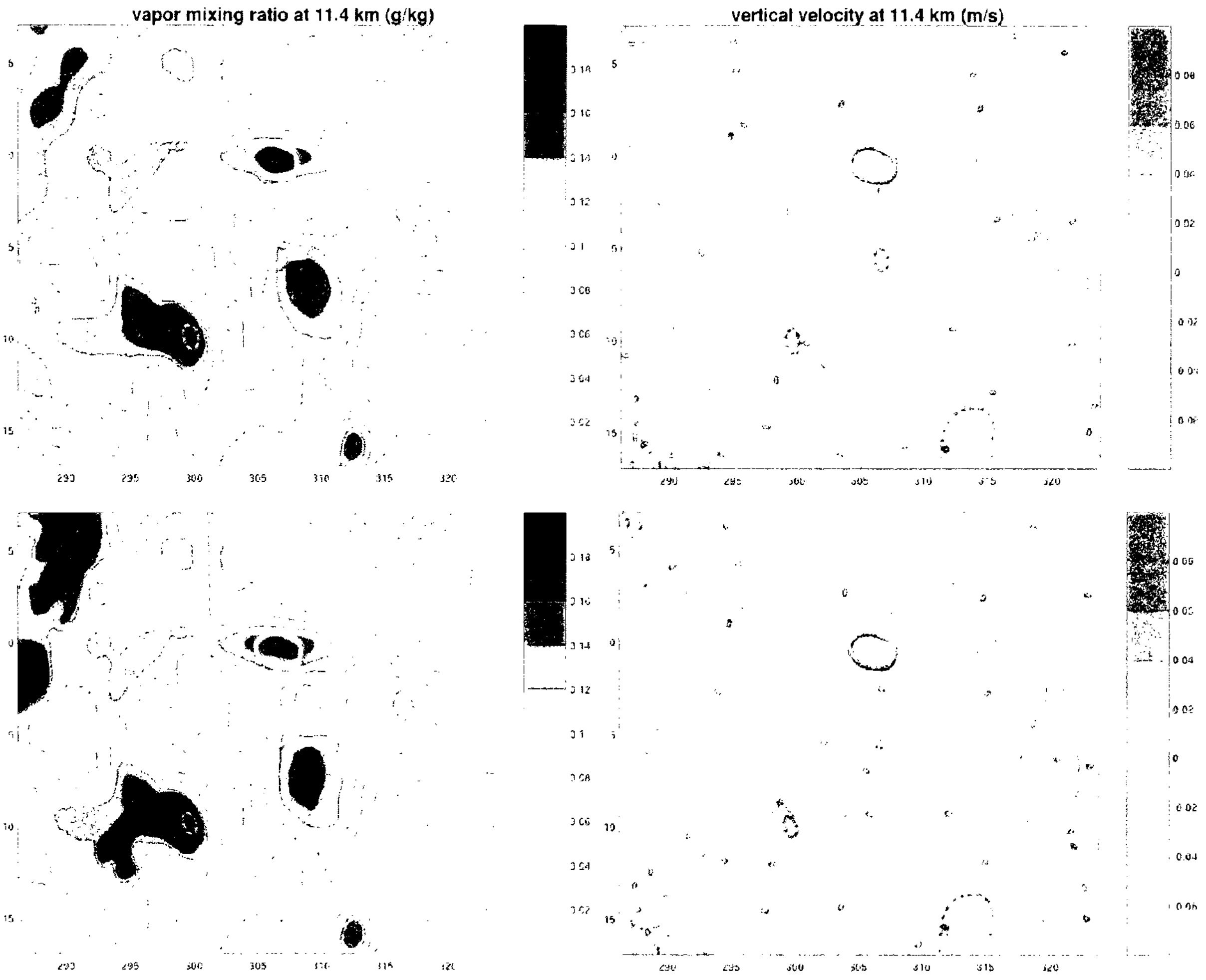

Figure 5.9. The experiment with 30 IN/L (top row) has an area with more vapor (left) at and near 11.4 km than the 60 IN/L experiment (bottom row) in an area of interest enclosed by the solid purple contour. The thin black contours on the vertical velocity plots in the right column are spaced every 0.01 m/s. In the 30 IN/L experiment, the area of interest has a slightly greater positive vertical velocity than the same area in the 60 IN/L experiment. The difference in water vapor between these two experiments spatially corresponds to, and most likely is explained by a difference in vertical velocity. The difference in vertical velocity between these experiments can not be directly attributed to IN-influenced air (shown by the red dashed contours) and must therefore be an indirect result; a "butterfly effect" of how energy is distributed differently in experiments with varying amounts and locations of IN activation. The plots shown here are from 1310 minutes into the UWNMS model runs.

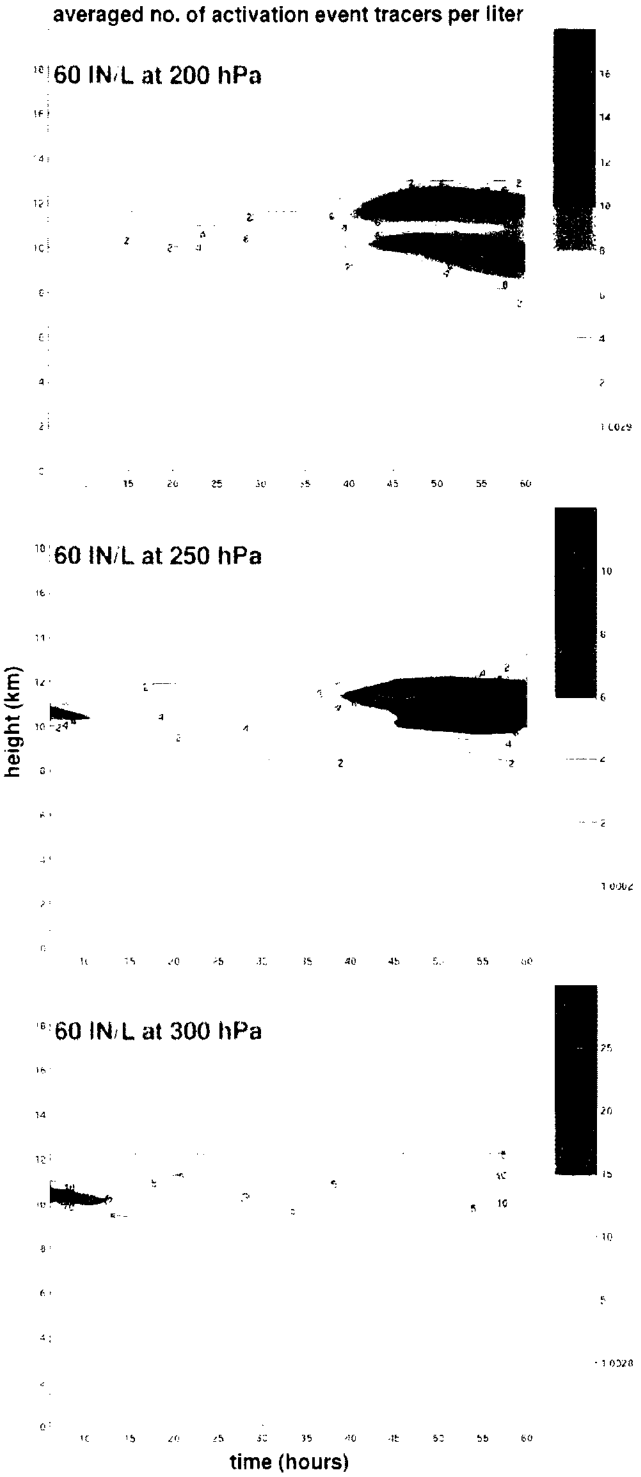

Figure 5.10. Horizontally averaged concentration of the IN-activation tracer, showing the extent and degree of air influenced by IN activation, for experiments initialized with 60 IN/L introduced as a sheet at 200 hPa (top), 250 hPa (middle), and 300 hPa (bottom).

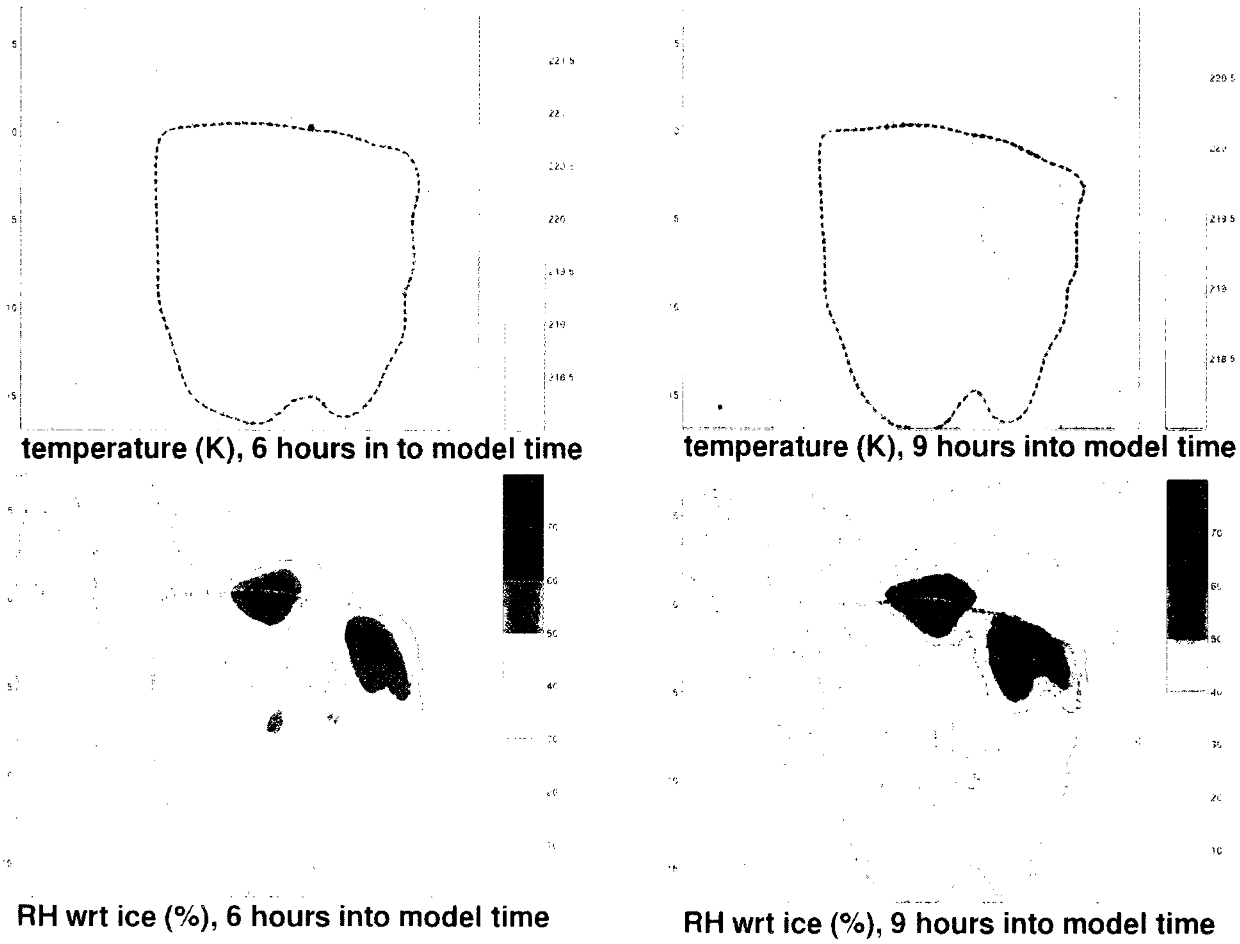

temperature (K), 6 hours in to model time

temperature (K), 9 hours into model time

RH wrt ice (%), 6 hours into model time

RH wrt ice (%), 9 hours into model time

Figure 5.11. Potential temperature (red-orange plots) and RH_i (blue-black) for the experiment with 60 IN/L initialized at 200 hPa. Data are shown for two different times—6 and 9 hours into model run time (at left and right, respectively), and at the approximate IN-injection altitude—12.4 km. The areas of unactivated IN are enclosed by dashed contours. These examples illustrate that conditions were insufficient for IN activation before 12 hours into the model run (please note the temperature color scale varies between the two times).

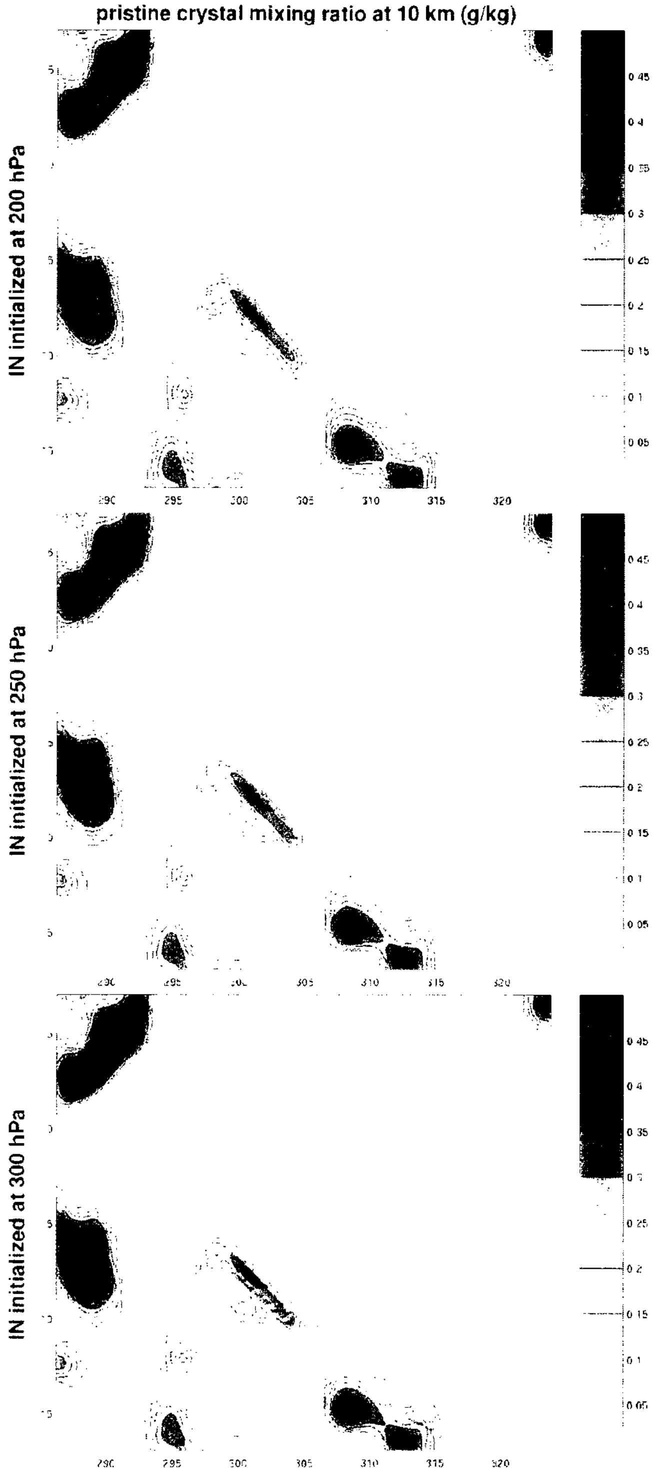

Figure 5.12. When IN are initialized at progressively lower altitudes (200 hPa, top; 250 hPa, middle; 300 hPa, bottom) IN activation conditions are more widespread and the bounds of IN-influenced air increases, shown by the red dashed lines here 51 hours into model run time at 10 km. Pristine crystal mass mixing ratio is also shown here, contoured in grey, in order to avoid having a really boring figure.

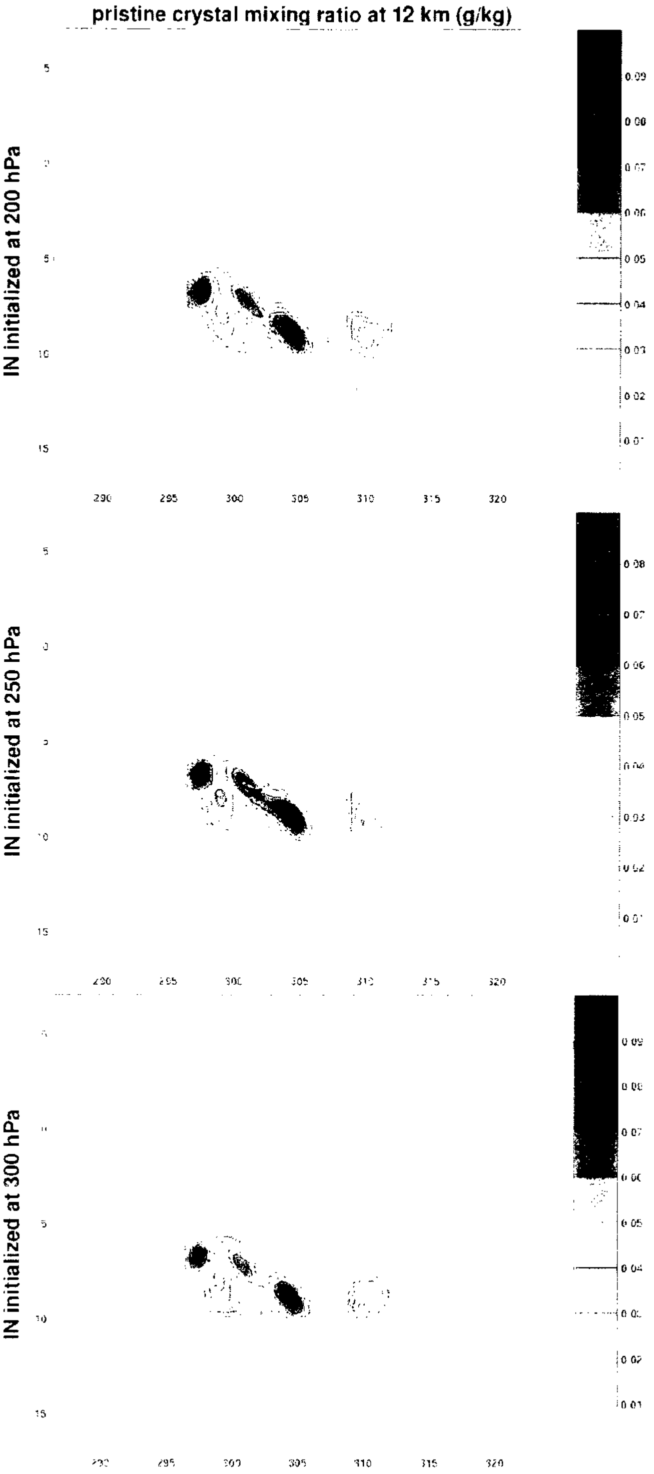

Figure 5.13. The bounds of IN-influenced air are enclosed by red dashed lines 51 hours into model run time at 12 km when IN are initialized at 200 hPa (top), 250 hPa (middle), and 300 hPa (bottom). The area influenced by IN-activation does not seem to depend on the distance away from the initial layer of IN, otherwise the area of influence at 12 km would be largest in the high-altitude (200 hPa) experiment.

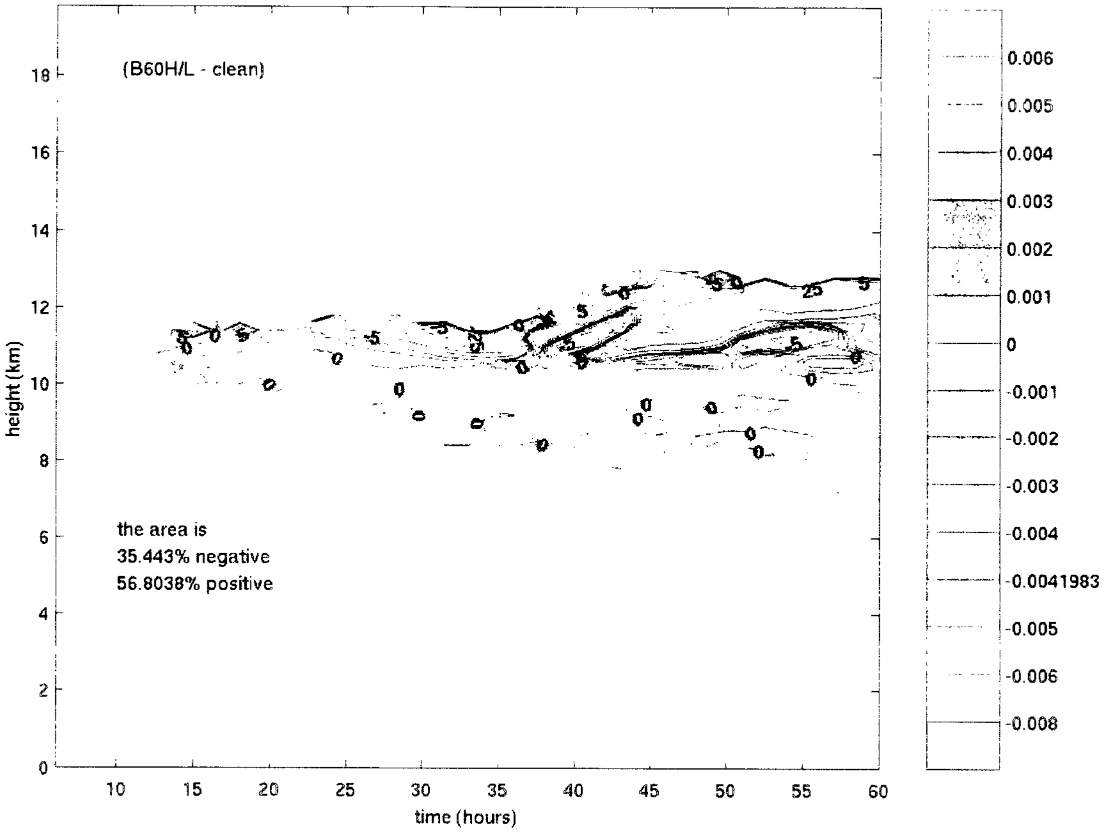

Figure 5.14. The change in pristine crystal mixing ratio when 60 IN/L are introduced as a sheet at 200 hPa, shown as an absolute difference (color, g/kg) and percent difference (contoured at -25, -10, -5, -2, -1, 0, 1, 2, 5, 10, and 25%).

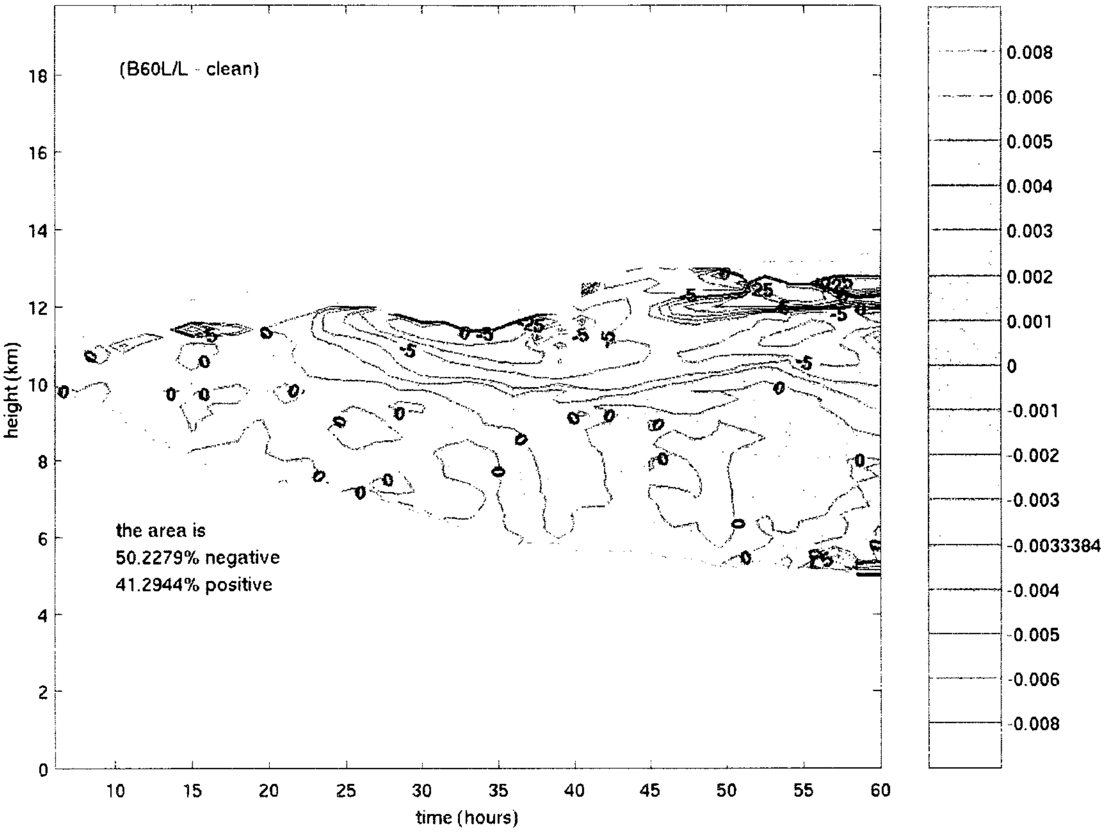

Figure 5.15. The change in pristine crystal mixing ratio when 60 IN/L are introduced as a sheet at 300 hPa, shown as an absolute difference (color, g/kg) and percent difference (contoured at -25, -10, -5, -2, -1, 0, 1, 2, 5, 10, and 25%).

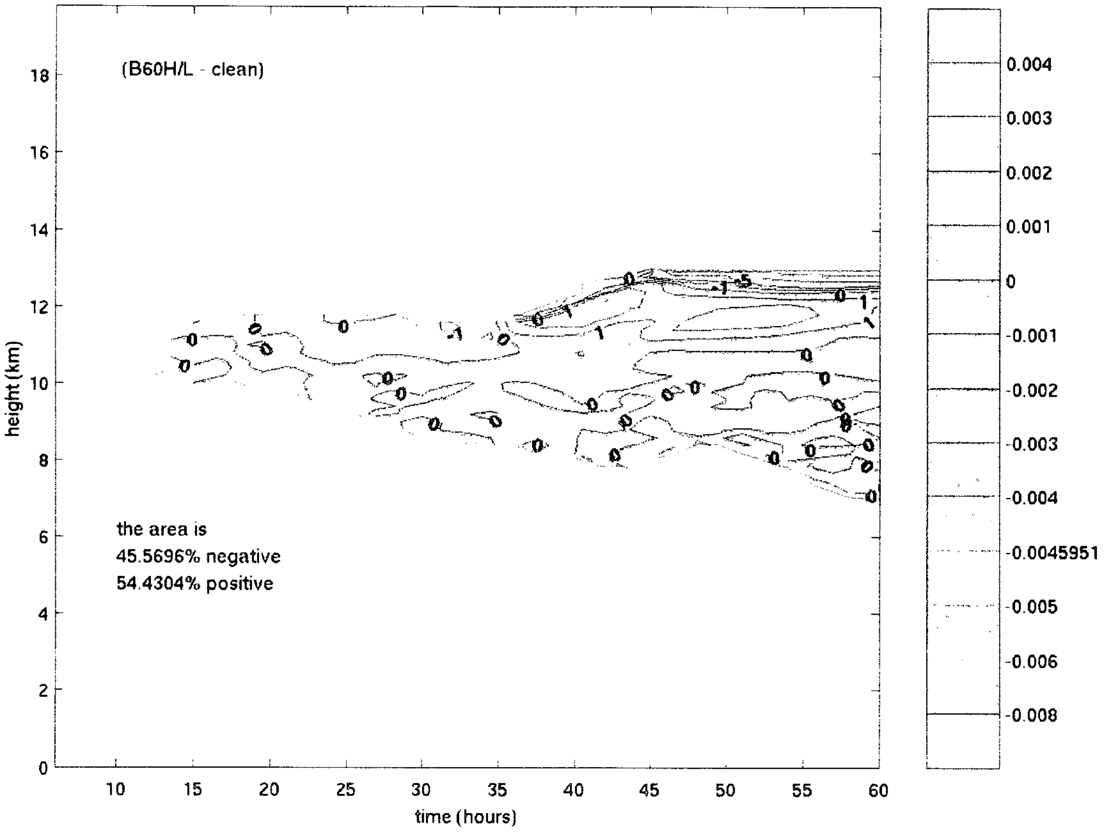

Figure 5.16. The change in vapor mixing ratio when 60 IN/L are introduced as a sheet at 200 hPa, shown as an absolute difference (color, g/kg) and percent difference (contoured at -25, -10, -5, -2, -1, 0, 1, 2, 5, 10, and 25%).

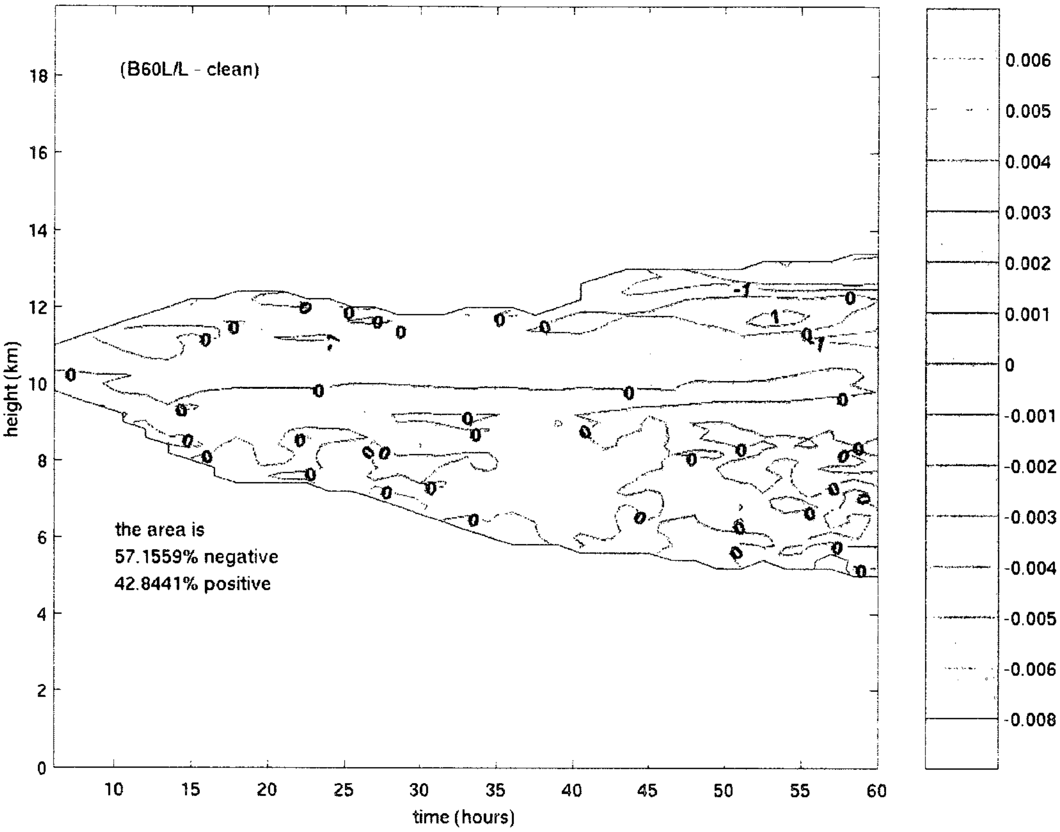

Figure 5.17. The change in vapor mixing ratio when 60 IN/L are introduced as a sheet at 300 hPa, shown as an absolute difference (color, g/kg) and percent difference (contoured at -25, -10, -5, -2, -1, 0, 1, 2, 5, 10, and 25%). The white part of the envelope (lower right) has values too negative to show on the color scale, which was intentionally kept constant for all these images for ease of comparison. The absolute difference in this area ranges from -0.008 to -0.025544 g/kg, a large difference but not large enough for the *percent* difference to be greater than 1% (see contours).

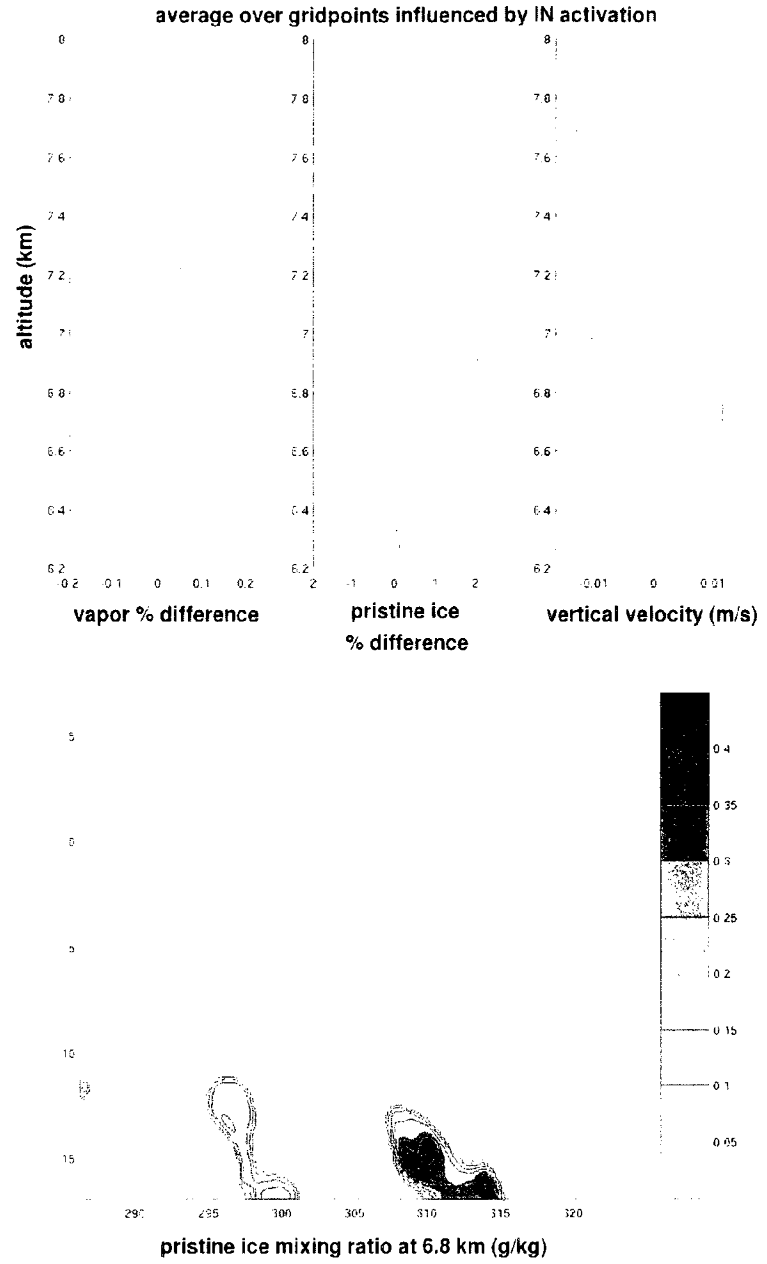

Figure 5.18. 57 hours into the experiment with IN initialized at 250 hPa, a very small area of air influenced by IN activation exists at a cloud edge at the southernmost part of the model domain near 315°E (circled in red) at 6.8 km. The area influenced by IN activation at and near this level, though small, shows a clear positive change in both vapor and pristine ice compared to a IN-free experiment, which appears to be the result of descending air (see plot of vertical velocity, top right) which brings pristine crystals and vapor down to and near 6.8 km, initiating some ice formation.

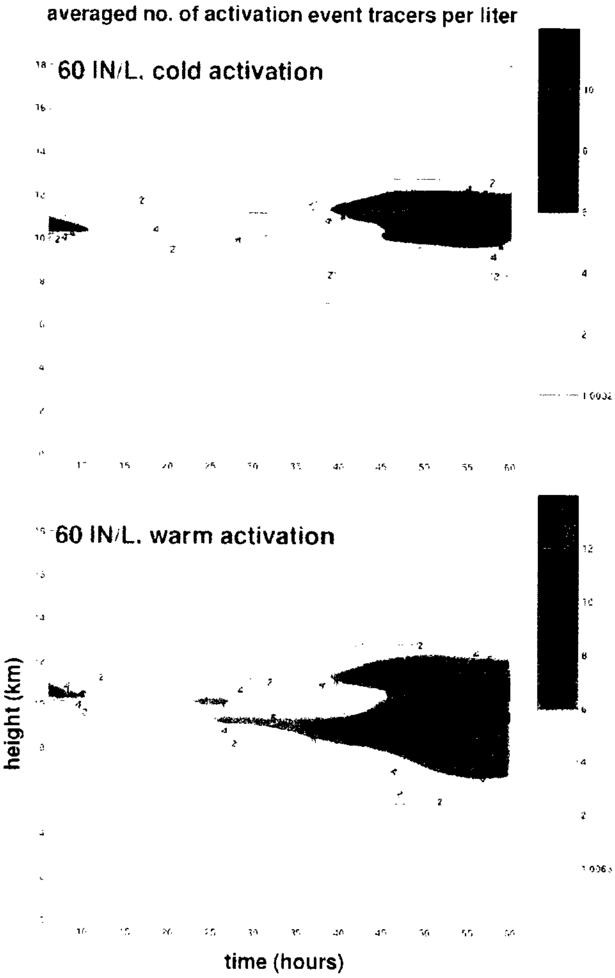

Figure 5.19. Horizontally averaged concentration of the IN-activation tracer, showing the extent and degree of air influenced by IN activation, for experiments initialized with 60 IN/L introduced as a sheet at 250 hPa and allowed to activate at when the air is saturated with respect to ice and the temperature is 238 K (top) or 273 K (bottom).

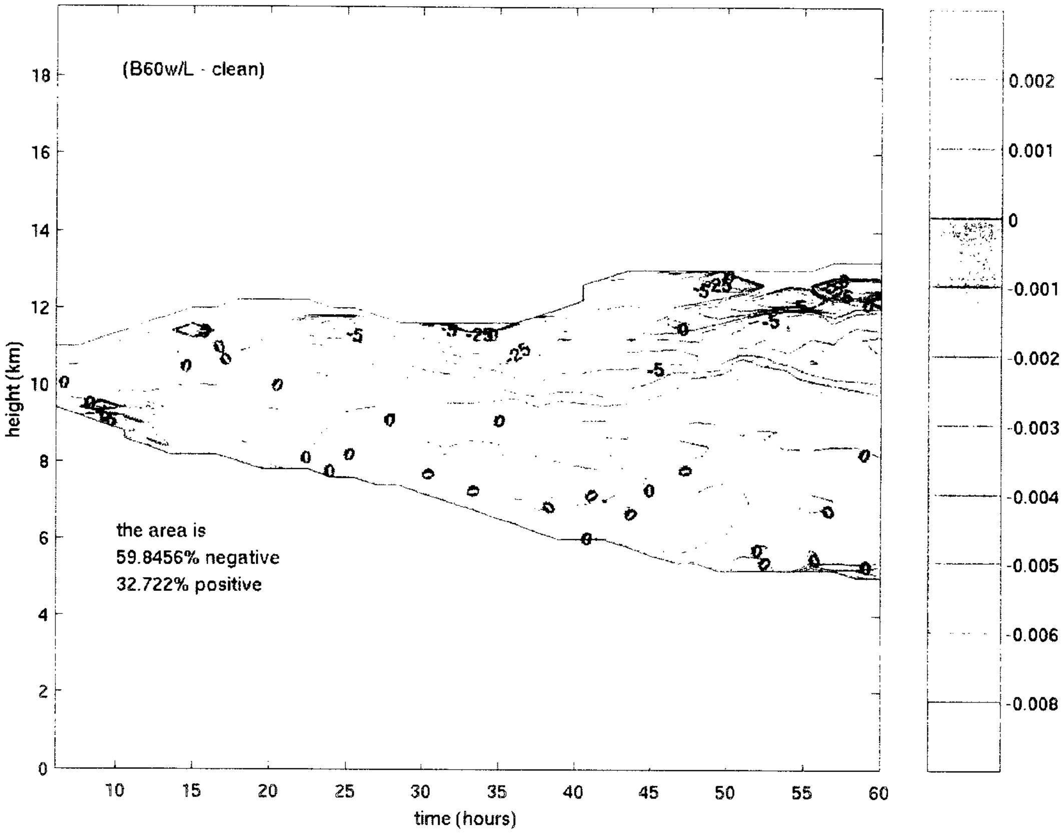

Figure 5.20. The change in pristine crystal mixing ratio when 60 IN/L initialized as a sheet at 250 hPa and are allowed to activate at 273 K, shown as an absolute difference (color, g/kg) and percent difference (contoured at -25, -10, -5, -2, -1, 0, 1, 2, 5, 10, and 25%).

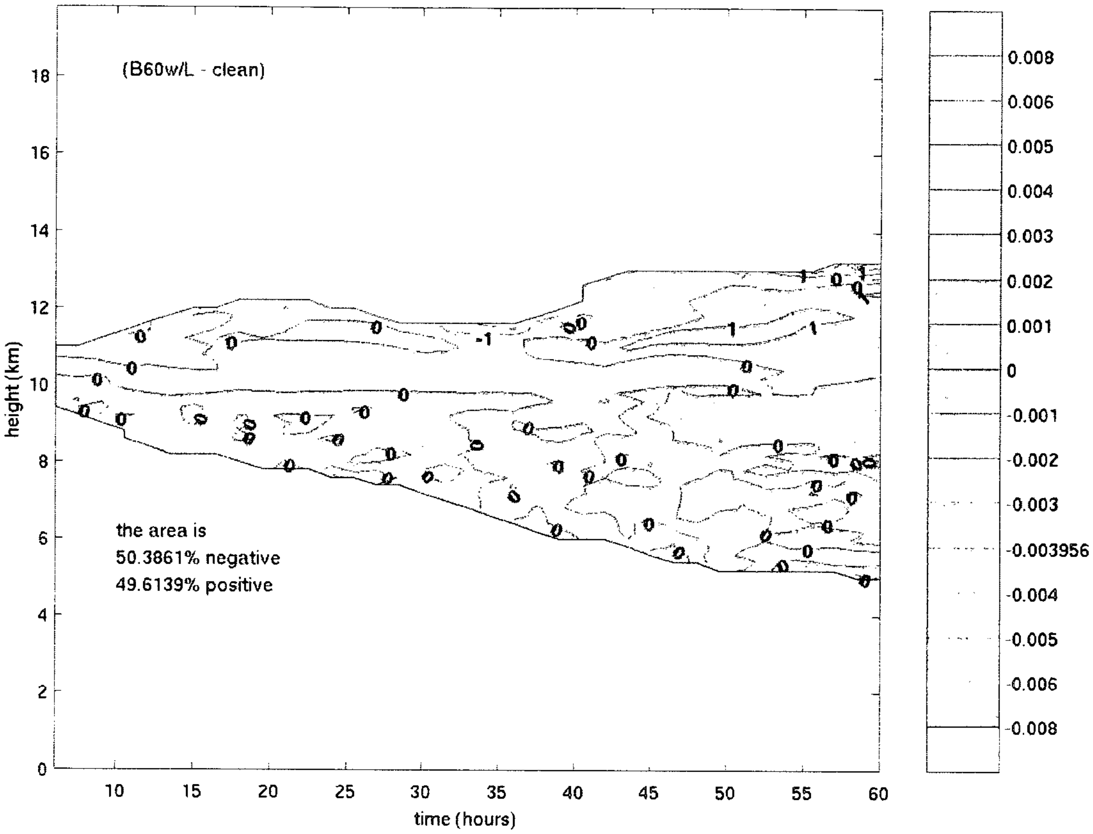

Figure 5.21. The change in vapor mixing ratio when 60 IN/L are initialized as a sheet at 250 hPa and allowed to activate at 273 K, shown as an absolute difference (color, g/kg) and percent difference (contoured at -25, -10, -5, -2, -1, 0, 1, 2, 5, 10, and 25%).

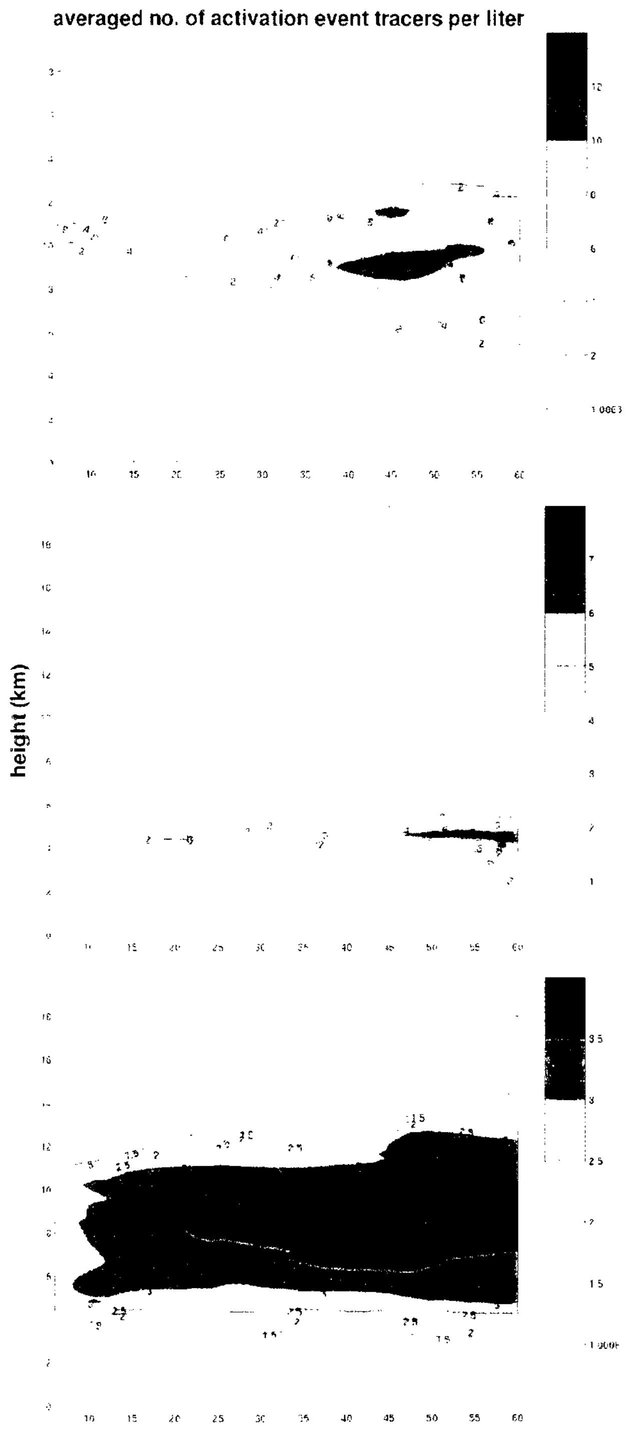

Figure 5.22. Horizontally averaged concentration of the IN-activation tracer, showing the extent and degree of air influenced by IN activation, for experiments initialized with 60 IN/L introduced as a sheet at 250 hPa (top), 120 IN/L introduced as a sheet at 925 hPa (center), and 60 IN/L introduced everywhere (bottom). Each IN population was allowed to activate at 273 K and when the air is saturated with respect to ice.

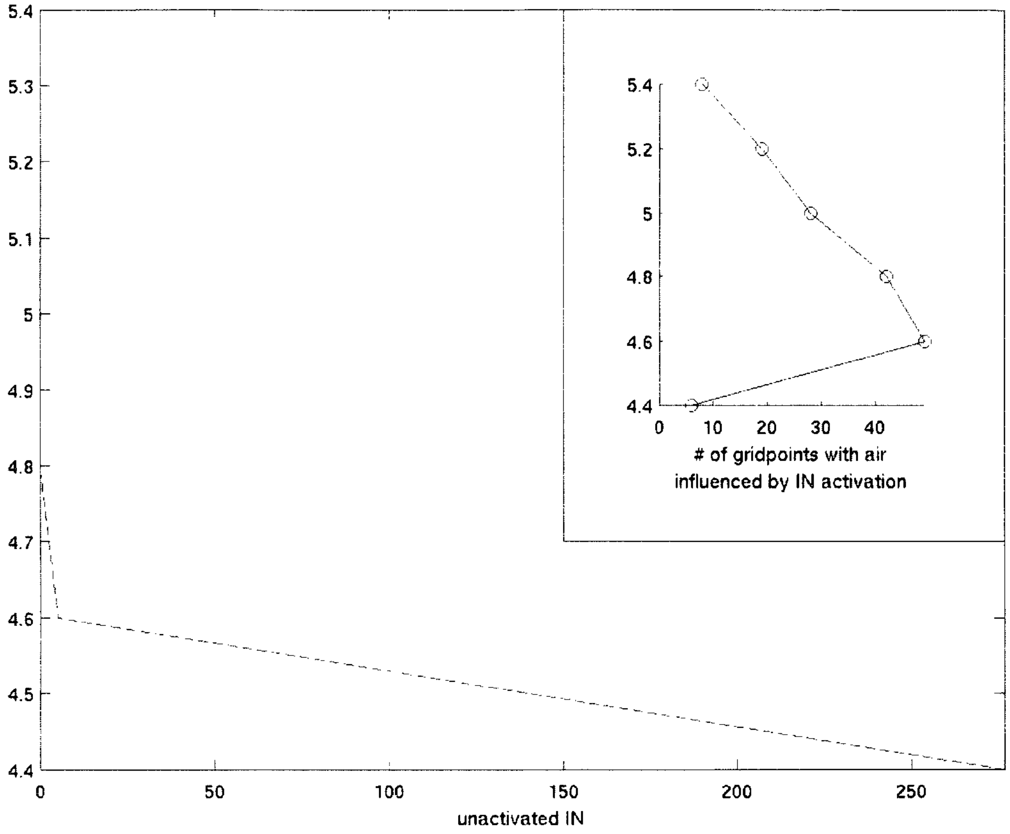

Figure 5.23. The number of unactivated ice nuclei in the experiment with 120 IN/L initialized at 925 hPa (shown only within the envelope of IN-influence), at 15 hours, as well as the number of gridpoints influenced by IN activation at the same time (inset). Ice nuclei at this time have been transported up to about 4.8 km, while the extent of IN-influence (via activation events) is slightly higher.

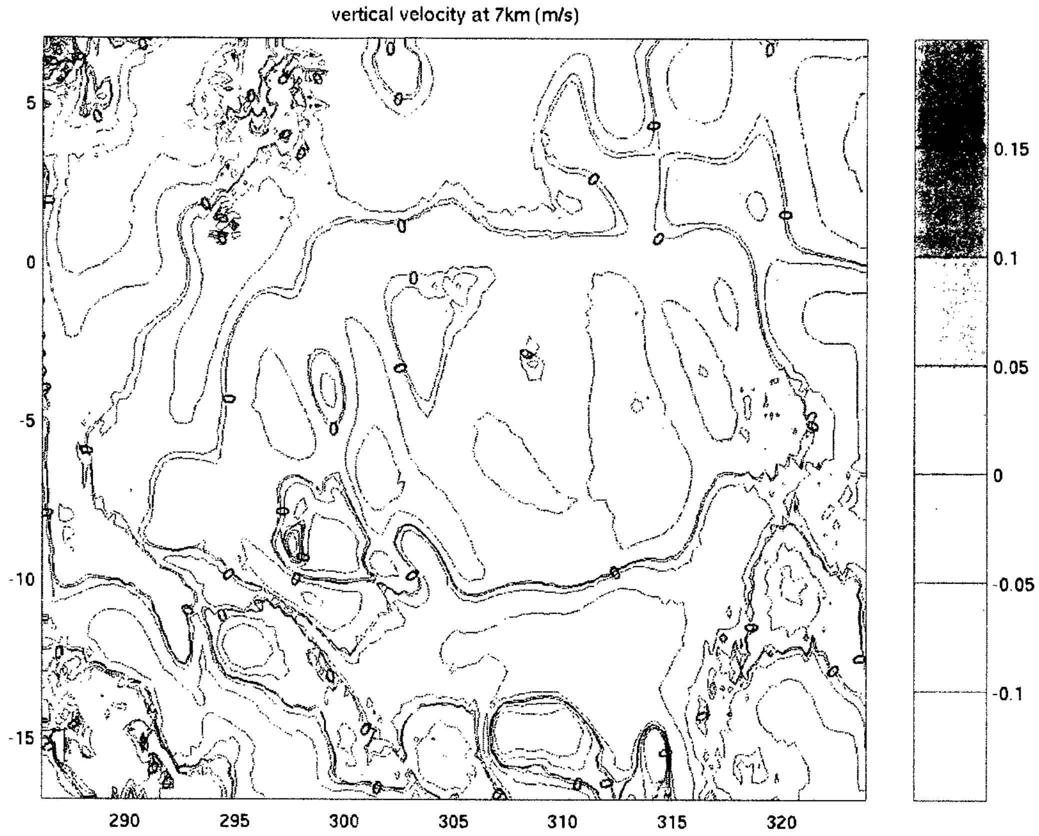

Figure 5.24. Vertical velocity (m/s) at 7 km, 27 hours into the experiment with 120 IN/L initialized at 925 hPa and allowed to activate at 273 K. The area influenced by IN activation is enclosed by the red dashed contour, along the southern boundary of the domain. During the periods of 25 – 30 and 44 – 48 hours, at the times of maximum height of IN-influenced air, the area of IN-influence is as shown, at the southern edge of the domain. It is possible that IN and activation-event tracers were not lofted further because of the influence of the average northwesterly winds, which may have kept the tracers out of areas with stronger upward motions (immediately north of the area of IN-influence above) and instead transported the tracers out of the domain.

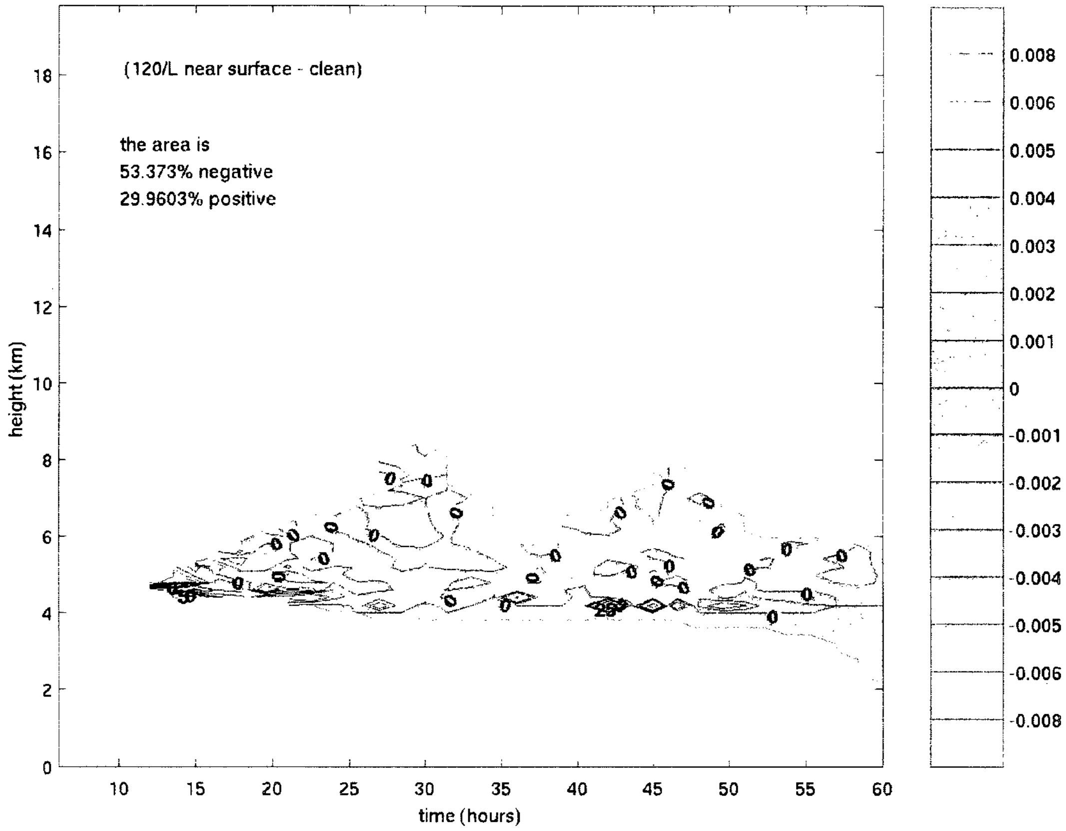

Figure 5.25. The change in pristine crystal mixing ratio when 120 IN/L are initialized as a sheet at 925 hPa and allowed to activate at 273 K, shown as an absolute difference (color, g/kg) and percent difference (contoured at -25, -10, -5, -2, -1, 0, 1, 2, 5, 10, and 25%).

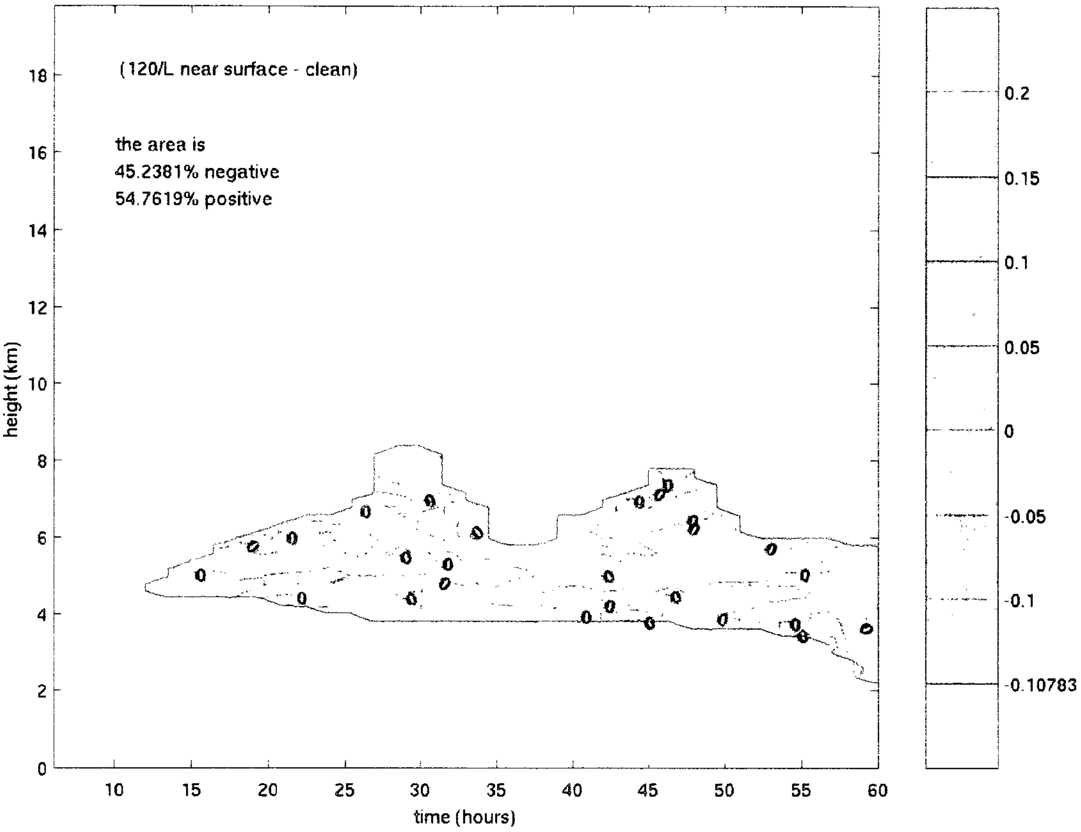

Figure 5.26. The change in vapor mixing ratio when 120 IN/L are initialized as a sheet at 925 hPa and allowed to activate at 273 K, shown as an absolute difference (color, g/kg) and percent difference (contoured at -25, -10, -5, -2, -1, 0, 1, 2, 5, 10, and 25%).

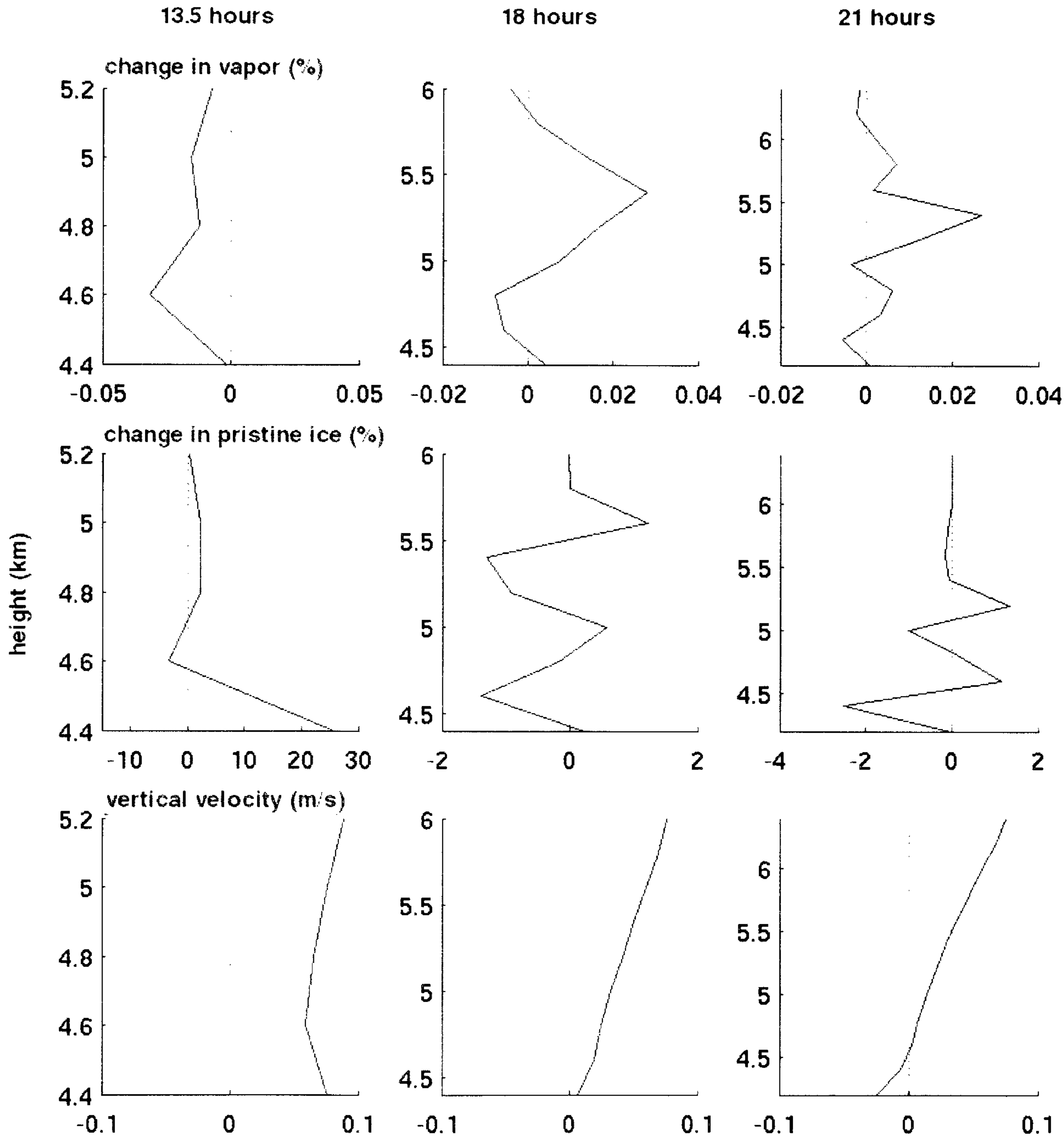

Figure 5.27. At the start of the experiment with 120 IN/L initialized at 925 hPa with a warm (273 K) activation threshold, changes in pristine ice were strong compared to the changes in ice during the remainder of the experiment. Above, changes in vapor (top row), changes in pristine ice (middle), and vertical velocity (bottom row) are shown during this early time, at 13.5 hours (left column), 18 hours (middle column), and 21 hours (right). Waves of IN activation in rising air creates corresponding increases in pristine ice and decreases in ice just above, as vapor is used to form "extra" ice below. This pattern dissipates after the air influenced by IN activation experiences descent (compare changes in ice here to those after 21 hours in Figure 5.25).

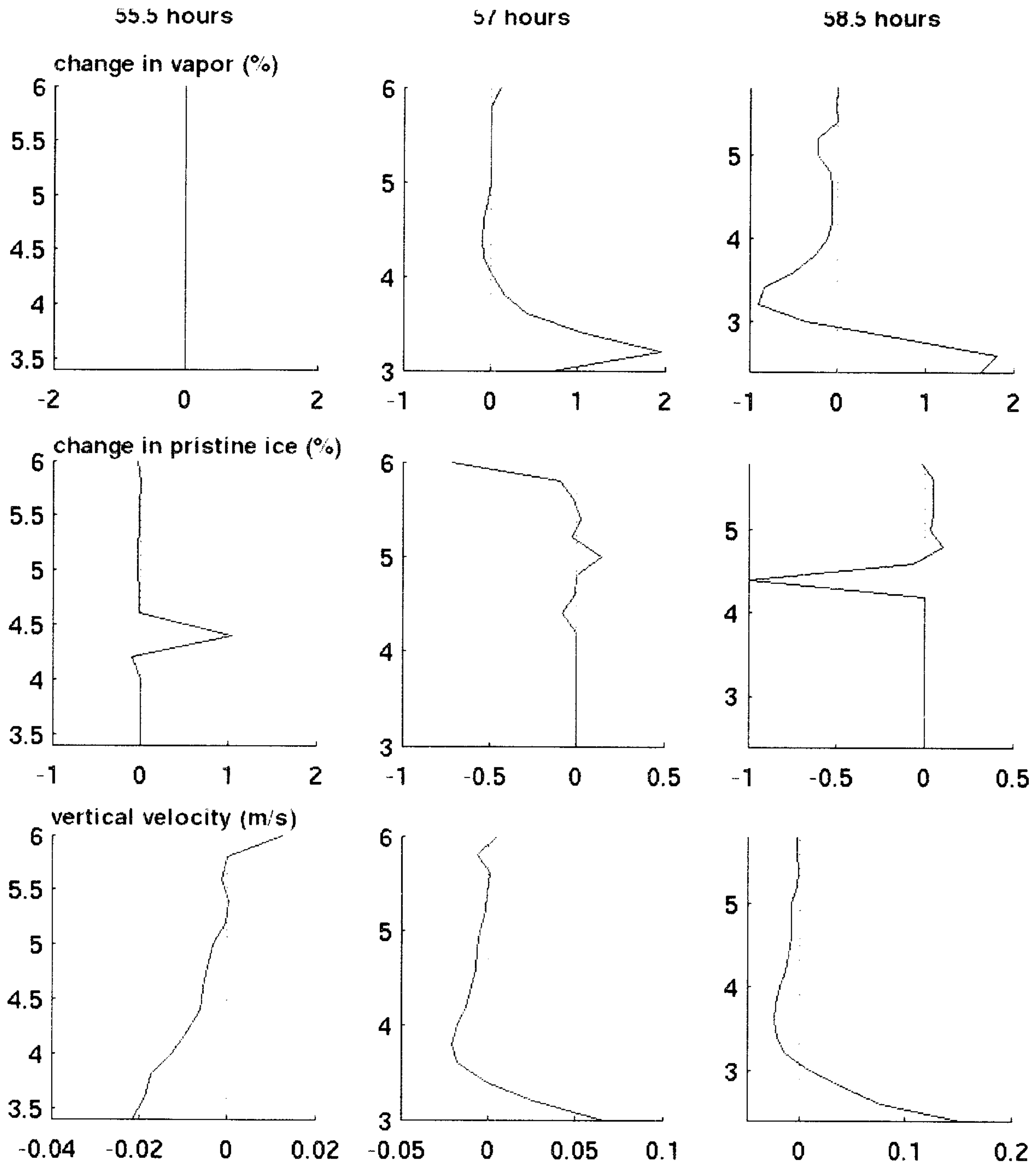

Figure 5.28. The change in vapor (top row) becomes increasingly positive at the lower bound of IN-influenced air at the end of the experiment with 120 IN/L initialized at 925 hPa with a warm activation. Changes in vapor at 55.5 hours exist but are on the order of .001%. It appears that the positive change in vapor is caused by areas with increased ice (middle row) descending, with the ice evaporating and moistening lower levels. Once the change in pristine ice declines and becomes negative, the change in vapor below decreases—note the decreased positive change in vapor below 3 km and the increasingly negative change in vapor above 3 km at 58.5 hours (top right).

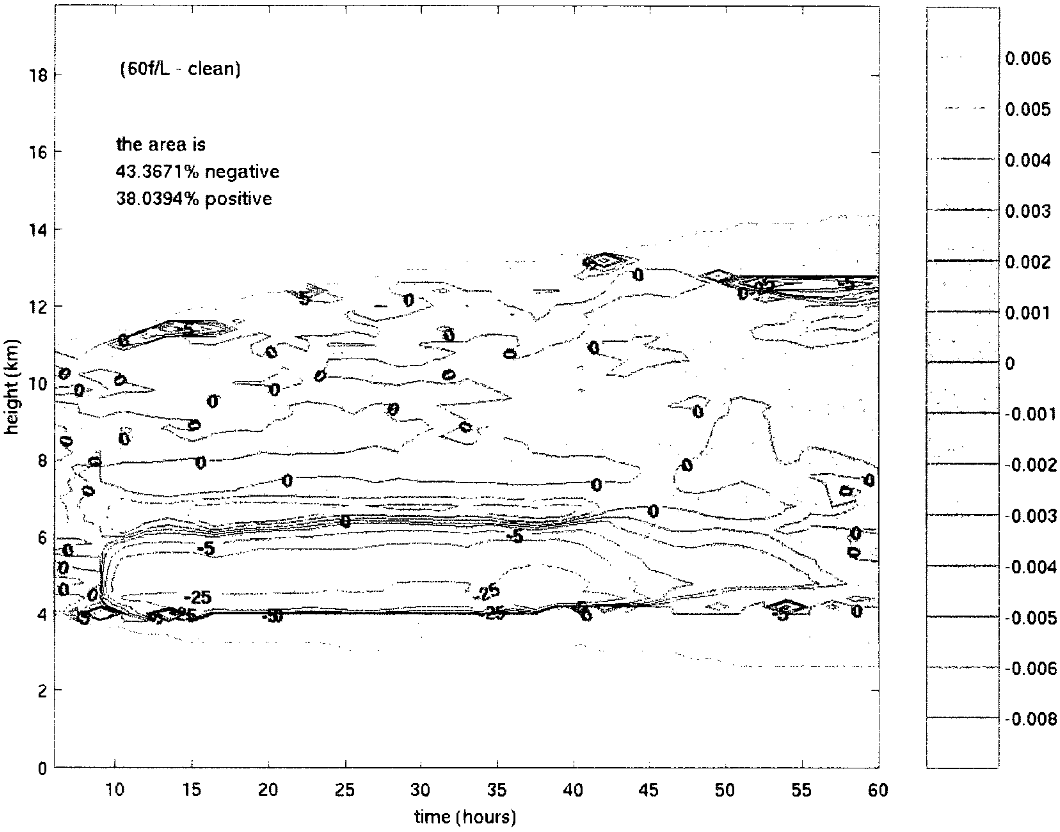

Figure 5.29. The change in pristine crystal mixing ratio when 60 IN/L are initialized uniformly throughout the model domain and allowed to activate at 273 K, shown as an absolute difference (color, g/kg) and percent difference (contoured at -25, -10, -5, -2, -1, 0, 1, 2, 5, 10, and 25%).

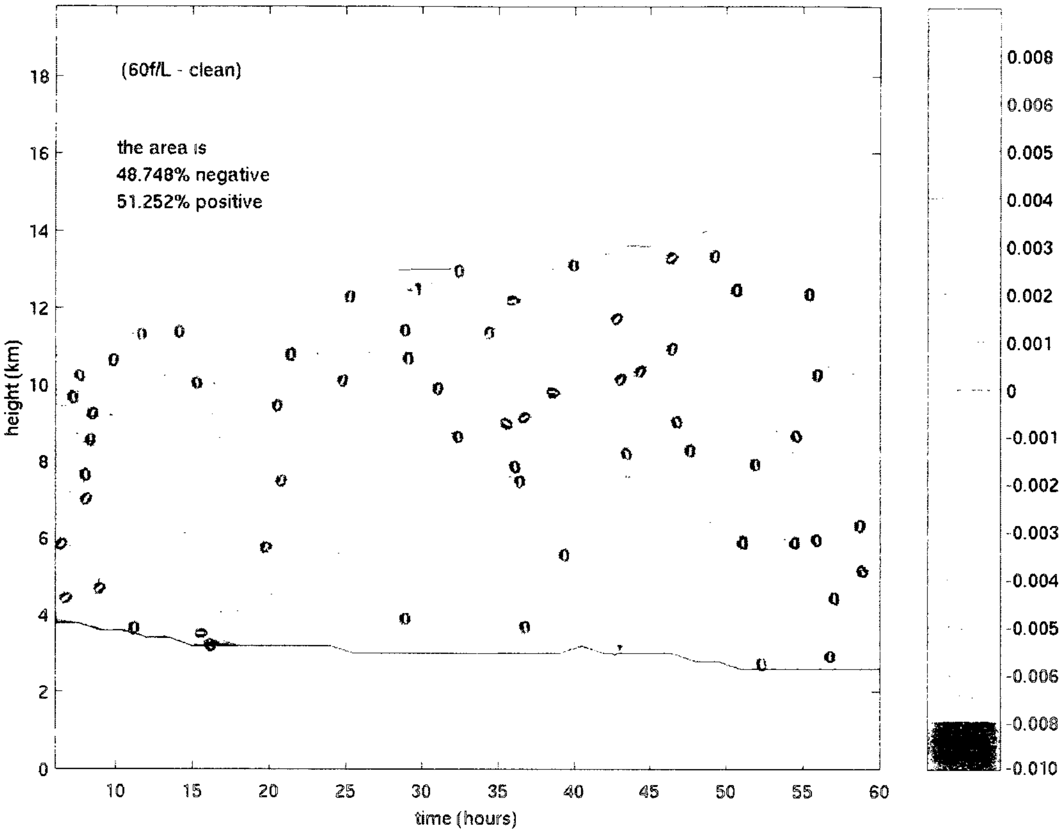

Figure 5.30. The change in vapor mixing ratio when 60 IN/L are initialized uniformly throughout the model domain and allowed to activate at 273 K, shown as an absolute difference (color, g/kg) and percent difference (contoured at -25, -10, -5, -2, -1, 0, 1, 2, 5, 10, and 25%).

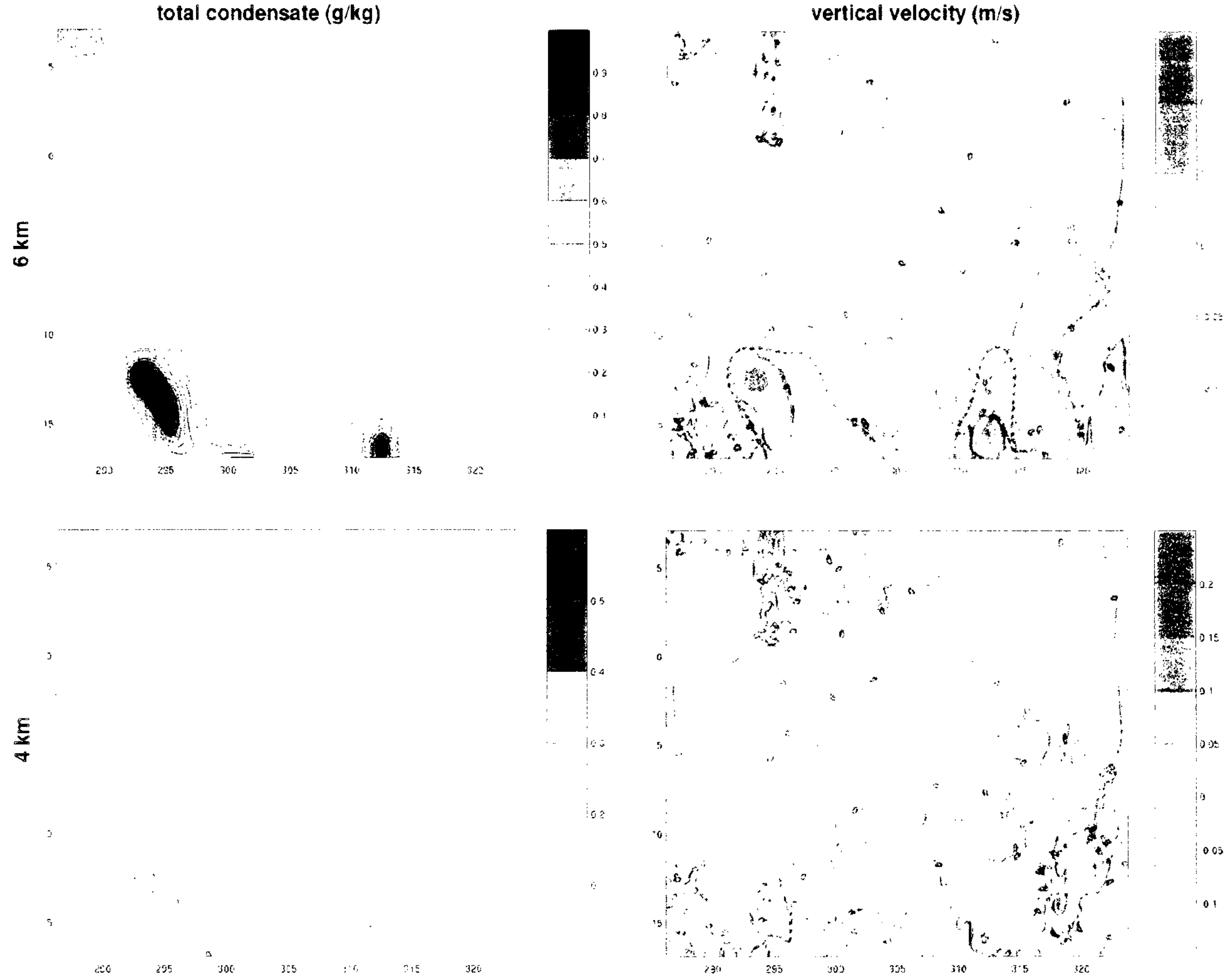

total condensate (g/kg)

vertical velocity (m/s)

Figure 5.31. Total condensate (left) and vertical velocity (right) at 4 and 6km (bottom and top rows, respectively), 10.5 hours into the experiment with 60 IN/L fumigated throughout the model domain. Areas with air influenced by IN activation are enclosed by red dashed contours. The layer between 4 and 6 km has a distinct decrease in ice when IN are present, here we see that air influenced by IN activation in this layer is often in cloudy, rising air.

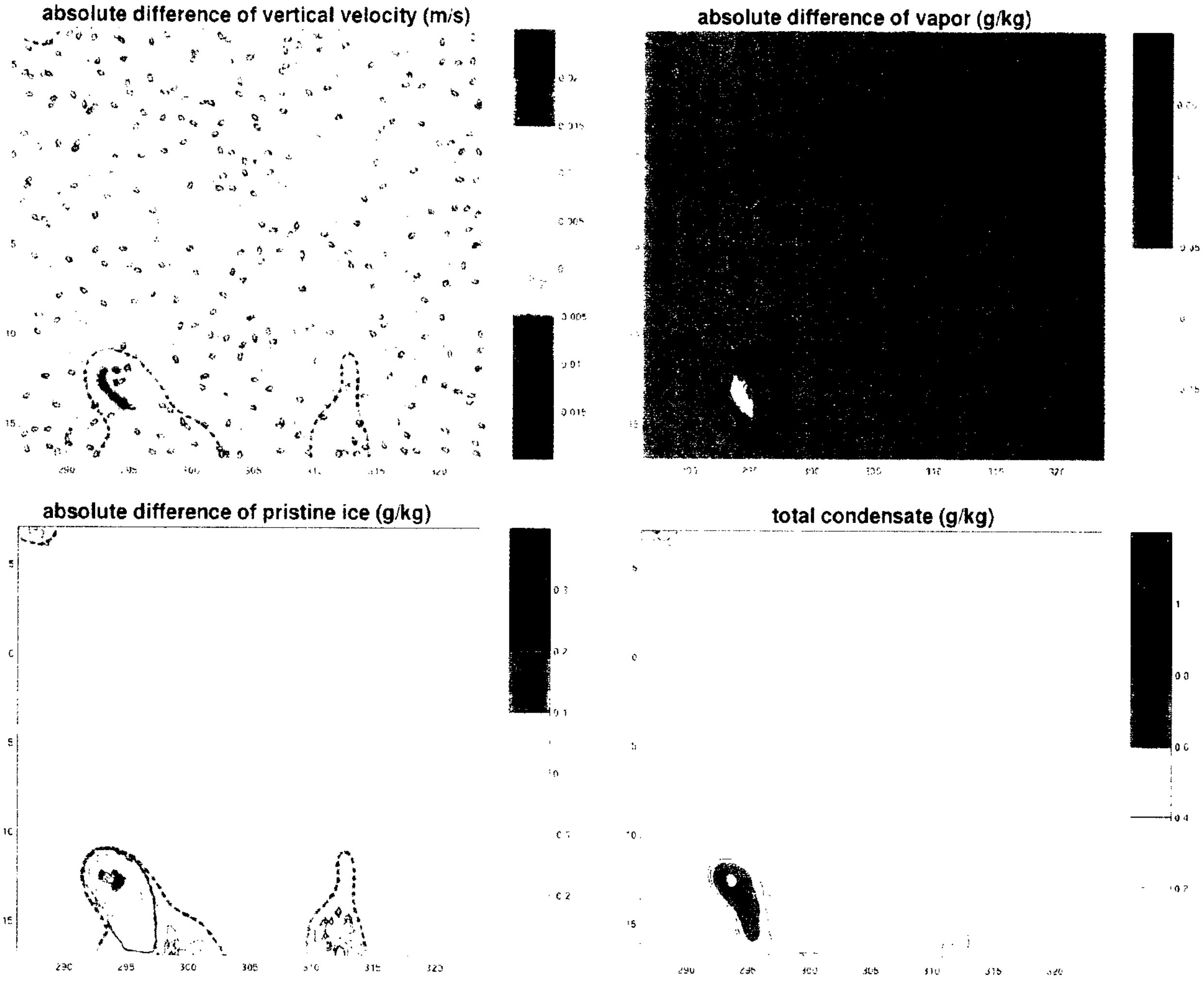
absolute difference of vertical velocity (m/s)

absolute difference of vapor (g/kg)

absolute difference of pristine ice (g/kg)

total condensate (g/kg)

Figure 5.32. Differences of vertical velocity (top left), vapor (top right), and pristine ice (bottom left), 10.5 hours into the experiment with 60 IN/L fumigated throughout the model domain. Air influenced by IN activation is enclosed by the red dashed contours, all plots show data for 5 km. At bottom right, the amount of condensate is also shown to indicate where cloudy areas are. At this altitude, a decrease in vapor is coincident with an increase in ice and an enhanced updraft (bottom left of plots), suggesting new ice formation in the updraft. Surrounding this feature, there is an increase in vapor and decrease in ice. It is possible that the increased crystal mass at higher altitudes has enhanced precipitation efficiency, and the precipitation is evaporating here.

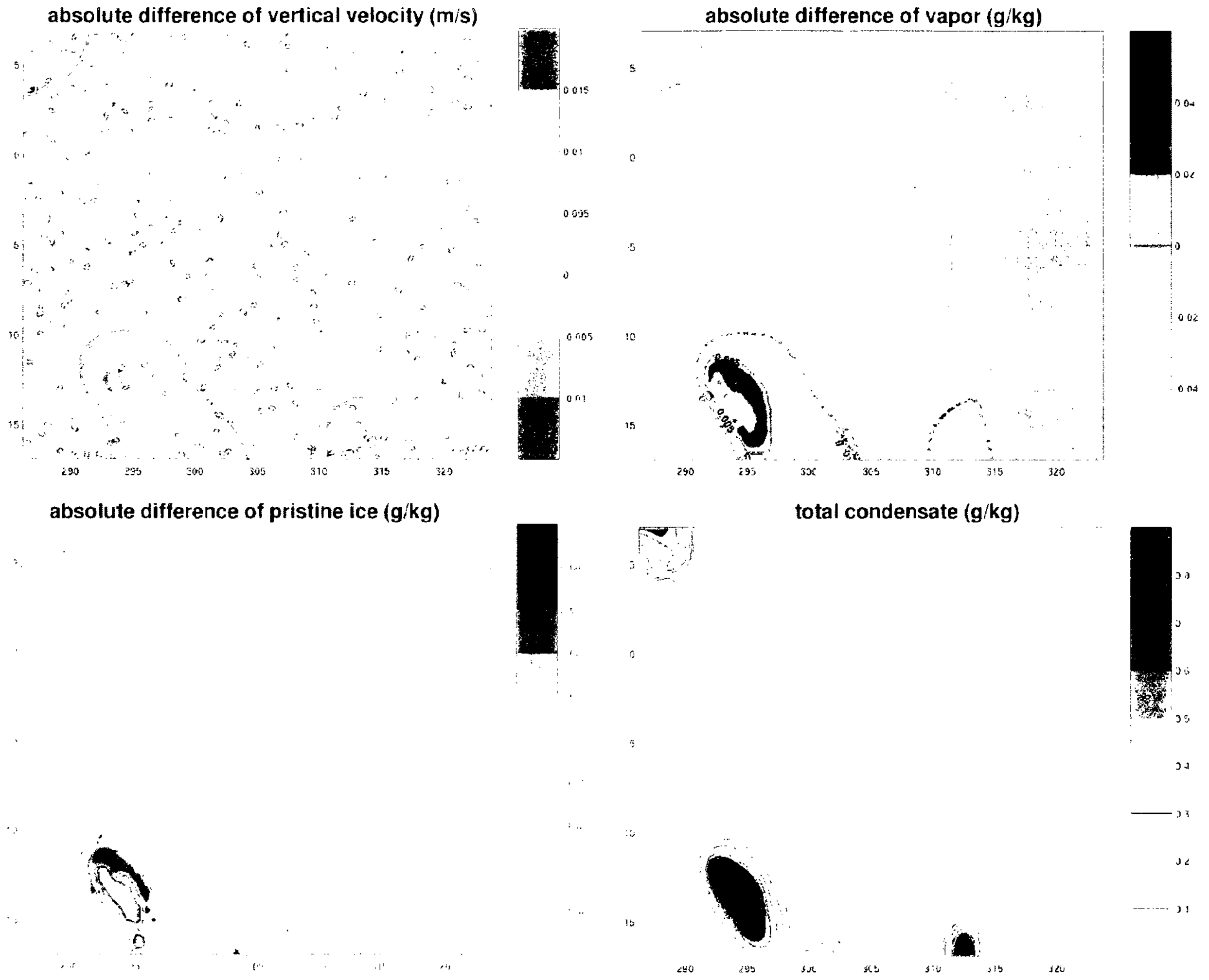

Figure 5.33. Differences of vertical velocity (top left), vapor (top right), and pristine ice (bottom left), 10.5 hours into the experiment with 60 IN/L fumigated throughout the model domain.Air influenced by IN activation is enclosed by the red dashed contours, all plots show data for 7 km. At bottom right, the amount of condensate is also shown to indicate where cloudy areas are. At this height the increase in vapor is coincident with an increase in ice near the edge of the cloudy area in the southwestern part of the domain. Though the vertical velocity anomaly is present (still) it weakens, as does vertical velocity itself, above this altitude, so it is possible that the increased vapor and ice are the result of detrainment. The decreases in ice at this level (and above) would result from an increased precipitation efficiency at lower levels.

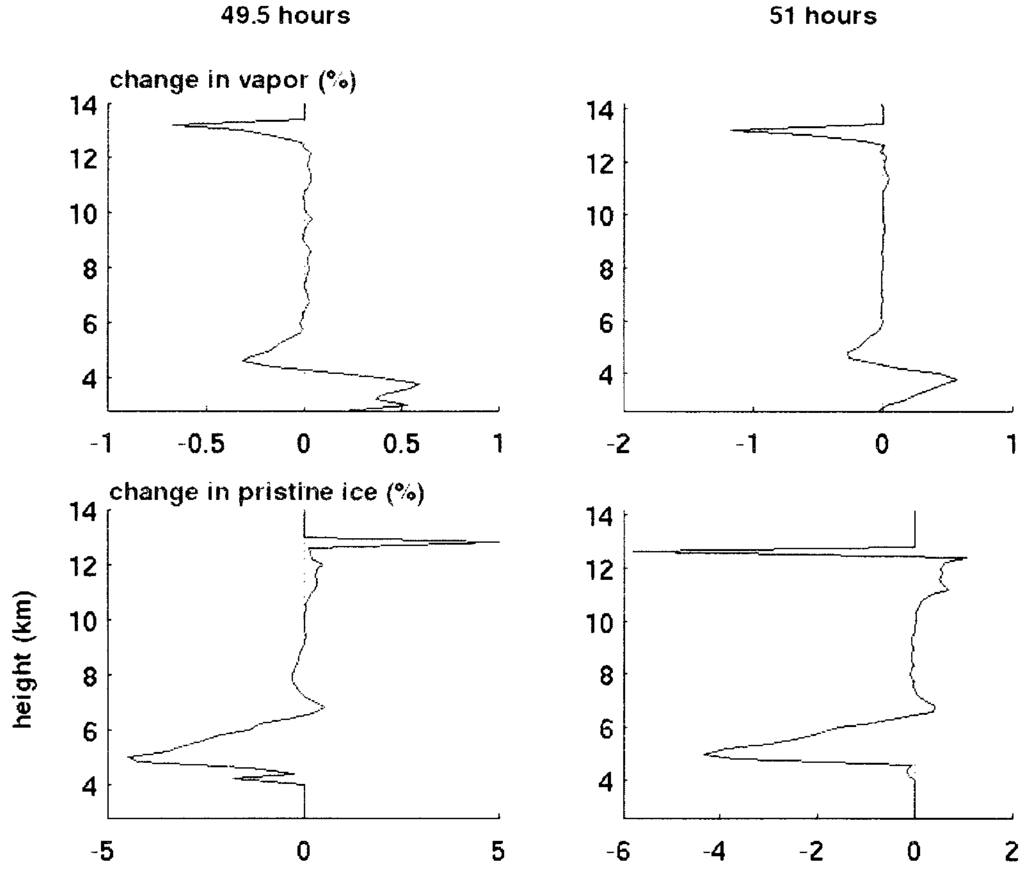

Figure 5.34. Changes in vapor (top) and ice (bottom) at 49.5 and 51 hours (left and right columns, respectively). These plots show the origin of the large negative change in pristine ice that starts near 50 hours at 12.6 km. At 49.5 hours, ice forms, indicated by a decrease in vapor and an increase in ice, but over time the ice falls to lower levels—the increase in ice seen between roughly 10.5 and 12.4 km.

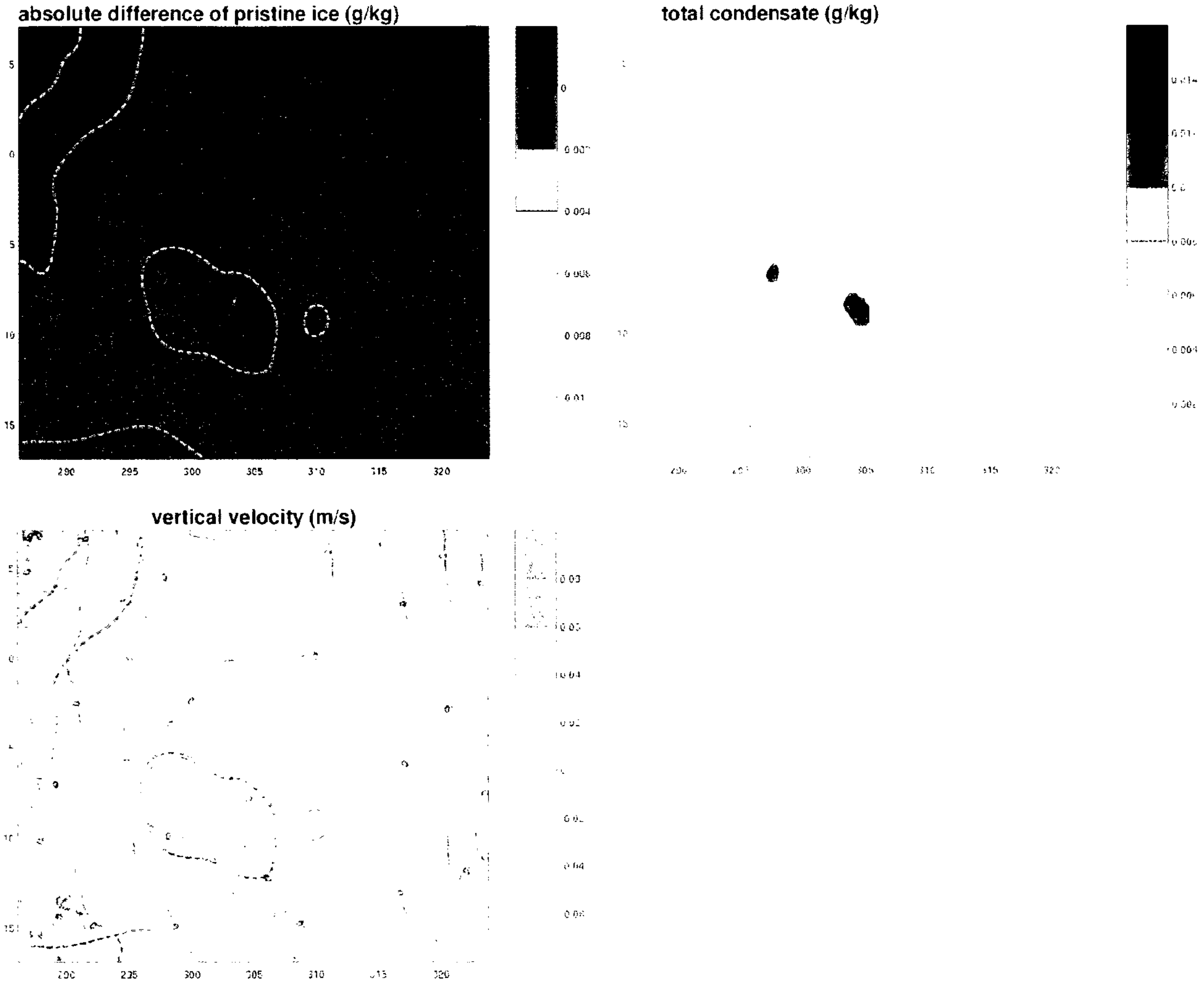

Figure 5.35. Differences of pristine ice (top left) along with the amount of condensate (top right) and vertical velocity (bottom left), 51 hours into the experiment with 60 IN/L fumigated throughout the model domain. Air influenced by IN activation is enclosed by the red dashed contours, all plots show data for 12.6 km. The strongly negative changes in pristine ice occur in very small parts of cloudy areas in descending air.

Chapter 6: the Dipole Feature

Four of the eight experiments had a common feature in plots of vapor difference: a dipole in vapor change, sometimes with a corresponding dipole in ice change, that forms in the second half of the UWNMS simulations with positive changes in vapor below and negative changes above an inflection point that varies between about 11 and 12 km. This feature stands out while looking at time-height plots of percent differences in vapor since the dipole exists over several hours. Since it is the more consistent of the two, for this and the following chapters the vapor dipole will be referred to as the dipole, while the quasi-dipole in ice will be referred to as such. Why do these dipoles form for these four experiments—with 120 and 60 IN/L initialized at 250 hPa and 60 IN/L initialized at both 200 and 300 hPa (Figures 6.1 – 6.4 respectively)—but not the other two (30 IN/L and 60 IN/L with a warmer activation temperature)? And why does the dipole form only in the latter half of the experiments?

Vapor distribution is controlled by air movement and phase changes. In order to understand the origin and maintenance of the dipole, we need to look at air movement in the vertical, which is very useful since it can affect phase changes. In order to better understand any phase changes, we should also observe how the distribution of pristine ice changes over time. Let us now explore the dipole features in Figures 6.5 – 6.8, which show averages over IN-influenced air of vertical velocity and how vapor and pristine ice change with height, and determine what patterns there are. Please keep in mind, in our preliminary exploration of the dipole, the meteorological conditions that exist: each of the dipoles "start" near 45 hours on average, which corresponds to 6 pm local time on the 27th of September 1992, when convective activity ahead of a stalled cold front begins and intensifies. We will see that the onset and decay of convective activity plays a large part in the creation and lifetime of the dipole.

In Figure 6.5, we see a time series of these plots for the experiment with 120 IN/L initialized at 250 hPa. The dipole first starts to form near 42 hours. Across the dipole at that time, pristine ice shows a negative change and air is ascending. At 43.5 hours the dipole in vapor is roughly matched by a dipole in pristine ice, both dipoles existing in rising air. At 51 hours and afterwards the vapor dipole exists in descending air. At 51 hours there are negative peaks in both vapor and pristine ice change at about 12.6

km and a peak in positive change near 11.9 km. At 55.5 hours these relationships seem to have swung about completely, such that there is a negative change in pristine ice where the vapor dipole is positive and a positive or zero change in pristine ice where the dipole is negative.

Figure 6.6 shows a time series for the experiment with 60 IN/L initialized at 250 hPa (about 11 km), again with vapor and pristine ice percent difference with the average vertical velocity over those gridpoints influenced by IN activation. The dipole first starts to form 45 hours into the model run (top row) and dissipates after 55.5 hours (bottom row). At 45 and 46.5 hours, the entire dipole exists in rising air, and where the change in vapor is negative, the change in pristine ice is also negative. At 48 and 51 hours, vertical velocity becomes increasingly negative across the dipole (though always less than 1 cm/s), and there is still a peak in the negative change of pristine ice roughly coincident with the negative peak in vapor difference. Fifty five and a half hours into the model run vertical velocity is again negative across the vapor-change dipole, however, where the change in vapor is negative (above about 12 km) the change in pristine ice is positive.

The evolution of the dipole feature present when 60 IN/L are initialized at 300 hPa (about 9.7 km) is shown in Figure 6.7. At 42 hours, vertical velocity is positive and the change in pristine ice is negative across the not-quite-formed dipole (the changes in vapor are less than 1% at this time), with an axis at about 12 km. At 52.5 and 55.5 hours, the dipole now exists, in descending air, and where the change in vapor is negative the change in pristine ice is positive. This is opposite to the pattern seen in the 120 and 60 IN/L dipoles, where negative peaks in both vapor and pristine ice were often coincident. At 58.5 hours, the dipole has weakened considerably, and the change in pristine ice has a negative peak where vapor is negative (a reversal from the previous two times) and vertical velocity is weakly negative. The strength of the negative portion of this dipole outlasts the positive portion, as the positive portion weakens to a vapor change of less than 1% at 55 hours, while the negative portion remains through the end of the experiment (60 hours).

Figure 6.8 shows a time series of plots over the lifetime of the dipole that forms when 60 IN/L are initialized at 200 hPa (about 12.5 km). The dipole forms near 45 hours, with the negative change in vapor in descending air and the positive change in vapor in weakly ascending air. This is unlike the other three dipoles, which all begin –both positive and negative parts-- in rising air. At 46.5 hours vertical velocity is mixed but mostly positive over the dipole, with a small, weakly descending portion of the positive vapor change near 11.5 km. From 48 to 55.5 hours of the model run the dipole exists in descending air, and from the origin of the dipole to 52.5 hours, it also exists where there are either more crystals or no change in crystal mass with IN present. At 52.5 hours part of the positive portion of the dipole in vapor change coincides with a negative change in ice. The dipole persists until the end of the model run (60 hours). At this final time the air containing the dipole is descending, with either no change or an increase in pristine ice in the presence of the idealized IN.

There are some patterns among these four experiments' dipoles, summarized below in Tables 6.1 and 6.2. In the 60 and 120 IN/L (both at 250 hPa) experiments' dipoles, where the change in vapor is negative the change in pristine ice is also negative. When 60 IN/L are initialized at 200 and 300 hPa the change in pristine ice is often positive (or zero) where there is a negative change in vapor. The vapor dipole is a much more consistent feature than the ice dipole, suggesting the ice dipole may be a by-product of the vapor dipole. When 60 IN/L are initialized at 250 and 300 hPa, and also when 120 IN/L are input at 250 hPa, the entire dipole forms in rising air at a time (near 45 hours) that coincides with the beginnings and intensification of convective activity ahead of a stalled cold front. In these three experiments, too, the dipole dissipates with descending air, corresponding to decaying convection.

One pattern that is consistent is that with greater numbers of initial IN and the higher altitude they are, the more *negative* the upper portion of the vapor dipole. The effect of concentration is small: when 60 IN/L are initialized at 300 and 250 hPa, the negative percent change in vapor is less than 4% in the dipoles, and when 120 IN/L are initialized the negative vapor change is as much as about 4.8%. When 60 IN/L are initialized at 200 hPa the negative vapor change is up to 17%. The altitude of IN and activation-influenced air has a much larger effect on the dipole's strength than the number of IN.

height	***dipole axis***	air rising △ ice negative △ vapor negative	air mostly rising △ ice negative △ vapor negative	air rising △ ice negative △ vapor negative	air descending △ ice positive △ vapor negative
		air rising △ ice negative △ vapor positive	air rising △ ice mixed △ vapor positive	air rising △ ice negative △ vapor positive	air rising △ ice positive △ vapor positive
		120 IN/L	**60 IN/L at 250 hPa**	**60 IN/L at 300 hPa**	**60 IN/L at 200 hPa**

Table 6.1. Quantities averaged over IN-influenced air, near the start of vapor dipole formation.

height	***dipole axis***	air descending △ ice positive or no change △ vapor negative	air mostly descending △ ice positive or no change △ vapor negative	air mostly rising △ ice negative or no change △ vapor negative	air movement is mixed △ ice positive or no change △ vapor negative
		air descending △ ice negative △ vapor positive	air descending △ ice negative △ vapor positive	air descending △ ice mixed △ vapor positive	air descending △ ice positive △ vapor positive
		120 IN/L	**60 IN/L at 250 hPa**	**60 IN/L at 300 hPa**	**60 IN/L at 200 hPa**

Table 6.2. Quantities averaged over IN-influenced air, near the end of a vapor dipole's lifetime (or the end of model run time).

Another consistent pattern is that no matter what the initial concentration or height of the IN layer, as we have seen in Figures 6.5 - 6.8, the area of positive vapor change originates in rising air. Therefore, it is highly likely that at least the positive part of the dipole is formed in growing convective towers. This region of positive change also exists when 30 IN/L are modeled (Figure 6.9). In fact, there are only little dynamical differences among experiments—the convective activity starts at the same time with similar intensities. Figure 6.10 shows that positive vapor change in the 30 IN/L experiment at four times, along with the percent change in pristine ice and the average vertical velocity for the gridpoints influenced by IN activation. The times shown cover the timespan of the dipoles in Figures 6.5 – 6.8. At 42 and 45 hours, the average vertical velocity over IN-influenced gridpoints is positive above about 10 km, then at 51 and 55.5 hours, the vertical velocity above 10 km is mostly negative. This fits the pattern seen in Figures 6.5 - 6.8 for vertical velocity above 10 km: from about 40 to 46 hours vertical velocity is positive over those gridpoints influenced by IN activation, between 46 and 49 hours vertical velocity is mixed, and after about 49 hours it is negative. There are some small changes in the magnitude of vertical velocity among the experiments at these altitudes, possibly caused by differing areal extent of activation-influence, but the overall dynamics varies little. We can therefore isolate the cause of the positive part of the dipole by studying the area of positive changes in vapor in the 30 IN/L experiment.

Figure 6.11 shows vertical velocity and absolute changes of vapor and pristine ice at 12 km and 42 hours into the experiment when 30 IN/L are initialized into the UWNMS, the time and height of the onset of 1% and greater positive changes in vapor. The picture is not simple: where both the changes in vapor and pristine ice averages to be positive, the sign of vapor and ice changes are in fact very mixed spatially over two areas influenced by IN activation. The area of influence on the right in the 12 km plots seems to show a very clear case—a large area of increased vapor results in a "cloud" of pristine ice, the IN-enhanced formation of which left a hole of sorts in the area of positive vapor change. (One could think that the increase in pristine ice is driving the increase in vapor via evaporation, but if this were the case the increase in vapor would overlap the area with an increase in ice.) This explains the increase in pristine ice but not the increase in vapor, and given that air is rising at this location, to explain the increase in vapor we will need to look at lower altitudes and back in time. Step 1: imagine an area of rising air at some altitude where IN enhance cloud formation, resulting in an increase in pristine ice and a corresponding decrease in vapor. This cloud may persist because of the indirect aerosol effect (smaller cloud particles), which would result in less precipitation—less vapor and ice at lower levels—step 2. If the air continues to rise, however slowly, the remaining cloud particles are likely to evaporate into the colder, drier air—step 3. Finally, this moistens the air above, and, if IN are present, a new cloud can form or be otherwise influenced by IN activation. This idea is illustrated by Figure 6.12, and supported by data seen in Figures 6.11 and 6.13. Plots of the ice and vapor differences at 11 km in Figure 6.13

correspond to the lower part of step 2, while the differences at 11.8 km in the same figure correspond to the upper part of step 2. In Figure 6.11 we see evidence of step 4, at 12 km.

The area of IN-influence on the left at 12 km shows almost no change in vapor and a weakly negative change in pristine ice. This appears to be caused by small changes in vertical velocity, as shown in Figure 6.14: where vertical velocity is slightly decreased, heavy condensate may not be suspended as easily, and where vertical velocity is slightly increased the opposite can occur and more condensate can be suspended, as seen at 11 km. These changes in vertical velocity are small and seem to have little-to-no coherent pattern in the UWNMS domain over time, and are likely a random, chaotic result of adding IN to the model.

That the *average* change for both vapor and pristine ice is positive at a given altitude above 10 km in the latter half of the experiments is, however, explained by the area with an increase in vapor initiating crystal formation, seen at 12 km when 30 IN/L are initialized (Figure 6.11). Figures 6.15 – 6.18, corresponding to 120 IN/L, 60 IN/L at 250 hPa, 60 IN/L at 300 hPa, and 60 IN/L at 200 hPa respectively, show horizontal cross-sections of vertical velocity, absolute change in pristine ice, and absolute change in vapor, at a time when the respective dipoles are strongest. The increases in vapor seen in these figures, and the accompanying increases in pristine ice, are likely the result of the process outlined above and in Figure 6.12. We can make an unsurprising generalization: in gently rising air (less than 1 cm/s) IN activation can result in smaller, more numerous crystals than without the influence of IN, and these smaller crystals are more likely to be transported to higher altitudes where they will evaporate in the drier air, moistening those upper levels. This result was hypothesized from the beginning of this research. The magnitude of the positive change in vapor does not seem to vary with IN concentration, with the maximum change between 2 and 5% depending on altitude (around 0.002 g/kg). This area of positive change exists in all six experiments with IN initialized at and above 300 hPa. What is still surprising, and yet unanswered, is why four of those experiments have a negative change in vapor at the highest portion of the envelopes of IN-influenced air.

Reviewing Figure 5.2, which illustrates that a greater initial IN concentration likely results in a greater number of unactivated IN, and remembering that the dipole is more negative with greater initial

IN concentration and/or height, it seems reasonable to think that after time some of those unactivated IN reach an altitude where they take up vapor (activate) to create tenuous ice clouds. If this were the case we'd see a decrease in vapor and a proportionate increase in pristine ice. It is also possible that the greater numbers of IN *did* activate earlier on and at lower levels, but on too small a scale to affect the average results, rather just enough here and there for there to be *slightly* more pristine ice in some areas which precipitates, decreasing atmospheric vapor here and there, slightly. If *this* were the case, it would be very hard to see; the average change in vapor at any time and height may be negative without any noticeable location(s) of negative vapor change. A third possibility is that a layer with drier air rose upward. Should this be the case we would be able to trace back negative features in time and height (downward). What do the data show?

Figure 6.19 shows vertical velocity, pristine ice mixing ratio, and the changes in pristine ice and vapor at the levels where the change in vapor is most negative in the experiment with 120 IN/L—at 51 hours and 12.4 km. There are two areas influenced by IN activation at this level. Spatially the change in vapor is mostly positive, though only weakly so. However the average change in vapor is negative, caused by the presence of a large curve of negative change that hugs the eastern and southern "cloud" boundary in the rightmost area influenced by IN. The contiguous cloud area has a decrease in pristine crystal mass. Somewhat similarly, the northwestern portion of the cloud gains pristine ice in the presence of IN, and an adjacent increase in vapor to the north-northwest. None of the three hypotheses for the negative part of the dipole fit here. Figure 6.20 shows that changes in vertical velocity are fairly well correlated to changes in pristine ice: where vertical velocity is decreased, so too is pristine ice, and vice versa. This is similar to what we saw in the westernmost area of IN influence in the 30 IN/L experiment at 12 and 11 km (Figures 6.11 and 6.13)--a decrease in vertical motion can mean ice is not held aloft as easily, or as the case here, the ice is descending more quickly, since the change in vertical velocity is about 0.3 cm/s and the existing (changed) vertical velocity is -0.7 cm/s (not shown). The change in vertical velocity also strongly affects the flux of vapor at this altitude (Figure 6.20). Putting this information together, this scenario represents a noisy equatorward shift in the cloudy area. But why are there changes in vertical velocity? The pattern of velocity changes seen at 12.4 km exists down to about

11 km, and throughout that depth remains on the order of a few mm/s (not shown). The changes are relatively unorganized, spatially, which, again, implies that the changes are mostly of the "butterfly effect" variety.

In Figures 6.21 - 6.23, vertical velocity, pristine ice, and changes to pristine ice, vapor, and vertical velocity are plotted for experiments with 60 IN/L initialized at 250 hPa, 60 IN/L initialized at 300 hPa, and 60 IN/L initialized at 200 hPa, respectively, for the time and altitude where the negative portion of the vapor-change dipole is strongest. The pattern of a negative change in pristine ice, flanked by a smaller area of negative vapor change, both influenced by a decrease in vertical velocity, repeats itself for each experiment. Though the values are too small to be definitive, it is possible that vapor was "nickel-and-dimed" --decreased in small increments by small amounts of IN activation-- to create the overall decrease seen in the 60 IN/L at 250 hPa experiment. In the IN-influenced area at left in Figure 6.21, some of the "cloud" appears to be enhanced by IN activation: there is a small decrease (less than 0.001 g/kg) in vapor and an increase in pristine ice of the same magnitude. For the experiment with IN initialized at a lower altitude (Figure 6.22) vapor may have been decreased slightly over time, since there is an overall decrease in vapor. Overall, for all experiments with a dipole, the negative portion of the dipole arose because of small—a few millimeters per second—changes in vertical velocity.

Changes in vertical velocity have a more pronounced effect on vapor and pristine ice at progressively higher altitudes, as we see here in the negative portion of the vapor-change dipole, where smaller amounts of vapor and ice make them more sensitive to small environmental changes. The negative portion of the dipole appears to be the result of noisy changes in vertical velocity between the clean and perturbed experiments—where there are noisily enhanced downward motions the changes in both ice and vapor are negative. At lower altitudes, such as in the realm of the positive-change portion of the dipole, changes in vertical velocity do not have such a significant impact.

It is possible that the changes in vertical motions are not only from noise (Appendix C) but also from changes in particle size. Since smaller particle sizes have less drag, an area with significant IN activation may see an increase in vertical velocity. Unfortunately the noisiness of the results excludes exploration and validation of this idea, especially since there is almost no variance in the magnitude of vertical velocity change with the number of IN or the amount of IN-influenced air.

In the beginning of this chapter we saw how much stronger the negative portion of the dipole is when IN are initialized at a higher altitude. There is a robust inverse correlation between the strength of the negative portion of the dipole and the total area influenced by IN: the greater the area, the weaker the negative part of the dipole. Compare Figures 6.22 and 6.23—when 60 IN/L are initialized at a lower altitude, more IN activate and the influence of IN spreads. The area influenced by IN activation is much smaller when IN are initialized at a higher altitude, since IN encountered fewer instances favorable for activation. A larger area influenced by IN will often have a smaller average change. It is possible for the negative change in vapor to be compounded by IN activation, since when IN are initialized at a higher altitude (or concentration) there are unactivated IN that can act at these higher altitudes. There is some evidence of this, though only in Figure 6.21, and not enough to draw a conclusion that this factor (as opposed to the differing areal averages) is important. Perhaps, if the UWNMS modeled a longer period of time we might see the effect of having more unactivated IN activate, adding to the negative portion of the dipole.

It is unsurprising and reassuring that for all experiments a widespread area of positive vapor change exists. This result supports part of the original hypothesis of this work: when IN activate and compete for water vapor with other ice nucleation mechanisms, smaller and more numerous ice crystals will result. The change in particle size will not necessarily change the ice mass mixing ratio at a gridpoint however, unless the ice in a certain area is *only* formed by IN with no competing nucleation mechanisms. When particle sizes are decreased, those ice particles are more likely to be held aloft longer, and possibly transported upward to drier altitudes and evaporate. The patterns in Figures 6.11 and 6.15 – 6.18 indicate this hydrating effect of IN at upper levels occurs readily in cloudy areas where vertical motion is positive—forming the positive portion of the dipole.

The formation of the dipole is constrained by height and mesoscale dynamics. The dipole (or even the area of positive vapor change) forms only at high altitudes because the effects of IN will be strongest where there are fewer ice nucleation mechanisms competing with the IN for vapor. Given the activation thresholds of temperature and moisture, our IN will have the greatest impact at higher, drier altitudes. The timing of dipole formation is controlled by cloud formation—remember from Chapter 4 that convective activity peaks in the late afternoon, and 3 pm local time on September 27th corresponds to 42 hours into the experiments—as convection intensifies and air moves upward, the positive (lower) part of the dipole forms, and IN and IN-influenced air move upward further to altitudes where small changes in vertical velocity can make an impact (the upper, negative part of the dipole). Convective transport of IN and moisture produces widespread activation near this time, as seen, for example, in Figure 5.1, which shows a dramatic increase in IN activation as well as an upward spread of IN-influenced air. And as we will see in detail in Chapter 8, the effects of IN take time to accumulate, especially since environmental conditions (such as a limit on available water vapor) prohibit massive amounts of ice nucleation by IN at any one time.

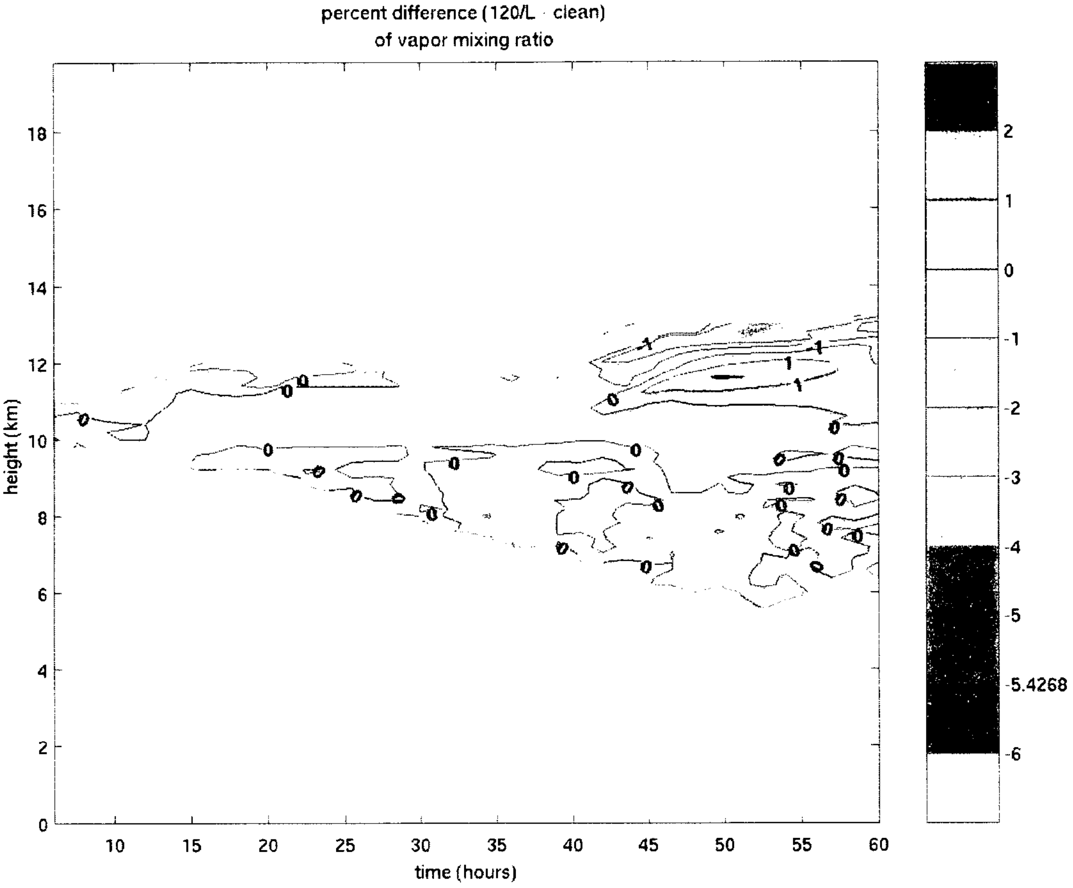

Figure 6.1. The percent difference of vapor mixing ratio when 120 IN/L are initialized into the UWNMS at 250 hPa. Data shown here are averaged over IN-influenced gridpoints only. The dipole in vapor starts near 42 hours (9 pm locally on September 27th), and dissipates near 57 hours (6 am locally on the 28th) in the upper half of the envelope.

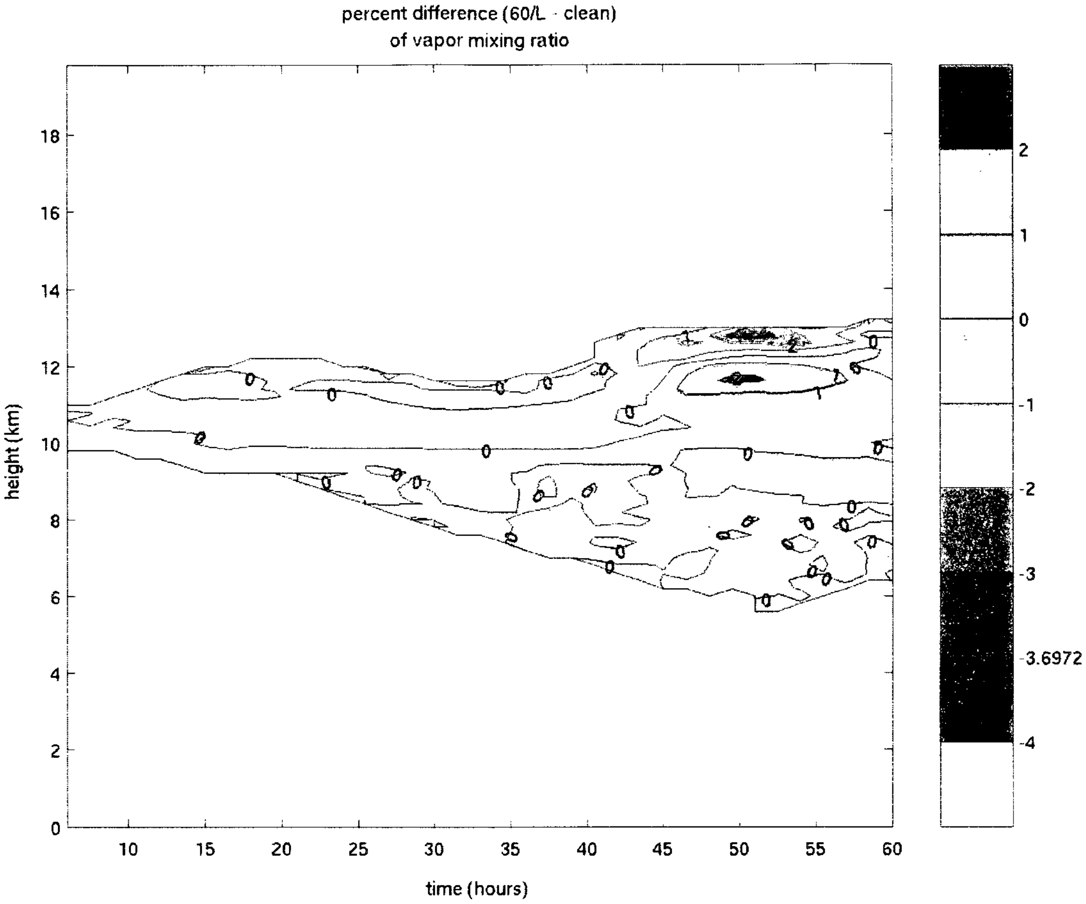

Figure 6.2. The percent difference of vapor mixing ratio when 60 IN/L are initialized into the UWNMS at 250 hPa. Data shown here are averaged over IN-influenced gridpoints only. The dipole in vapor starts just before 45 hours (6 pm locally on September 27th), and dissipates near 57 hours (6 am locally on the 28th) in the upper half of the envelope.

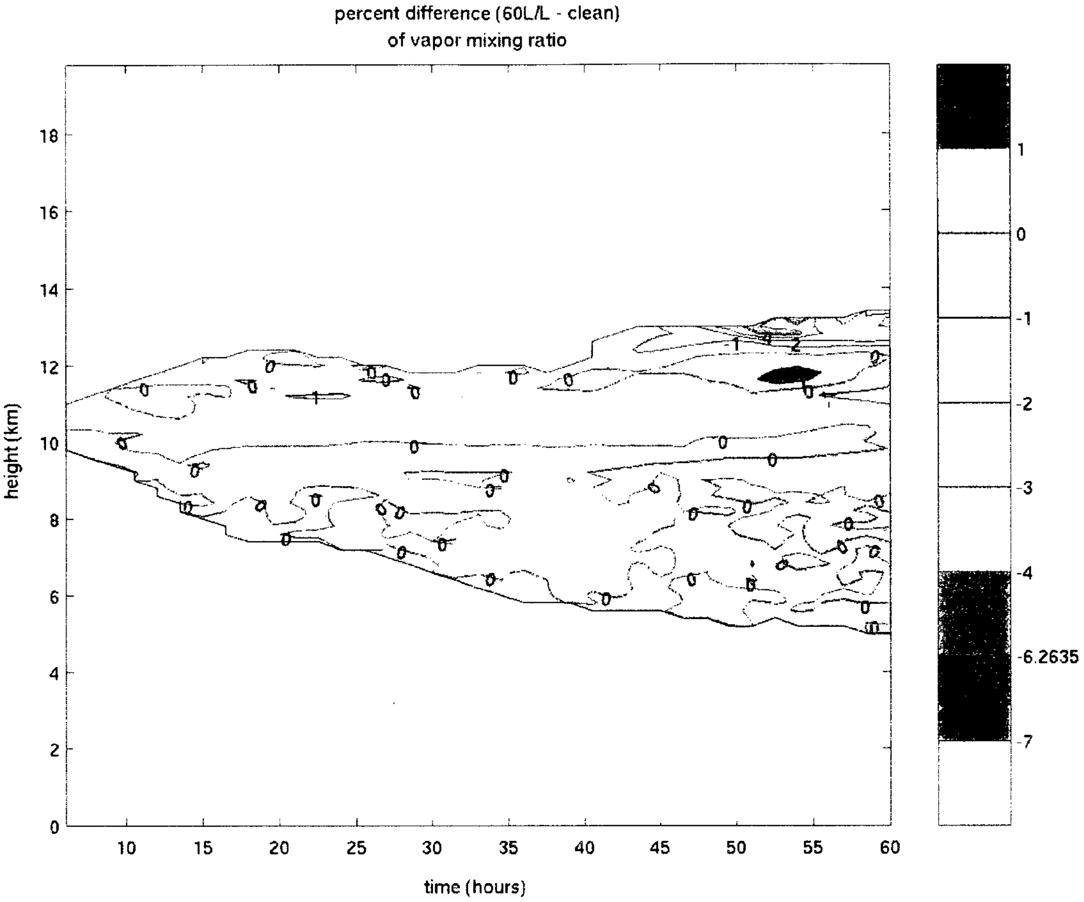

Figure 6.3. The percent difference of vapor mixing ratio when 60 IN/L are initialized into the UWNMS at 300 hPa. Data shown here are averaged over IN-influenced gridpoints only. The dipole in vapor starts near 52 hours (1 am locally on September 28th), and dissipates near 55 hours (4 am locally on the 28th) in the upper half of the envelope.

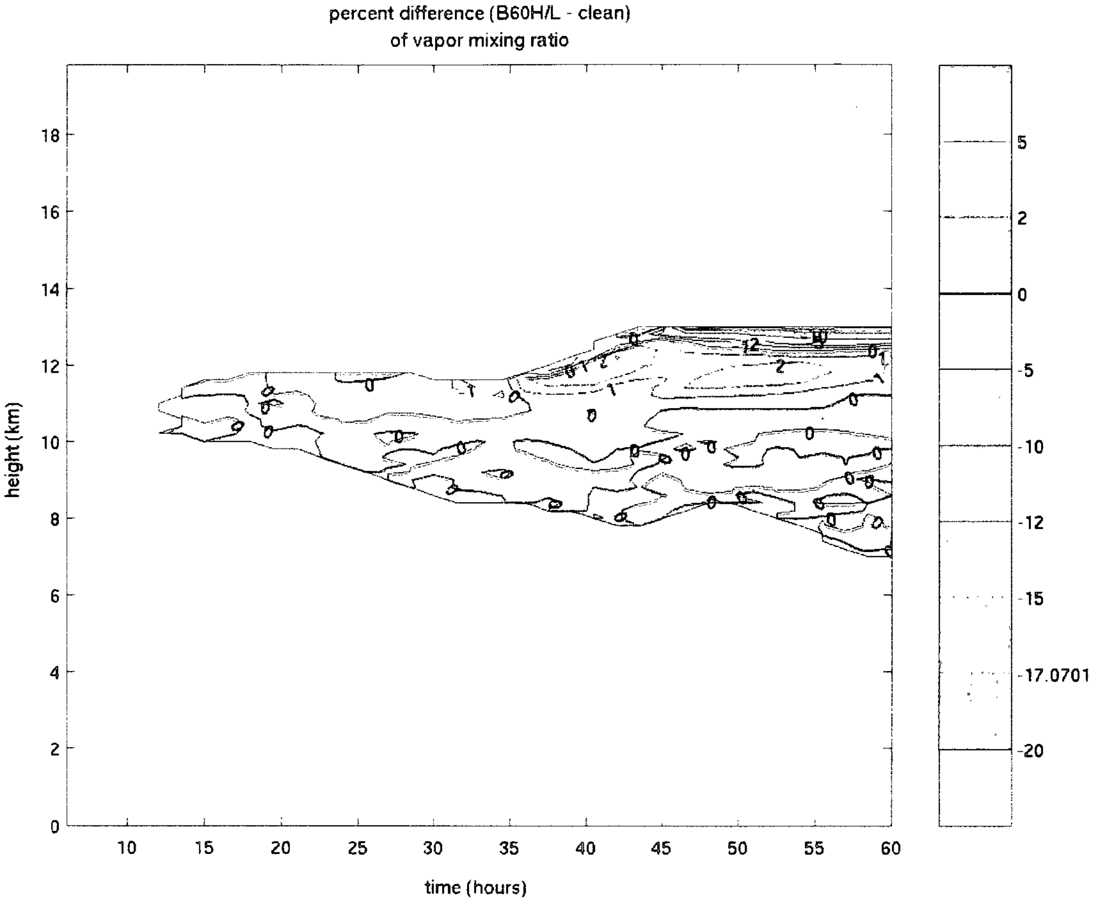

Figure 6.4. The percent difference of vapor mixing ratio when 60 IN/L are initialized into the UWNMS at 200 hPa. Data shown here are averaged over IN-influenced gridpoints only. The dipole in vapor starts just before 45 hours (6pm locally on September 27th), and dissipates near the end of the model run (60 hours or 9 am locally on the 28th) in the upper half of the envelope.

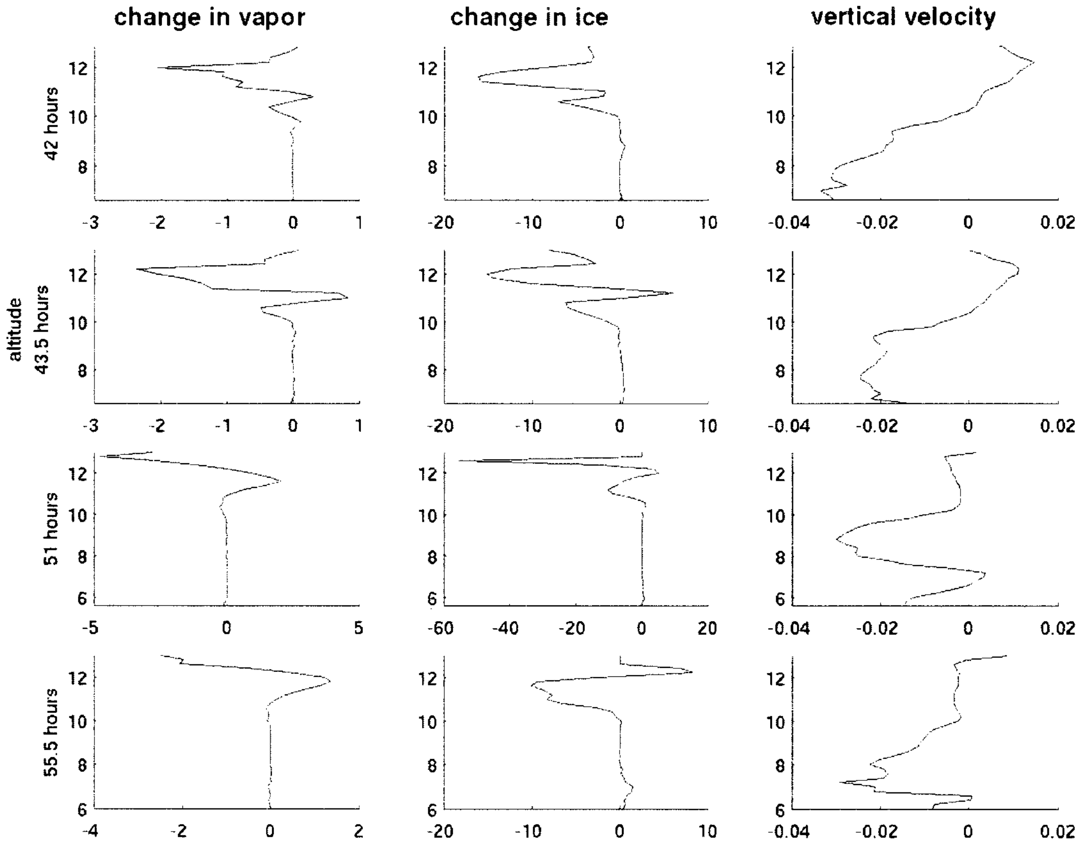

Figure 6.5, showing the evolution (time increases downward in the rows) of the dipole feature that exists above 10 km when 120 IN/L are initialized into the UWNMS at 250 hPa. The dipole starts in a layer of rising air near 42 hours (top row) and dissipates after 55.5 hours (bottom row) as the air begins to descend. From left to right: the percent change in vapor mass mixing ratio, the percent change in pristine ice mass mixing ratio, and vertical velocity. Data plotted are an average of IN-influenced air only.

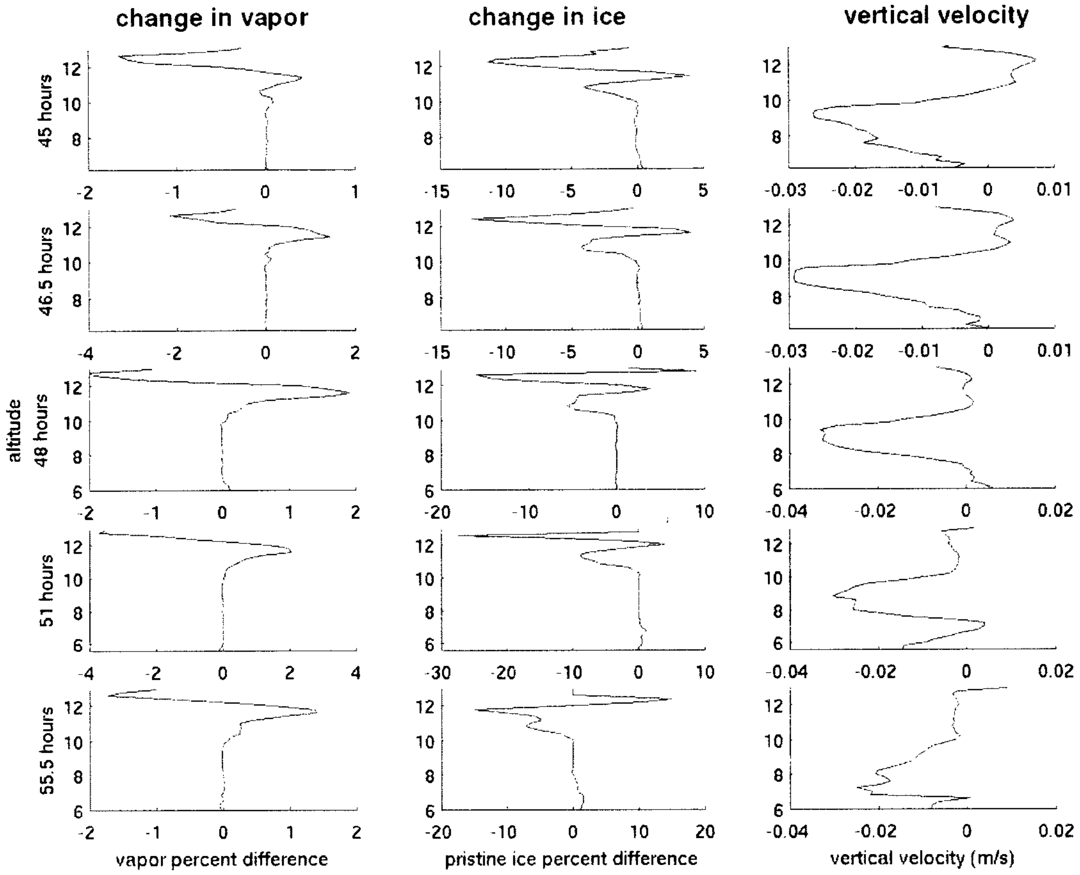

Figure 6.6, showing the evolution (time increases downward in the rows) of the dipole feature that exists above 10 km when 60 IN/L are initialized into the UWNMS at 250 hPa. The dipole starts in a layer of rising air near 45 hours (top row) and dissipates after 55.5 hours (bottom row) as the air begins to descend. From left to right: the percent change in vapor mass mixing ratio, the percent change in pristine ice mass mixing ratio, and vertical velocity. Data plotted are an average of IN-influenced air only.

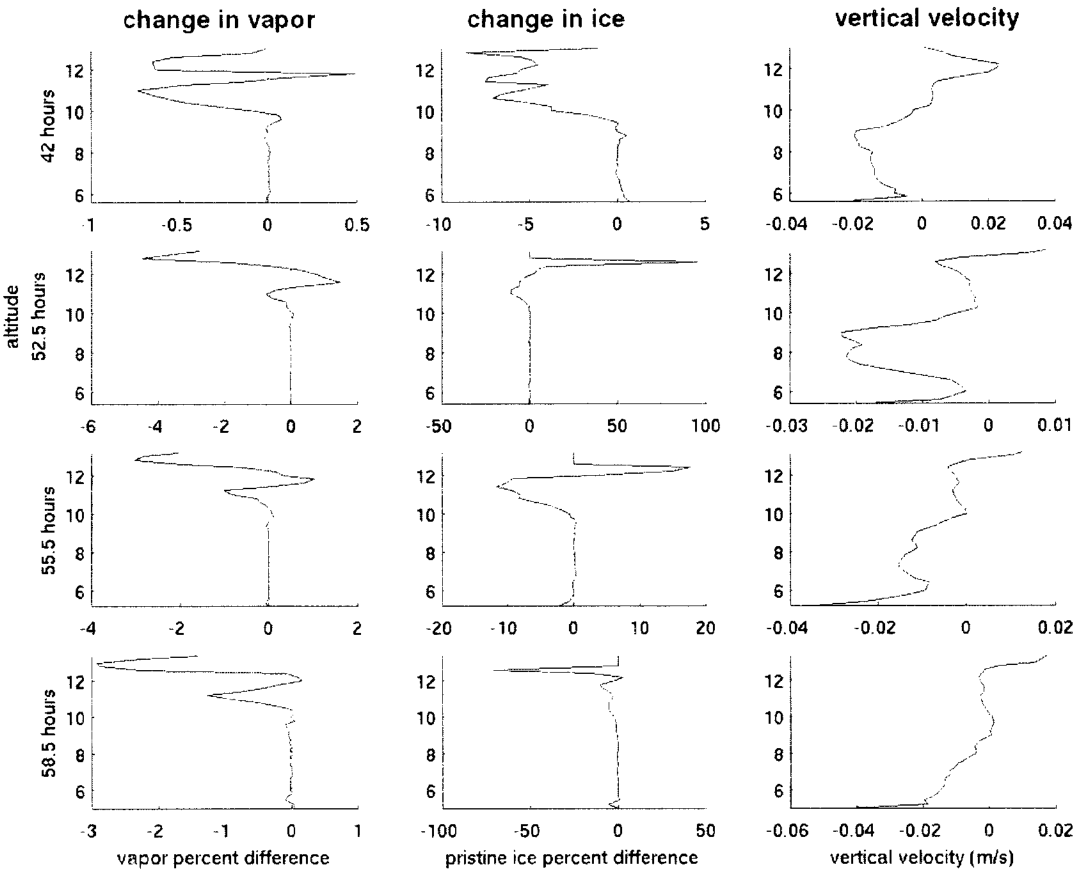

Figure 6.7, showing the evolution (time increases downward in the rows) of the dipole feature that exists above 10 km when 60 IN/L are initialized into the UWNMS at 300 hPa. The dipole starts in a layer of rising air near 52.5 hours (top row) and dissipates after 55.5 hours (bottom row) as the air begins to descend. From left to right: the percent change in vapor mass mixing ratio, the percent change in pristine ice mass mixing ratio, and vertical velocity. Data plotted are an average of IN-influenced air only.

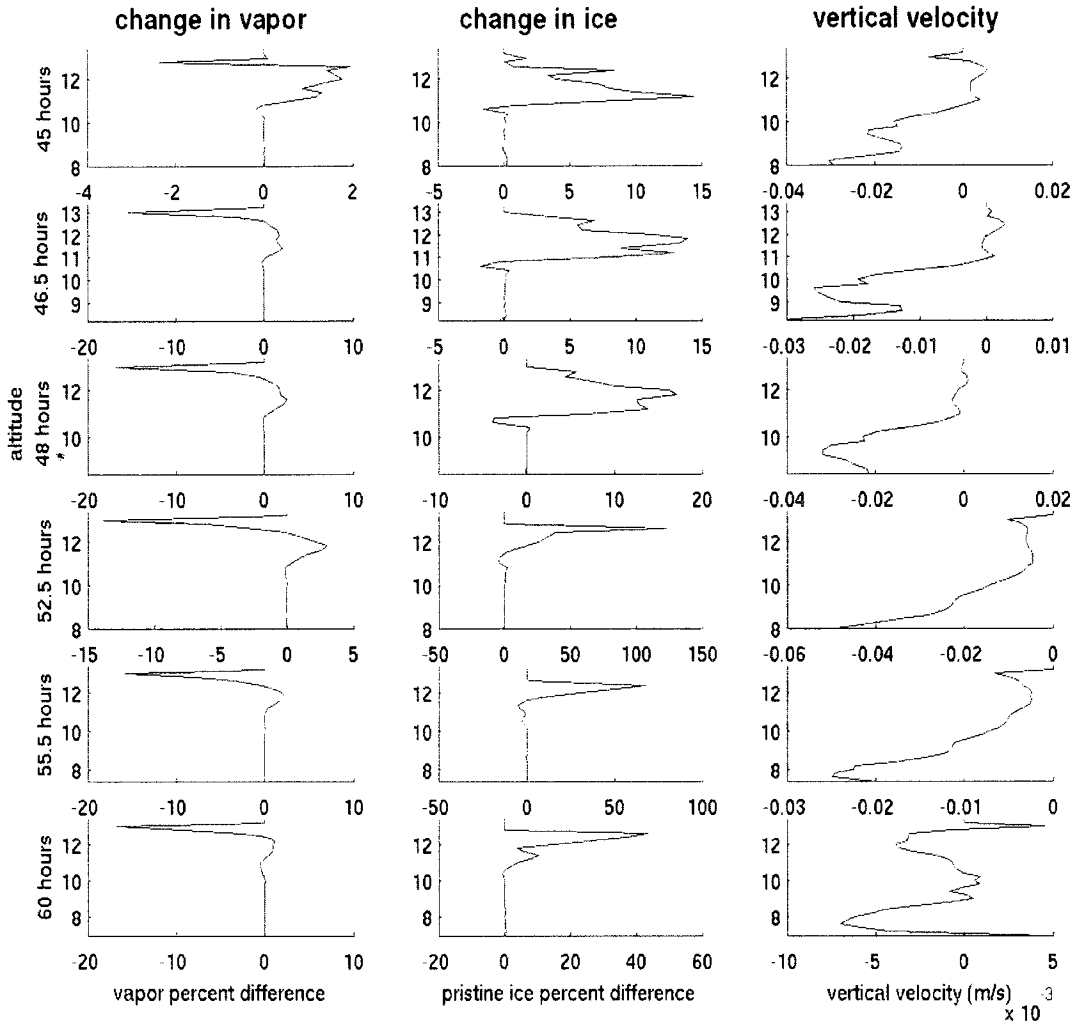

Figure 6.8, showing the evolution (time increases downward in the rows) of the dipole feature that exists above 10 km when 60 IN/L are initialized into the UWNMS at 200 hPa. The dipole starts in a layer of rising air near 45 hours (top row) and is maintained through 60 hours (bottom row) even as the air begins to descend. From left to right: the percent change in vapor mass mixing ratio, the percent change in pristine ice mass mixing ratio, and vertical velocity. Data plotted are an average of IN-influenced air only.

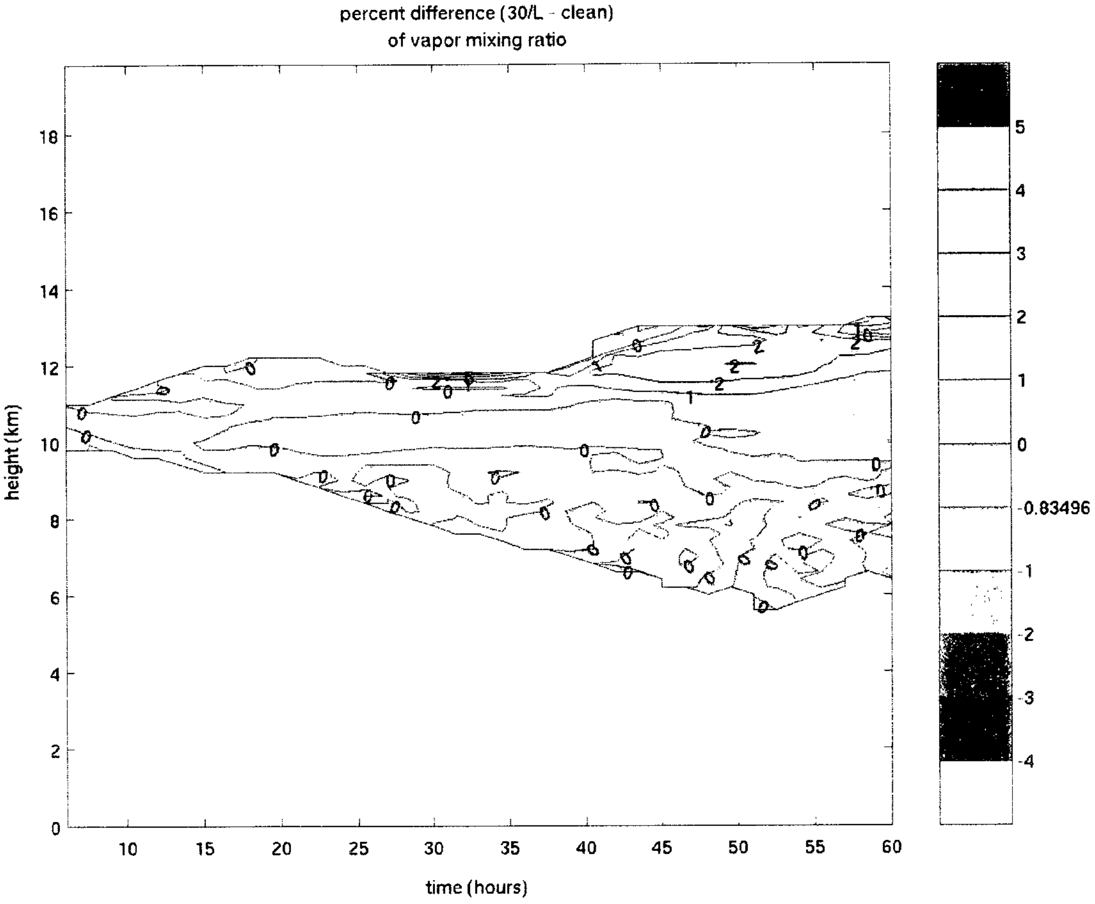

Figure 6.9. The percent difference of vapor mixing ratio when 30 IN/L are initialized into the UWNMS at 250 hPa. Data shown here are averaged over IN-influenced gridpoints only.

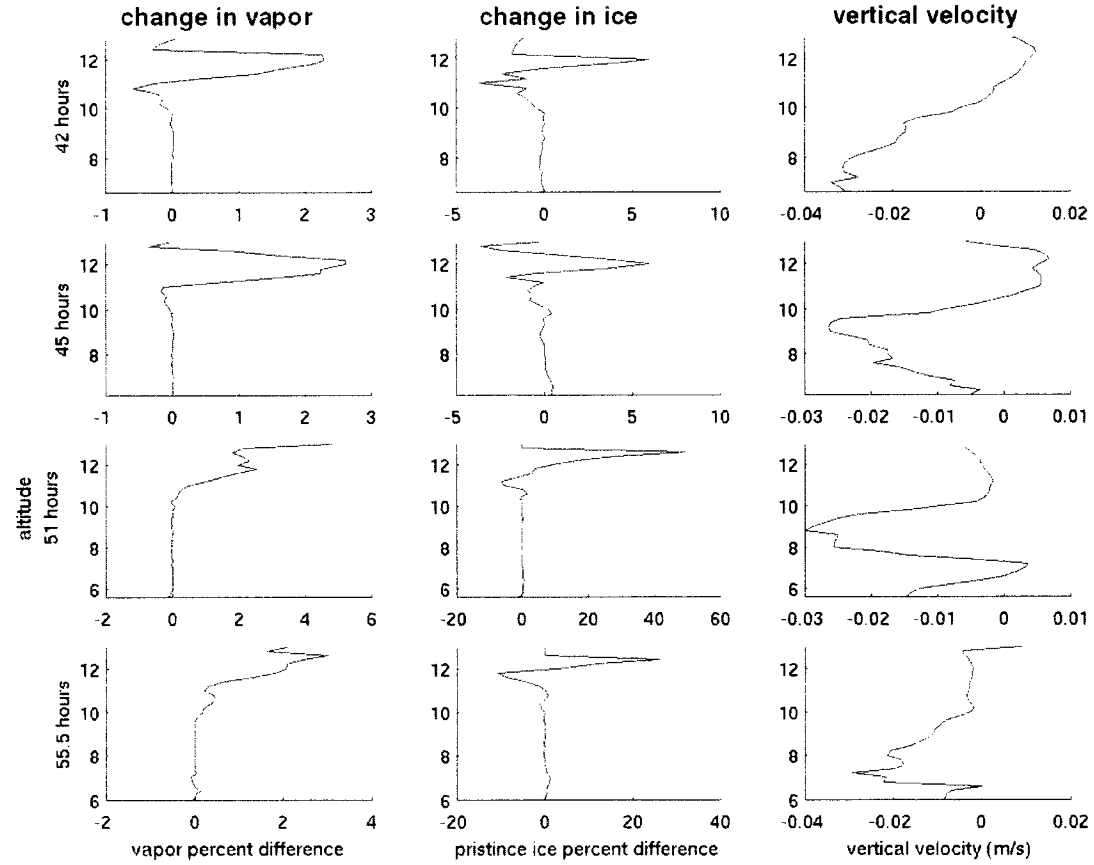

Figure 6.10, showing a time series of "no dipole" data –when 30 IN/L are initialized into the UWNMS at 250 hPa-- to compare with the dipoles seen in Figures 6.5 – 6.9. From left to right: the percent change in vapor mass mixing ratio, the percent change in pristine ice mass mixing ratio, and vertical velocity. Data plotted are an average of IN-influenced air only.

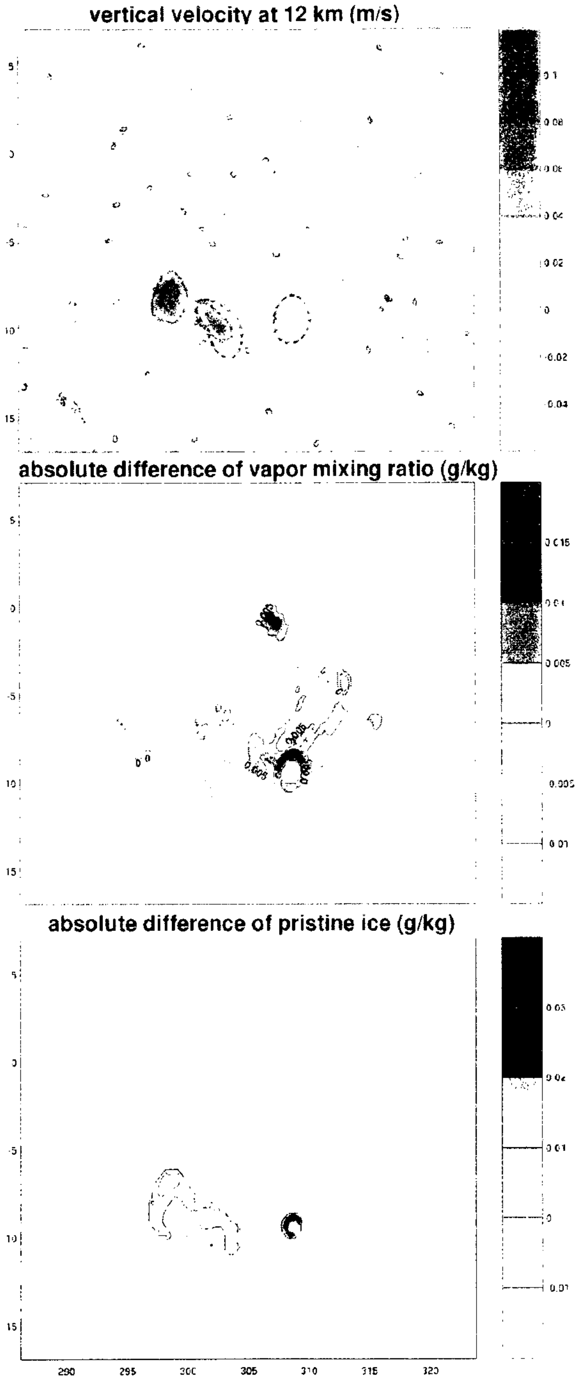

Figure 6.11. Data from 42 hours into the UWNMS run with 30 IN/L initialized at 250 hPa: vertical velocity, the absolute change in vapor mixing ratio, and the absolute change in pristine ice mixing ratio at 12 km. Areas of IN influence are bounded by red dashed lines. The area of IN-influenced air has a higher vapor mixing ratio where the vertical velocity is weakly positive. Some of this "extra" moisture is used in the formation of pristine ice. The (leftmost) area of IN-influenced air with a stronger upward vertical velocity has changes in pristine ice that are explained below in Figure 6.14.

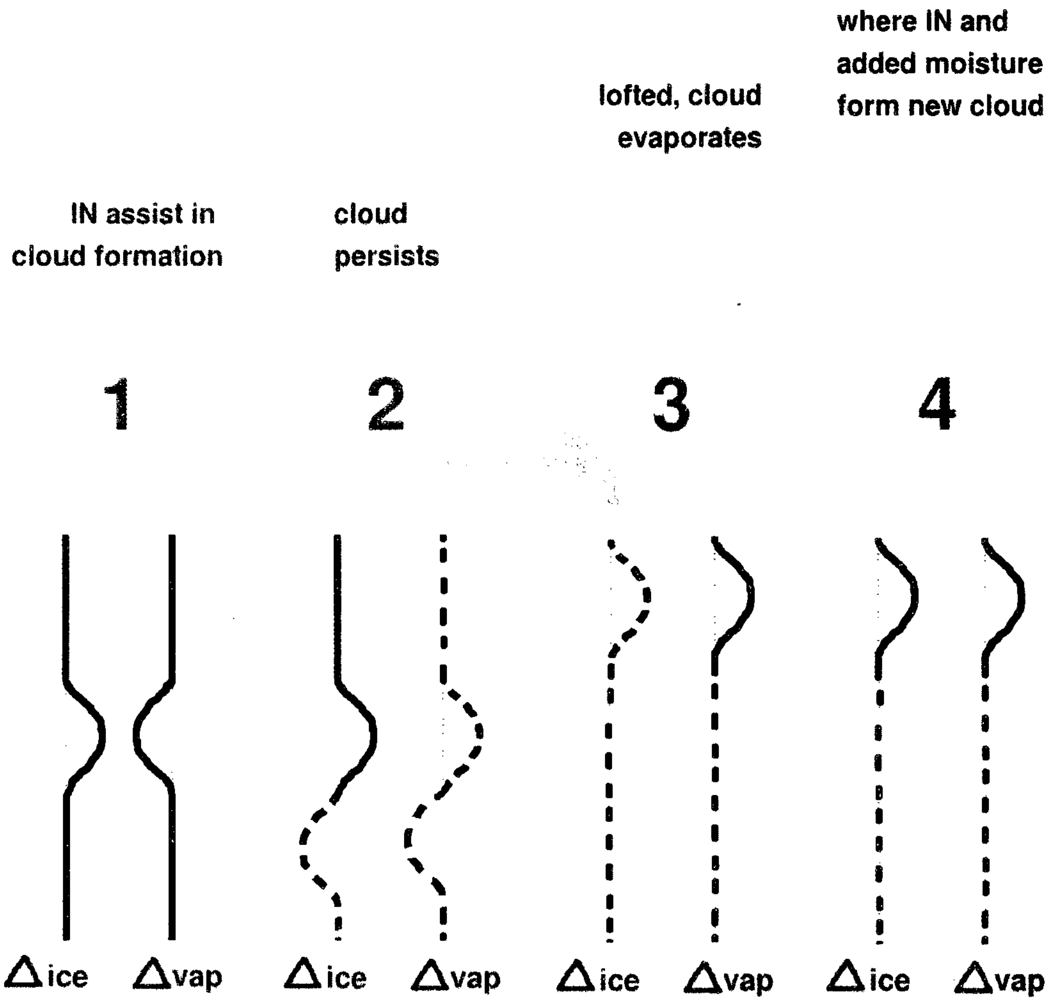

Figure 6.12. How areas of IN-influence aloft can become positive--step 1: IN enhance cloud formation, resulting in an increase in pristine ice and a corresponding decrease in vapor. This cloud may persist (step 2) because of the indirect aerosol effect, and in turn reduce precipitation—less vapor and ice at lower levels. If the air rises, the remaining cloud particles are likely to evaporate into the colder, drier air —step 3. This moistens the air above, and, if IN are present, a new cloud can form or be otherwise influenced by IN activation (step 4). Dashed lines in the idealized plots of the change in vapor and ice represent *possible* or uncertain effects. Step 4 is seen exactly in Figure 6.11, step 2 is seen below in Figure 6.13.

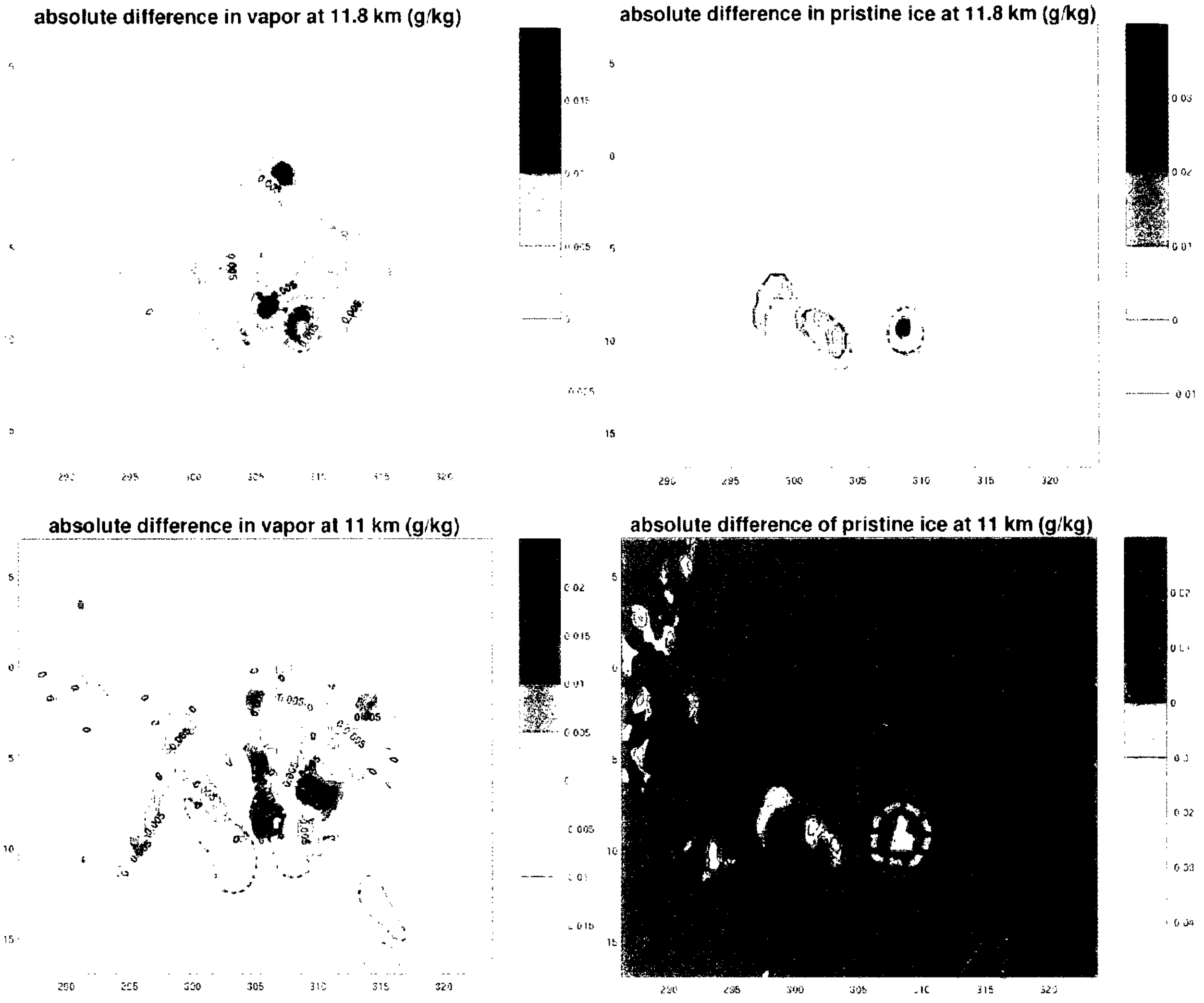

absolute difference in vapor at 11.8 km (g/kg)

absolute difference in pristine ice at 11.8 km (g/kg)

absolute difference in vapor at 11 km (g/kg)

absolute difference of pristine ice at 11 km (g/kg)

Figure 6.13. Vapor (left) and pristine ice (right) mass mixing ratios at 11.8 km (top) and 11 km (bottom), 40.5 hours into the model run with 30 IN/L. At 11.8 km, the rightmost (green-circled) area of IN-influence shows a growing/persistent area of pristine ice. With smaller particle sizes, the ice particles are less likely to precipitate (quickly if at all), and vapor and pristine ice are reduced below, at 11 km. This corresponds to step 2 in Figure 6.12.

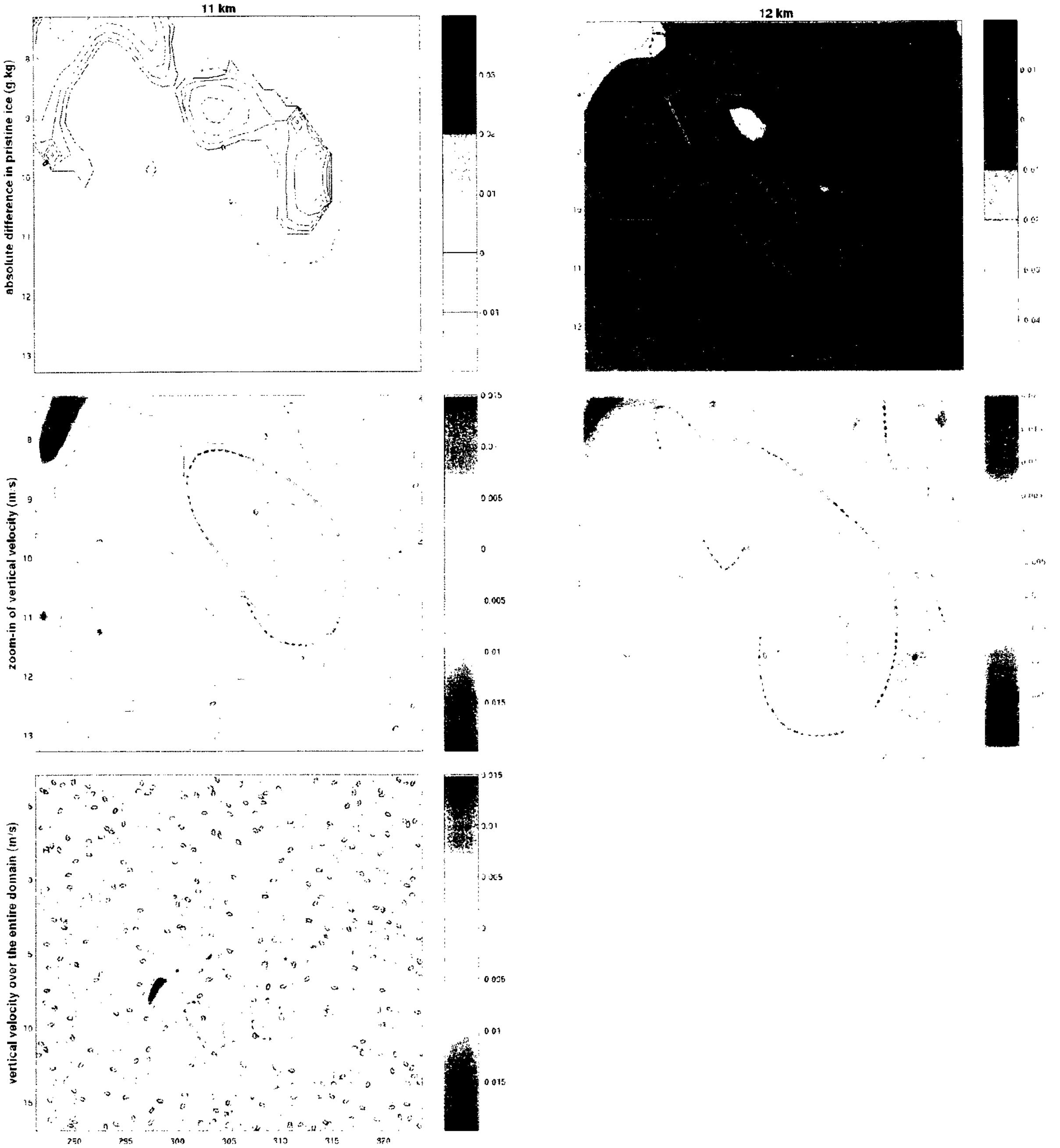

Figure 6.14. The introduction of IN produces changes in vertical velocity (mostly < 1 cm/s), and, as seen in the bottom row, these changes appear to be random. The bottom row shows the whole domain, the top two rows "zoom in" on areas of IN-influence, enclosed by red dashed contours. The (noisy) changes in vertical velocity correlate very strongly with changes in pristine ice, seen in the top two rows –for the experiment with 30 IN/L, at 42 hours-- at left, 11 km, and at right, 12 km. Absolute difference in pristine ice is also contoured at -0.005, -0.0025, and -0.001 g/kg. A slight decrease in vertical velocity can mean that ice is not as well suspended, it may fall and decrease compared to the experiment with no IN. Conversely an increase in vertical velocity can increase in pristine ice, as it is better suspended.

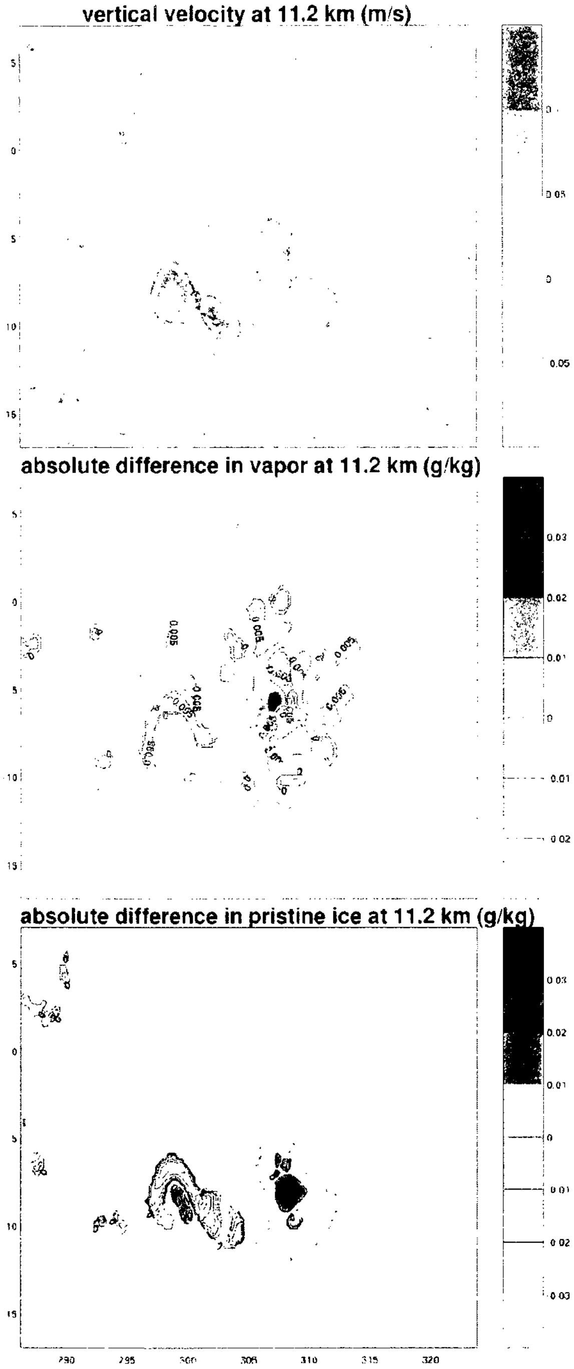

Figure 6.15. When 120 IN/L are initialized into the UWNMS at 250 hPa, a dipole forms in the vapor change plots, with an average positive change below and average negative change above about 12 km. The data shown are from 11.2 km, at the highest-altitude positive portion of the dipole at 43.5 hours. Areas of IN-activation influenced air are enclosed by the red dashed contours. Like the positive change in vapor seen at 42 hours in the 30 IN/L experiment, an increase in vapor causes a change in pristine ice, the increase in vapor likely caused by the process depicted in Figure 6.12.

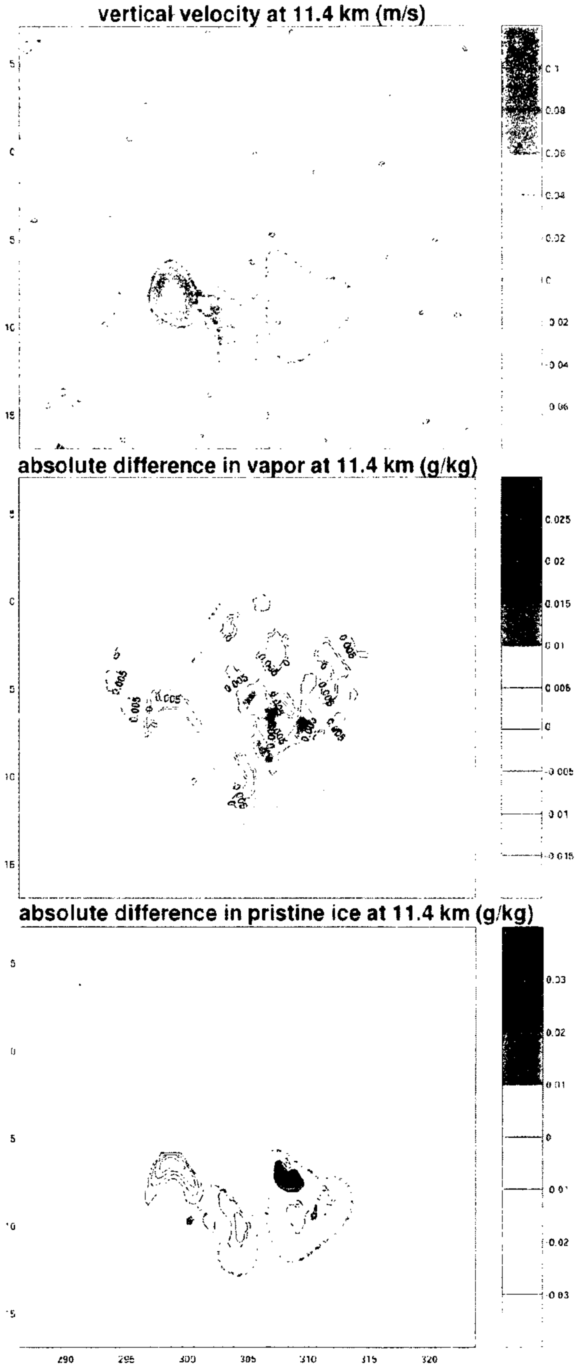
vertical velocity at 11.4 km (m/s)

absolute difference in vapor at 11.4 km (g/kg)

absolute difference in pristine ice at 11.4 km (g/kg)

Figure 6.16. When 60 IN/L are initialized into the UWNMS at 250 hPa, a dipole forms in the vapor change plots, with an average positive change below and average negative change above about 12 km. The data shown are from 11.4 km, within the positive portion of the dipole at 45 hours. Areas of IN-activation influenced air are enclosed by the red dashed contours. Like the positive change in vapor seen at 42 hours in the 30 IN/L experiment, an increase in vapor causes an increase in pristine ice, the increase in vapor likely caused by the process depicted in Figure 6.12.

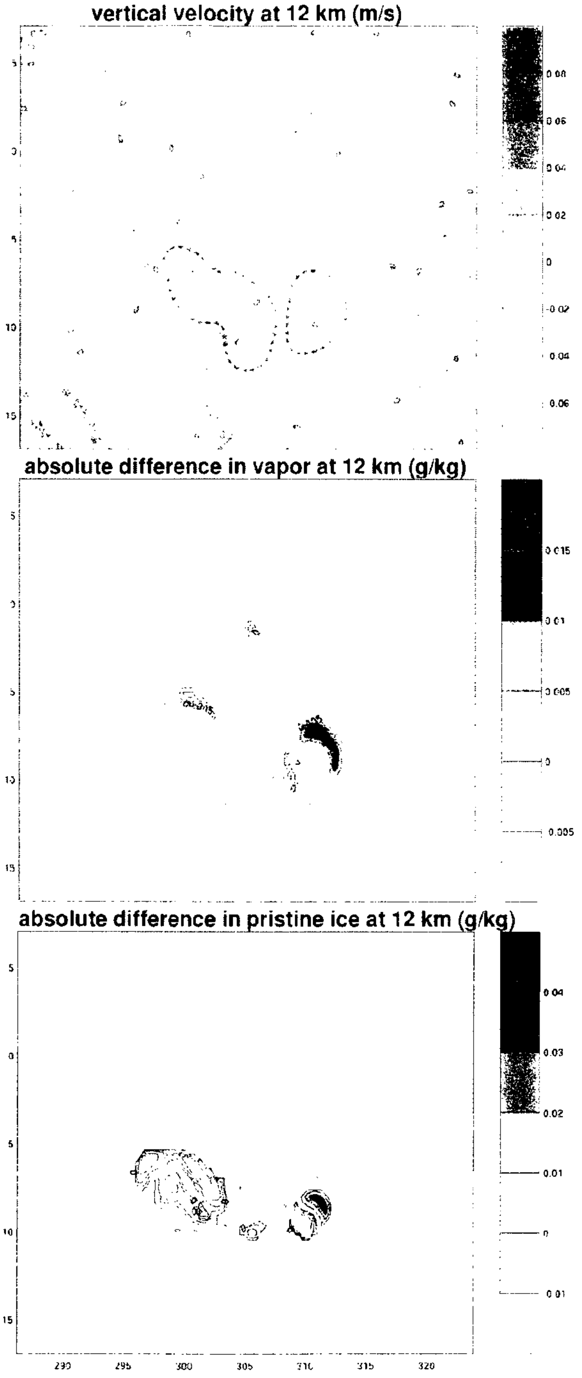

vertical velocity at 12 km (m/s)

absolute difference in vapor at 12 km (g/kg)

absolute difference in pristine ice at 12 km (g/kg)

Figure 6.17. When 60 IN/L are initialized at 300 hPa, a dipole forms with positive changes below and negative changes above about 12 km. These data are from 12 km, at the highest-altitude positive portion of the dipole at 52.5 hours. Areas of IN influence are enclosed by red dashed contours. An increase in vapor causes an increase in pristine ice, the increase in vapor likely caused by the process depicted in Figure 6.12. Unlike the dipoles that form in the 120 and 60 IN/L experiments, the sign of the average pristine ice is not the same as the sign of the vapor change.

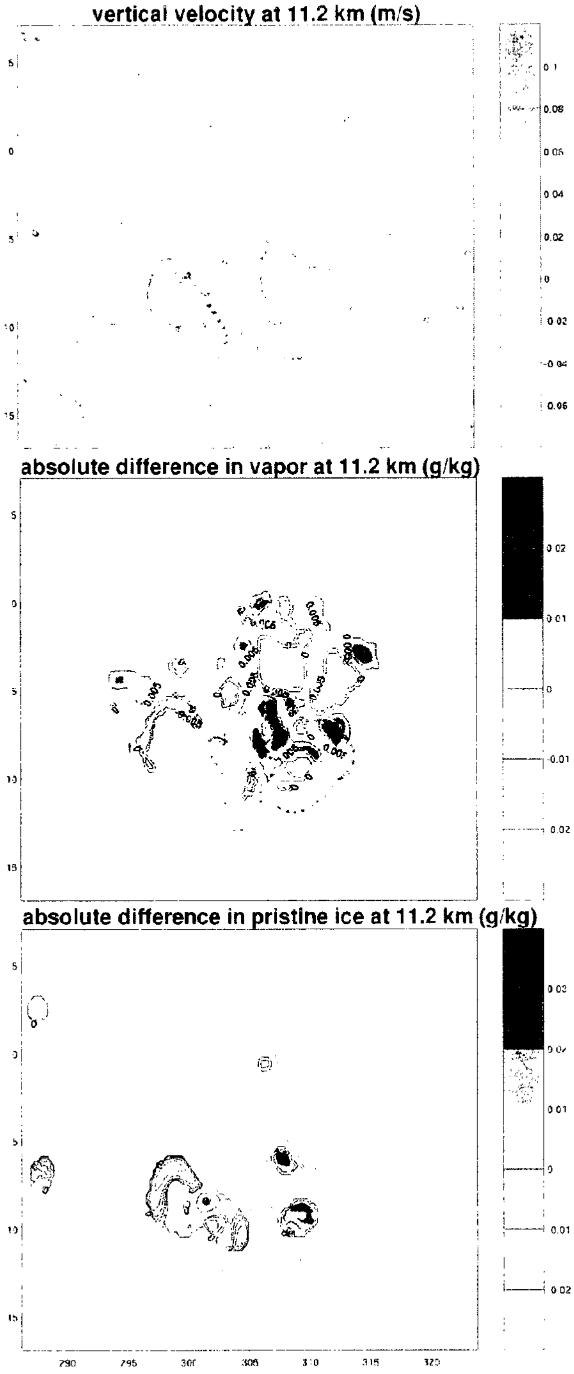

vertical velocity at 11.2 km (m/s)

absolute difference in vapor at 11.2 km (g/kg)

absolute difference in pristine ice at 11.2 km (g/kg)

Figure 6.18. When 60 IN/L are initialized into the UWNMS at 200 hPa, a dipole forms in the vapor change plots, with an average positive change below and average negative change above about 12.5 km. The data shown are from 11.2 km, within the positive portion of the dipole at 45 hours. Areas of IN-activation influenced air are enclosed by the red dashed contours. Like the positive change in vapor seen at 42 hours in the 30 IN/L experiment, an increase in vapor causes an increase in pristine ice, the increase in vapor likely caused by the process depicted in Figure 6.12.

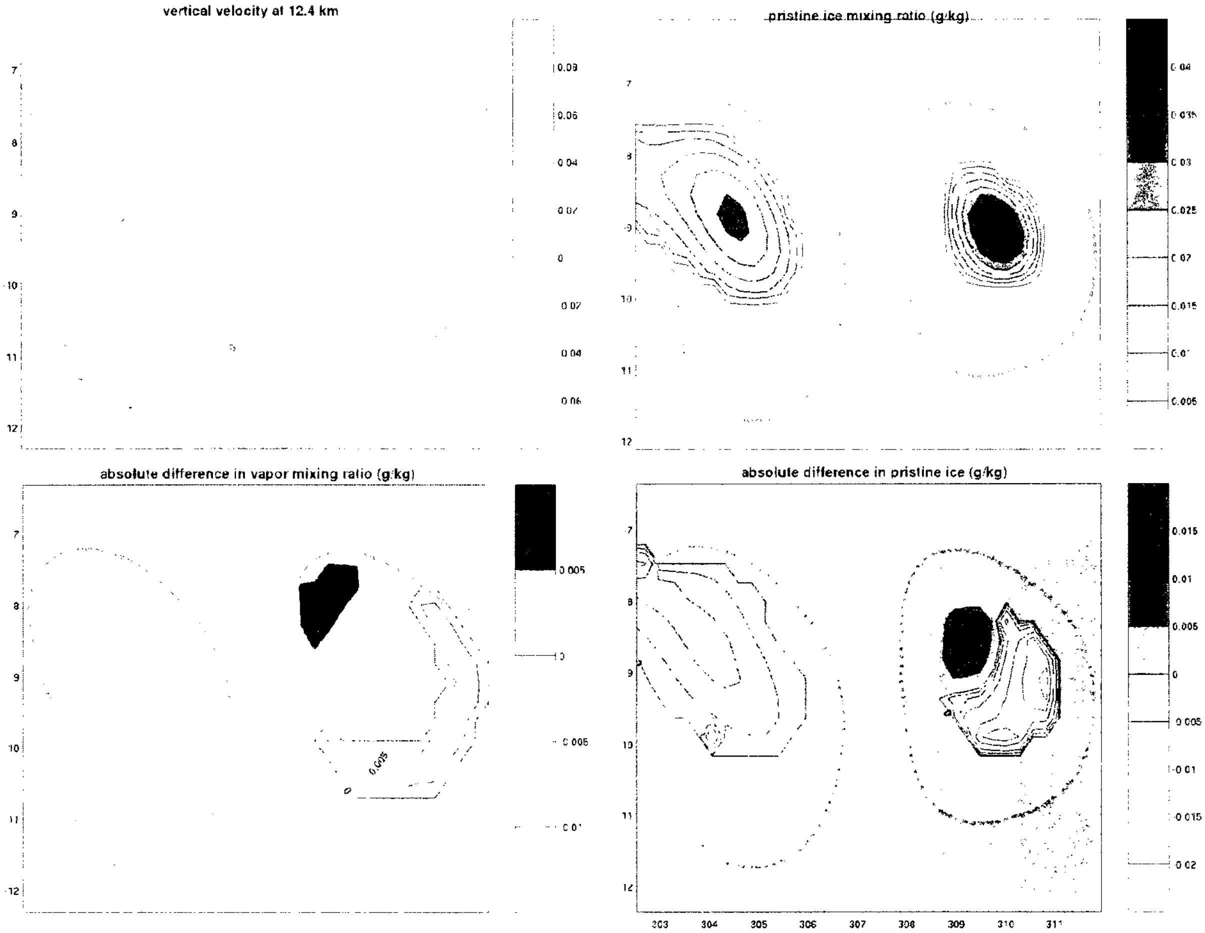

Figure 6.19. When 120 IN/L are initialized into the UWNMS, the most negative part of the dipole in vapor-change occurs at 51 hours and 12.4 km. The top row shows vertical velocity and pristine ice mass mixing ratio, the bottom row shows how vapor (bottom left) and ice (bottom right) have changed in the presence of IN. Absolute difference in pristine ice is also contoured at -0.005, -0.0025, and -0.001 g/kg. The combination of decreased vertical velocity and decreased pristine ice likely increased entrainment and loss of vapor from this level.

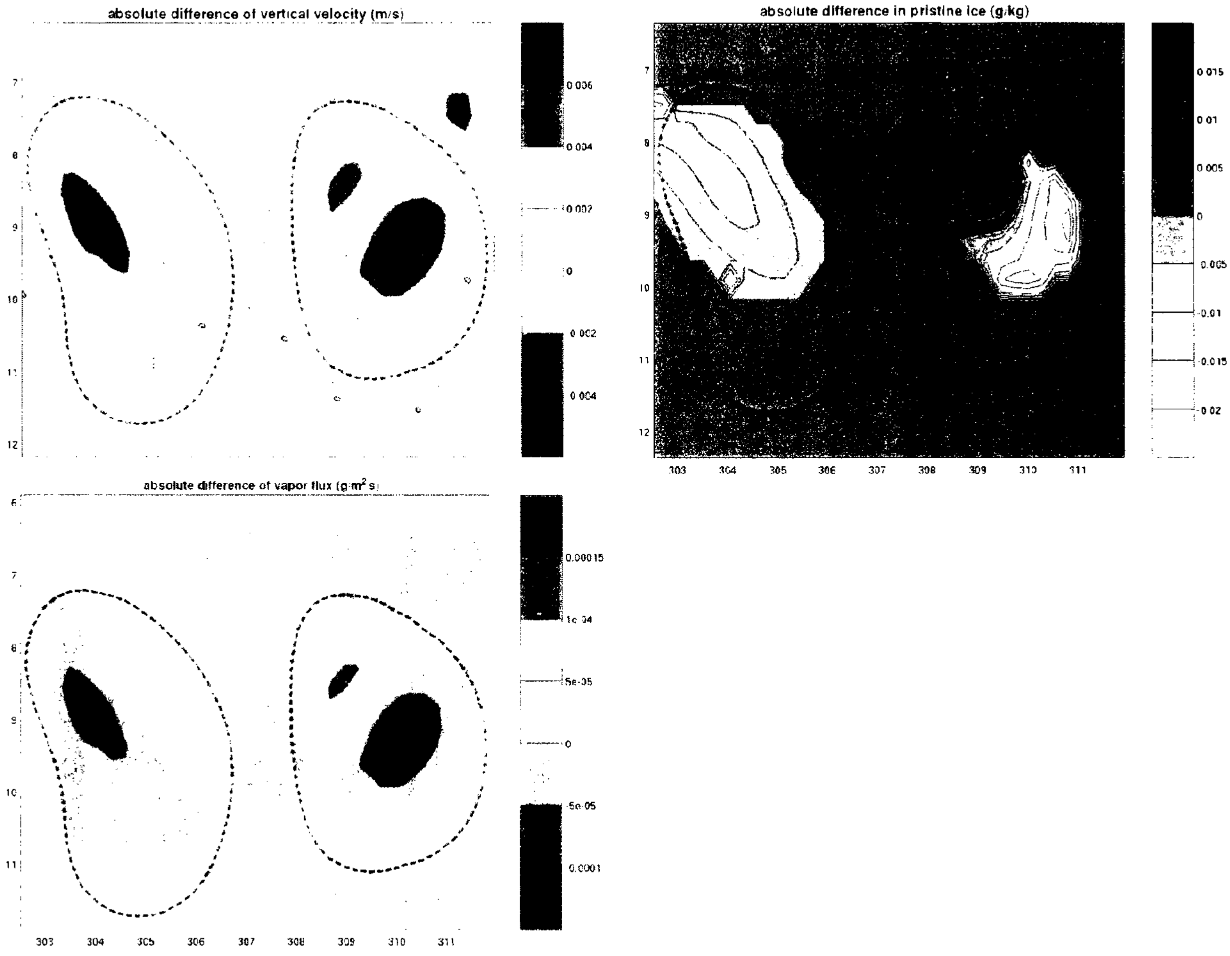

Figure 6.20. When 120 IN/L are initialized into the UWNMS, the most negative part of the dipole in vapor-change occurs at 51 hours and 12.4 km. The top row shows the change in vertical velocity (top left) and change in pristine ice mass mixing ratio (top right), the bottom row shows how the vapor flux has changed in the presence of IN, all data from 12.4 km. Absolute difference in pristine ice is also contoured at -0.005, -0.0025, and -0.001 g/kg. The noisy changes in vertical velocity are very likely to be the cause of the patterns of change in ice and vapor at this altitude, as the changes in velocity correspond to an equatorward shift in cloud position.

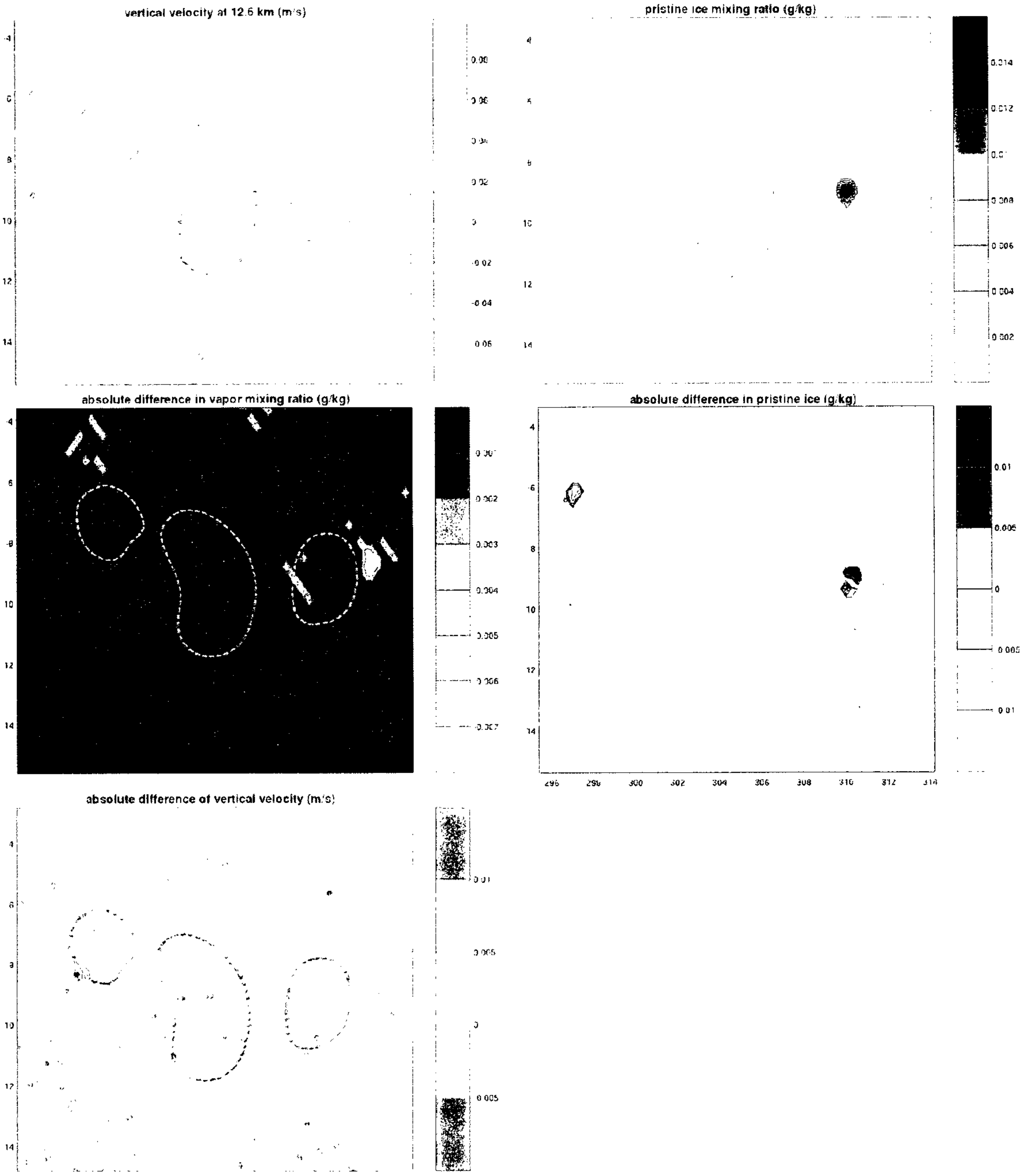

Figure 6.21. When 60 IN/L are initialized into the UWNMS at 300 hPa, the most negative part of the dipole in vapor-change occurs at 52.5 hours and 12.6 km. The top row shows vertical velocity and pristine ice mass mixing ratio, the bottom two rows show how those fields have changed in the presence of IN, along with the change in vapor. Absolute difference in pristine ice is also contoured at -0.005, -0.0025, and -0.001 g/kg. The noisy changes in vertical velocity are very likely to be the cause of the patterns of change in ice and vapor at this altitude, as the changes in velocity correspond to a slight northeastward shift in cloud position.

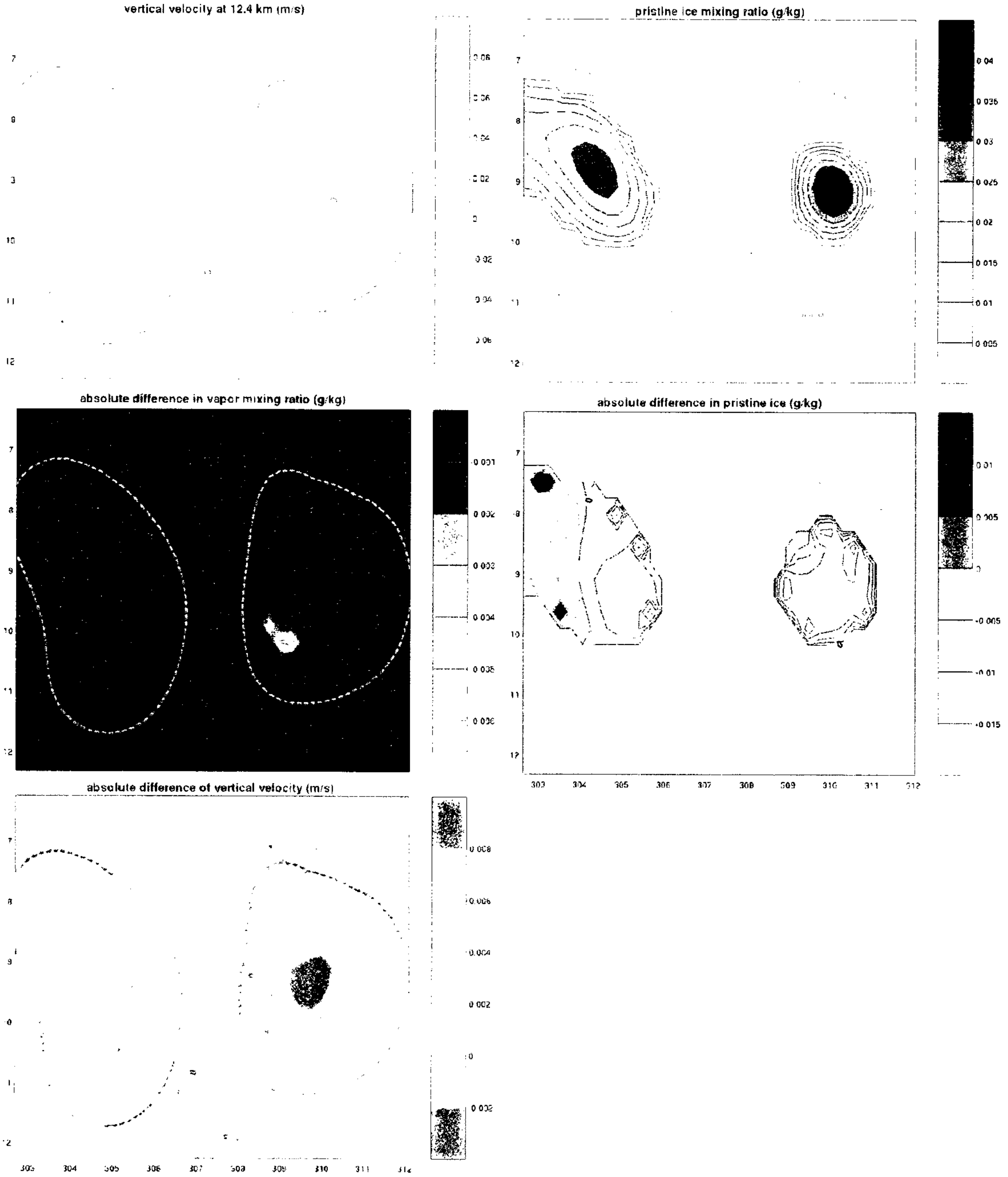

Figure 6.22. When 60 IN/L are initialized into the UWNMS at 250 hPa, the most negative part of the dipole in vapor-change occurs at 51 hours and 12.4 km. The top row shows vertical velocity and pristine ice mass mixing ratio, the bottom two rows show how those fields have changed in the presence of IN, along with the change in vapor. Absolute difference in pristine ice is also contoured at -0.005, -0.0025, and -0.001 g/kg. The noisy changes in vertical velocity are very likely to be the cause of the patterns of change in ice and vapor at this altitude.

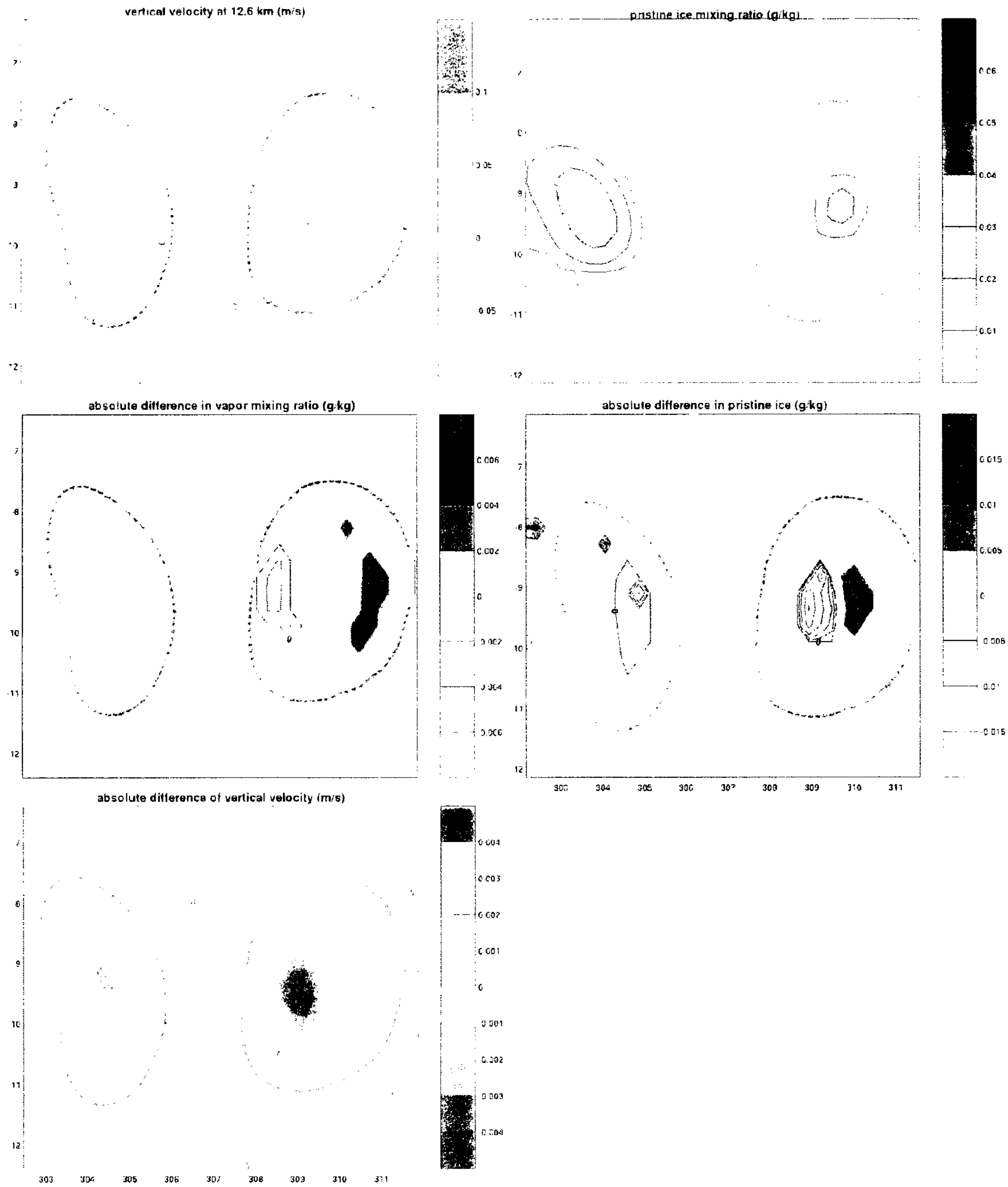

Figure 6.23. When 60 IN/L are initialized into the UWNMS at 200 hPa, the most negative part of the dipole in vapor-change occurs at 48 hours and 12.6 km. The top row shows vertical velocity and pristine ice mass mixing ratio, the bottom two rows show how those fields have changed in the presence of IN, along with the change in vapor. Absolute difference in pristine ice is also contoured at -0.005, -0.0025, and -0.001 g/kg. The noisy changes in vertical velocity are very likely to be the cause of the patterns of change in ice and vapor at this altitude, as the changes in velocity correspond to a slight eastward shift in cloud position.

Chapter 7: Surprisingly Negative Areas

In addition to the dipole-like feature visible in plots of vapor change, the percentage of IN-activation-influenced gridpoints that show a negative change in vapor and/or pristine ice is also surprising and warrants exploration. For example, Figures 5.3 through 5.8 show that the number of IN-influenced gridpoints with negative changes in either pristine ice or vapor increases as the concentration of IN increases from 30 to 120 IN/L. In some experiments, such as the experiment with 120 IN/L initialized at 250 hPa, negative changes in both ice and vapor are coincident. Why can the area of IN-influence be negative overall, and how can negative changes in ice be coincident with negative changes in vapor? The reason for coincident negative changes in vapor and ice (often seen above 10 km), and it's analogue—why there are coincident positive changes in both, seen often below 10 km is (almost deceptively) simple: when there is less vapor in an area, any new ice formation or growth will be limited —a negative vapor change can lead to a decrease of pristine ice. Conversely, when there is more vapor (ice) present, there is a greater chance for ice formation (evaporation and increase in vapor).

Regardless of coincident signs of changes in vapor and ice, the changes in ice and vapor are unexpectedly *not* balanced in amount and sign across space. Are the increasingly extensive negative areas a function of IN activation or a function of the dynamics within the areas? This chapter will show that the negativity is a function of both. Dynamical differences among IN-laden experiments are on the order of noise (Figure 7.1, also Appendix C), and the resulting distribution of conditions ripe for IN activation show similarly noisy, small, differences (Figure 7.2). At times these small dynamical differences are enough to make an impact—such as the area of positive change between 30 and 35 hours in the 30 IN/L experiment, discussed in Chapter 5. Though dynamic *differences* play a role in the extent of negative changes in ice and vapor in the experiments, overall dynamics and the differences in the apportionment of IN influence (via IN number, location and/or activation threshold) have the largest effects.

Let's see if we can isolate where the majority of this negativity occurs in time and space. First, space: similar to Figures 5.3 - 5.8, height-averaged changes in vapor and pristine ice were calculated, but divvied up—10 km is an approximate middle height of the envelope of IN-influence, so the number of gridpoints with negative changes were calculated for areas below and above 10 km. Above 10 km, the negative changes in the 120 IN/L experiment are more pervasive than below 10 km: for both vapor and ice more than 60% of the area of IN influence was negative above 10 km, while below 10 km the area was at least 55% positive. The separation is stronger for ice than for vapor. This is interesting. What could it mean? Tables 7.1 and 7.2 give the most frequent sign of change (either positive or negative) and the percentage of IN-influenced area with that sign above and below 10 km for experiments with 60 IN/L initialized at 200 and 250 hPa, 30 IN/L initialized at 250 hPa, 60 IN/L initialized at 300 hPa, and 60 IN/L initialized at 250 hPa with a warm activation temperature (T_{act} = 273 K). The following trends can be seen:

- with lower and more numerous IN initially, negative changes in vapor and pristine ice occur more frequently above 10 km
- conversely, with fewer and higher-altitude initial IN concentrations, changes in vapor and pristine ice are more frequently positive above 10 km
- generally, the areas below 10 km experience more positive changes in both vapor and pristine ice. With a warm activation, however, there are more frequent negative changes in pristine ice than positive changes.

	120 IN/L	***60 IN/L (high alt.)***	***60 IN/L***	***30 IN/L***	***60 IN/L (low alt.)***	***60 IN/L (warm)***	***120 IN/L (low alt., warm)***
above 10 km	negative (68%)	positive (54%)	negative (54%)	positive (67%)	negative (80%)	negative (54%)	
below 10 km	positive (55%)	positive (54%)	positive (60%)	positive (55%)	positive (58%)	positive (52%)	positive (55%)

Table 7.1. The most frequent sign of change in vapor mixing ratio within the area of IN influence, with the percent of area with that sign, over 60 hours of experiment time, for the above-listed experiments, separated by altitude.

	120 IN/L	***60 IN/L (high alt.)***	***60 IN/L***	***30 IN/L***	***60 IN/L (low alt.)***	***60 IN/L (warm)***	***120 IN/L (low alt., warm)***
above 10 km	negative (61%)	positive (51%)	negative (58%)	positive (47%)	negative (61%)	negative (69%)	
below 10 km	positive (69%)	positive (64%)	positive (70%)	positive (63%)	positive (56%)	negative (54%)	negative (53%)

Table 7.2. The most frequent sign of change in pristine ice mixing ratio within the area of IN influence, with the percent of area with that sign, over 60 hours of experiment time, for the above-listed experiments, separated by altitude.

Now, let's look at a temporal distribution of the number of IN-influenced gridpoints with negative changes—Figures 7.3 and 7.4 show the sign of change for the average number of gridpoints per level influenced by IN activation when 120 IN/L are input, for changes in vapor and ice respectively, over the last half of the experiment as well as over the whole experiment (60 hours). The vertical distribution of positive and negative changes in both vapor and ice are similar over both time periods. Most importantly, the averaged number of gridpoints with negative changes appears to accumulate over time, though there are heights with more negative gridpoints in that last part of the experiment (the maximum averaged number of gridpoints with a negative change in ice in the last part of the experiment is more than half the number of the count over the entire experiment, for example).

Investigating the changes over the same times and heights in the 30 IN/L case (Figures 7.5 and 7.6), we see that in this experiment there are more positive changes than negative ones. The number of negatively-influenced gridpoints still appears to accumulate over time, as it does in the 120 IN/L experiment. Remember Figure 5.2—when there are greater numbers of IN (such as 120/L), there will be greater numbers of *unactivated* IN which can act at later times, so the increasing extent of negativity must be a cumulative effect as those "leftover" IN activate later. When only 30 IN/L are input, activation is at the right (lesser) amount for the areas affected to experience fewer negative changes in ice and vapor.

How does IN activation/formation of crystals translate to more gridpoints with negative changes in vapor and ice? With a greater chance for more activation events over time, greater numbers of IN can create more numerous ice crystals. What happens to the crystals, in any experiment, then depends on ambient humidity, which in turn depends on dynamics. Figure 7.7 shows vertical velocity averaged over those gridpoints influenced by IN activation for the experiments with 30, 60, and 120 IN/L initialized at 250 hPa. The average vertical velocity experienced by IN-influenced air is negative (downward)--the multitudinous crystals formed with IN activation appear to be precipitated more often than lofted. This is unsurprising: vertical motions in the free troposphere (between about 4 and 14 km in the tropics) are downward, averaging on the order of 1 cm/s (Gage et al., 1991). The result of this is a decrease in vapor and ice aloft (at altitudes wherever the majority of the IN population exists) and an increase in ice below.

The more IN exist, the more vapor concentrations can be chipped away by IN activation, and the more ice concentrations aloft will be lessened with time when IN-formed ice falls, removing vapor from layers of air, serein-like, where it might remain otherwise. With fewer IN present (the 30 IN/L experiment), there would be fewer opportunities for a "nickel-and-diming" of water vapor. For a given initial IN altitude, negative changes in vapor and ice would become more pervasive with increasing concentration. If the sporadic, small-scales of activation that constitute this nickel and diming *are* occurring and causing these negatively-changed areas in ice and vapor, the extent of area(s) affected by IN activation (if not the amount of negativity in any area) at any level and time should be relatively independent of initial IN concentration. That is, there should only be small differences in where activation can occur and any significant differences instead are in the amount of activation. This is the case here—we saw in Figure 7.2 how little activation conditions vary, Figures 5.1 and 7.8 show how the extent of air influenced by IN activation varies very little, and Figure 7.9 shows how the concentration of activation-event tracers (i.e. the amount of activation) *does* vary among the experiments with 30, 60, and 120 IN initialized at 250 hPa.

When IN are initialized at different altitudes, we see the effects of limiting vapor. When IN are initialized at a higher, drier altitude (200 hPa, or 12.5 km) the dehydration effect above 10 km of IN-assisted ice crystal formation and subsequent descent is lessened enough that the majority of IN-influenced gridpoints experience a positive change in vapor and ice amounts, similar to the 30 IN/L experiment. When the IN are initialized at a lower, more moist altitude (300 hPa, or 9.7 km), the dehydration effect is pronounced as more numerous IN-produced ice crystals grow, or as more activation occurs, as seen in Figure 7.10. The degree of dehydration aloft is even greater in this case than with increased numbers of IN (the extent of negative changes in vapor above 10 km is larger for 60 IN/L initialized at 300 hPa than 120 IN/L initialized at 250 hPa). Two examples of the increased dehydration aloft when the height of the initial IN population is lowered can be seen in Figure 7.11—with 60 IN/L initialized at 250 hPa there is more vapor than there is with 60 IN/L initialized at 200 hPa, but more vapor than there is with 60 IN/L initialized at 300 hPa.

The amount of water in any phase is not only limited by altitude, as it can also be limited by air motions and the timing of IN activation. In the case of 60 IN/L with a "warm" activation threshold of 273 K, there is less pristine ice compared to the 60 IN/L experiment with a colder activation threshold (238 K). The initial IN-layer for each experiment is at 250 hPa. When differencing various parameters late in these two experiments, a relationship between pristine ice and vertical velocity becomes clear: where air has a decreased vertical velocity there is less ice. In Figure 7.12, pristine ice and vertical velocity differences are shown (values from the 60 IN/L warm activation case less values from the 60 IN/L colder activation case), 52.5 hours into each experiment. With a weaker upward velocity, crystals are not supported aloft as readily in the warm activation case and any vapor added by evaporation at earlier times would not be lofted as high, reducing crystal formation and/or growth at altitudes later. This robust relationship is just as we saw in the explanation of the upper, negative portion of the "dipole" features discussed in the previous chapter. The origin of the relationship is not so clear. In Figure 7.13 we can see the earliest indication of this relationship between a decrease in vertical velocity and a decrease in pristine crystal mixing ratio, at 21 hours into the experiments. The difference of vertical velocities at this level and time appears to have little coherence, and is likely to be the result of noise. The largest decrease in pristine ice relative to the cold activation case coincides with an area of decreased vertical velocity, in the westernmost area of IN influence in Figure 7.13. The second area of IN-influence that shows less ice mass in the warm activation case is at the southern boundary of the domain. At this location, there is no relationship between vertical velocity and changes in ice amount.

Instead, the increase in the number of gridpoints with a negative change in ice may be due to differences in the timing and amount of IN activation between the two experiments.

Ice nuclei in 60 IN/L warm-activation experiment can activate more readily, and at lower altitudes. This affects the distribution of vapor over time and height. Over short time periods, there can be *more* ice in the warm-activation experiment, and with vapor "tied up" as ice, less vapor is transported aloft (if air is rising) to form ice aloft. Over long time periods however, the causes of differences in ice between these two experiments becomes much less clear, as IN activate, ice forms in areas with increased vapor, or doesn't form where there isn't enough vapor, there can be more precipitation, less (or more) evaporation, etc. --the initial effects of differential timing of IN-activation interweave and propagate. Fortunately, in the southernmost area of IN-influence at 11.2 km 21 hours into the experiment with 60 IN/L with warm activation (Figure 7.13), we have an example of the short-term variety of the cause of the decreased ice mass compared to the cold-activation experiment: in Figure 7.14 we see that at this height (11.2 km) and just below at 11 km, there are more activation-event tracers in the warm activation experiment, and there is more ice on the edges of a cloudy area in rising air (not shown)--more ice below led to less vapor and ice above.

The effects of activation timing and vertical velocity differences discussed in the previous two paragraphs best address the increased negative areas of both vapor and ice above 10 km in the warm-activation experiment. Below 10 km, the warm-activation experiment has a dramatically greater area of negative changes in pristine ice compared to all the other experiments. Why is this so? Because warm-activation IN can activate more readily, the effects of (warm) activation on vapor and ice are distributed across a greater range of heights (note the vertical extent of the envelope of IN-influence in Figure 5.20), and can be more evenly distributed, especially if and where IN-influenced air has resided for some time. In Figure 7.15, we see that there are many fewer unactivated ice nuclei in the warm activation case at the end of the experiment, notably at and below 10 km. The average vertical velocity at this time is much less negative as well in the experiment with warm activation. This means that in the cold activation case, the effects of IN-activation are regularly transported to lower levels, while in the warm activation case, where there is more activation at lower levels, the effects are distributed more locally and evenly. Thus, the net transport of vapor and ice downward in the cold activation case is not present in the warm activation case.

The changes in vapor and ice are similarly proportioned in the experiment with 120 IN/L initialized at 925 hPa with a warm activation (all IN-influence exists below 10 km) as they are in the experiment with 60 IN/L with warm activation below 10 km—the changes in vapor are well-mixed and tend positive, and changes in ice are, overall, negative (Tables 7.1 and 7.2). Though the extent of the area with negative changes in ice are similar (54% of gridpoints below 10 km in the 60 IN/L with warm activation case and 53% of gridpoints in the 120 IN/L at 925 hPa/warm activation case show negative changes in pristine ice), there is a notable difference in the area with positive changes. 30% of the area influenced by IN is positive in the 120 IN/L low altitude/warm activation experiment compared to 45% of the area below 10 km in the 60 IN/L warm activation experiment. Why is there such a decrease in the area of positive changes in ice between the two experiments, when all else is so similar? The answer lies in the causes of positive changes in ice: activation of ice nuclei and an IN-influenced increase in vapor allowing for more crystal formation. The number and distribution of activation-event tracers in Figure 5.22 suggest that activation events in the 60 IN/L warm activation experiment occur more often in space and time, especially in the last half of the experiments where IN are the most widely distributed (not shown). This seems reasonable since IN initialized at a higher altitude are more likely to encounter temperatures at and below the activation threshold. In the 60 IN/L warm activation experiment, bursts of IN activation appear at 11 km/4.5 hours, 10 km/22 hours, 9.5 km/25 hours, 11.5 km/40-45 hours, and 9 km/35-45 hours. In the 120 IN/L low altitude/warm activation experiment bursts of IN activation appear at 4.5 km/17-20 hours and 4.5 km/37-50 hours. With fewer bursts of activation events in the 120 IN/L low altitude/warm activation experiment, there are fewer and smaller areas of positive changes in ice in the area of IN-influence, and more IN-influenced air experiences a wash of trickle-down effects of those activation bursts. As for the second, less direct and probably less important means of increasing ice in the 120 IN/L low altitude/warm activation experiment, changes in vapor caused by these bursts of activation may not be substantial enough changes to incite additional ice formation given the large amounts of vapor present at the low, humid altitudes where IN-influence exists.

The story that explains the surprisingly extensive areas with negative changes in ice and vapor is now complete. With greater numbers of IN, the bulk of which are found above 10 km (the 250 hPa injection height is approximately 11 km high), there is a "nickel-and-diming" of vapor for IN-assisted ice formation. The majority of these crystals are caught in descending air, transporting water below 10 km: in the average of descending air, moisture is lost aloft and gained below (note the amount of air experiencing positive and negative vertical velocity in Figure 7.16). The potentially extensive positive changes in vapor and ice we could see below 10 km are lessened and muddied by IN activation and ice production at those lower levels. Concurrent negative changes in ice and vapor may result from this mixing at lower levels, and also when vapor is limited aloft.

Remember this discussion is about the amount of negativity (Tables 7.1 and 7.2 show the number of gridpoints experiencing negative changes), not the strength of the negativity. Though features like the dipole (Chapter 6) are evident, the magnitude of negative changes in vapor and ice appear to be on the "small" side—changes in vapor are usually less than 5%, and changes in ice are less than 25%. What this means will be discussed in the next chapter.

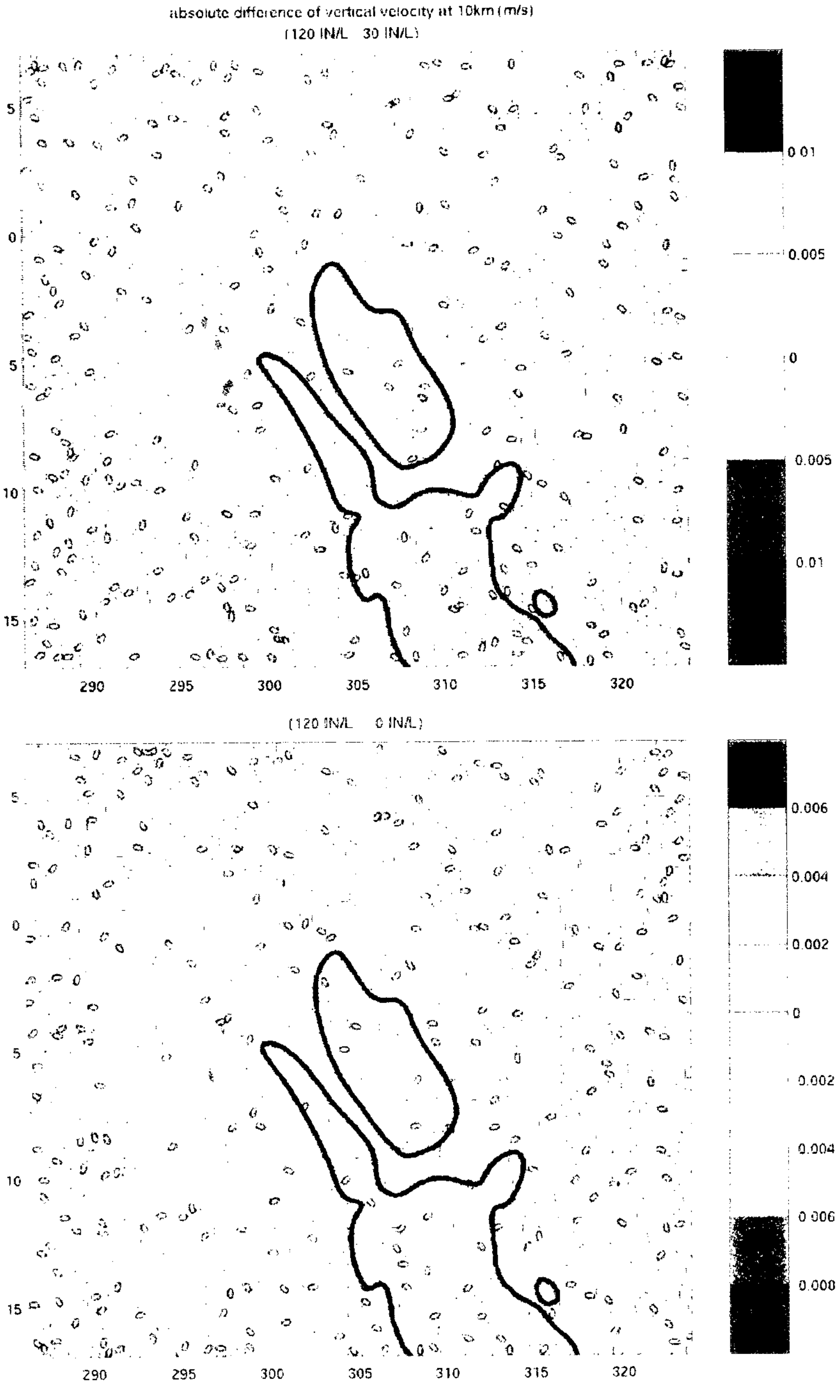

Figure 7.1. An example of how similar dynamics are among experiments with different numbers of ice nuclei. At top, the difference in vertical velocity between the experiments with 120 and 30 IN/L, shown here at 10 km 58.5 hours into each experiment's modeled time. For comparison, the difference in vertical velocity between the experiment with 120 IN/L and a control experiment with no ice nuclei is also shown (bottom). Vertical velocity differences in each case are on the order of millimeters per second.

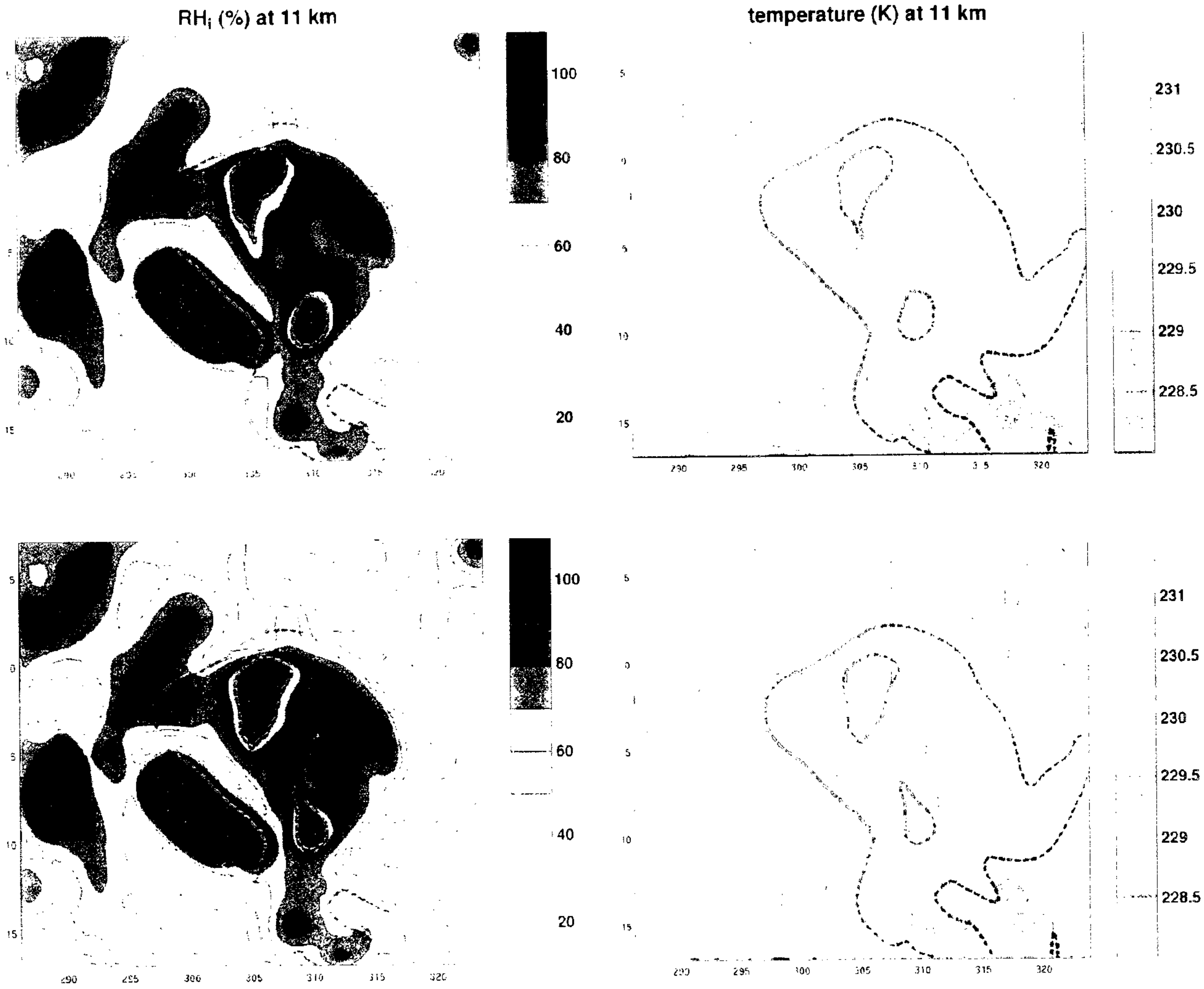

RH$_i$ (%) at 11 km

temperature (K) at 11 km

Figure 7.2. Ambient conditions between experiments vary little. Here, relative humidity with respect to ice and temperature are shown at 11 km, 58.5 hours into two experiments—with 30 IN/L input (top) and with 120 IN/L input (bottom). There are minimal if any differences in the temperature distributions. The bounds of air influenced by IN-activation are enclosed by dashed contours. Areas of potential IN-activation occuring at this time and height are highlighted in green (where an RH$_i$ of at least 100% exists with a temperature less than 238 K, activation can occur). There are slight differences in contours of relative humidity which may have been caused by earlier IN activation and subsequent changes in the distribution of water.

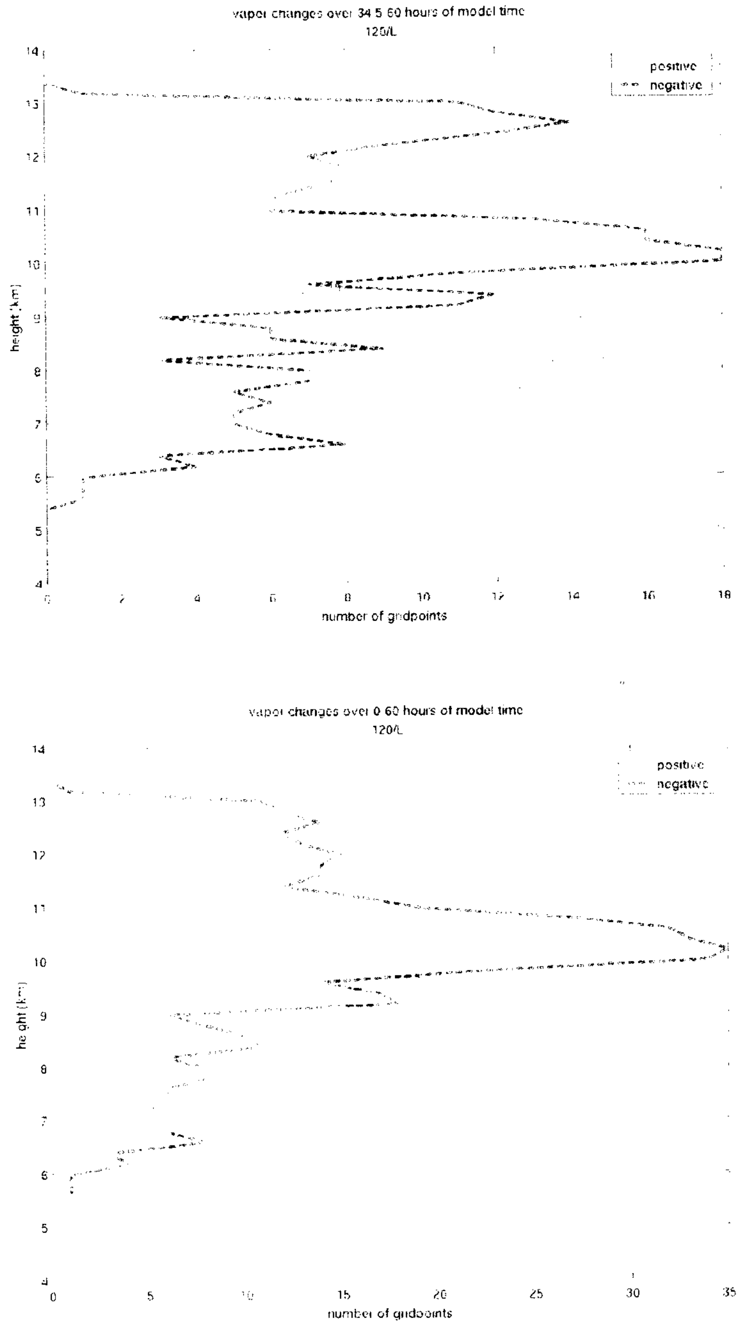

Figure 7.3. For the experiment with 120 IN/L initialized at 250 hPa, the number of points with positive (solid green lines) or negative (dashed pink likes) changes in vapor, from the plot of horizontally-averaged vapor differences in Figure 5.8. Negative changes in vapor are seen to accumulate over time, as the number of negative gridpoints in the last half of the experiment (top) is about half that of the total (bottom).

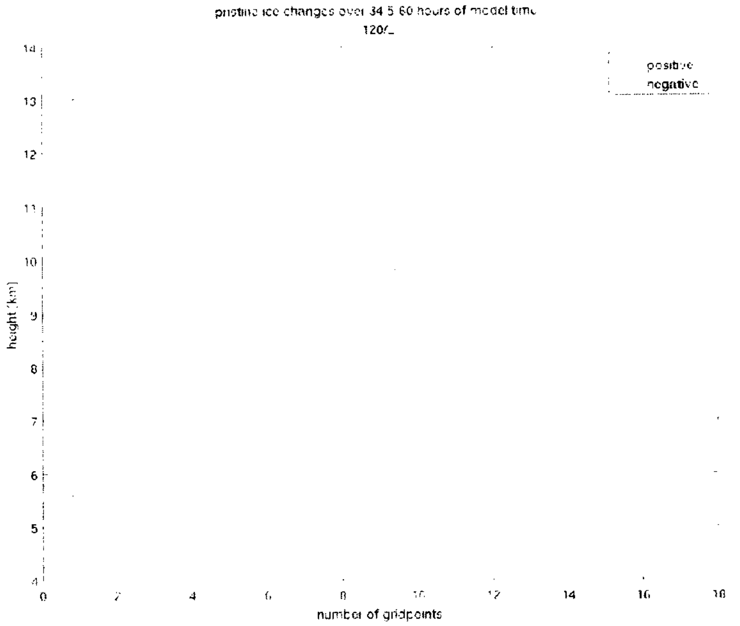

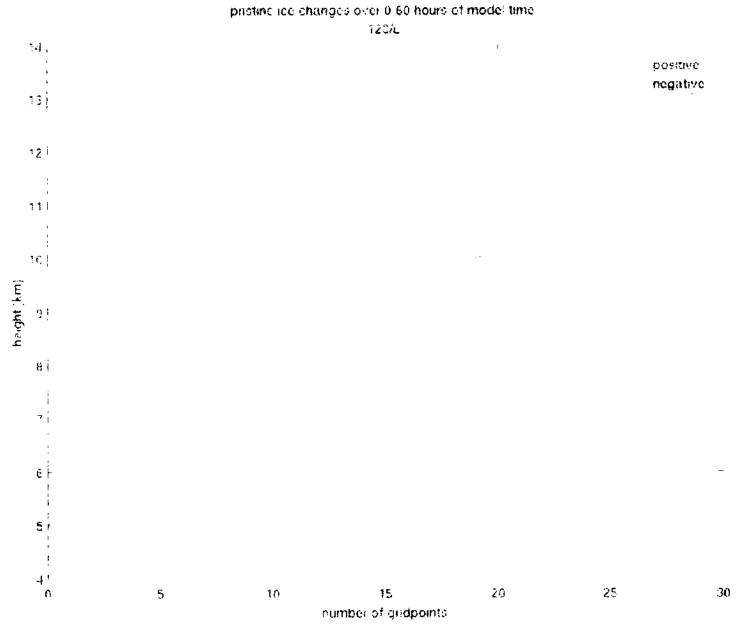

Figure 7.4. For the experiment with 120 IN/L initialized at 250 hPa, the number of points with positive (solid green lines) or negative (dashed pink likes) changes in pristine ice, from the plot of horizontally-averaged vapor differences in Figure 5.5. Negative changes in ice are seen to accumulate over time, as the number of negative gridpoints in the last half of the experiment (top) is about half that of the total (bottom).

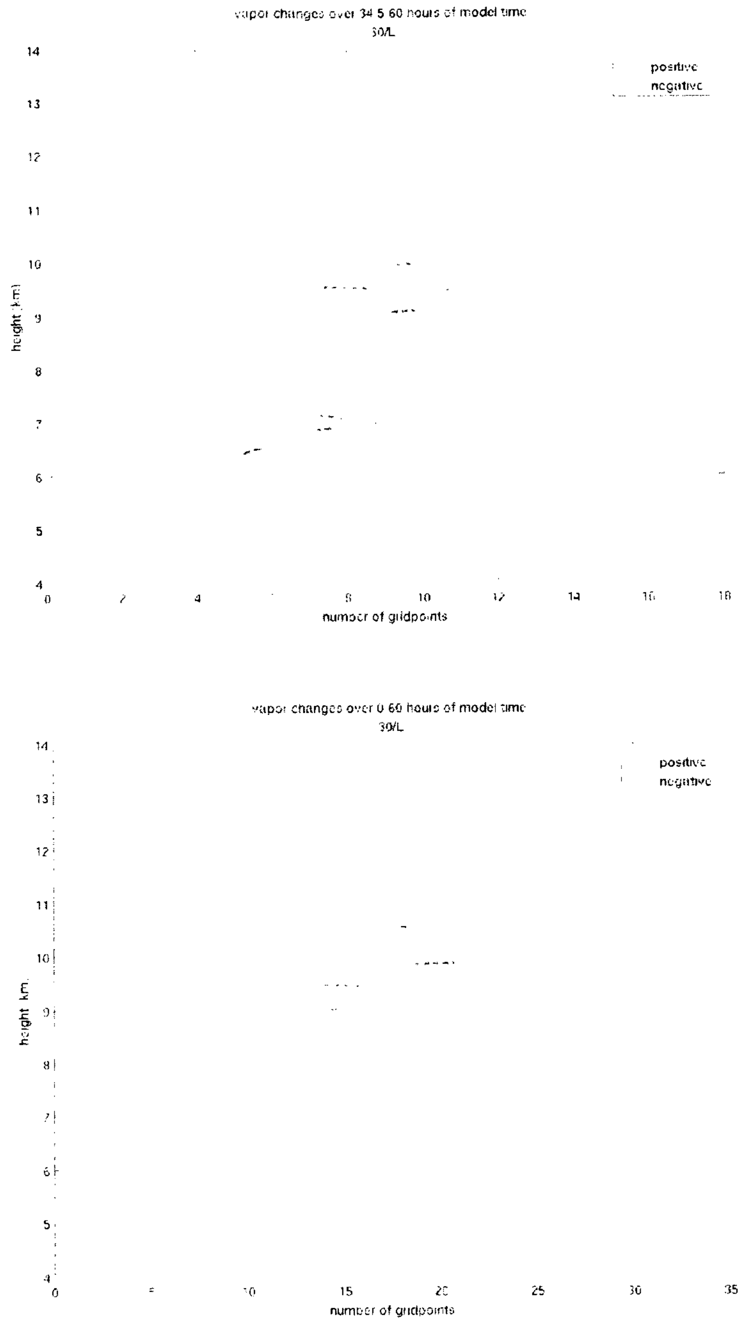

Figure 7.5. For the experiment with 30 IN/L initialized at 250 hPa, the number of points with positive (solid green lines) or negative (dashed pink likes) changes in vapor, from the plot of horizontally-averaged vapor differences in Figure 5.6. Negative changes in vapor are seen to accumulate over time, as the number of negative gridpoints in the last half of the experiment (top) is about half that of the total (bottom).

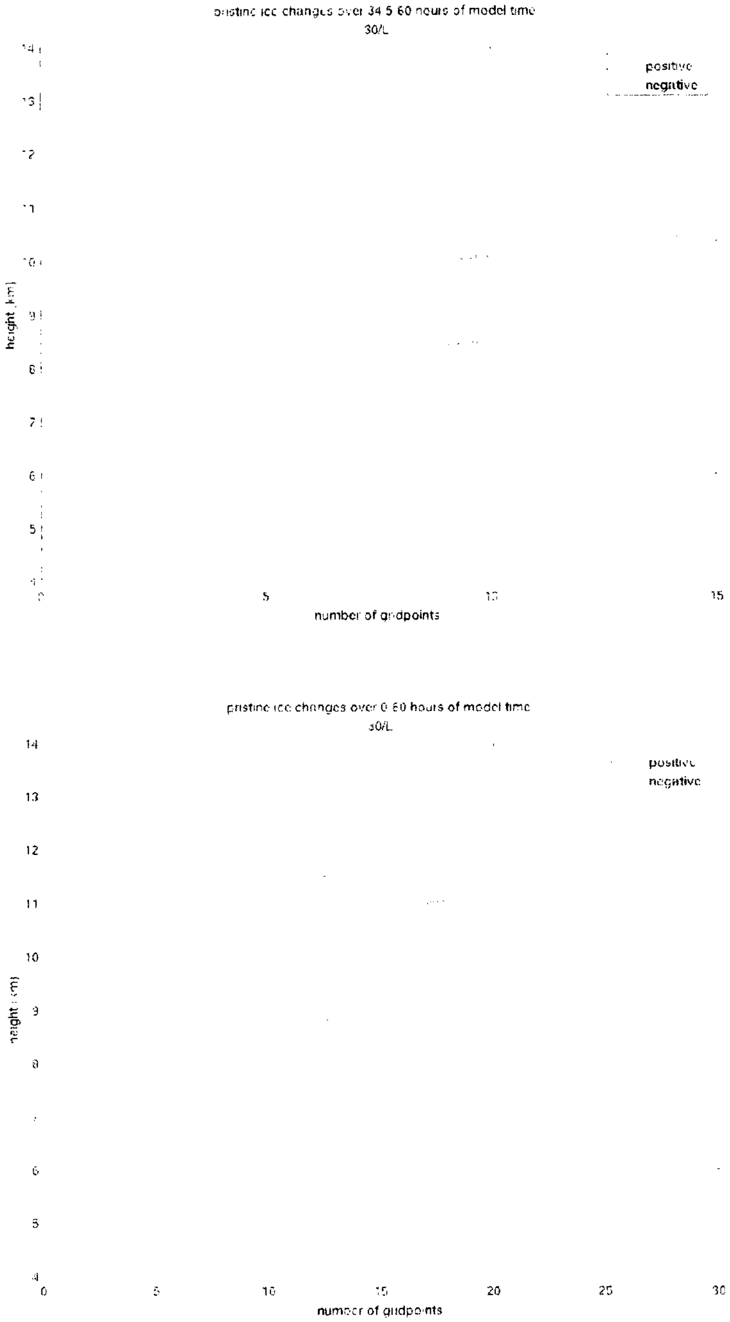

Figure 7.6. For the experiment with 30 IN/L initialized at 250 hPa, the number of points with positive (solid green lines) or negative (dashed pink likes) changes in pristine ice, from the plot of horizontally-averaged vapor differences in Figure 5.3. Negative changes in ice are seen to accumulate over time, as the number of negative gridpoints in the last half of the experiment (top) is about half that of the total (bottom).

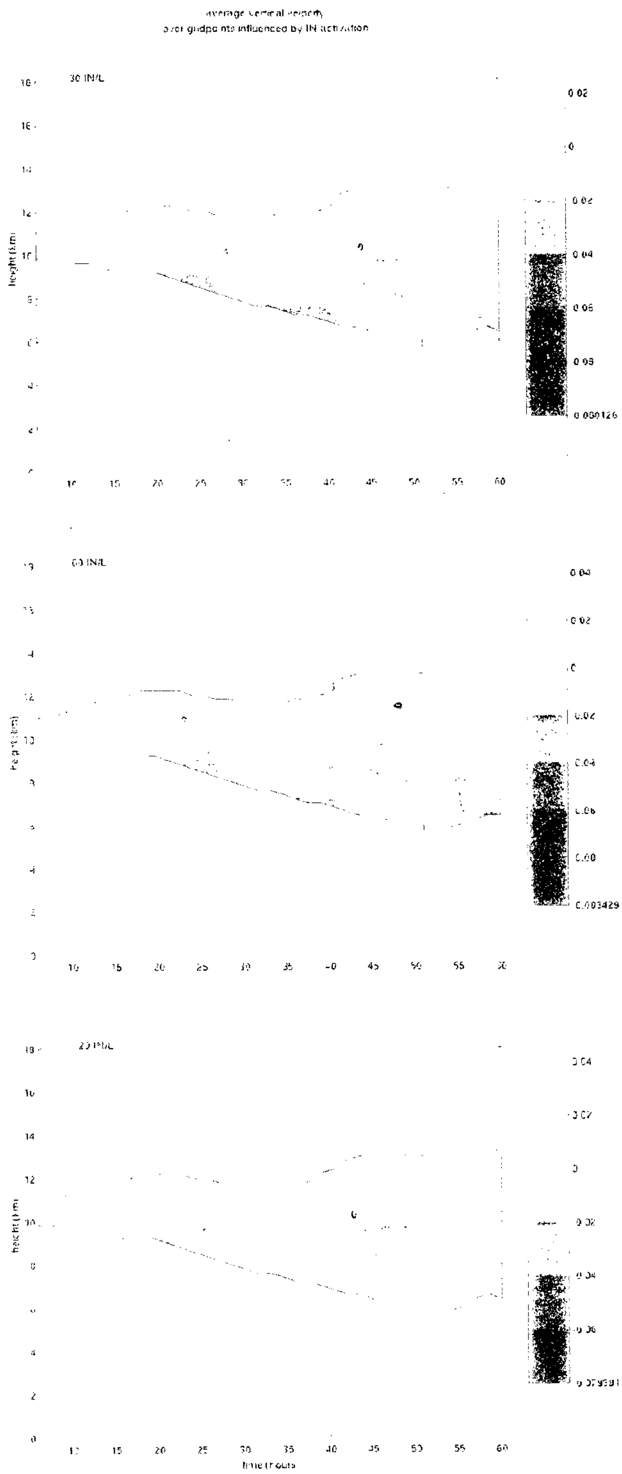

Figure 7.7. Vertical velocity averaged over gridpoints influenced by IN activation with 30 IN/L (top), 60 IN/L, and 120 IN/L (bottom), all initialized at 250 hPa. Most IN-influenced gridpoints experience a negative vertical velocity on the order of a couple centimeters per second, consistent with the average vertical velocity in the free troposphere found by Gage et al (1991).

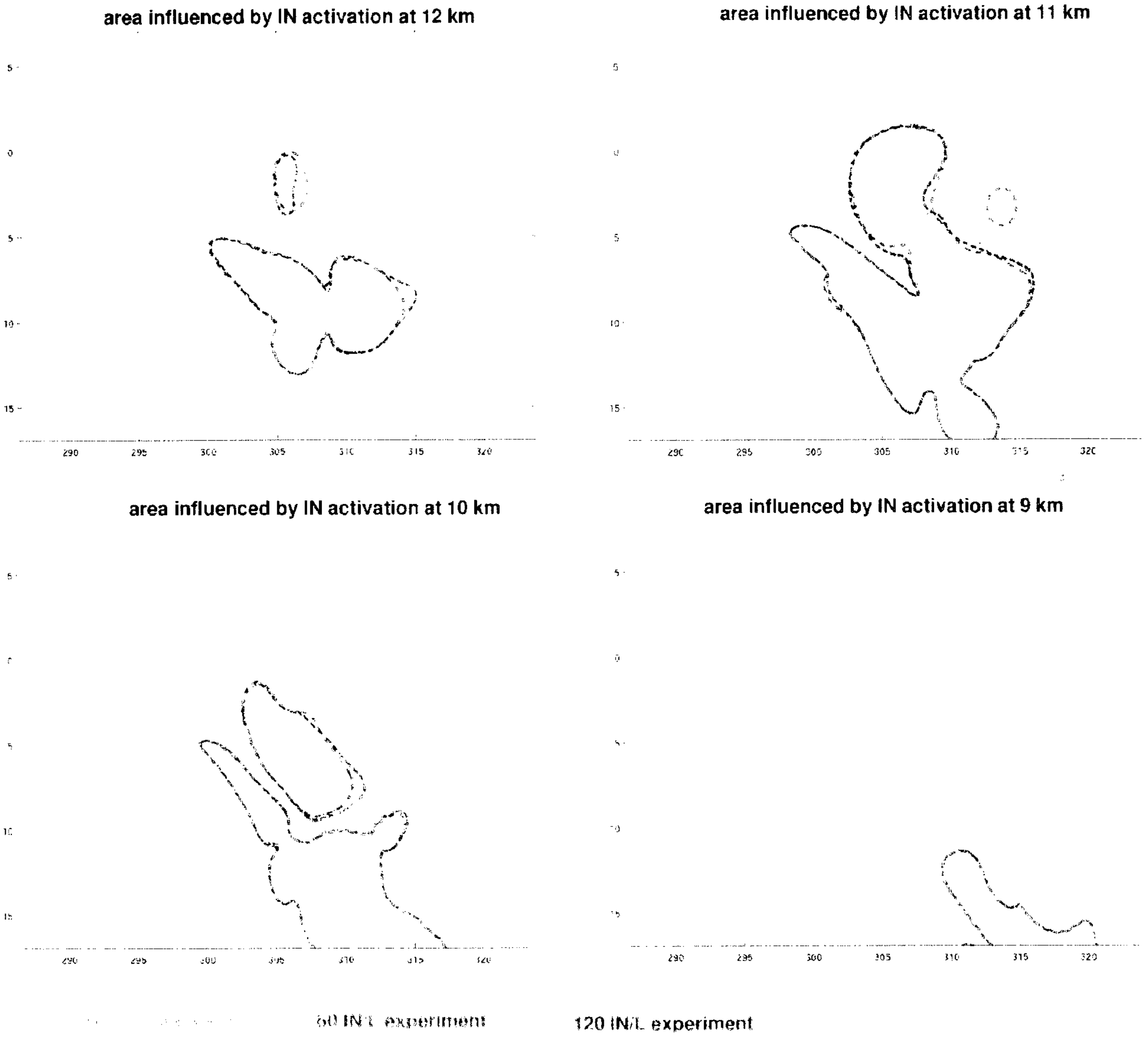
area influenced by IN activation at 12 km

area influenced by IN activation at 11 km

area influenced by IN activation at 10 km

area influenced by IN activation at 9 km

Figure 7.8. Area influenced by IN activation for the experiments listed above at 12 km (upper left), 11 km (upper right), 10 km (lower left) and 9 km (lower right). That there are only very small differences in the extent of air influenced by IN activation, but changes in the number of activation-event tracers (Figure 7.9), indicates the increasingly negative average changes with increasing IN concentration are caused by sporadic, small-scale IN activation events.

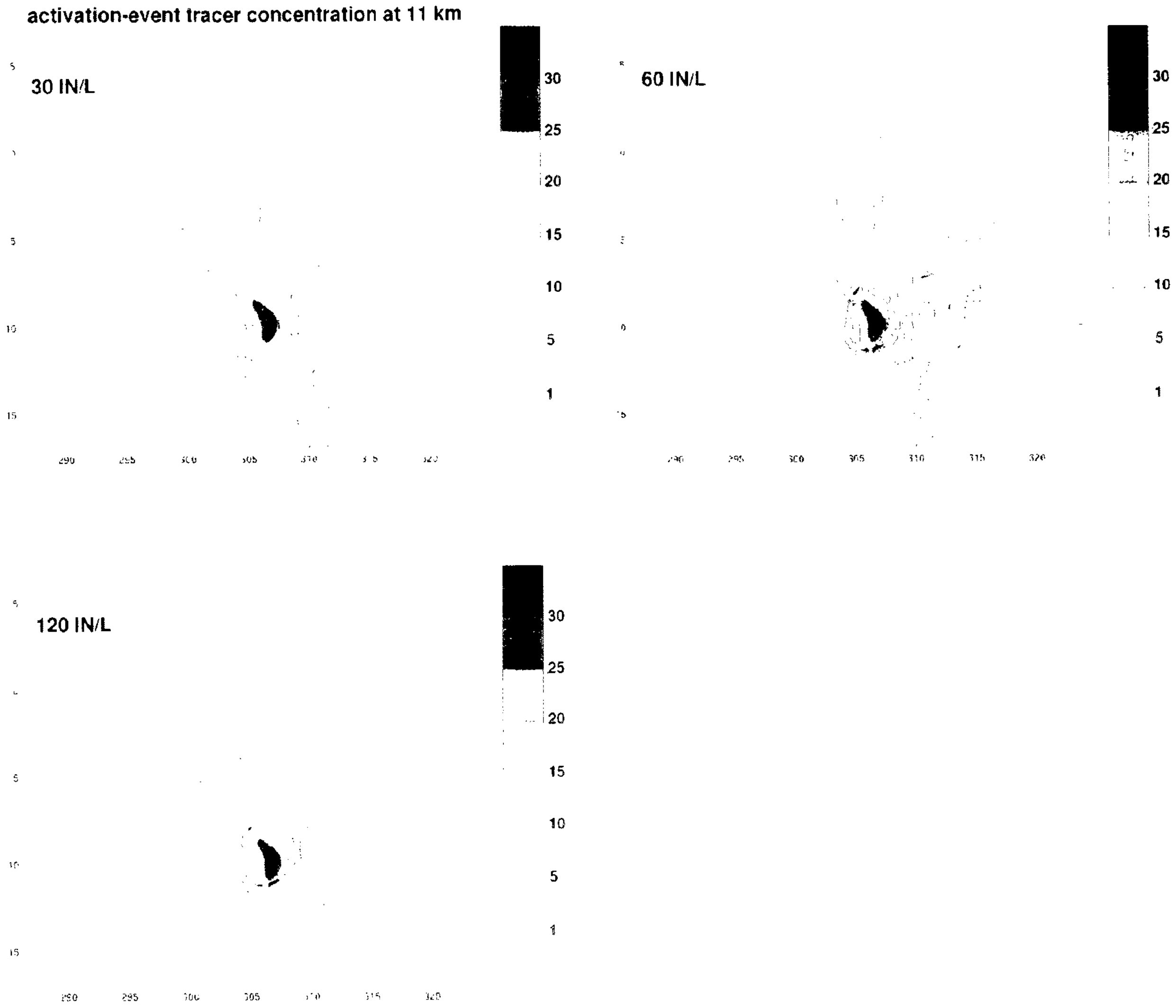

Figure 7.9. Activation-event tracer concentration (#/L) are shown at 11 km and 58.5 hours into the experiments with 30 IN/L (upper left), 60 IN/L (upper right), and 120 IN/L (lower left).With increasing concentration there are slightly more activation tracers. The differences in tracer concentration between the 30 IN/L and 60 IN/L plots are circled in green, the differences between the 60 IN/L and 120 IN/L plots are circled in blue. Since there are only small differences in in the environmental conditions and where these tracers are found (Figures 7.2 and 7.8 respectively), that the changes in vapor and ice are more negative with increasing IN concentration appears to be a result of additional IN activation. This additional activation occurs very well-distributed numbers, except for the green and blue areas circled above.

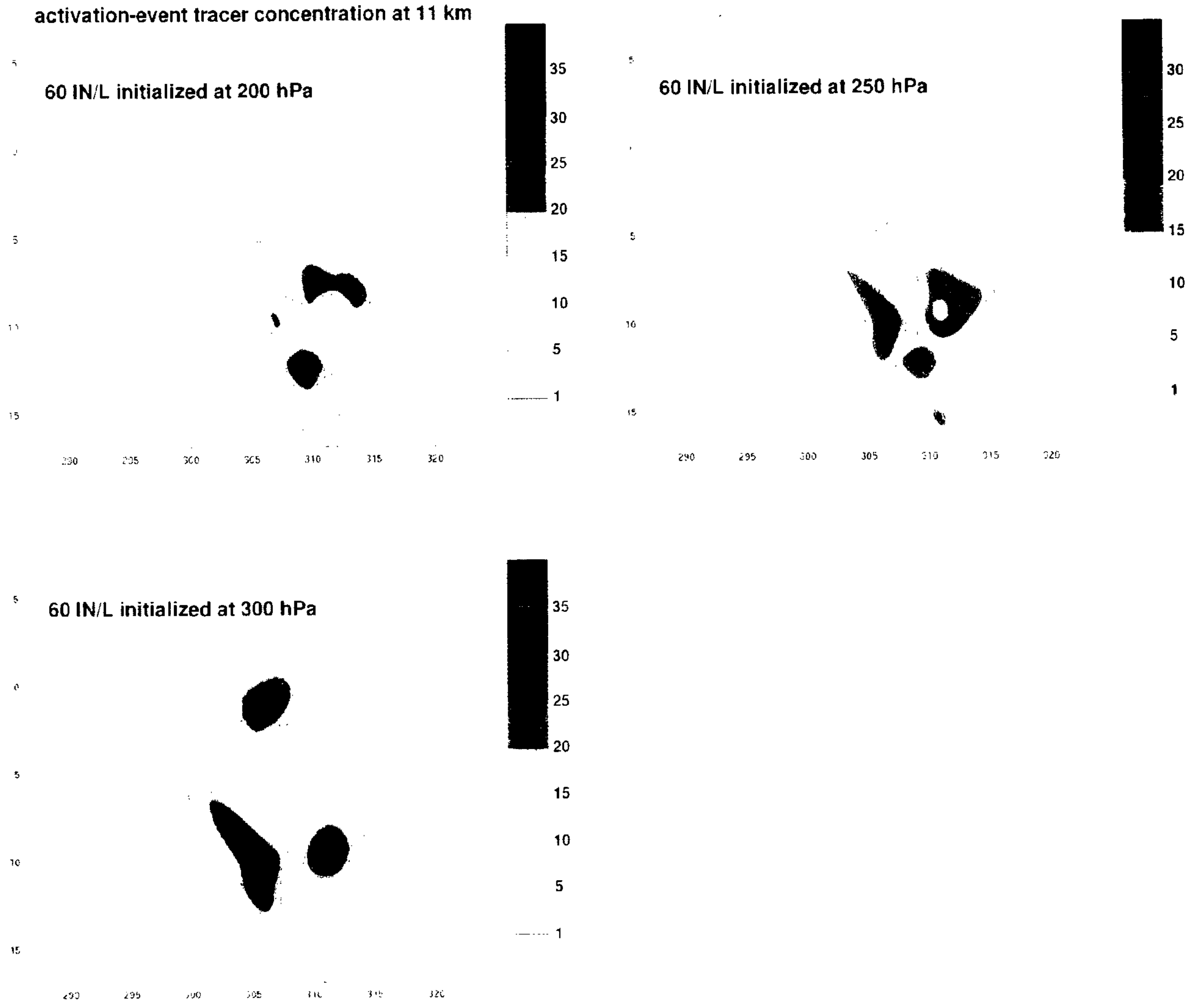

Figure 7.10. For a given initial IN concentration, the lower the altitude of the IN population, the more activation may take place—assuming the temperature at these heights is less than or equal to the activation temperature, there will be more activation lower in the atmosphere where there is on average more water vapor. This effect is seen above, as with lower initial IN heights, there are more activation-event tracers at 11 km and 58.5 hours. Then, the more (IN-produced) crystals, the dehydrating effect of downward motions in the free troposphere negatively affect both vapor and ice mixing ratios at higher altitudes.

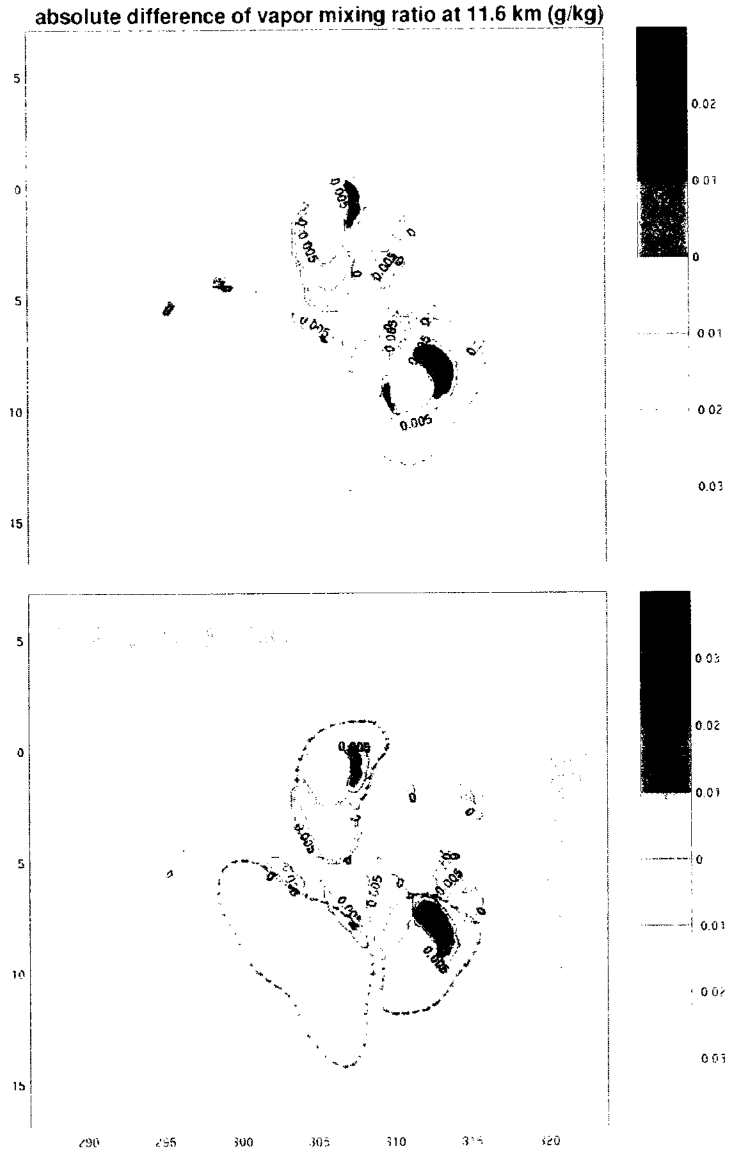

Figure 7.11. The difference in vapor between experiments with IN introduced at different heights as noted above. The higher-placed the initial IN concentration, the fewer opportunities for activation, since vapor is more limited. With less activation, there is less dehydration as a result of the (fewer) crystals formed being transported downward with the mean free tropospheric vertical velocity. The result: more vapor exists, on average, in the 60 IN/L initialized at 200 hPa experiment compared to the 60 IN/L initialized at 250 hPa experiment (the average difference between the two is positive, top plot); more vapor exists, on average, in the 60 IN/L initialized at 250 hPa experiment compared to the 60 IN/L initialized at 300 hPa experiment (the average difference between the two is negative, bottom plot). The bounds of air influenced by IN-activation are also shown by the red, dashed contours. At top, the bounds of IN-influenced air is shown for the high-altitude 60 IN/L experiment, below, the bounds of IN-influenced air for the low-altitude 60 IN/L experiment.

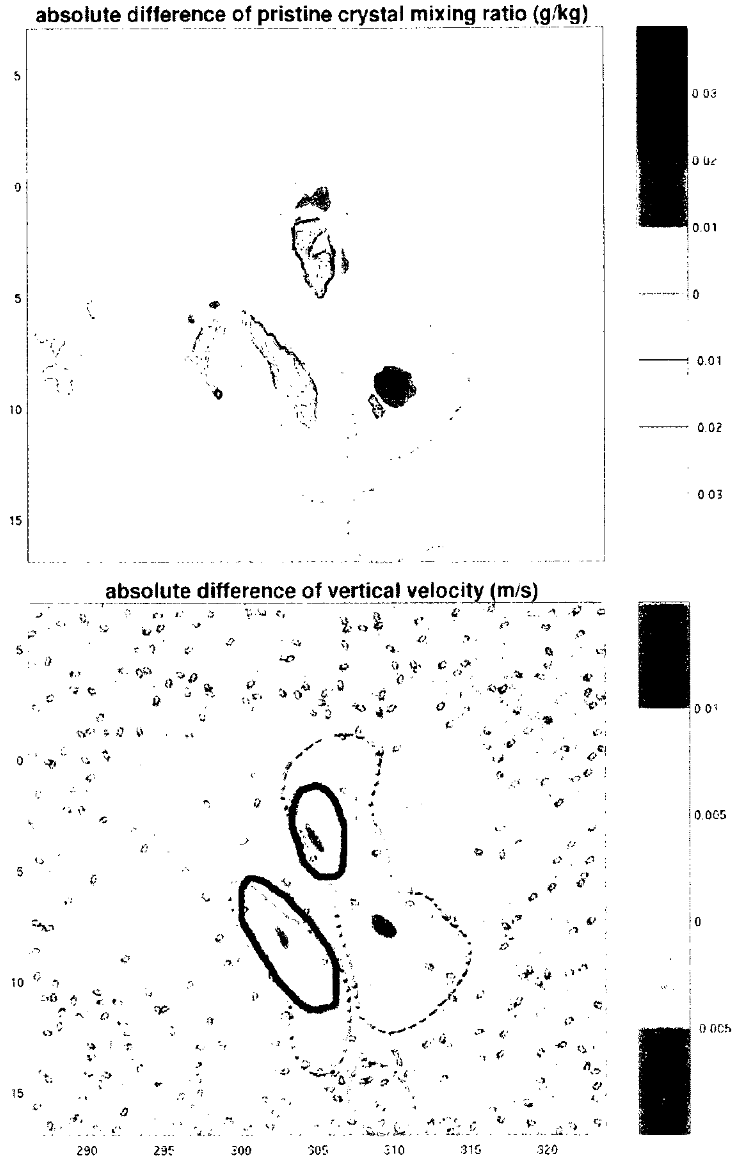

Figure 7.12. There is much less ice in the 60 IN/L with warm activation experiment than there is in the 60 IN/L cold activation experiment. Areas at 11 km, 52.5 hours into each experiment, where the difference in ice is most negative, are circled in above in magenta (top) and in black (bottom). Where the differences in pristine ice are negative (less ice in the warm activation experiment) corresponds to areas with a negative change in vertical velocity (the upward movement of air is weaker). With a weaker upward velocity, crystals are not supported aloft as readily and any vapor added by evaporation at earlier times would not be lofted as high, reducing crystal formation and/or growth at altitudes later.

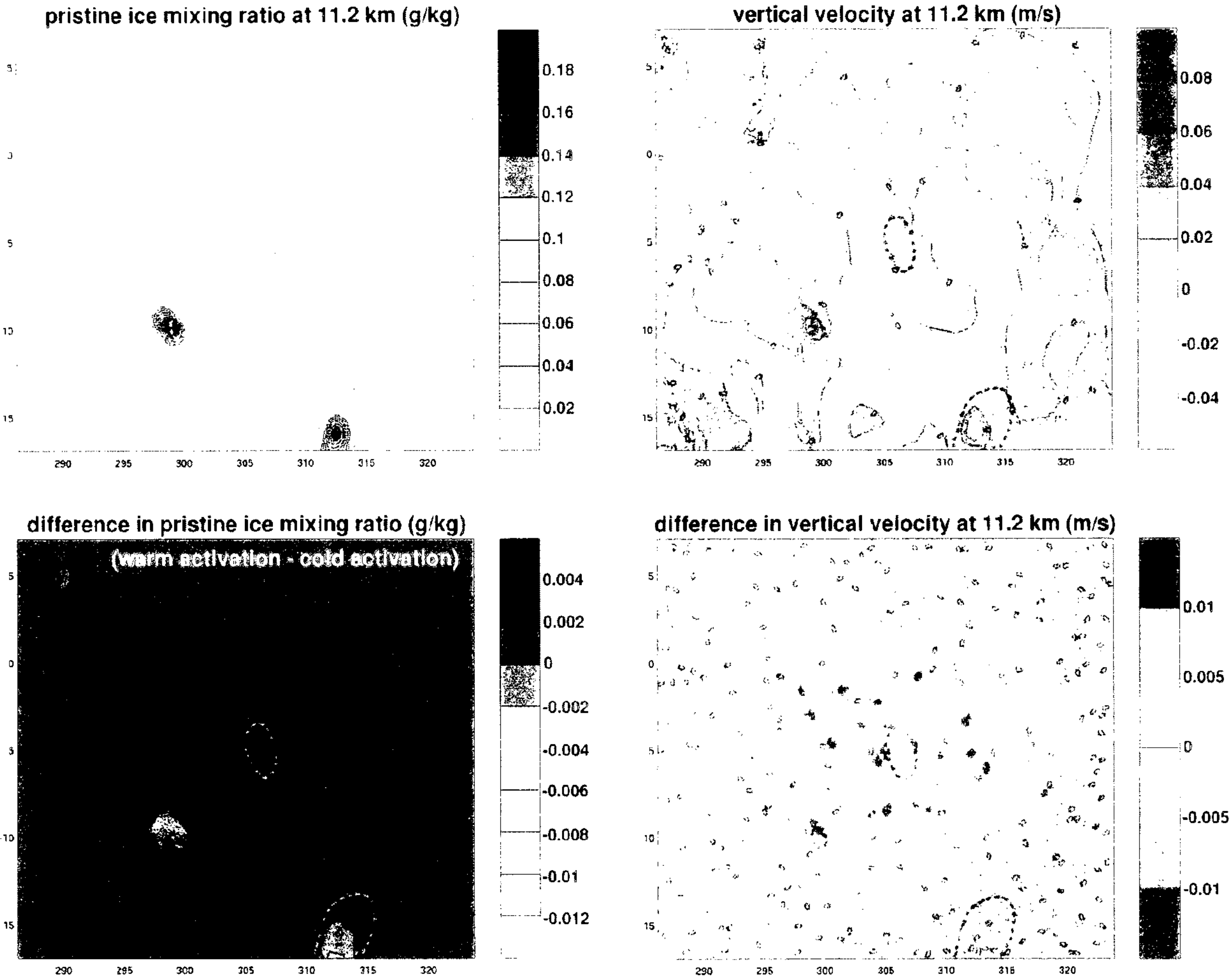

Figure 7.13. The top row: pristine ice (top left) and vertical velocity (top right) for the experiment with 60 IN/L with warm activation, at 11.2 km and 21 hours into the model run. In the bottom row: the difference between the values of pristine ice (lower left) and vertical velocity (lower right) in the 60 IN/L warm activation experiment less the values of the same parameters at the same height and time from the 60 IN/L cold activation experiment. Air influenced by IN activation in the 60 IN/L warm-activation experiment is bounded by the red dashed contours on all four plots. The largest decrease in pristine ice relative to the colder activation case coincides with an area of decreased vertical velocity, in the westernmost area of IN-influence. The second area of IN-influence that shows less ice mass than the cold activation case is at the southern boundary of the domain. Here there is no relationship between vertical velocity and changes in ice amount, instead, the decrease in ice may be due to differences in the timing and amount of IN activation between the two experiments (Figure 7.14).

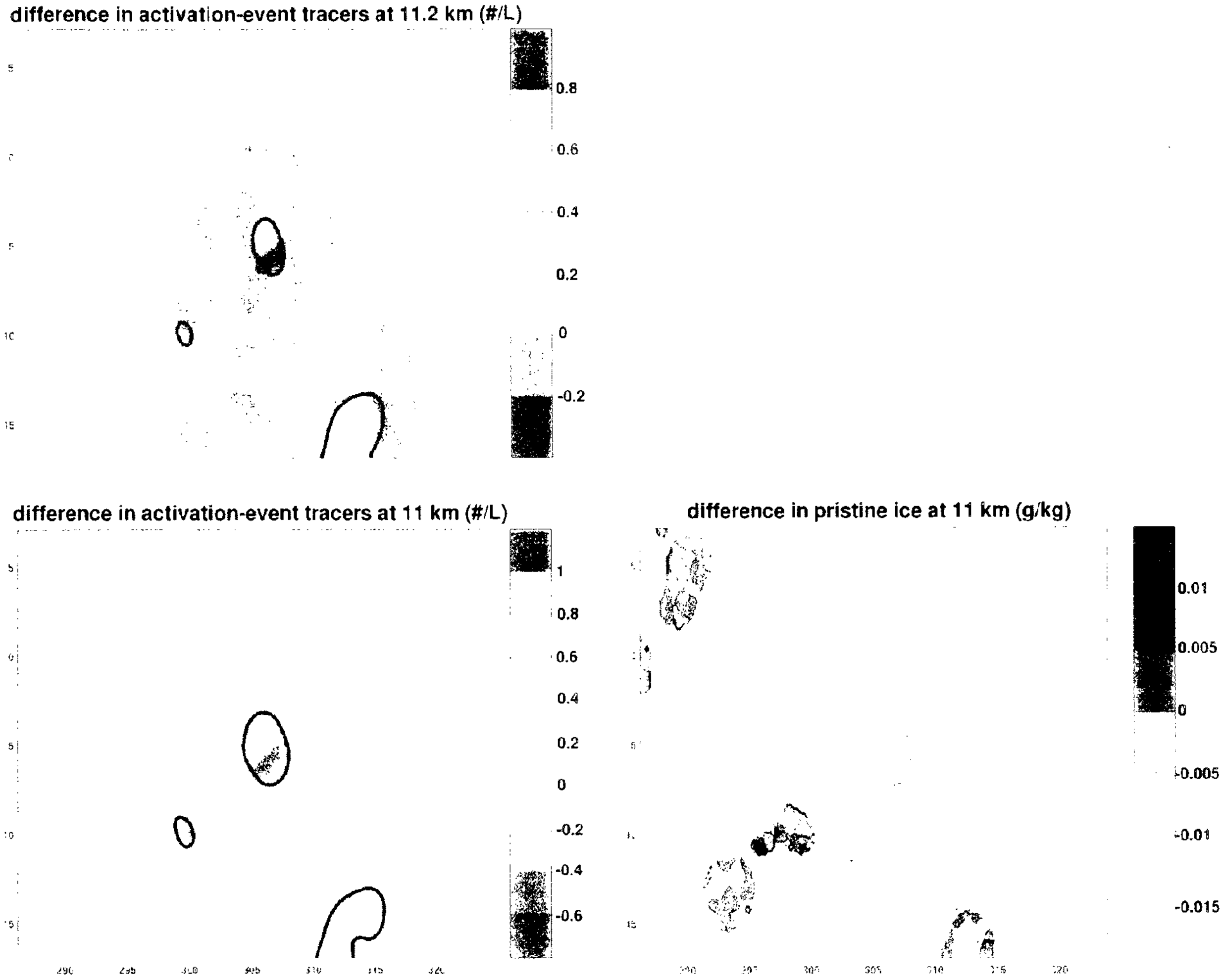

difference in activation-event tracers at 11.2 km (#/L)

difference in activation-event tracers at 11 km (#/L)

difference in pristine ice at 11 km (g/kg)

Figure 7.14. The difference of activation-even tracers (warm activation's tracers less the tracers in the cold activation experiment) at 11.2 km (top, corresponding to Figure 7.13) and 11 km (bottom left), 21 hours into each experiment. The southernmost area of IN-influence has more activation-event tracers in the warm-activation experiment, as well as more ice at 11 km. It appears that IN-formed ice in this area at 11 km may have limited the vapor and ice amounts above.

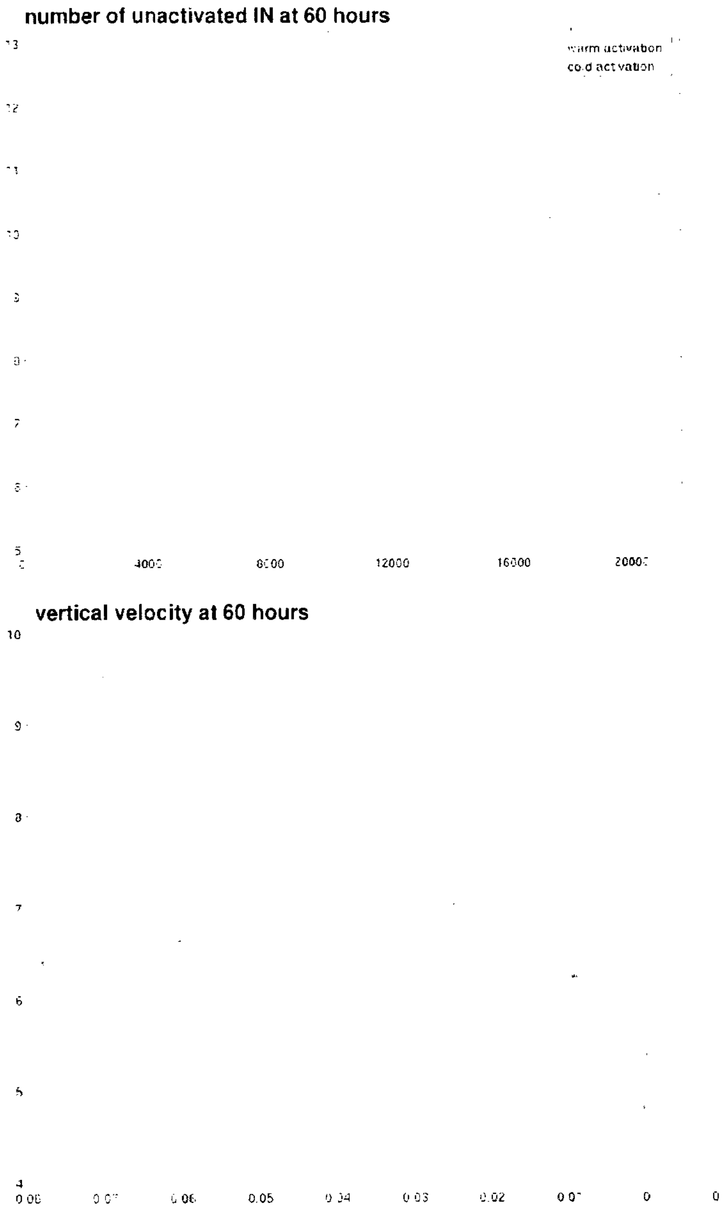

Figure 7.15. At the end of the experiments with 60 IN/L initialized at 250 hPa with warm (273 K) and cold (238 K) activation temperatures, the number of unactivated ice nuclei (top) is much less in the warm-activation experiment than the cold-activation experiment, especially at lower (warmer) levels. The vertical velocity at lower levels, averaged over gridpoints influenced by IN-activation, show that in the cold activation case, IN-influenced air is moving downward, while in the warm-activation case, air motions are more mixed. The changes in vapor and ice in the warm-activation experiment are therefore more evenly distributed vertically and in amount.

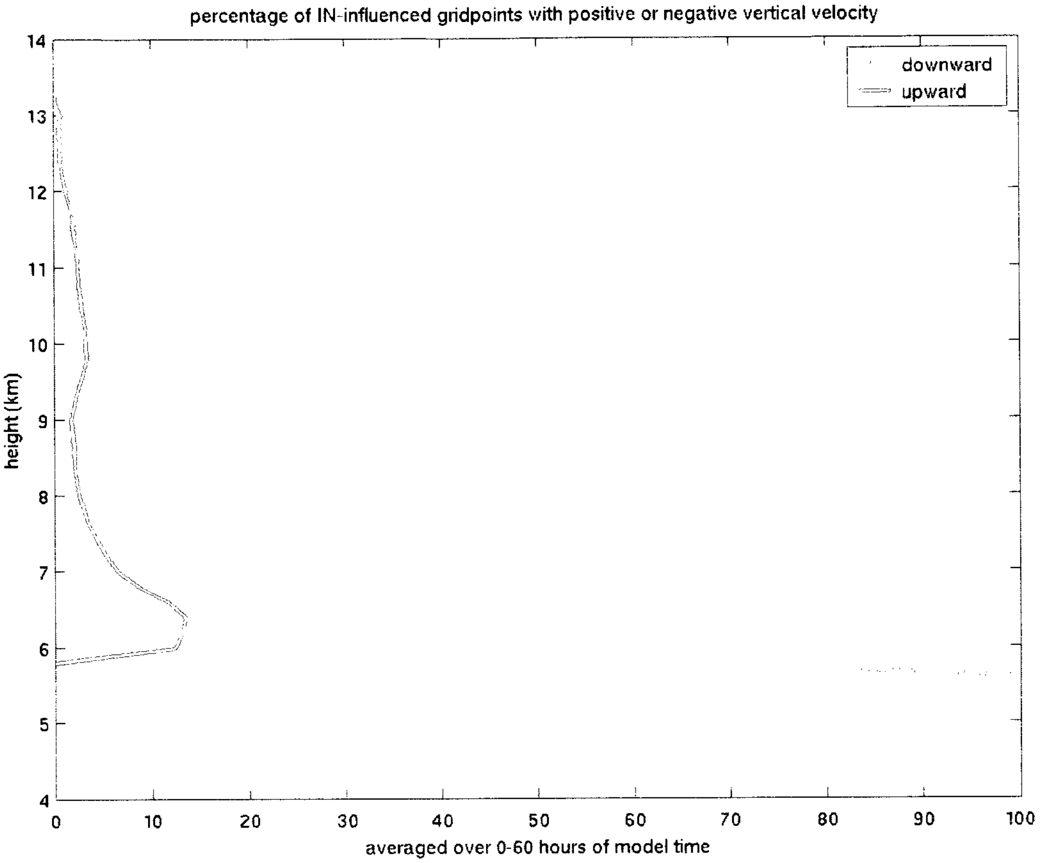

Figure 7.16. Averaged over 60 hours, the fraction of IN-influenced gridpoints in the 120 IN/L experiment that experience an upward or downward vertical velocity (solid magenta and dashed green lines, respectively) at each height where IN-influence exists. IN-influenced gridpoints with a vertical velocity of 0 m/s are counted as part of the total number of IN-influenced gridpoints. More IN-influenced gridpoints exist in descending air than in rising air, especially at lower levels. This likely has an effect on the negative changes in ice above 10 km and the positive changes in ice below 10 km in Figures 7.4, as crystals fell to lower levels.

Chapter 8: Conclusions

The spatial coincidence of aerosol loading from biomass burning, a high frequency of cirrus, and circulations tending to bring air into the stratosphere suggests that biomass burning-derived IN are likely to have some impact on tropical cirrus, which would then impact the transport of vapor into the lower stratosphere, as Rosenfeld et al. (1998) found. Unfortunately our knowledge of cloud-aerosol interactions is still lacking. Even cloud seeding, a process that has been investigated and used for decades, is poorly understood. As Woodley et al. (2003) state, "the passage of time has not obviated the need for [a coordinated research effort] . . . includ[ing] directed but basic research observations [emphasis added]." Cloud seeding studies, like most studies of cloud-aerosol interaction, have focused on the microphysical changes of water droplets in the presence of aerosol. Aerosol-*ice* particle interaction is a relatively new research topic. Some measurements exist of the composition of some species of organic IN, but not enough to explain their structure, nucleating behavior, and concentration (Chapter 3). As an exploratory study, eight experiments to explore the effects of populations of idealized ice nuclei have been conducted in three categories—the effect of concentration, the effect of activation temperature, and the effect of the location and extent of the initial IN population. The differences among the eight experiments are listed below in Table 8.1. The sensitivity of the environment to these scenarios was seen by horizontally averaging changes in ice and vapor over gridpoints influenced by IN activation, and plotting those changes as a function of time and height.

initial concentration	***initial location/extent***	***activation temperature***
30/L	sheet at 250 hPa	238K
60/L	sheet at 250 hPa	238K
60/L	sheet at 200 hPa	238K
60/L	sheet at 300 hPa	238K
60/L	sheet at 250 hPa	273K

initial concentration	***initial location/extent***	***activation temperature***
60/L	fumigation of entire domain	273K
120/L	sheet at 250 hPa	238K
120/L	sheet at 925 hPa	273K

Table 8.1. The different properties of the eight experiments conducted for this study.

With the exceptions of IN introduced near the surface (120 IN/L at 925 hPa, 60 IN/L fumigation), substantial effects on ice and vapor as a result of IN activity (at least 0.001 g/kg, or 1 ppmv) were found to be concentrated in the latter part of the experiments, after about 35 hours. This is near the beginning of convective activity along a stalled stationary front (Chapter 4). One pattern was that more gridpoints experienced negative changes in vapor and ice than positive changes over the course of the 60 hours modeled for each experiment. With the onset of convection in the last half of the model runs, a second pattern emerged in several experiments, above 10 km: a dipole that persists for several hours, with positive changes in vapor below and negative changes above an inflection point that varies between about 11 and 12 km. The prime factor in the creation of both of these patterns is vertical velocity, as we saw in Chapters 6 and 7. Rising air with smaller and more numerous crystals leads to evaporative moistening of upper levels—the expected result from the hypothesis that initiated this work, seen in the creation of the positive portion of the dipoles. Downward-moving air that has been influenced by IN activation tends to experience negative changes in vapor and ice via precipitation. But, as Jensen et al. (1996(b)) illustrate, the many degrees of freedom in cloud processes make this a much more nuanced story than the generalizations we can make based on the sign of vertical velocity. For example, noisy *changes* in upward-moving air are what produce the upper, negative portion of the dipole feature. Understanding this, and knowing how little is known about the behavior and concentration of IN in the real world, these modeled studies should be taken as a first-order estimate of the effects of IN, and guidance for future studies when more information about IN is available.

Secondary to the effects of vertical velocity on the sign of changes in vapor and ice in IN-influenced air, the amount of IN-activation influences both the magnitude of the negative portion of the dipole and the areal extent of negative changes throughout the volume of IN-influence. For example, the more IN activate, negative changes in vapor and ice occur more frequently (Chapter 7). Still, when reviewing spatially-averaged changes in vapor and ice for each experiment (such as Figures 5.3-8), it is difficult to rank categories of experiments. Though there are differences in the extent of air influenced by IN-activation that depend on the initial geometry of the IN population and the activation temperature, significant trends in the magnitude of changes (estimated by the ranges of absolute and percent changes) are not evident. However, we have learned, in Chapters 6 and 7 especially, that results are strongly height-dependent, so it is possible to categorize IN-induced changes based on the height at which an IN population exists.

Many gridpoints at low altitudes (below 10 km), experience descending air that can result in an increase in vapor and ice concentrations as IN-formed ice precipitates (Chapter 7). However, the effects are muddied as the IN compete more often for vapor with other (non-anthropogenic) ice-nucleating mechanisms. Closer to the melting level, phoretic contact nucleation and splintering become more important than they are at high altitudes (Chapter 3) Experiments with notable amounts of IN-influenced air extending well below 10 km are: 60 IN/L initialized at 300 hPa, 60 IN/L initialized at 250 hPa with a warm activation, 120 IN/L initialized at 925 hPa, and 60 IN/L fumigated throughout the domain with warm activation. On average there is more than 1 g/kg of vapor present at gridpoints below 10 km. Spatially-averaged changes in vapor and ice for these experiments are often less than 1% below 10 km, varying from -8 to 8 ppmv (-0.008 to 0.008 g/kg), though the actual, unaveraged changes can be greater —for the 60 IN/L fumigation experiment, changes are on the order of 10% of total vapor (0.02 – 0.2 g/kg) There can be more significant changes in ice (5-50%) when IN are present near the melting level (about 4 km), but percentage changes in vapor are small in the same location, since there is less ice than vapor. In rising air, these changes in ice can propagate upward and forward in time, as seen in the experiment with 120 IN/L initialized near the surface (Chapter 5, Figure 5.25).

As altitude increases above 10 km, the environment becomes more sensitive to IN. The largest IN-influences, percentage-wise, are often where vapor concentrations are lowest--small changes in the apportionment of vapor will have a large effect. Also, the effects of IN will be strongest where there are fewer ice nucleation mechanisms competing with the IN for vapor. As altitude increases, changes in ice and vapor become more sensitive to changes in vertical velocity. The dipole (or even the area of positive vapor change in the 30 IN/L experiment) is one of the strongest, if not the strongest feature, with spatially-averaged vapor changes of at least 1% (> 1 ppmv at 11 km). Above 10 km, where changes in vertical velocity are positive, there are more positive changes in vapor and ice, but when there are negative changes in vertical velocity, there are likely to be negative changes in vapor and ice.

Changes in vapor and ice are even more strongly tied to vertical velocity differences between the clean and IN-laden experiments at altitudes greater than 12 km (above most cloud tops in these experiments). There, a lack of vapor and fewer IN transported to these higher altitudes meant that there were too few IN activation events to leverage small differences in vertical velocity. Differences in vertical velocity above about 12 km are on the order of a few millimeters per second when the vertical velocity is less than a couple centimeters per second—differences in vertical velocity are themselves more significant at these heights than below, where the differences are a much smaller fraction of the vertical velocities experienced by IN-influenced air.

IN-induced changes in vapor and ice are clearly sensitive to vertical velocity. Local dynamics can affect the distribution and phase of vapor—for example, the formation of the positive portion of the dipole feature, as well as the layered changes in ice and vapor seen in the 60 IN/L fumigation experiment. Variations in vertical velocity between clean (IN-free) and IN-laden experiments have also affected whether there are positive or negative changes in ice and vapor (the negative portion of the dipole feature). Are IN-influenced changes in vapor and ice at a gridpoint as sensitive to whether that gridpoint is in cloud or clear sky? In fact vapor changes are not, and of course there are no ice changes out-of-cloud. Since our IN populations are not completely depleted by activation (Figure 8.1 shows unactivated IN in the experiment with 60 IN/L initialized at 250 hPa with cold activation), activation occurs often enough, either within or to create "cloud," for there to be relatively equal magnitudes of in-and out-of-cloud changes in vapor and ice. That is, downstream changes from past activation, which would tend to include more "out of cloud" areas, can be somewhat balanced by changes resulting from recent activation events "in cloud." More significantly, with time IN-influenced air spreads to include more area with clouds associated with the stationary front (Chapter 4). With both cloudy areas and IN activation undiminished over the modeled time period, it is unfortunately impossible to quantify the magnitude of changes associated with air newly influenced by IN activation vs. changes upstream in time and space. An example of the similar scale of vapor changes inside and outside "cloud" is seen in Figure 8.2, again for the experiment with 60 IN/L initialized at 250 hPa with cold activation. Note that the dipole in vapor is visible in the out-of-cloud vapor difference plot (Figure 8.2), reinforcing the idea of the positive portion of the dipole forming as a result of evaporation (creating out-of-cloud areas with increased vapor).

The magnitude of vapor and ice changes is most sensitive to the amount of IN activation, which in turn, depends on all three parameters investigated in this study: number of IN, initial geometry of the IN population, and activation temperature. Activation temperature has the largest impact on area of IN-influence, more than the geometry and number of the initial IN population. It doesn't matter how many IN are present at a gridpoint if the temperature (or humidity) does not support activation. In terms of the sign of vapor and ice changes, when more IN activate, negative the changes in vapor and ice are more frequent. In Chapter 6 we saw that there is a relationship between the magnitude of vapor change in the negative portion of the dipole and the initial number of IN, as well as a robust inverse correlation between the strength of the negative portion of the dipole and the total area influenced by IN (initial geometry). The negative portion of the dipole is the result of noisy vertical velocity differences, suggesting a role for chaos theory in affecting modeled precipitation processes at high altitudes.

The magnitude of change

How realistic are these results? Using the equations introduced into the UWNMS in Chapter 3, it was calculated that if 60 IN/L activate at one gridpoint where the temperature is 238 K at 200 hPa for a 20 second timestep, there will be a 1.69×10^{-6} g/kg (1.69×10^{-3} ppmv) change in vapor. A 1 ppmv

(0.001 g/kg) change for the same conditions at one gridpoint would require either 7.1 x 10^5 IN/L activating in one second, or the equivalent of 60 IN/L activating at that gridpoint each second for about 3 hours, 15 minutes. Though there are many more than one gridpoint with IN, not all gridpoints experience activation conditions, and the effects of IN activation spread out, so it takes time for effects on the order of 1 ppmv to be seen, especially in a horizontal average. For example, changes in vapor and ice near 11 km in the experiment with 60 IN/L initialized at 250 hPa (activation at 238 K) are only a few tenths of 1 ppmv—this is the height at which the IN were introduced and only 1.5 hours after the IN were introduced to the model. The timing of when the effects of IN become larger than 1 ppmv seems dependent on activation temperature. Areal-averaged changes greater than 1 ppmv can be seen near the start of the three experiments where IN are allowed to activate at 273 K (60 IN/L initialized at 250 hPa with warm activation, 120 IN/L initialized at 925 hPa with warm activation, and 60 IN/L fumigated with warm activation), since more IN can and will activate with a warmer, less constraining, activation temperature. The amount of vapor change we can expect for 60 IN/L activating at 273 K and 500 hPa (about 6 km) is about 1 x 10^{-5} g/kg for one 20-second timestep—it would take a little under 33 minutes for a 1 ppmv change to manifest in this scenario, which correlates very well with the much earlier onset of noteable changes in the experiment with 60 IN/L fumigation and warm activation.

Regardless of where relatively large changes in ice and vapor occur, the magnitude of changes in (spatially-averaged) vapor and ice appear to be on the "small" side—changes in vapor are usually less than 5%, and changes in ice are less than 25%. Changes in vapor are understandably a smaller percentage than changes in ice, since there is much more vapor in the atmosphere than ice. The absolute changes seen for both vapor and ice, on the order of a couple ppmv, seem realistic. The percent changes seen in spatially-averaged results are low, indicating low significance. Does the averaging disguise more significant changes? what conditions would need to exist for larger, significant changes in vapor and ice to occur?

When we look at changes in ice and vapor that have *not* been spatially averaged, it is clear that averaging these values can hide the true "strength" of IN influence, mostly where there is a large area influenced by IN. For example, IN-influence is more prevalent in the lower portion of the dipole features discussed in Chapter 6. Figures 6.15-18 show that the changes in vapor and ice in the positive portion of the dipole are tens of parts per million by volume (ppmv, with 1 ppmv = 0.001 g/kg), 10 times greater than the averaged changes in vapor and ice seen in the Hovmöller-style figures in Chapter 5. A 10 ppmv change in vapor or ice above 11 km, where the ambient humidity is at most 100 ppmv, is more significant than the averaged value! With smaller areas of IN influence, such as in the higher altitude, negative portion of the dipoles, the average changes more accurately reflect the order of magnitude of change in vapor and ice at a gridpoint.

In order to see a non-trivial amount of vapor (or ice) change at a gridpoint, such as 10 ppmv, there would need to be either an extremely large number of IN initialized at once, or a long period of time with continual injections of IN. It would take 9.4×10^7 IN/L activating over one second to manifest a 10 ppmv change in vapor or ice at 200 hPa (or 2.1×10^7 IN/L at 250 hPa), for example, which seems like a fantastically high number. More realistically, repeated injections of IN from biomass burning over a couple weeks—18 ¼ days, to be exact—with a continual 60 IN/L at 200 hPa approximating the results of convective transport can produce changes of 10 ppmv. Of course, where and when changes of this magnitude are possible depend on local dynamics much more than the number of IN or the amount of time modeled. The amount of activation is limited by the amount of vapor available, which strongly depends on the strength and extent of convective updrafts.

The vertical extent of IN-induced changes

The influence of IN over 60 hours only goes as high as ~12 - 14 km (or about cloud top height, Figure 4.14, for example). Averaged changes in vapor and ice can be as much as 2-4 ppmv near and above 12 km (as they are in the 60 IN/L initialized at 200 hPa experiment), though the amount of air influenced by IN activation at these altitudes is small. Is it possible for IN influence in this model to extend up into the tropical tropopause layer and even the stratosphere? What, if any limits are there on the strength of convection during this modeled period of time? Is 60 hours not enough time for the influence to spread upwards? Is it possible that a 10 ppmv change in vapor apportionment can occur at higher altitudes?

We know from Chapter 4 that the modeled cloud top heights, from which we can infer convective strength, are fairly well supported by ISCCP cloud top pressure data, though there are some discrepancies that result from the model's convective parameterization and grid spacing. The cloud top heights (and the convective strength we can infer from them) are representative of convection in this region (Cetrone and Houze, 2006, Fueglistaler et al., 2009). For IN to reach the TTL, it helps to have IN at the right place and time. When 60 IN/L were fumigated throughout the model, IN activation and influence occurred in the northwestern portion of the domain, which experienced persistent cloudiness over the 60 hours modeled (e.g. Figures 4.6, 4.10, and 4.15). IN influence extended up to 14.4 km here, just within the TTL, in an area with an upward vertical velocity of about 2 cm/s. In the column above this region of IN influence, the upward vertical velocity decreases to be about 1 cm/s (Figure 8.3)—it would take air at this level at least 57 hours for the air influenced by IN activation to reach the lower stratosphere, around 18.5 km (Fueglistaler et al., 2009). If we assume an average ascent rate of 1 cm/s, it would take 180 hours for air to rise from 12 km (where much IN influence exists in the 60 hours modeled) to the lower stratosphere.

With time, then, it is possible for the IN-induced changes we've seen to be transported into the lower stratosphere. Even 1% of the (not spatially-averaged) 10 ppmv changes seen at 11 and 12 km, if transported to the TTL, would be significant when added up over the course of a burning season—several *weeks* of IN loading! It remains to be seen how much vapor change would be transported however, since the amount transported depends on the number of crystals and the ambient humidity. The larger the crystals (with fewer or no IN) and more humid the environment, the more likely those crystals will grow and precipitate. It is possible that with humidity enhanced in an area (the positive portion of the dipole features, for example) crystal growth and precipitation would also be enhanced such that IN would be more a dehydration mechanism than positively influencing stratospheric vapor concentrations.

Summary and future work

We've investigated some interesting patterns seen in realistic results, but the changes are relatively small. It seems that activation conditions and location are the biggest factors in creating change—the extent of IN influence depends on where/when IN can activate, of course. However, for a given activation temperature, the geometry of the initial distribution of IN has only a small influence on the magnitude of changes seen in vapor and ice. The number of IN that activate (which depends on all three categories—raw number, activation temperature, and geometry) greatly affects the sign of the changes we see, if not always the magnitude of change. In this study the magnitude of changes may have been limited to the fact that our idealized IN represent only a possible species of IN, with one set of activation conditions. In reality there are many unique species of IN, which may come from the same source (such as a fire) and have overlapping populations.

In the experiments with IN initialized in sheets, as if convectively detrained at and above 300 hPa (approximately 9.7 km), results validate our hypothesis of IN activation leading to a moistening of upper altitudes, if we disregard the noisy generation of the negative portion of the dipole features. When IN are initialized at lower altitudes, our hypothesis is unproven. It may be that with additional time modeled, or increased initial IN concentrations at the lower levels, the effects will be similar to the higher-initial-altitude experiments.

While modeling these IN with a mesoscale model, a few issues arose that necessitate both care in interpreting these results and caution when modeling in the future. First, given the grid spacing used here (30 km square), we have only a gross estimate of vertical motions. This not only affects how IN are transported, but would also affect how ice crystals grow and precipitate. Secondly, the UWNMS' microphysics are calculated in bulk. This has an advantage for speedy calculations, but there are disadvantages too—such as when different cloud particle size spectra may exist, as they would likely exist in the presence of IN. Noise will probably be an issue in any model study, and we have seen its effects here. Noise in pristine ice was filtered with a threshold test, but the vapor and vertical velocity fields were not filtered for noise (Appendix C). Some of these issues could be resolved by using a finer grid spacing, spatial noise filtering, and/or using a different numerical model. Even then, though, parameterizations will still need to be made to model the effects of IN.

Much more work is needed to refine our understanding of the relationships between IN and the apportionment of water in the upper troposphere and lower stratosphere. Most importantly, we need more knowledge of IN in order to do a more realistic, non-idealized study with known IN activation conditions. Secondly, experiments need to model longer periods of time, for a week or more, so that IN and/or IN-influenced air has a chance to enter the TTL. Different time periods and locations should be modeled. How does convective strength, which varies in space and time, affect the magnitude and distribution of IN-induced changes? Provided additional information about activation conditions for organic IN, I would suggest future work modeling varying IN concentrations over the maritime continent, where organic aerosols are also regularly loaded into the atmosphere from biomass burning, and where convective towers reach the TTL more readily than they do over the Amazon basin.

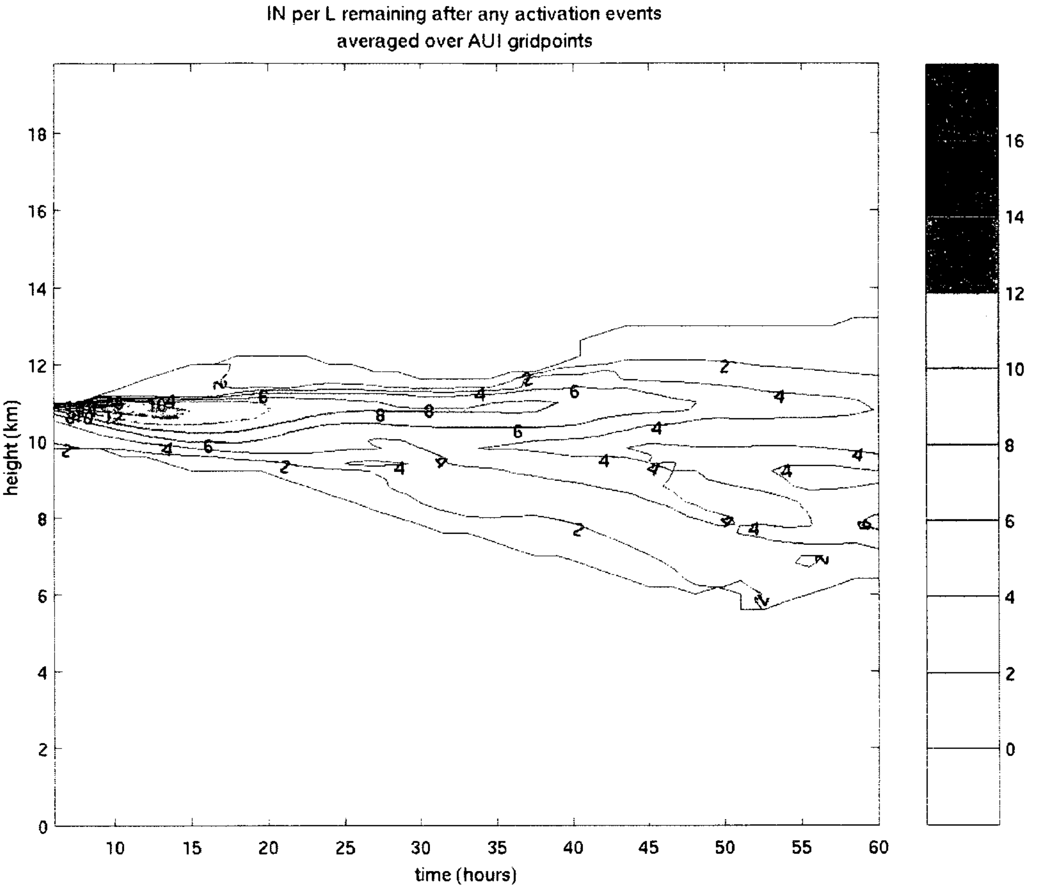

Figure 8.1. Unactivated IN in the experiment with 60 IN/L initialized at 250 hPa and with an activation temperature of 238 K. Though the number of IN is depleted over time via activation, the IN are far from being completely "used up" by activation. Since IN are present and continuing to activate over the 60 hours modeled, changes in vapor and ice are continually accruing in-cloud and spreading to both cloudy and non-cloudy areas. The result is that downstream changes from past activation, which would tend to include more "out of cloud" areas, are continually altered by changes resulting from recent activation events "in cloud," as seen in Figure 8.2.

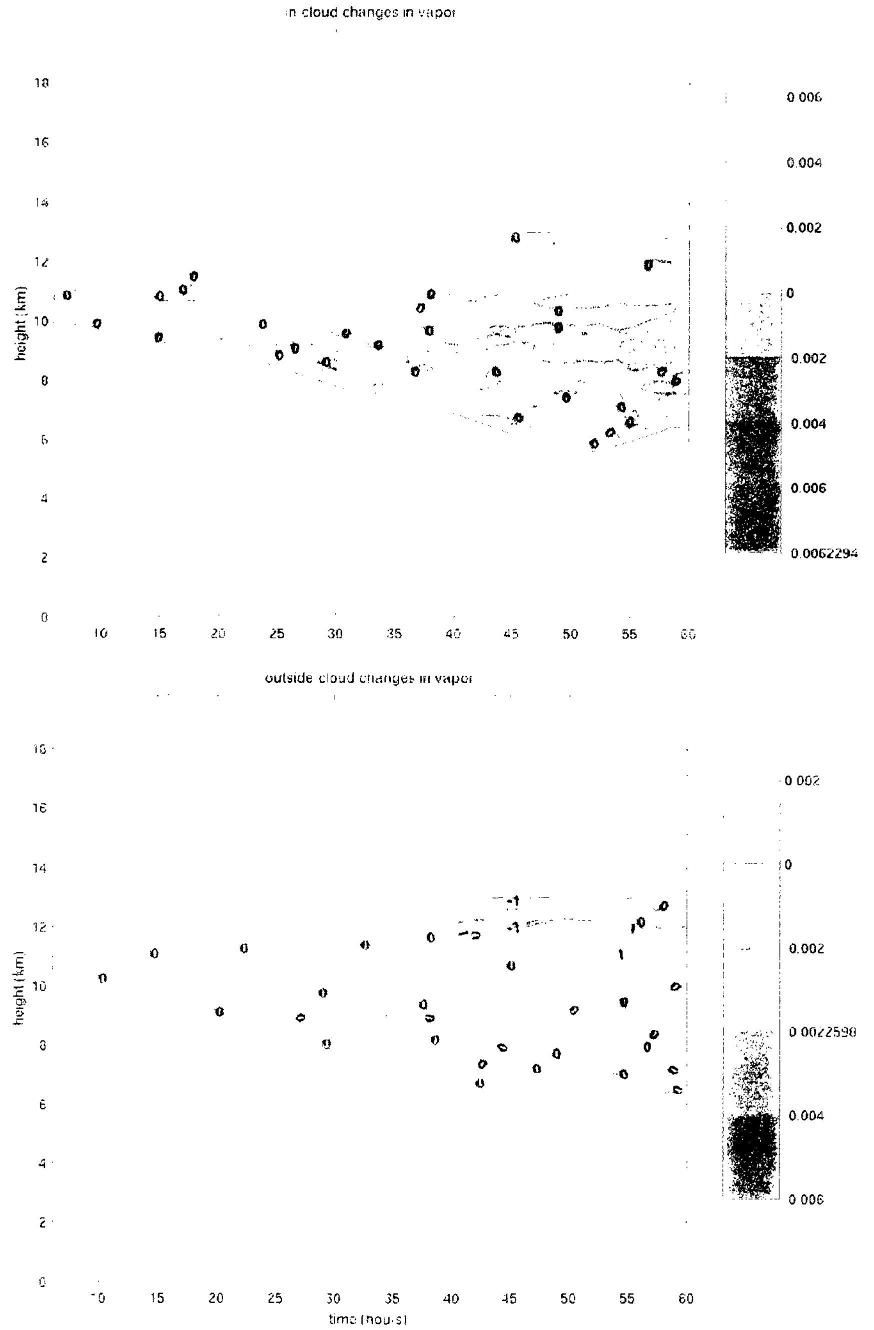
in cloud changes in vapor

outside cloud changes in vapor

Figure 8.2. Vapor changes both inside and outside of cloudy areas, though distributed differently, are of the same magnitude overall. Data are averaged over IN-influenced areas from the experiment with 60 IN/L initialized at 250 hPa. Downstream changes from past activation, which would tend to include more "out of cloud" areas, can be balanced by changes resulting from recent activation events "in cloud." More significantly, with time IN-influenced air spreads to include more area with clouds associated with a stationary front (Chapter 4). With both cloudy areas and IN activation undiminished over the modeled time period, it is unfortunately impossible to quantify the magnitude of changes associated with air newly influenced by IN activation vs. changes upstream in time and space.

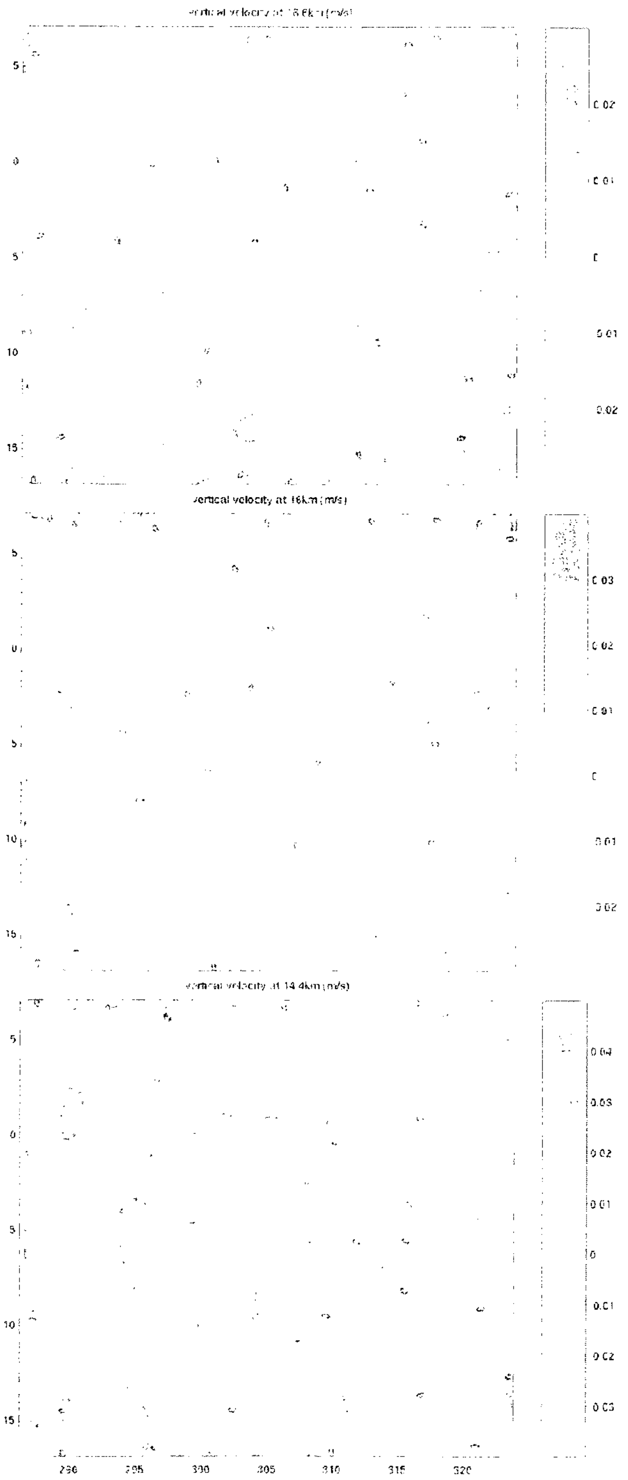

Figure 8.3. Vertical velocity at 16.6, 16, and 14.4 km (top, center, bottom, respectively), 60 hours into the experiment with 60 IN/L fumigated throughout the model domain. The highest-altitude area of IN-influence for this experiment is at 14.4 km, in the northwestern part of the domain, enclosed by the red dashed contour (bottom).

Appendix A—the NMSTASK

```
$START
!!!!!!!!!!!!!!!!!!!!!!!!!!!!!!!!!!!!!!!!!!!!!!!!!!!!!!!!!!!!!!!!!!!!!
!       The model outputs either analysis or history files
!       which are identical in structure.  The advantage
!       of having the two options is that  one can flip/flop
!       on history writes (hot start option) where the
!       file name written is alternately  hfilout(1) or
!       hfilout(2).  This way , disk space doesnt accumulate
!       beyond 2 files (1 if both names are the same)  and
!       there is always something recent to restart from if the computer
!       crashes or the model perhaps exceeds CFL.  At the same
!       time as hot start hist files are made, ioutput=5
!       allows analysis files to be written less frquently,
!       with unique names that allow long term stroage at a
!       given frequency which may be longer than the history frequency.
!
! IFILSTR                     IOUTPUT
! 0--INITIAL START AT T=0.    0--No Output
! 1--START FROM HISTORY FILE   1--Permanent History Files
! 2--START FROM ANALYSIS FILE  2--Analysis Files
!                             3--Hot-Start History Files
!                             4--Permanent History and Analysis Files
!                             5--Hot-Start History and Analysis Files
!!!!!!!!!!!!!!!!!!!!!!!!!!!!!!!!!!!!!!!!!!!!!!!!!!!!!!!!!!!!!!!!!!!!!!!

          ! Output file naming convention

IFILSTR=1,                ! 0 - Initial start; 2 - Start from history file
TIMSTR=140400.,                  ! Starting model (s) time of this run segment.
TIMMAX=216000.,             ! Ending model time (s) of this run segment
IOUTPUT=5,               ! History file output type (see above)
HFILIN ='Mon1.Bnil.2340m' .     ! input history/analysis file name

AFILOUT(1)='Mon1.Bnil.',     ! History Filename Prefix
HFILOUT(1)='Mon.Bnil.',     ! History Filename Prefix
HFILOUT(2)='Mon.Bnil.',     ! History Filename Prefix
VISFIL='1.MonicaVuvP1.Bnil.'.          ! Visualization Filename Prefix
GMETAFNM='MonicagUVp1.Bnil.f'.       ! Gmeta Filename Prefix
```

```
HFUNITS='m',AFUNITS='m',VFUNITS='M',! history/analysis/vis filename time units
FRQHIS  = 900.,
FRQANL  = 10800., ! history/anal file frequency

           ! Variable Initialization Files (varfil)
           !and their corresponding model times (vtime)

! TERRAIN DATA FILE INFORMATION
  INTERR = 'UWNMS.TERRFILE',        ! TERRAIN FILE NAME
  TOPOWLN= -180.00, TOPOSLT= -90., ! WEST LON, SOUTH LAT
  TERSPC =      0.16666666,        ! GRID SPACING IN DEGREES
  ITERX=2161,JTERY=1081,
  ITOPOSM=0,                   ! number of 1-2-1 smoothers on topo

  TILEFILE='/usr/terrain/a10g.dec',
        '/usr/terrain/b10g.dec',
        '/usr/terrain/c10g.dec',
        '/usr/terrain/d10g.dec',
        '/usr/terrain/e10g.dec',
        '/usr/terrain/f10g.dec',
        '/usr/terrain/g10g.dec',
        '/usr/terrain/h10g.dec',
        '/usr/terrain/i10g.dec',
        '/usr/terrain/j10g.dec',
        '/usr/terrain/k10g.dec',
        '/usr/terrain/l10g.dec',
        '/usr/terrain/m10g.dec',
        '/usr/terrain/n10g.dec',
        '/usr/terrain/o10g.dec',
        '/usr/terrain/p10g.dec',

! SEA SFC DATA FILE INFORMATION
  INSST = '/usr/terrain/SSTNH',      ! TERRAIN FILE NAME
  INSST = 'GRIB',      ! TERRAIN FILE NAME
  SSTWLN= -180.00, SSTSLT=1.0,   ! WEST LON, SOUTH LAT
  SSTSPC =      1.0,           ! GRID SPACING IN DEGREES
  ISSTX=360,
  ISSTY=90,
C
```

```
INITIAL =   2,     ! Initial fields - 1=horiz.homogeneous, 2=variable
IPBLFIX=1,          ! ATM T, RV adjustment over water
DATSRC='ECMWF','ECMWF','ECMWF','ECMWF','ECMWF','ECMWF',
    'ECMWF','ECMWF','ECMWF','ECMWF','ECMWF','ECMWF',
    'ECMWF','ECMWF','ECMWF','ECMWF','ECMWF','ECMWF',
    'ECMWF','ECMWF','ECMWF','ECMWF','ECMWF','ECMWF',
VTIME =  000000.,
      43200., 86400.,  129600., 172800.,
      216000.,259200.,302400.,345600.,
      388800.,432000.,475200.,518400.,
      561600.,604800.,648000.,691200.,
      734400.,777600.,820800.,864000.,
      907200.,950400.,993600.,
VARFIL='ECMWF.SEP1992',
    'ECMWF.SEP1992',
    'ECMWF.SEP1992',
    'ECMWF.SEP1992',
    'ECMWF.SEP1992',
    'ECMWF.SEP1992',
    'ECMWF.SEP1992',
    'ECMWF.SEP1992',
    'ECMWF.SEP1992',
    'ECMWF.SEP1992',
    'ECMWF.SEP1992',
    'ECMWF.SEP1992',
    'ECMWF.SEP1992',
    'ECMWF.SEP1992',
    'ECMWF.SEP1992',
    'ECMWF.SEP1992',
    'ECMWF.SEP1992',
    'ECMWF.SEP1992',
    'ECMWF.SEP1992',
    'ECMWF.SEP1992',
    'ECMWF.SEP1992',
    'ECMWF.SEP1992',
    'ECMWF.SEP1992',
    NMCX=45,NMCY=27,WLON=-50.,SLAT=12.5,
    NMCX=144,NMCY=73,WLON=0.,SLAT=-90.,
```

```
                ! Output Frequencies

FRQIPR  = 21600., FRQIST=300.,       ! Integral print and store
FRQSND  = 1000000.,        ! Frequency of STVJAS type sounding output
FRQTRM  = 1000000.,        ! Frequency of Term Analysis

IVIS    =  0     ,        ! IVIS=0 for no visualizations
                    !    =1 for visualizations old vis5d format
                    !    =2 for new vis5d format
INFPLFL  = 0,              !  1=0n/0=off standard "fancy" plots on pressure
I4PNL   = 0,               !  1=0n/0=off standard "fancy" plots on pressure
ICLMAP=0,                ! Flag to make a color map
                    ! surfaces

                ! Other Output switches

ICLNSTR= 1,         ! 0 clean/1 verbose  output
INITFLD =1,         ! switch to turn on (1) or off (0) plots of initial time
ISUPCEL  = 0,       ! 0 for no supercell indx, >1 for supercell indx
IGRBWRT  = 0,        ! 0 for no GRIB output, >1 for GRIB output
IGRBMOHR= 1,          ! Flag for monnth/hour on grib
FRQGRB  = 10800.,     ! Frequency of GRIB output

                ! Time Differencing
 DTLONG=20.                   ,! Long time step and ratio

               ! Simulation title (64 chars)
  EXPNME  = 'Monica',

$END

 !
 ! This contains input file stuff common to all time periods
 !

$GRIDS
 NGRIDS  =   1,                 ! Number of grids for run
                         !
 NNXP    = 90, 152,  194,    202,     ! Number of x gridpoints
 NNYP    = 60, 128,  194,    202,     ! Number of y gridpoints
```

```
   NNXP   = 140, 152,  194,   202,    ! Number of x gridpoints
   NNYP   = 90, 128,  194,   202,    ! Number of y gridpoints
   NNZP   =  100,  40,  40,   40,    ! Number of z gridpoints

   NNZG   =  5,  5,   5,    5,     ! Number of soil gridpoints
               !
   NXTNEST =  1,  1,   2,    3,     ! Grid number which is the next
                                    !   coarser grid
           !  !
           !  !                     ! Nest ratios between this grid
           !  !                     !  and the next coarser grid.
   NSTRATX =  1,  3,   4,    2,     ! x-direction
   NSTRATY =  1,  3,   4,    2,     ! y-direction
   NSTRATZ =  1,  1,   1,    1,     ! z-direction
   NNDTRAT =  1,  3,   4,    1,     ! time
   NNRATIO=   4,  4,   4,   10,
   NFRATIO=   2,  2,   2,    2,
   NITOPBC=   0,  0,   0,    0,
   NIMPL=     1,  1,   1,    1,
   SSPCTN=    0.,  0.,  0.,   0.,   !Acoustic Step
   UMX   =  80., 80., 80.,  80.,    ! Max Hor Vel for checking  timestep
   WMX   =  10., 10., 10.,  10.,    ! Max vert vel for checking timestep

C              High Resolution topography file
   HIRESTOPO='NONE','NONE','NONE','NONE',  !Place to store topo for grid to avoid

C              Temporary Grid File

   TOPOFILE='NONE','NONE','NONE','NONE', !Place to store topo for grid to avoid
c                    reinterpolating all of the time.
c                    set to 'NONE' to force topo to be interpolated from
c                    master topo file

                ! Numerical Filtering
   NFORDH=   4,   4,    4,  4,     ! Order of hor filter (even number)
   NFORDV=   6,   6,    6,  6,     ! Order of hor filter (even number)
                                   ! in horizontal
                                   ! in vertical
   FILT4V=  .005,  .005,   .005, .025,    ! Fraction of maximum smoothing used
   FILT4H=  .10,  .1,   .1,  .1 ,   ! Fraction of maximum smoothing used
```

```
                ! Turbulence Kinetic energy prediction
IDIFFKH =  3,  3,   3,    3,     ! no TKE prediction=0,
IDIFFKV =  3,  3,   3,    3,     ! no TKE prediction=0,
NITKEFG =   1,  1,   1,    0,     ! no TKE prediction=0,

                ! Surface Layer parameterization
NISFCL =   1,  1,  1,    1,    ! 0-specified surface layer gradients
            !                  ! 1-soil model (Tremback/Kessler)
            !                  ! 2-soil model (McCumber/Mahrer/Pielke)
            !
FRQSFL=  60., 20.0,  10., 10.,     ! Frequency (seconds) for soil calls
                               ! on each grid

                ! Radiation parameterization
NIRAD   =   1,  1,   1,    1,    ! Radiation flag, 0-off, 1-on 2-interp
FRQRAD=  3600.,1800.,300.,60.,     ! Frequency (seconds) for radiation

                ! Convection parameterization
NNQPARM =  4,  0,   0,   1,     ! convective parameterization flag
                               ! Parameterization activated by
                               ! including appropriate parameteriza-
                               ! tion packet at compile time, however
                               ! nnqparam=1 includes only two extra
                               ! 3d variables (moisture and theta
                               ! source) needed for Kuo, while
                               ! nnqparam=2 includes a third variable
                               ! for emanuel schemes, an nnqparam=3
                               ! includes a total of 4  needed for
                               ! kain/fritsch (runnaverage w, two
                               ! ice and rain tendencies)
CONFRQ  = 20.,300.,600.,            ! Frequency of conv param. calls which
                               ! should be  close to timestep


                               ! for emanuel, about 1800s for kain
E2DTCRIT=-1.00,-1.00,-0.01,-.01,          ! Assumed vertical motion of
E2SIGMA=0.10,0.10,0.15,.05,         ! Greatest fraction of domain which
E1BETA=0.10,0.10,0.10,
E1ALPHA=0.80,0.80,0.15,.05,         ! Greatest fraction of domain which
```

```
  E2DTCRIT=-0.01,-0.01,-0.01,-.01,        ! Assumed vertical motion of
  E2SIGMA=0.50,0.50,0.15,.05,         ! Greatest fraction of domain which
  E1BETA=0.99,0.99,0.99,
  E1ALPHA=1.25,1.25,0.15,.05.         ! Greatest fraction of domain which

!  E2DTCRIT=-2.00,-2.00,-0.01,-.01,        ! Assumed vertical motion of
!  E2SIGMA=0.10,0.10,0.15,.05,         ! Greatest fraction of domain which
!  E1BETA=0.10,0.10,0.10,
!  E1ALPHA=0.80,0.80,0.15,.05,         ! Greatest fraction of domain which

  NE2CNPRT=1,1,0,0,                ! Printout summarizing param activity
  NE2DADJ=1,1,1,1,               ! Flag to turn on the dry adjustment
  CAPFCT =  0.,0.,1.,1.,          ! vertical motion needed

!  E2SIGMA=0.10,0.10,0.15,.05,         ! Greatest fraction of domain which
!  E1BETA=0.01,0.01,0.10,
!  E1ALPHA=0.80,0.80,0.15,.05,         ! Greatest fraction of domain which
  NE2CNPRT=1,0,0,0,                ! Printout summarizing param activity
  NE2DADJ=1,1,1,1.               ! Flag to turn on the dry adjustment
!  E2DTCRIT=-1.00,-1.00,-0.01,-.01.        ! Assumed vertical motion of
  CAPFCT =  0.,0.,1.,1.,          ! vertical motion needed
                                ! at cloud base for convection
                                ! to start--used only by kuo scheme
                                ! at cloud base for convection
                                ! updrafts can occupy

                    !  Surface topography
  NETA   =  1,  1,   1,    1,    ! Flag to turn ETA coordinate on

                    !  Chemistry and tracers to be added
  NIECFL  =  0,  0,   0.    0,    ! Elemental Carbon Tracer     =0
  NISO2FL =  0,  0,   0,    0,    ! Sulfer Dioxide Tracer       =0
  NINO2FL =  0,  0,   0,    0,    ! Nitrogen Dioxide Tracer     =0
  NIAGIFL =  0,  0,   0,    0,    ! Silver Iodide Tracer        =0
  NIO3FL  =  1,  0,   0,    0,    ! Ozone Tracer                =0
  NITR1FL =  0,  0,   0,    0,    ! Generic Tracer 1            =0
  NITR2FL =  0,  0,   0,    0,    ! Generic Tracer 2            =0
  NITR3FL =  0,  0,   0,    0,    ! Generic Tracer 3            =0
  NITR4FL =  1,  0,   0,    0,    ! "anti-IN" quasi-tracer      =0
```

```
NIHINFL = 1,  0,   0,    0,    ! Ice Nucleus Tracer needs to be on always
                          ! change INfile in vin_grib_settings.HALOE
                          ! to "null" if you don't want the IN "on."

              ! Microphysical setup
NLEVEL  =  3,  3,   3,    3,    ! moisture complexity level
     !                     ! 0-completely dry,
     !                     ! 1-vapor passive tracer
                           ! 2-supersaturation condensed
                           ! 3-microphysics
NIRCNFL  =  3,  3,   3,    3,   ! Microphysics flags
NIPCNFL  =  5,  5,   5,    5,   !-------------------
NISCNFL  =  3,  2,   2,    2,   ! where x= R - rain
NIACNFL  =  2,  2,   2,    2,   !        P - pristine crystals
NIGCNFL  =  3,  2,   2,    2,   !        S - snow
     !                !      A - aggregates
RDISTPN  =.08, .08, .08, .08,   !        G - graupel
PDISTPN  = 0.,  0.,  0.,  0.,   !
SDISTPN  = .014,  .08,  .08,  .08,  ! NIxCNFL = 0 - no species
ADISTPN  = .33,  .33,  .33,  .33,   !        1 - diagnostic concen.
GDISTPN  = .071,  .03,  .03,  .03,  !        2 -

!  NIRCNFL  =  3,  3,  3,  3,  3,  5, 5,5,  ! Microphysics flags
!  NIPCNFL  =  5,  5,  5,  5,  5,  5, 5,5,  !-------------------
!  NISCNFL  =  3,  3,  3,  3,  3,  3, 3,3,  ! where x= R - rain
!  NIACNFL  =  2,  0,  2,  2,  2,  2, 2,2,  !        P - pristine crystals
!  NIGCNFL  =  3,  0,  3,  3,  3,  3, 5,5,  !        S - snow


              ! Grid Positioning
NKNEST  =   1,    1,    1,    1,    ! k-point (only loc)
IMOVE   =   0,    2,    2,    2,    ! Flag to activate grid moving

XLNNST1 =  -55.0, -55.0, -73.0, -76.1,! Final location (m) of x anchor point
YLTNST1 =  -5.0,  14.56,  26.7,  30.4,! Final location (m) of y anchor point

XLNNST2 =  -55.0, -72.0, -77.0, -77.0,! Final location (m) of x anchor point
YLTNST2 =  -5.0,  17.5,  34.5,  34.5,! Final location (m) of y anchor point

TFINISH =   0.,   345600., 345600., 345600.,   ! time nest reaches finish point
```

```
 TFINISH =   0.,   648000., 648000., 648000.,   ! time nest reaches finish point

$END

$INDAT
 IFLG15=1,
 IFLG18=1,
 IFLG17=0,
 IFLG19=2,
 IFLG16=2,
IFLG18=2,

   !  Debugging Options
 IDEBUG  = 0   ! 0 - DONT print out debug print statements in vdv_tmh
               ! 1 - DO   print out...

 IFLG1=0,
 ISYMT=0,            ! Flag to turn on symmetry checking
 ISTPOFF=0,          ! Flag to turn on  all terms and execute model flow only

 IEXFG=1,1,1,1,1,1,1,1,1,1, ! 6 is diffuse,8 is cuparm,9 is thpert,2 is windin
      1,1,1,1,1,1,1,1,1,1, ! 13 is filt4,14 is corlos,15,16,17 are advection
      1,1,1,1,1,1,1,1,1,1,  ! leav on 1,7,21,35,41,45
      1,1,1,1,1,1,1,1,1,1,
      1,1,1,1,1,1,1,1,1,1,
 NOMICRO=0,          ! Flag to turn off micro tendencies
 ISTRMDN=1,          ! Flag to turn on density weighting of streamfunctions
 ITRMFG =0,          ! Flag to turn term anal on
 NTPNT  =1,          ! Number of term anal points
 ITPNT  =1,          ! Term i points
 JTPNT  =1,          ! Term j points
 KTPNT  =1,          ! Term k points
 NGPNT  =1,          ! Grid of point


   !  Description of Rotated Spherical Grid
 LATLON  = 1,           ! Flag that turns on spherical grid (instead
                     ! Pole makes with a true north-south line on Earth.
 ELATORIG= -5.0,         ! Latitude of Earth at origin of local spherical
                     ! grid.
```

```
ELONORIG= -70.0,        ! Longitude of Earth at origin of local spherical

                  ! grid.
ANGPOLE=0.,           ! Angle a line running from local origin to Earth's

ICENTFG=0,            ! If =12 then define center using pot vort max
                  ! rather than just press min for moving grid



              !  GRID SPACING
          !  Of outer grid (others are specified interger
          !  ratios of these values.  "x lengths" are defined at the  equator
          !  of the local spherical grid if used.

DELTAX  = 30000.0,   DELTAY  = 30000.0,   ! X AND Y GRID SPACING
DELTAZ  =  200.,   DZRAT  =   1.00, DZMAX=1000.,
NCONSTDZ  = 5,        ! First vertical gridpoint to use stretched dz's
                     ! attained after which the spacing is held
                     ! constant above..
                     ! If one wishes to customize the  vertical
                     ! spacing, one can set the "w" points,
                     ! for "nzp" points, beginning with a surface
                     ! value of "0. meters".  To tell the model
                     ! that the customized zz values are to be
                     ! used, set DELTAZ=0. also

! ZZ = 0.,500.,1500.,2500.,3000.,4000.,5000.,6000.,7000.,
!      8000.,9000.,10000.,11000.,12000.,13000.,14000.,14200.,14400.,
!      14600.,14800.,15000.,15200.,15400.,15600.,15800.,16000.,
!      16200.,16400.,16600.,16800.,17000.,17200.,17400.,17600.,
!      17800.,18000.,18200.,18400.,18600.,18800.,19000.,19500.,
                     !  The soil levels are set here
                     ! going from the  bottom up
SLZ     = -.32,-.16,-.04,-.01,0.0,

              ! Flags to turn miscelaneous functions
OFFSETX=0.0,    ! Offset to determine centering of moving grid
OFFSETY=0.0,

              ! Topography setup and smoothing
```

```
NZSMTH =      0,  ! Number of passes for topography smoother
IZFLAT =      0,  ! Width of flat margin around domain (in grid points)
PSLDTDZ = 0.0077,   ! Flag for lapse rate for eta psl reduction

             !  MEAN PRESSURE
                 !  How to specify mean pressure( which
                 !  is not unique because the model has a finite top
IPMNFG  =      1 , ! =1 Remove mean mass divergence in lateral B. C.
IPMNTYP = 2,       ! 0 - dont do anything, let it drift
                 ! 1   outer domain mean surface pressure held constant
                 ! 2   outer domain mean surface pressure form
                 !    external variable init outer model, ie thbal
             ! Computation of Cape for printed output

PARMIX = 0.,          ! Ratio of mixing of parcel with environment
                 ! per 1000m of ascent when saturated. Does not
                 ! mix when unsaturated. (to mimic TKE effect).
                 ! Formerly pert20 [Steve]
IWPARMIX = 0,       ! Saturated if 1, Dry if 0. Formerly  [Steve]

             !ARTIFICIAL PERTURBATIONS
             !    for
          ! Horizontally homogeneous initializations

            ! 1.    "Warm Bubble"
ITHERMAL  =   0,   ! Prescribed initial thermal
                 !    1 - - BUBFRC
                 !    2 - - DWNFRC
                 !    3 - - BAKFRC
                 !    4 - - BAKFRC1
                 !    5 - - THFRC

            ! 2.   "Witch of Agnesi Mountain"
HGTMTN  = 0.,       ! Height for Witch of Agnese Mountain
HFWLMTN = 0.,        ! Left  side half width for Witch of Agnese Mountain
HFWRMTN = 0.,        ! Right side half-width for Witch of Agnese Mountain
GNDMTN  = 0.,       ! Distance in X where mountain hits the ground

            ! 3.  Topography spin up
TIMSCL =     0.,  ! Initial wind spin-up - time scale
```

```
KSPIN  =    33,  !                 - below this level (velocity)
KMSPIN =     0,  !                 - below this level (momentum)

          !  Lateral and Upper Boundary Conditions
IBND   =     1,  ! Lateral boundary condition flags
JBND   =     1,  ! 1-Klemp/Wilhelmson, 2-Klemp/Lilly, 3-Orlanski
            ! 4-cyclic, 0-Hack/Schubert normal mode
            ! =0 Do Not remove mean momentum divergence across LBC
TAUTRND = 10800.,
CPHAS  =    30.,  ! Phase speed if IBND or JBND = 1
LSFLG  =     2,  ! Large-scale gradient flag for variables other than
            ! normal velocity:
            ! 0 = zero gradient inflow and outflow
            ! 1 = zero gradient inflow, radiative b.c. outflow
            ! 2 = constant inflow, radiative b.c. outflow
NFPT   =    6 ,  ! Rayleigh friction - number of points from the top
DISTIM =   600.,  !                 - dissipation time scale
NFPTH  =   25 ,  ! Rayleigh friction in horizontal for var init bc.
DISTIMH =  1800.,  ! Dissipation time scale in horizontal
NRFEXP =     1 ,  ! Power of ramping function for horizontal dis (c=r**i10)

          ! Miscellaneous Physics settings
ICORFLG=      2,  ! Coriolis flag/2D v-component - 0 = off
            !                  1 = f plane
            !                  2 = var f
OMEGA = 7.292E-5,  ! Rotation rate of earth for Coriolis param
IPRSPLT =     0,  ! precipitation time-split scheme - 0=off, 1=on
IADVH  =     2,  ! Order of horizontal advection - Leapfrog - 2 or 4
IADVV  =     2,  !  "   "  vertical     "      - Forward  - 2 or 6
IDADVH  =     2,  ! Order of horizontal advection - Leapfrog - 2 or 4
IDADVV  =     4,  !  "   "  vertical     "      - Forward  - 2 or 6

          ! Grid Independent  Microphysics constants
CCN = 300.,
CCN= 100.,          ! CCN concentration
AMI0=1.5E-09,
AMI0=4.8E-10,        ! initial crystal mass (g)
THOMO  =   10.0,     ! homogeneous nucleation temperature

          ! Grid Independent RADIATION PARAMETERS
```

```
 ISWRTYP =   1,   ! Shortwave radiation type 0-Mahrer/Pielke, 1-Chen
 ILWRTYP =   1,   ! Longwave radiation type 0-Mahrer/Pielke, 1-Chen
 RADFRQ  = 1800.,  ! Frequency of radiation tendency update in seconds
 IRADL=2,        ! Longwave Raidation type (Cotton 1,Panegrossi 2)
 IRADS=2,        ! Shortwave Raidation type  (Cotton 1,Panegrossi 2)

             ! IF LONRAD=1, STRTIM is GMT
 LONRAD =   1,   ! Longitudinal variation of shortwave  (0-no, 1-yes)
             !   if  1, STRTIM is local time of  X(1)
IMONTH1 =  09,   ! Month  (if no variable init)
IDATE1  =  26,   ! Date  (if no variable init)
IYEAR1  =  92,   ! Year  (if no variable init)
STRTIM=0.,
             ! Grid Independent Cumulus parameterization parameters
 CPTIME=0.,        ! Time after which cumulus parameterization is activated
              ! Should be zero except for kuo

              ! Surface layer
 ZIINIT  =  0.,    ! Initial PBL height fo O'brien K
 USTMIN  =  .05,   ! Minimum U_* in surface layer parameterization
 UBMIN   =  1.0,  ! Minimum U value to use in computing U_*
 IWF=0            ! flag to turn on the w flux at top of PBL
 MICROLYR=0,       ! 1:Stull Microlayer,2: Pielke Micro Layer,
 ZMU= 0.005,       !  depth of micro layer
 ISTARS = 3,
 ISTARS  =   1,    ! surface layer param. 1-Businger, 2-Louis 3-Bulk
 ISRCALB =  0,      ! Flag for souce of albedo - 0 = RAMSIN, 1 = var input
 ALBEDO  =  0.18,   ! constant albedo when not running soil model
 ISRCZ0  =  0,      ! Flag for souce of albedo - 0 = RAMSIN, 1 = var input
 ZROUGH  =  0.01,   ! constant roughness if for all domain
 ZROUGH  =  1.00,   ! constant roughness if for all domain
 PERT20=0.95,

             ! SOIL MODEL
 PCTLCON =  0.,    ! constant land percentage if for all domain
 NSLCON  =   6,    ! constant soil type if for all domain
 SEATMP  = 280.0,   ! constant water surface temperature
 DTSLMN=60.,
 DTSLMN=3.,        ! Soil timestep
 ISOILM  =   1,    ! soil moisture model flag 0-temp only, 1-temp+moist.
```

```
DTHCON  =  0.,    ! constant surface layer temp gradient for no soil
DRTCON  =  0.,    ! constant surface layer moist gradient for no soil
SOILDZ  =  0.,    ! soil model grid spacing
ISFCINIT =  3,    ! Flag for how to initialize soil temp/moisture
ISFCINIT =  1,    ! Flag for how to initialize soil temp/moisture
              ! 1 - Tremback method of temp=air-4,moisture=sfc relhum
              ! 2 - New method of tempsfc=air+tsadd,
              !     tempdeep=tdeepc,
              !     relhum=slz
              ! 3 - New method of tempsfc=air+tsadd,
              !     tempdeep=sst(i,j) from NMC data,
              !     relhum=slz
TSADD  = 0.,      ! Value in celsius of temp added to air temp to get
              ! surface soil temp
TDEEPC  = 20.,    ! Deep Soil temperature in Celsuis
DRYLAT = 80.,     ! Latitude above which we assume soil is dry
              !(for emulating
              ! non-active vegitation.  Top soil moisture is set to
              ! slmnorth north of this, and linearly decreased
              ! from normal value in the translat degrees south of this.
TRANSLAT = 5.,    ! Delta latitude in which we decrease from slmstr
              ! (NZS) to drylat
SLMNORTH = .30,   ! Soil RH to be applied to top soil level above drylat
ISNOWSRC = 0,     ! Flag to use latitude (0) or grided data (1)
              ! to determine snow cover
MSLPSLVR=3,

PERT3=4.e-3,
              ! to determine snow cover
SLTFRZ=80.0,      ! Latitude north of which soil is frozen
SLTSNW=80.0,      ! Latitude north of which soil is snowcovered
ICANADA=0,IGTLKS=0,

              !  (isnowsrc=1)
SLMSTR  =  0.6,0.56,0.48,0.41,0.36,       ! initial soil moisture
SLMSTR  =  0.69,0.56,0.48,0.41,0.36,       ! initial soil moisture

SLZ    = -.32,-.16,-.04,-.01,0.0,

  ! Eddy diffusion coefficient parameters
```

```
             !  TURBULENCE SCHEME
IWDIFFK = 0,      ! 0=K computed at thermo point, 1=at w point
IVSCALE = 6,      ! Vertical scale length
IVSCALE = 1,      ! Vertical scale length
             !   1 - delta z
             !   2 - sqrt(delta z**2 + delta x**2 + delta y**2)
             !   3 - (delta z * delta x * delta y) ** 1/3
             !   4 - "old RAMS" dependent on Richardson number
             !   5 - Deardorff (.76*sqrt(E/EN)) if stable; 3 if unst.
             !   6 - Deardorff (.76*sqrt(E/EN)) if stable; 1 if unst.
IHSCALE = 3,      ! Horizontal scale length
             !   1 - use vertical scale length
             !   2 - sqrt(delta x**2 + delta y**2)
             !   3 - sqrt(delta x * delta y)
IVDEF = 4,       ! Use of deformation in vert/horiz K
IHDEF = 4,       !   0 - no
             !   2 - use vertical parts only
             !   3 - use horizontal parts only
IVEN = 1,        ! Use of Brunt-Vaisalla frequency in vert/horiz K
IHEN = 0,        !   0 - no
             !   1 - yes (only when unstable)
IWETEN = 1,       ! 0 - Don't use / 1 - Use : moist Brunt Vaisalla freqency
VDKR=0.21,        ! Adjustable parameter, deformation vert. K's coefficient
HDKR = 0.21,      ! Adjustable parameter, deformation horiz. K's coefficient
AKMIN = 0.00,     ! Ratio of minimum horizontal eddy viscosity coefficient
IRAMP=0,         ! Flag to set "ramp" distance for ramping up mix coef
             ! horizontal scale lengths as lateral grid
             !boundary approached.

                 !   4-6 order Filter Setup

ISM4H=0,         ! Horiz tracer 4th ord diff flag - 0=on, 1=off
ISM4V=0,         ! VERT  tracer 4th ord diff flag - 0=on, 1=off
ISMDEN=1,         ! Filter with 1d base state density or evolving density
I4BAL=0,         ! Filter velocity against outer grid solution?

$END

$SOUND
```

```
          ! SOUNDING SPECIFICATION
      !  (ONLY USED for HORIZONTALLY HOMOGENOUS INITIALIZATION)

 SNDLON=-95. ,SNDLAT=44.0.    !I,J LOCATION OF POINT WHICH SOUNDING IS
 ITMPFL=0              ,!TEMPERATURE FORM(0-C, 1-K)
 IRH0FL=0              ,!HUMID FORM(0-DP C. 1 DP K, 2 RT G/KG, 3 RH %
 IWSRC=-1              ,!INITIAL WIND SRC (< OR = 0 -SNDG, 1-PROFILE)
 KMEAN1=0               ,!BASE LVL FOR UMEAN CALC OR UMEAN IF IWSRC < 0
 KMEAN2=0               ,!BASE LVL FOR VMEAN CALC OR VMEAN IF IWSRC < 0
IUVFLG=1               ,!WIND FORM (1 - DIR,SPD    0 - U,V )

  !  Below the $ END is formatted input of the horizontally
  !  homogeneous sounding (5f10.0 format,
 !  p(mb)     t(c)    td(c)       dir spd (m/s)
$END
  1000.0    -8.00    -9.00
   960.0   -10.40   -18.00
   920.0   -13.00   -19.00
   870.0   -13.00   -22.00
   820.0   -14.00   -24.00
   800.0   -15.40   -25.00
   700.0   -23.50   -32.40
   500.0   -45.00   -51.00
   430.0   -55.00   -59.00
   415.0   -55.00   -61.00
   400.0   -55.00   -59.00
   370.0   -58.00   -64.00
   350.0   -58.50   -64.50
   300.0   -59.00   -65.00
   200.0   -61.00   -68.00
   100.0   -61.00   -68.00
    50.0   -61.00   -68.00
     5.0   -61.00   -68.00

$PRNT
        !   SOUNDING OUTPUT
        !    Sounding points to be saved for later analysis

 ISNDPT(1)=0,
```

```
ISNDPT(2)=0,
ISNDPT(3)=0,
ISNDPLT(1,1)=0,
JSNDPLT(1,1)=0,
ISNDPLT(1,2)=0,
JSNDPLT(1,2)=0,
ISNDPLT(1,3)=0,
JSNDPLT(1,3)=0,

    ! 4 PANEL CONTROL
FRQ4PNL =3600. , 900.,900., ! Frequency of 4 panel outputs

  FRQ4PL( 1,1)=3600., !I4SFTYP( 1,1)=0,    !'SFC1'
  FRQ4PL( 2,1)=7200., !I4SFTYP( 2,1)=0,    !'8501'
  FRQ4PL( 3,1)=7200., !I4SFTYP( 3,1)=0,    !'7001'
  FRQ4PL( 4,1)=7200., !I4SFTYP( 4,1)=0,    !'5001'
  FRQ4PL( 5,1)=7200., !I4SFTYP( 5,1)=0,    !'2501'
  FRQ4PL( 6,1)=21600., I4SFTYP( 6,1)=0,    !'TMX1'
  FRQ4PL( 7,1)=21600., I4SFTYP( 7,1)=0,    !'TMN1'
  FRQ4PL( 8,1)=3600., !I4SFTYP( 8,1)=0,    !'AP1A'
  FRQ4PL( 9,1)=3600., !I4SFTYP( 9,1)=0,    !'AP1B'
  FRQ4PL(10,1)=21600., I4SFTYP(10,1)=0,    !'CPLI'
  FRQ4PL(11,1)=21600., I4SFTYP(11,1)=0,    !'SSCP'
  FRQ4PL(12,1)=21600., I4SFTYP(12,1)=0,    !'SSMX'
  FRQ4PL(13,1)=21600., I4SFTYP(13,1)=0,    !'ISTB'
  FRQ4PL(14,1)=21600., I4SFTYP(14,1)=0,    !'LLJ1'
  FRQ4PL(15,1)=21600., I4SFTYP(15,1)=0,    !'SRH1'
  FRQ4PL(16,1)=21600., I4SFTYP(16,1)=0,    !'STE1'
  FRQ4PL(17,1)=21600., I4SFTYP(17,1)=0,    !'THK1'
  FRQ4PL(18,1)=21600., I4SFTYP(18,1)=0,    !'TRP1'
  FRQ4PL(19,1)=172800.,!I4SFTYP(19,1)=0,    !'SSK1'
  FRQ4PL(20,1)=21600., I4SFTYP(20,1)=0,    !'7MV1'
  FRQ4PL(21,1)=21600., I4SFTYP(21,1)=0,    !'TEP1'
  FRQ4PL(22,1)=21600., I4SFTYP(22,1)=0,    !'THP1'
  FRQ4PL(23,1)=43200., !I4SFTYP(23,1)=0,    !'SKN1'
  FRQ4PL(24,1)=21600., !I4SFTYP(24,1)=0,    !'5DF1'
  FRQ4PL(25,1)=21600., !I4SFTYP(25,1)=0,    !'SDF1'
  FRQ4PL(26,1)=21600., I4SFTYP(26,1)=0,    !'LASA'
  FRQ4PL(27,1)=21600., I4SFTYP(27,1)=0,    !'LASB'
  FRQ4PL(28,1)=21600. ,!I4SFTYP(28,1)=0,    !'SNFL'
```

```
FRQ4PL(29,1)=3600., !I4SFTYP(29,1)=0,     !'AP2A'
FRQ4PL(30,1)=3600., !I4SFTYP(30,1)=0,     !'AP2B'
FRQ4PL(31,1)=21600., !I4SFTYP(31,1)=0,     !'8df1'
FRQ4PL(32,1)=21600., !I4SFTYP(32,1)=0,     !'7DF1'
FRQ4PL(33,1)=21600., !I4SFTYP(33,1)=0,     !'2DF1'
FRQ4PL(34,1)=300., !I4SFTYP(34,1)=0,     !'T001'
FRQ4PL(35,1)=21600., I4SFTYP(35,1)=0,     !'T051'
FRQ4PL(36,1)=21600., I4SFTYP(36,1)=0,     !'CACP'
FRQ4PL(37,1)=21600., I4SFTYP(37,1)=0,     !'BCAL'
FRQ4PL(38,1)=3600.,  I4SFTYP(38,1)=0,     !'CAP1'
FRQ4PL(39,1)=21600., I4SFTYP(39,1)=0,     !'7PV2'
FRQ4PL(40,1)=21600., I4SFTYP(40,1)=0,     !'7MV2'
FRQ4PL(41,1)=21600., I4SFTYP(41,1)=0,     !'LASA'
FRQ4PL(42,1)=21600., I4SFTYP(42,1)=0,     !'LLJ2'
FRQ4PL(43,1)=21600., I4SFTYP(43,1)=0,     !'LLJ3'
FRQ4PL(44,1)=21600., I4SFTYP(44,1)=0,     !'LLJ4'
FRQ4PL(45,1)=3600.,  I4SFTYP(45,1)=0,     !'EML1'
FRQ4PL(46,1)=21600., I4SFTYP(46,1)=0,     !'LASI'
FRQ4PL(47,1)=3600.,  I4SFTYP(47,1)=0,     !'TKE1'
FRQ4PL(48,1)=3600.,  I4SFTYP(48,1)=0,     !'CNV1'

FRQ4PL( 1,2)=900.,   !I4SFTYP( 1,2)=0,     !'SF3A'
FRQ4PL( 2,2)=21600., I4SFTYP( 2,2)=0,     !'8503'
FRQ4PL( 3,2)=21600., I4SFTYP( 3,2)=0,     !'7003'
FRQ4PL( 4,2)=1800.,  !I4SFTYP( 4,2)=0,     !'5003'
FRQ4PL( 5,2)=21600., I4SFTYP( 5,2)=0,     !'TMX3'
FRQ4PL( 6,2)=21600., I4SFTYP( 6,2)=0,     !'TMN3'
FRQ4PL( 7,2)=21600., !I4SFTYP( 7,2)=0,     !'AP3A'
FRQ4PL( 8,2)=21600., !I4SFTYP( 8,2)=0,     !'AP3B'
FRQ4PL( 9,2)=900.,   I4SFTYP( 9,2)=0,     !'CPLI'
FRQ4PL(10,2)=21600., I4SFTYP(10,2)=0,     !'SSCP'
FRQ4PL(11,2)=21600., I4SFTYP(11,2)=0,     !'RIHL'
FRQ4PL(12,2)=3600., ! I4SFTYP(12,2)=0,     !'2DF1'
FRQ4PL(13,2)=3600., !I4SFTYP(13,2)=0,     !'7DF1,
FRQ4PL(14,2)=3600.,  !I4SFTYP(14,2)=0,     !'8DF1'
FRQ4PL(15,2)=3600.  .!I4SFTYP(15,2)=0,     !'SDF1'
FRQ4PL(16,2)=3600.,  !I4SFTYP(16,2)=0,     !'5DF1'
FRQ4PL(17,2)=3600.,  !I4SFTYP(17,2)=0,     !'LLJ1'
FRQ4PL(18,2)=3600.,  I4SFTYP(18,2)=0,     !'BCAL'
FRQ4PL(19,2)=21600., I4SFTYP(19,2)=0,     !'THP1'
```

```
FRQ4PL(20,2)=21600., !I4SFTYP(20,2)=0,     !'SKN3'
FRQ4PL(21,2)=21600., !I4SFTYP(21,2)=0,     !'SSMX'
FRQ4PL(22,2)=21600., !I4SFTYP(22,2)=0,     !'SSK2'
FRQ4PL(23,2)=900., ! I4SFTYP(23,2)=0,     !'SNFL'
FRQ4PL(24,2)=900.,  !I4SFTYP(24,2)=0,     !'AP2A'
FRQ4PL(25,2)=900.,  !I4SFTYP(25,2)=0,     !'AP2B'
FRQ4PL(26,2)=21600., I4SFTYP(26,2)=0,     !'T851'
FRQ4PL(27,2)=21600., I4SFTYP(27,2)=0,     !'T901'
FRQ4PL(28,2)=21600., I4SFTYP(28,2)=0,     !'T951'
FRQ4PL(29,2)=21600., I4SFTYP(29,2)=0,     !'T001'
FRQ4PL(30,2)=21600., I4SFTYP(30,2)=0,     !'T051'
FRQ4PL(31,2)=21600., I4SFTYP(31,2)=0,     !'LLJ3'
FRQ4PL(32,2)=21600., I4SFTYP(32,2)=0,     !'LLJ4'
FRQ4PL(33,2)=21600., I4SFTYP(33,2)=0,     !'LLJ5'
FRQ4PL(34,2)=3600.,  I4SFTYP(34,2)=0,     !'CAP1'
FRQ4PL(35,2)=7200.,  I4SFTYP(35,2)=0,     !'EML1'
FRQ4PL(36,2)=21600., I4SFTYP(36,2)=0,     !'TKE1'
FRQ4PL(37,2)=21600., I4SFTYP(37,2)=0,     !'CNV1'

FRQ4PL( 1,3)=900.,  !I4SFTYP( 1,3)=0,     !'SF3A'
FRQ4PL( 2,3)=21600., !I4SFTYP( 2,3)=0,     !'8503'
FRQ4PL( 3,3)=21600., !I4SFTYP( 3,3)=0,     !'7003'
FRQ4PL( 4,3)=1800., !I4SFTYP( 4,3)=0,     !'5003'
FRQ4PL( 5,3)=21600., I4SFTYP( 5,3)=0,     !'TMX3'
FRQ4PL( 6,3)=21600., I4SFTYP( 6,3)=0,     !'TMN3'
FRQ4PL( 7,3)=900.,  !I4SFTYP( 7,3)=0,     !'AP3A'
FRQ4PL( 8,3)=900.,  !I4SFTYP( 8,3)=0,     !'AP3B'
FRQ4PL( 9,3)=3600.,  I4SFTYP( 9,3)=0,     !'CPLI'
FRQ4PL(10,3)=21600., I4SFTYP(10,3)=0,     !'SSCP'
FRQ4PL(11,3)=21600., I4SFTYP(11,3)=0,     !'RIHL'
FRQ4PL(12,3)=900., !I4SFTYP(12,3)=0,     !'LLJ1'
FRQ4PL(13,3)=21600., I4SFTYP(13,3)=0,     !'LLJ2,
FRQ4PL(14,3)=3600.,  I4SFTYP(14,3)=0,     !'SRH3'
FRQ4PL(15,3)=3600. , I4SFTYP(15,3)=0,     !'SFWT'
FRQ4PL(16,3)=21600., I4SFTYP(16,3)=0,     !'7PV3'
FRQ4PL(17,3)=21600., I4SFTYP(17,3)=0,     !'7MV3'
FRQ4PL(18,3)=3600.,  I4SFTYP(18,3)=0,     !'BCAL'
FRQ4PL(19,3)=21600., I4SFTYP(19,3)=0,     !'THP1'
FRQ4PL(20,3)=21600., I4SFTYP(20,3)=0,     !'SKN3'
FRQ4PL(21,3)=21600., I4SFTYP(21,3)=0,     !'SSMX'
```

```
    FRQ4PL(22,3)=21600., I4SFTYP(22,3)=0,    !'SSK2'
    FRQ4PL(23,3)=900.,   I4SFTYP(23,3)=0,    !'SNFL'
    FRQ4PL(24,3)=900.,   !I4SFTYP(24,3)=0,   !'AP2A'
    FRQ4PL(25,3)=900.,   !I4SFTYP(25,3)=0,   !'AP2B'
    FRQ4PL(26,3)=21600., I4SFTYP(26,3)=0,    !'T851'
    FRQ4PL(27,3)= 900.,  I4SFTYP(27,3)=0,    !'LLS1'
    FRQ4PL(28,3)=21600., I4SFTYP(28,3)=0,    !'T951'
    FRQ4PL(29,3)=21600., I4SFTYP(29,3)=0,    !'T001'
    FRQ4PL(30,3)=21600., I4SFTYP(30,3)=0,    !'T051'
    FRQ4PL(31,3)=21600., I4SFTYP(31,3)=0,    !'LLJ3'
    FRQ4PL(32,3)=21600., I4SFTYP(32,3)=0,    !'LLJ4'
    FRQ4PL(33,3)=21600., I4SFTYP(33,3)=0,    !'LLJ5'
    FRQ4PL(34,3)=3600.,  I4SFTYP(34,3)=0,    !'CAP1'
    FRQ4PL(35,3)=21600., I4SFTYP(35,3)=0,    !'EML1'
    FRQ4PL(36,3)=21600., I4SFTYP(36,3)=0,    !'TKE1'
    FRQ4PL(37,3)=21600., I4SFTYP(37,3)=0,    !'CNV1'

      !STANDARD PLOTTED OUTPUT
      ! Specifies the fields to be printed during the simulation
      ! YOU MUST SPECIFY SEPARATE PARAMETERS FOR EACH GRID
      ! THIS FILE SET UP FOR 3 GRID SYSTEM

!Available parameters:
    ! NPLT(MAXGRDS):       Number of different fields to plot
    ! FRQPRT(maxgrds):     Frequency at which plots are made
    ! IPLFLD(50,MAXGRDS):  Name of Field to be ploted (a8) (see list)
    ! IXSCTN(50,MAXGRDS):  Cross section of plots (x/z:1, y/z:2, x/y:3)
    ! IPLVECT(50,MAXGRDS): Vector frequency (0-no vectors, 1-every point,
    !                      2-every 2 points, etc
    ! ISBVAL(50,MAXGRDS):  Slab of cross section, (k value for x/y
    !                      cross section)
    ! IAA(50,MAXGRDS):     Number of points to chop off left side
    ! IAB(50,MAXGRDS):     Number of points to chop off right side
    ! JOA(50,MAXGRDS):     Number of points to chop off top
    ! JOB(50,MAXGRDS):     Number of points to chop off of bottom
    ! PLCONIN(50,MAXGRDS): Contour increment (if zero, is calcualted)
    ! PLCONLO(50,MAXGRDS): Contour high value(if zero, is calcualted)
    ! PLCONHI(50,MAXGRDS): Contour low value (if zero, is calcualted)
    ! NAAVG(50,MAXGRDS):   Plot averaged points, averaged naavg in abcissa
    ! NOAVG(50,MAXGRDS):   Plot averaged points, averaged noavg in ordinate
```

```
   ! PLFMT(50,MAXGRDS):  Format (8 characters, field of 7)
   ! PLTIT(50,MAXGRDS):  Title other than default to put on plot (a8)
   ! IPLTYP(50,MAXGRDS):  Ncar graphics-'PL', print-'PR', both-'BO'

NPLT(1)  = 9,     ! number of fields to be printed at each time
FRQPRT(1)=1800.,    !Frequency for plotting on this grid
                 !    for various cross-sections (limit of 50)
IPLFLD(1,1) = 'MSLP','SPEED','THETA','W','RR','W','RS',
         'PCPTEND','PCPTOT','NSLTEX','TG','SLM','TG','SLM',
PLCONIN(1,1) =0.,0.,0.,0.,0.,0.,0.,0.,0.,0.,0.,0.,0.,
           ,0.,0.,0.,0.,0.,0.,0.,0.,0.,0.,0.,0.,
PLCONLO(1,1) = 0.,0.,0.,0.,0.,0.,
           ,0.,0.,0.,0.,0.,0.,0.,0.,0.,0.,0.,0.,
           ,0.,0.,0.,0.,0.,0.,0.,0.,0.,0.,0.,0.,
PLCONHI(1,1) = 0.,0.,0.,0.,0.,0.,
           ,0.,0.,0.,0.,0.,0.,0.,0.,0.,0.,0.,0.,
           ,0.,0.,0.,0.,0.,0.,0.,0.,0.,0.,0.,0.,
           0.,
IXSCTN(1,1) =  3,3,3,3,3,3,3,3,3,1,1,
ISBVAL(1,1) =  1,1,1,15,15,35,35,1,1,
IPLVECT(1,1) = 0.5,0,0,0,0,0,0,0,0,0,0,0,0,0,0,0.
!IAA(1,1)   = -16,-16,-16,-16,-16,-16,-16,-16,-16,-16,-16,
IAB(1,1)   = 0,0,0,0,0,0,0,0,0,0,0,0,0,
JOA(1,1)   = 0,0,0,0,0,0,0,0,0,0,0,0,0.
!JOB(1,1)   = 0,0,0,0,0,-20,-20,-20,-20,-20,-20,-20,0,0,0,0,0,0,0,0,0,0
IPLTYP(1,1) = 'PL','PL','PL','PL','PL','PL','PL','PL',
         'PL','PL','PL','PL','PL','PL','PL','PL',
         'PL','PL','PL','PL','PL','PL','PL','PL',
         'PL','PL','PL','PL','PL','PL','PL','PL',
!PLTIT(23,1)='VECTORS',PLTIT(29,2)='VECTORS',

NPLT(2)  = 4,   ! number of fields to be printed at each time
FRQPRT(2)=1800.,   !Frequency for plotting on this grid
IPLFLD(1,2) = 'MSLP','W','THETA E','SPEED',
PLCONIN(1,2) =0.,0.,0.,0.,0.,0.,0.,0.,0.,0.,0.,0.,0.,0.,0.,0.,0.,
PLCONLO(1,2) =0.,0.,0.,0.,0.,0.,0.,0.,0.,0.,0.,0.,0.,0.,0.,0.,0.,
PLCONHI(1,2) =0.,0.,0.,0.,0.,0.,0.,0.,0.,0.,0.,0.,0.,0.,0.,0.,0.,
IXSCTN(1,2) = 3,3,3,3,3,
ISBVAL(1,2) =  1,3,2,3,1,1
IPLVECT(1,2) = 0,0,0,0,0,0,2,0,0,2,0,0,2,
```

```
!IAA(1,2)   = -16,-16,-16,-16,-16,-16,-16,-16,-16,-16,-16,
IAB(1,2)   = 0,0,0,0,0,0,0,0,0,0,0,0,0,0,
JOA(1,2)   = 0,0,0,0,0,0,0,0,0,0,0,0,0,0,
JOB(1,2)   = 0,0,0,0,-20,-20,-20,-20,-20,0,0,0,0,0,0,0,0,0,0
IPLTYP(1,2) = 'PL','PL','PL','PL','PL','PL','PL','PL',
            'PL','PL','PL','PL','PL','PL','PL','PL',
            'PL','PL','PL','PL','PL','PL','PL','PL',
            'PL','PL','PL','PL','PL','PL','PL','PL',

NPLT(3)  = 20,   ! number of fields to be printed at each time
FRQPRT(3)=1800.,   !Frequency for plotting on this grid
IPLFLD(1,3)='PCPTOT','PCPTEND','THETA E','SPEED','MSLP','DNALL',
        'DNALL','RH','W','SPEED','THETA','THETA E','THVP',
        'DNALL','RH','W','SPEED','THETA','THETA E','THVP',
IXSCTN(1,3) =  3,3,3,3,3,3,
             1,1,1,1,1,1,1,
             2,2,2,2,2,2,2,
ISBVAL(1,3) =  1,1,2,4,1,15,
             99,99,99,99,99,99,99,
             99,99,99,99,99,99,99,
PLCONIN(1,3) =0.,0.,2.,2.,4.,0.,
            0.,0.,.2,2.,2.,2.,2.,
            0.,0.,.2,2.,2.,2.,2.,
PLCONLO(1,3) =0.,0.,0.,0.,0.,0.,
            0.,0.,-10.1,0.,0.,0.,0.,
            0.,0.,-10.1,0.,0.,0.,0.,
PLCONHI(1,3) =0.,0.,0.,0.,0.,0.,
            0.,0., 10.1,,0.,0.,0.,0.,
            0.,0., 10.1,,0.,0.,0.,0.,
IPLVECT(1,3) = 0,0,0,4,
IPLTYP(1,3) = 'PL','PL','PL','PL','PL','PL','PL','PL',
            'PL','PL','PL','PL','PL','PL','PL','PL',
            'PL','PL','PL','PL','PL','PL','PL','PL',
            'PL','PL','PL','PL','PL','PL','PL','PL',

NPLT(4)  = 16,   ! number of fields to be printed at each time
FRQPRT(4)=600.,   !Frequency for plotting on this grid
IPLFLD(1,4)='PCPTOT','PCPTEND','THETA E','SPEED','MSLP','DNALL',
        'DNALL','DNALL','W','W',
        'DNALL','W','SPEED','DNALL','W','SPEED',
```

```
PLCONIN(1,4) =0.,0.,2.,5.,4.,0.,0.,0.,5.,2.,0.,2.,2.,0.,5.,2.,
PLCONLO(1,4) =0.,0.,0.,0.,0.,0.,0.,0.,-41.,-41.,0.,-41.,0.,0.,-41.,0.,0.,0.,
PLCONHI(1,4) =0.,0.,0.,0.,0.,0.,0.,0.,41.,41.,0.,41.,0.,0.,41.,0.,0.,0.,
IXSCTN(1,4) =  3,3,3,3,3,3,3,3,3,3,1,1,1,2,2,2,
ISBVAL(1,4) =  1,1,2,4,1,15,10,20,10,20,102,102,102,102,102,102,
IPLVECT(1,4) = 0,0,0,0,
IPLTYP(1,4) = 'PL','PL','PL','PL','PL','PL','PL','PL',
          'PL','PL','PL','PL','PL','PL','PL','PL',
          'PL','PL','PL','PL','PL','PL','PL','PL',
          'PL','PL','PL','PL','PL','PL','PL','PL',

$END

$VIS

!Available parameters:
  ! NVIS(MAXGRDS):       Number of different fields to vis
  ! FRQVIS(maxgrds):     Frequency at which vis files are made
  ! IVISFLD(50,MAXGRDS): Name of Field to be vised (max 30e, see list)

  !     OLD VIS FILES (IVIS=1)

  ! IVISIA(MAXGRDS):     Number of points to chop off left side x
  ! IVISIB(MAXGRDS):     Number of points to chop off right side x
  ! IVISJA(MAXGRDS):     Number of points to chop off left side x
  ! IVISJB(MAXGRDS):     Number of points to chop off right side x
  ! IVISKA(MAXGRDS):     Number of points to chop off left side x
  ! IVISKB(MAXGRDS):     Number of points to chop off right side x
  ! IVISIAVG(MAXGRDS):   Average this number in x direction
  ! IVISJAVG(MAXGRDS):   Average this number in y direction
  ! IVISKAVG(MAXGRDS):   Average this number in z direction
  ! VISTOP(MAXGRDS):     Top of domain vised (km)
  ! ICNTVISG(MAXGRDS):   Method used to find Center of vis domainm
  ! VOFFSETX(MAXGRDS):   X Offset of vis domain from center position
  ! VOFFSETY(MAXGRDS):   Y Offset of vis domain from center position

  !   New Style Vis filles (IVIS=2)

  ! IVISNXP(MAXGRDS):    Number of x vis points (centered)
  ! IVISNYP(MAXGRDS):    Number of y vis points (centered)
```

```
 ! IVISNZP(MAXGRDS):    Number of z vis points (centered)

FRQVIS= 20., 1200., 600.,300.! Printout frequencies for each grid
NVIS(1) = 15,    ! number of fields to be visualized
IVISFLD(1,1) ='U','V','W','PRES','MSLP','THETA E','TDK','THETA','RV','RH',
    !  'LDNALL','VEG','PZLIM',
       'RP','RVSTRAT','RPSTRAT','HINP','TR4P',
    !  'TBAL','THBAL2','RVBAL','PBAL2','PBAL1','THBAL','THBALDIF',
    !  'TOPO3D','TOPO','PCTLND','SSTF','UBAL','VBAL','THBAL','RVBAL',
    !  'PBAL', 'PZ','EU','EV','O3P',

IVISIA(1)=-1,
IVISIB(1)=-1,
IVISJA(1)=-1,
IVISJB(1)=-1,
IVISKA(1)=0,
IVISKB(1)=-2,
IVISIAVG(1)=1,
IVISJAVG(1)=1,
IVISKAVG(1)=1,
ICNTVISG(1)=0,
VISTOP(1)=30.E3,
IVSTRUCT(1)=0,
VOFFSETX(1)=0.,
VOFFSETY(1)=0.,
IVISNXP(1)=138,
IVISNYP(1)=88,
IVISNZP(1)=100,


GRID 2

NVIS(2) = 24,    ! number of fields to be visualized (limit of 8)
IVISFLD(1,2) ='U','V','W','PRES','MSLP','T','TDK','THETA',
      'THETA E','RV','LOG DNL','LOG DNI','LDNALL',
      'PZLIM',
      'SNOW12','PCPTOT','PCPCNV','SNOWFALL','PRCPFALL','CNVFALL',
      'TOPO3D','TOPO','PCTLND','SSTF',

IVISIA(2)=-1,
```

```
IVISIB(2)=-1,
IVISJA(2)=-1,
IVISJB(2)=-1,
IVISKA(2)=0,
IVISKB(2)=-2,
IVISIAVG(2)=2,
IVISJAVG(2)=2,
IVISKAVG(2)=1,
ICNTVISG(2)=0,
VISTOP(2)=6.E3,
IVSTRUCT(2)=0,
VOFFSETX(2)=0.,
VOFFSETY(2)=0.,
IVISNXP(2)=150,
IVISNYP(2)=128,
IVISNZP(2)=34,



NVIS(3)  = 24.      ! number of fields to be visualized (limit of 8)
   !NOTE IVIS*A AND IVIS*B SHOULD BE DIVISIBLE BY IVIS*AVG
IVISFLD(1,3) ='U','V','W','SPEED','PRES','MSLP','T', 'TDK','THETA',
      'THETA E','RV','RH','LDNALL','TKE','THVP','PZLIM',
      'PCPTOT','PCPCNV','PRCPFALL','CNVFALL',
      'TOPO3D','TOPO','PCTLND','SSTF',
   !NOTE IVIS*A AND IVIS*B SHOULD BE DIVISIBLE BY IVIS*AVG
IVISKA(3)=0,
IVISIAVG(3)=2,
IVISJAVG(3)=2,
IVISKAVG(3)=1,
ICNTVISG(3)=0,
VISTOP(3)=5.E3,
IVSTRUCT(3)=0,
VOFFSETX(3)=0.,
VOFFSETY(3)=0.,
IVISNXP(3)=188,
IVISNYP(3)=188,
IVISNZP(3)=34,

NVIS(4)  = 30,      ! number of fields to be visualized (limit of 8)
```

```
    !NOTE IVIS*A AND IVIS*B SHOULD BE DIVISIBLE BY IVIS*AVG
 IVISFLD(1,4) ='U','V','W','SPEED','PRES','MSLP','T', 'TDK','THETA',
       'THETA E','RV','RH','LDNALL','TKE','THVP','PZLIM',
       'LDNRC','LDNRR','LDNRP','LDNRS','LDNRA','LDNRG',
       'PCPTOT','PCPCNV','PRCPFALL','CNVFALL',
       'TOPO3D','TOPO','PCTLND','SSTF',
    !NOTE IVIS*A AND IVIS*B SHOULD BE DIVISIBLE BY IVIS*AVG
 IVISKA(4)=0,
 IVISIAVG(4)=2,
 IVISJAVG(4)=2,
 IVISKAVG(4)=1,
 ICNTVISG(4)=0,
 VISTOP(4)=5.E3,
 IVSTRUCT(4)=0,
 VOFFSETX(4)=0.,
 VOFFSETY(4)=0.,
 IVISNXP(4)=194,
 IVISNYP(4)=194,
 IVISNZP(4)=34,


 $END
                  LIST OF PLOT OR VIS VARIABLES

                  Raw Model Variables

 U   V    W    PIP  THETAIL  TKE    DEN  THETA  PP    PC
 PRES  PSL    MSLP   SPEED VECTORS  U-REL   V-REL U-RELU  V-RELV  PI0
 TH0  DN0    P0    UBAL  UBALDIF  UBAL2-1  VBAL  VBALDIF VBAL2-1 THBAL
 PBAL  THBALDIF THBAL2-1 RVBAL RVBALDIF RVBAL2-1 UBAL2 VBAL2   THBAL2
RVBAL2
 TOPO  TOPO3D   ETA    ELATT ELONT   TOPORAT  DXETA DYETA   DZETA  K1ETA
 TR1P  TR2P    TR3P   TR4P

                  Thermodynamic Variables

 T    TC   TF   THETA   THETA V THETA E TD     THVP   THVP3D THVVP
 THVVPK1  THVPX  DENVP LI    CAPE1  CAPE   SHCAPE  CAPEOLD SCELL  SCELLB
 SCELLMAX TOTALS SWEAT HELICY  BULK   LLM    FORCE   CAPORG  HCAPMAX
CAPMAX
```

THEMIN WF3000 WM5KM WM510KM WMLFC WFLFC UPPERSHR CONVCAP ZTOLFC CONVTEMP
CINHIBIT FREE GP

Microphysics quantities

RT RR RP RG RS RA RL RI CP CS
CR CG RCOND RV RC RH DNT DNV DNC DNR
DNP DNG DNS DNA DNL DNI LOG DNL LOG DNI LDNALL DNALL
COL CLD PRTEND PSTEND PATEND PPTEND PGTEND PCNTEND PCPTEND PCPR PCPP
PCPS PCPG PCPCNV PCPT PCPTOT PCPLIQ PCPICE ECP SO2P NO2P
AGIP HINP O3P

Derived dynamic quantities

QZ QY QX KE F3M F2U F1V HOR RICH PZ PZM
PZS PZSS PZSX PZSY PZSZ PZ AD PZ DI PZAVG PZMID PZIL
PZIL2 PLAVG U-GEO V-GEO U-AGEO V-AGEO S-AGEO THA-AGEO THE-AGEO W-AGEO
SS-AGEO QV CNV QV-PHI QVYP QVXP XGEO YGEO SIGMAS U-THM V-THM
VORT-THM NHPP VTAN MZ INR STB1 INR STB DEF2 BVF RICH VKM
VKH HKMPCT HKM HKH TKL

Surface Layer Derived and Turbulent Flux

TG SLM TGF TBOTF TSURF SST TH-SST RV-RSS SFC T SFC TD
SFC RV SFC RH SFC U SFC V SFC SPD TSMAX TTSMX TSMIN TTSMN
TPKGST NSLTEX ALBEDO RADFLX PCTLND Z0 EQ RD T USTARL USTARW TSTARL
TSTARW RSTARL RSTARW UW VW TFZ QFZ KEFZ SFZ WFZ
PZFZ PKGST

Tendencies of all types!

DRIDT1 DRIDT DRLDT DRLDT1 DRLIDT DRCDT DRRDT Q1M Q1M1
THDOTFZ THDOTML QR THDOTCD THDOTEV PXDOTM PYDOTM PZDOTM PLDOTALL
PLDOTL PLDOTR PLDOTP PLDOTS PLDOTA PLDOTG PVDOTQ1M PVDOTCD PVDOTEV
PVDOTML PVDOTQR DRAG PVDOTDG PVDOTWV PVDOTKM PVDOTQ1K PLDOTKH PVDOTMX
PVDOTVT PLDOTVT PVDOTQ1W PVDOTQ1 THDOTS THDOTTOT THDOTRES THDOTADM

THDOTWB
Q1Q2 MSFX CUMAREA Q1 Q2 Q1S Q2S Q2W Q2K
PVDOTTOT PVDOTMS PVDOTQ1S PVDOTS1 THDOTS1 QVDOTS1 PVDOTS PVDOTMOM
PVDOTTH
NUPHVI SPLVI VDVR VDVP VDVS VDVA VDVG MLSR MLAR
VDVC CLCR CLCP CLCG CLRG FRZRAIN SNOW2GR VDVC TG
DS VS VG AUTO SCAVEC SCAVSO2 SCAVNO2 SCAVAGI SCAVO3
CONPR CONP CONH CONM FU FV FTHRD MLGR DG
Q1K PLDOTI PVDOTFZ PVDOTTR Q1W Q2M NUSDVI SCAVIN

Normal Mode Analysis and Balance analysis

UBALDN BALDN NBALDN NUBALDN UBALTH BALTH NBALTH NUBALTH UBALPI
NBALPI NUBALPI ROS RDNL ROS RADL EQ DEPTH VNTHETA NTHETA NTHVPWV
NTHVPWX
NTHVPOW NBLDNPW NUBDNPW NBLTHPW NUBTHPW NWPOW NWPWV N PI VN
DIV
STRMPSI STRMVORT STRMVR STRMWR ROT Z IROT Z PSI Z CHI Z UROT Z
UDIV Z VDIV Z VORT3 Z DIVFUV DIV3 Z BALPI N DIV VROT Z NTHVPWXV

Appendix B—Derivation of capacitance

At temperatures below about -22° C, ice crystals grow preferentially columnar. Pruppacher and Klett (1997) give the following formulation for the capacitance of a columnar crystal:

$$C_0 = \frac{A}{\left(\ln\frac{(a + A)}{b}\right)}, \ with\ A = \sqrt{(a^2 - b^2)},$$

where a is the length of the crystal's a-axis (its basal plane) and b is the length of the b-axis (the axis perpendicular to basal plane). Though the capacitance of a crystal will change as it changes size, we assume the changes in capacitance are sufficiently small enough to ignore. Thus we have calculated capacitance using the initial crystal mass corresponding to a sphere of ice with a radius of 5 microns. Using the idea of equivalent volumes,

$$\frac{4}{3}\pi r^3_{sphere} = \pi r^2_{column} h .$$

If we let h = $2r_{column}$, we find r_{column}, or the length of the b-axis, to be 7.469 x 10^{-4} cm, and h, the length of the a-axis to be 1.493 x 10^{-3} cm. The capacitance is then 9.825 x 10^{-4} cm.

Appendix C—Noise

With greater model complexity comes a greater chance for noisy results, often from truncation errors, which creates computational, or numeric noise. This type of noise may not appear until many timesteps have passed, and can become more evident after even more timesteps and calculations, i.e., the noise propagates.

Often such noise can be filtered out, either within the model, during any checks and balancing operations (the UWNMS has many of these sprinkled throughout, as small-scale checks in the thermodynamics routines, for example, and also complete numerical and time filters), filtered with post-processing algorithms, or not filtered at all. The UWNMS' internal filters are too extensive a topic to cover here. Instead, interested readers may review Kalnay (2003) and Tripoli (1992).

One post-processing filter has been applied in this work, a filter for pristine ice mass mixing ratio. Figure C.1 shows pristine ice at 11 km, 90 minutes into an experiment with 30 IN/L. The zig-zag, maze-like distribution of pristine ice is not at all realistic. There is one small area, in the easternmost part of the domain near the equator, that seems to have a realistic "cloud." The quantity of this apparent noise is on the order of a milligram of ice per kilogram of dry air—at 11 km the maximum noisy pristine ice value is 0.0012 g/kg, at 11.8 km it is 0.0025 g/kg (not shown). From this images and others, it was determined to filter out all pristine ice mixing ratio values equal to or below 0.01 g/kg, and all plots of pristine ice in the main body of this work reflect this filtering.

Though no other data have been filtered, noise still needs to be taken into account, especially when interpreting vertical velocity information. We saw in Chapter 6 how slight variations in vertical velocity played a noticeable part in the distribution of water above 11 km. Small, seemingly random differences in vertical velocity seen in Figures such as 6.14 may be a "butterfly effect" of IN activation and associated changes in ice mass, precipitation, or lofting of ice. However, these small differences can be found very early on in model simulations, even before IN are allowed to activate! In Figure C.2 we see a vertical slice of vertical velocity difference at 16.5 degrees S, two minutes into the experiment with 30 IN/L. The difference in velocities appears as a spike of noise at the northeastern edge of the Andes, in

Bolivia. These slight differences (on the order of 10^{-7} m/s), for this time and experiment, are on the order of machine precision. After 13.5 hours of growth and decay of both positively and negatively buoyant regions, however, the values of differences in vertical velocity have grown to the order of 1 mm/s and cover the whole domain (Figure C.3). In Figure C.4, the difference in vertical velocity is plotted for 90 minutes into the *exact same* experiment, performed with different operating systems and compilers. Again the differences are on the order of 1 mm/s. Though ideally the type of machine set-up should not affect model output, with different external "settings" such as these, optimization schemes will differ, and truncation-induced noise is often the result.

Making a decision as to what constitutes vertical velocity "noise" and what might be real changes in vertical velocity with varying IN loads (this includes butterfly-effect changes) seems too subjective—it would provide another layer of uncertainty. For example, would noise-adjusted vertical velocity be adjusted positively or negatively by that 1 mm/s or so? There's little (and more likely no) way to tell which direction is the correct one. Therefore, vertical velocity data presented in this work remains unfiltered.

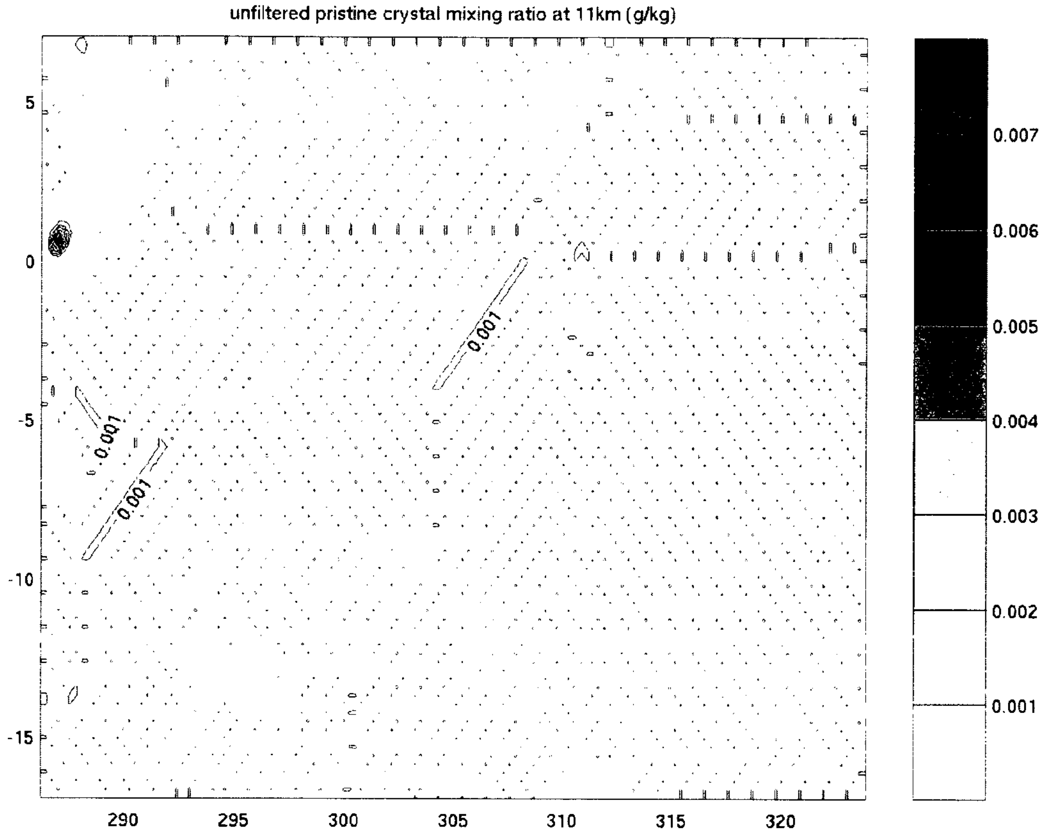

Figure C.1. Pristine ice mass mixing ratio, at 11 km and 90 minutes into a model run with 30 IN/L input at 250 hPa. What appear to be small dots are areas enclosed by the 0.001 g/kg contour. The majority of the pristine ice distribution can best be described as noise.

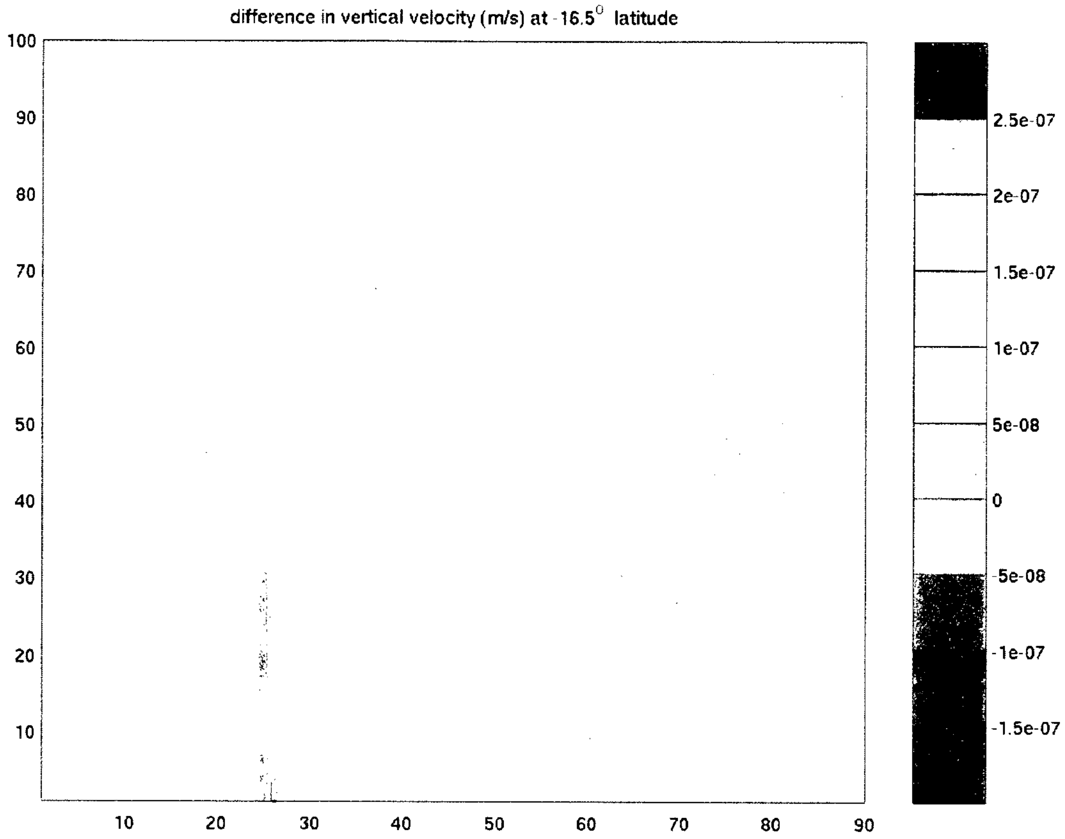

Figure C.2. A vertical slice at 16.5°S of the difference in vertical velocity between two experiments at 2 minutes into each—one experiment with no IN and one where 30 IN/L were input at 250 hPa. The number of vertical gridpoints is on the y-axis, number of longitudinal gridpoints on the x-axis. The difference "spikes," on the order of machine precision, in the foothills of the Andes in Bolivia. This noise was likely generated at the surface and very rapidly propagated upward.

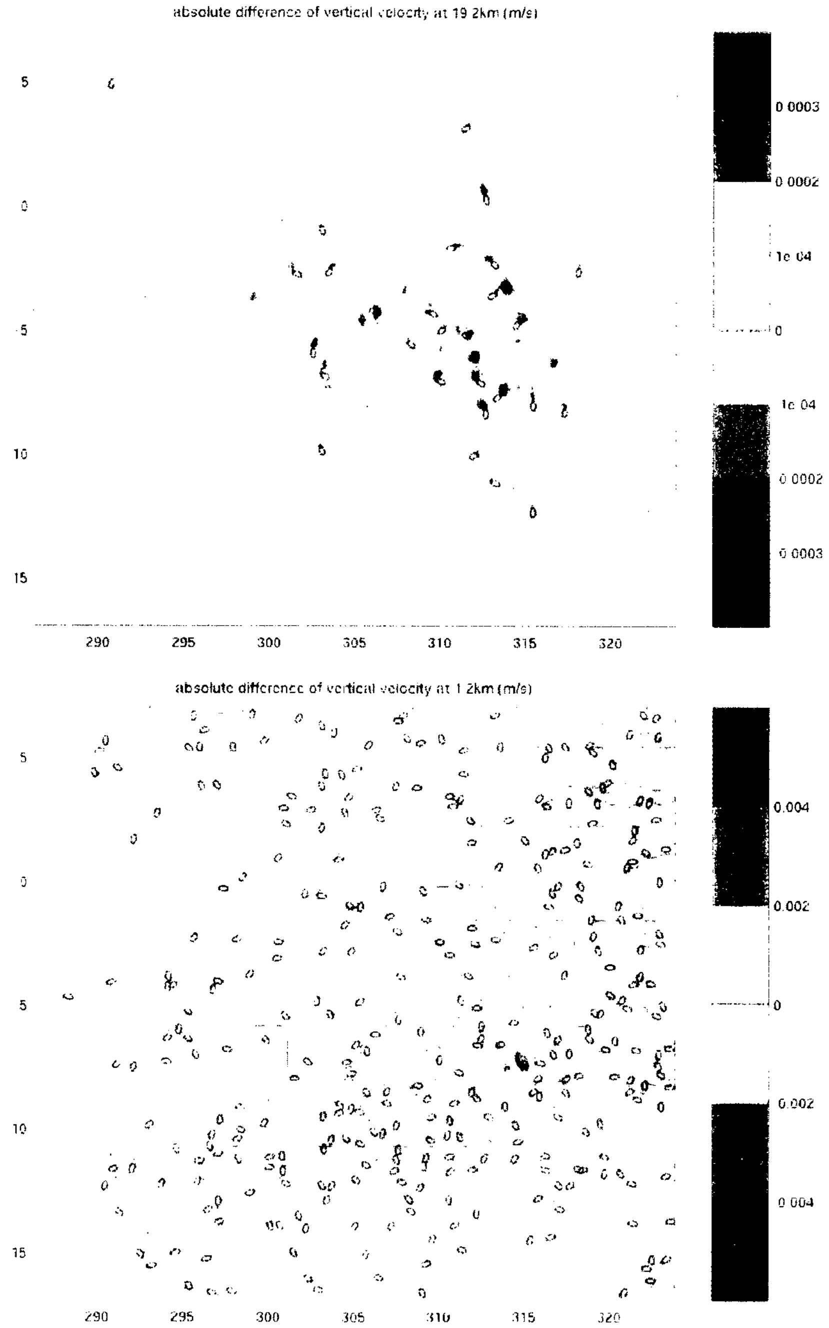
absolute difference of vertical velocity at 13.2km (m/s)

absolute difference of vertical velocity at 1.2km (m/s)

Figure C.3. Planar views at 13.2 and 1.2 km of the difference in vertical velocity between two experiments at 13.5 hours (810 minutes) into each—one experiment with no IN and one where 30 IN/L were input at 250 hPa. With time the noise seen earlier (Figure C.2) has propagated throughout the domain.

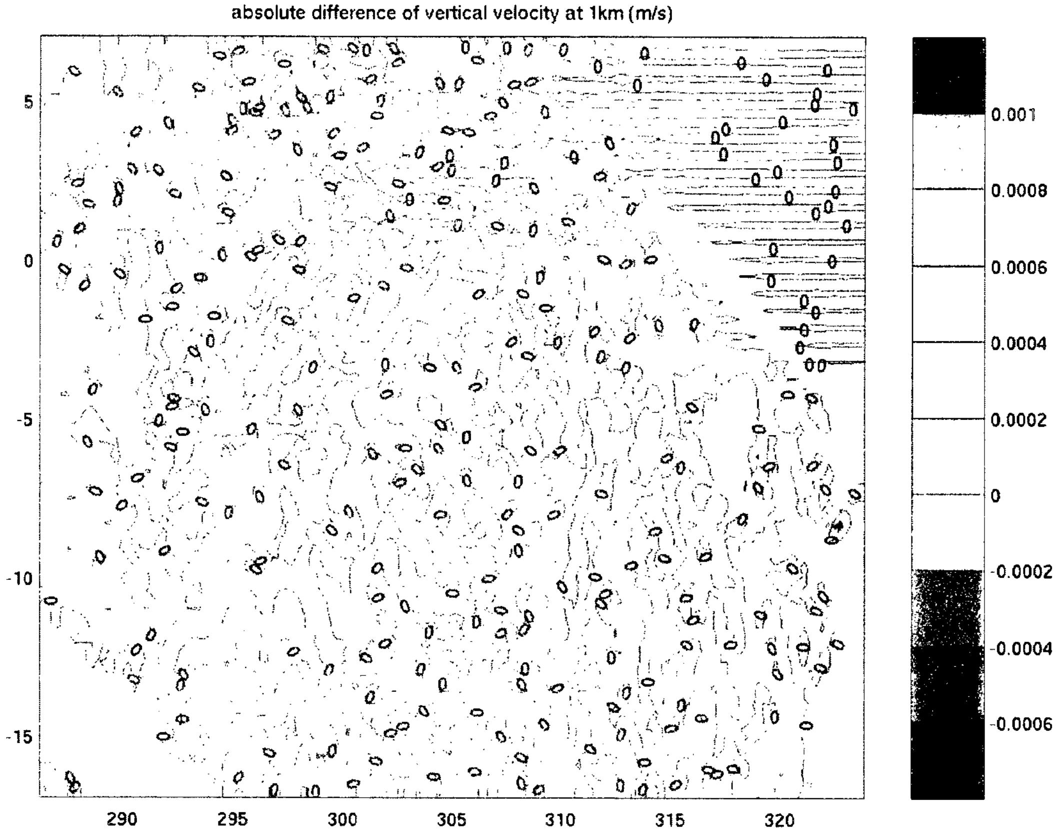

Figure C.4. A planar view at 1 km of the difference in vertical velocity between two experiments at 90 minutes into each—each with no IN, but conducted on a machine before and after the operating system was replaced and a new compiler version was implemented. With new systems comes different optimization schemes and the possibility of truncation differences, the likely results of which are seen here.

References

Andreae, M. O., E. Atlas, H. Cachier, W. R. Cofer III, G. W. Harris, G. Helas, R. Koppmann, J.-P. Lacaux, and D. E. Ward, 1996. Trace gas and aerosol emissions from savannah fires. In Biomass Burning and Global Change, vol. 1. ed. J.S. Levine, pp. 278-295, Cambridge, Massachusetts, MIT Press.

Andreae, M. O., D. Rosenfeld, P. Artaxo, A. A. Costa, G. P. Frank, K. M. Longo, and M. A. F. Silva-Dias, 2004. Smoking rain clouds over the Amazon. Science, vol. 303, pp. 1337-1342.

Artaxo, P., E. T. Fernandes, J. V. Martins, M. A. Yamasoe, P. V. Hobbs, W. Maenhaut, K. M. Longo, and A. Catanho, 1998. Large-scale aerosol source apportionment in Amazonia. J. Geophys. Res., vol. 103, no. D24, pp. 31837-31847.

Bachmeier, A. S., and H. E. Fuelberg, 1996. A meteorological overview of the TRACE A period. J. of Geophys. Res., vol. 101, no. D19, pp. 23881-23888.

Bates, J. J., and D. L. Jackson, 2001. Trends in upper-tropospheric humidity. Geophysical Res. Lett., vol. 28, no. 9, pp. 1695-1698.

Bertschi, I., R. J. Yokelson, D. E. Ward, R. E. Babbitt, R. A. Susott, J. G. Goode, and W. M. Hao, 2003. Trace gas and particle emissions from fires in large diameter and belowground biomass fuels. J. Geophys. Res., vo. 108, no. D13, pp. 8472-8482.

Betts, A. K., and C. Jakob, 2002. Study of diurnal cycle of convective precipitation over Amazonia using a single column model. J. Geophys. Res., vol. 107, no. D23, doi: 10.1029/2002JD002264.

Board, A. S., H. E. Fuelberg, G. L. Gregory, B. G. Heikes, M. G. Schultz, D. R. Blake, J. E. Dibb, S. T. Sandholm, and R. W. Talbot, 1999. Chemical characteristics of air from differing source regions during PEM-Tropics A. J. Geophys. Res., vol. 104, no. D23, pp. 16181-16196.

Brewer, A. W, 1949. Evidence for a world circulation provided by the measurements of helium and water vapor distribution in the stratosphere. Quart. Jour. Royal Met. Soc., vol. 75, pp. 351-363.

Cetrone, J., and R. A. Houze, Jr., 2006. Characteristics of tropical convection over the ocean near Kwajalein. Monthly Weather Review, vol. 134, no. 3, pp. 834-853.

Chelliah, M., 1994. The global climate for September-November 1992: Weak warm ENSO episode conditions linger in the tropical Pacific. J. Climate, vol. 7, pp. 1565-1580.

Chen, C., and W. R. Cotton. 1983. A one-dimensional simulation of the stratocumulus-capped mixed layer. Boundary-layer Meteorology, vol. 25, pp. 289-321.

Christopher, S. A., J. Chou, J. Zhang, X. Li, T. A. Berendes, and R. M. Welch, 2000. Shortwave direct radiative forcing of biomass burning aerosols estimated using VIRS and CERES data. Geophysical Res. Lett., vol. 27, no. 15, pp. 2197-2200.

Clarke, A. D., W. G. Collins, P. J. Rasch, V. N. Kapustin, K. Moore, S. Howell, and H. E. Fuelberg, 2001. Dust and pollution transport on global scales: Aerosol measurements and model predictions. J. Geophys. Res., vol. 106, no. D23, pp. 32555-32570.

Clarke, A. D., F. Eisele, V. N. Kapustin, K. Moore, D. Tanner, L. Mauldin, M. Litchy, B. Lienert, M. A. Carroll, and G. Albercook, 1999. Nucleation in the equatorial free troposphere: Favorable environments during PEM-Tropics. J. Geophys. Res., vol. 104, no. D5, pp. 5735-5744.

Crutzen, P. J., and M. O. Andreae, 1990. Biomass burning in the tropics: Impact on atmospheric chemistry and biogeochemical cycles. Science, vol. 250, no. 4988, pp. 1669-1678.

Curry, J. A., and P. J. Webster, 1999. Thermodynamics of the Atmospheres and Oceans. San Diego, California, Academic Press, 467 p.

Cziczo, D. J., P. J. DeMott, S. D. Brooks, A. J. Prenni, D. S. Thomson, D. Baumgardner, J. C. Wilson, S. M. Kreidenweis, and D. M. Murphy, 2004. Observations of organic species and atmospheric ice formation. Geophys. Res. Lett., vol. 31, no. L12116, doi: 10.1029/20046L019822.

Dessler, A. E., 1998. A reexamination of the "stratospheric fountain" hypothesis. Geophys. Res. Lett., vol 25, no. 22, pp. 4165-4168.

Emanuel, K. A., 1991. A scheme for representing cumulus convection in large-scale models. J. Atmos. Sci., vol. 48, pp. 2313-2335.

de F. Forster, P. M, and K. P. Shine, 1999, Stratospheric water vapour changes as a possible contributor to observed stratospheric cooling. Geophys. Res. Lett., vol. 26, no. 21, pp. 3309-3312.

Fueglistaler, S., A. E. Dessler, T. J. Dunkerton, I. Folkins, and Q. Fu, 2009. Tropical tropopause layer. Reviews of Geophysics, vol. 47, doi: 10.1029/2008RG00267.

Fuelberg, H. E., R. E. Newell, D. J. Westberg, J. C. Maloney, J. R. Hannan, B. D. Martin, M. A. Avery, and Y. Zhu, 2001. A Meteorological overview of the second Pacific Exploratory Mission in the Tropics. J. Geophys. Res., vol. 106, no. D23, pp. 32427-32443.

Fuelberg, H. E., R. E. Newell, S. P. Longmore, Y. Zhu, D. J. Westberg, E. B. Browell, D. R. Blake, G. L. Gregory, and G. W. Sachse, 1999. A meteorological overview of the Pacific Exploratory Mission (PEM) Tropics period. J. Geophys. Res., vol. 104, no. D5. pp. 5585-5622.

Fuelberg, H. E., R. O. Loring Jr., M. V. Watson, M. C. Sinha, K. E. Pickering, A. M. Thompson, G. W. Sasche, D. R. Blake, and M. R. Schoeberl, 1996. TRACE A Trajectory intercomparison 2. Isentropic and kinematic methods. J. Geophys. Res., vol. 101, no. D19, pp. 23927-23939.

Fishman, J., J. M. Hoell Jr., R. D. Bendura, R. J. McNeal, and V. W. J. H. Kirchhoff, 1996. NASA GTE TRACE A Experiment (September-October 1992): Overview. J. Geophys. Res., vol. 101, no. D19, pp. 23865-23879.

Gage, K. S., J. R. McAfee, D. A. Carter, W. L. Ecklund, A. C. Riddle, G. C. Reid, and B. B. Balsley, 1991. Long-term Mean Vertical Motion over the Tropical Pacific: Wind-Profiling Doppler Radar Measurements. Science, vol. 254, no. 5039, pp. 1771-1773.

Gao, S., D. A. Hegg, P. V. Hobbs, T. W. Kirchstettner, B. I. Magi, and M. Sadilek, 2003. Water-soluble organic components in aerosols associated with savanna fires in southern Africa: Identification, evolution, and distribution. J. Geophys. Res., vol. 108, no. D13, doi: 10.1029/2002JD002324.

Gettelman, A., J. R. Holton, and A. R. Douglass, 2000. Simulations of water vapor in the lower stratosphere and upper troposphere. J. Geophys. Res., vol. 105, no. D7, pp. 9003-9023.

Greco, S., R. Swap, M. Garstang, S. Ulanski, M. Shipman, R. C. Harriss, R. Talbot, M. O. Andreae, and P. Artaxo. Rainfall and surface kinematic conditions over central Amazonia during ABLE 2B. J. Geophys. Res., vol. 105, pp. 17001-17014.

Gregory, G. L., D. J. Westberg, M. C. Shipham, D. R. Blake, R. E. Newell, H. E. Fuelberg, R. W. Talbot, B. G. Heikes, E. L. Atlas, G. W. Sashse, B. A. Anderson, and D. C. Thorton, 1999. Chemical characteristics of Pacific tropospheric air in the region of the Intertropical Convergence Zone and South Pacific Convergence Zone. J. Geophys. Res., vol. 104, no. D5, pp. 5677-5696.

Gregory, G. L., H. E. Fuelberg, S. P. Longmore, B. E. Anderson, J. E. Collins, and D. R. Blake, 1996. Chemical characteristics of tropospheric air over the tropical South Atlantic Ocean: Relationship to trajectory history. J. Geophys. Res., vol. 101, no. D19, pp. 23957-23972.

Hartmann, D. L., J. R. Holton, and Q. Fu, 2001. The heat balance of the tropical tropopause, cirrus and stratospheric dehydration. Geophys. Res. Lett., vol. 28, no. 10, pp. 1969-1972.

Hastenrath, S., 1997. Annual cycle of upper air circulation and convective activity over the tropical Americas. J. Geophys. Res., vol. 102, no. D4, pp. 4267-4274.

Hobbs, P. V., and J. D. Locatelli, 1969. Ice nuclei from a natural forest fire. J. Applied Met., vol. 8, pp. 833-834.

Hoell, J. M., D. D. Davis, D. J. Jacob, M. O. Rodgers, R. E. Newell, H. E. Fuelberg, R. J. McNeal, J. L. Raper, and R. J. Bendura, 1999. Pacific Exploratory Mission in the tropical Pacific: PEM Tropics A, August-September 1996. J. Geophys. Res., vol. 104, no. D5, pp. 5567-5583.

Jensen, E. J., O. B. Toon, H. B. Selkirk, J. D. Spinhirne, and M. R. Schoeberl, 1996(a). On the formation and persistence of subvisible cirrus clouds near the tropical tropopause. J. Geophys. Res., vol. 101, no. D16, pp. 21361-21375.

Jensen, E. J., O. B. Toon, L. Pfister, and H. B. Selkirk, 1996(b). Dehydration of the upper troposphere and lower stratosphere by subvisible cirrus clouds near the tropical tropopause. Geophys. Res. Lett., vol. 23, no. 8, pp. 825-828.

Jiang, J. H., H. Su, M. R. Schoeberl, S. T. Massie, P. Colarco, S. Platnick, and N. J. Livesey, 2008. Clean and polluted clouds: Relationships among pollution, ice clouds, and precipitation in South America. Geophys. Res. Lett., vol. 35, L14804, doi: 10.1029/2008GL034631.

Justice, C. O., J. D. Kendall, P. R. Dowty, and R. J. Scholes, 1996. Satellite remote sensing of fires during the SAFARI campaign using NOAA advanced very high resolution radiometer. J. Geophys. Res., vol. 101, no. D19, pp. 23851-23863.

Kalnay, E., 2003: *Atmospheric modeling, data assimilation and predictability*. Cambridge Univ. Press, 341 pp.

Karcher, B., and U. Lohmann, 2002. A parameterization of cirrus cloud formation: Homogeneous freezing including effects of aerosol size. J. of Geophys. Res., vol. 107, no. D23, doi:10.1029/2001JD001429.

Kaufman, Y. J., and R. S. Fraser, 1997. The effect of smoke particles on clouds and climate forcing. Science, vol. 227, pp. 1636-1639.

Kojima, T., P. R. Buseck, J. C. Wilson, J. M. Reeves, and M. J. Mahoney, 2004. Aerosol particles from tropical convective systems: Cloud tops and cirrus anvils. J. Geophys. Res., vol. 109, no. D12201, doi: 10.1029/2003JD004504.

Lahoz, W., A. Geer, R. Swinbank, D. Jackson, H. Thornton, A. Dethof, and D. Fonteyn, 2004. Modelling and assimilation: evaluation of MIPAS water vapour data. Proceedings of the Second Workshop on the Atmospheric Chemistry Validation of ENVISAT.

Lin, J. C., T. Matsui, R. A. Pielke Sr., and C. Kummerow, 2006. Effects of biomass-burning-derived aerosols on precipitation and clouds in the Amazon Basin: a satellite-based empirical study. J. of Geophys. Res., vol. 111, D19204, doi: 10.1029/2005JD006884.

Liu, H.-C., P. K. Wang, and R. E. Schlesinger, 2003a. A numerical study of cirrus clouds. PartII: Effects of ambient temperature, stability, radiation, ice microphysics, and microdynamics on cirrus evolution. J. of the Atm. Sciences, vol. 60, pp. 1097-1119.

Liu, H.-C., P. K. Wang, and R. E. Schlesinger, 2003b. A numerical study of cirrus clouds. Part I: Model description. J. of the Atm. Sciences, vol. 60, pp. 1075-1084.

Nakajima, T., A. Higurashi, K. Kawamoto, and J. E. Penner, 2001. A possible correlation between satellite-derived cloud and aerosol microphysical parameters. Geophys. Res. Lett., vol. 28, no. 7, pp. 1171-1174.

Newell, R. E., and S. Gould-Stewart, 1981. A Stratospheric Fountain? J. Atmospheric Sciences, vol. 38, pp. 2789-2796.

Omar, A. H., and C. S. Gardner, 2001. Observations by the Lidar In-Space Technology Experiment (LITE) of high-altitude cirrus clouds over the equator in regions exhibiting extremely cold temperatures. J. Geophys. Res., vol. 106, no. D1, pp. 1227-1236.

Pfister, L., K. R. Chan, T. P. Bui, S. Bowen, M. Legg, B. Gary, K. Kelly, M. Proffitt, and W. Starr, 1993. Gravity waves generated by a tropical cyclone during the STEP tropical field program: A case study. J. Geophys. Res., vol. 98, no. D5, pp. 8611-8638.

Pickering, K. E., A. M. Thompson, H. Kim, A. J. DeCaria, L. Pfister, T. L. Kucsera, J. C. Witte, M. A. Avery, D. R. Blake, J. H. Crawford, B. G. Heikes, G. W. Sachse, S. T. Sandholm, H. Singh, and R. W. Talbot, 2001. Chemical characteristics of air from different source regions during the second Pacific Exploratory Mission (PEM-Tropics B). J. Geophys. Res., vol. 106, no. D23, pp. 32609-32626.

Pitari, G., E. Mancini, V. Rizi, and D. T. Shindell, 2002. Impact of future climate and emission changes on stratospheric aerosols and ozone. J. Atm. Sci., vol. 59, pp. 414-440.

Potter, B. E., and J. R. Holton, 1995. The role of monsoon convection in the dehydration of the lower tropical troposphere. J. Atm. Sci., vol. 52, no. 8, pp. 1034-1050.

Prenni, A. J., P. J. DeMott, S. M. Kreidenweis, D. E. Sherman, L. M. Russell, and Y. Ming, 2001. The effects of low molecular weight dicarboxylic acids on cloud formation. J. Phys. Chem. A, vol. 105, pp. 11240-11248.

Prins, E. M., and W. P. Menzel. 1994. Trends in South American biomass burning detected with the GOES visible infrared spin scan radiometer atmospheric sounder from 1983 to 1991. J. Geophys. Res., vol. 99, no. D8, pp. 16719-16735.

Pruppacher, H. R., and J. D. Klett, 1997. Microphysics of clouds and precipitation. Boston, Kluwer Academic Press, 954 p.

Randel, W. J., F. Wu, H. Vomel, G. E. Nedoluha, and P. Forster, 2006. Decreases in stratospheric water vapor after 2001: Links to changes in the tropical tropopause and the Brewer-Dobson circulation. J. Geophys. Res., vol. 111, D12312, doi: 10.1029/2005JD006744.

Randel, W. J., F. Wu, S. J. Oltmans, K. Rosenlof, and G. E. Nedoluha, 2004. Interannual changes of stratospheric water vapor and correlations with tropical tropopause temperatures. J. Atm. Sci., vol. 61, pp. 2133-2148.

Roberts, G. C., A. Nenes, J. H. Seinfeld, and M. O. Andreae, 2003. Impact of biomass burning on cloud properties in the Amazon Basin. J. Geophys. Res., vol. 108, no. D2, doi:10.1029/2001JD000985.

Rosenfeld, J. E., D. B. Considine, M. R. Schoeberl, and E. V. Browell, 1998. The impact of subvisible cirrus clouds near the tropical tropopause on stratospheric water vapor. Geophys. Res. Lett., vol. 25, no. 11, pp. 1883-1886.

Rosenlof, K. H., S. J. Oltmans, D. Kley, J. M. Russell, E. W. Chiou, W. P. Chu, D. G. Johnson, K. K. Kelly, H. A. Michelsen, G. E. Nedoluha, E. E. Remsberg, G. C. Toon, and M. P. McCormick, 2001. Stratospheric water vapor increases over the past half-century. Geophys. Res. Lett., vol. 28, no. 7, pp. 1195-1198.

Rossow, W. B., A. W. Walker, D. E. Beuschel, and M. D. Roiter, 1996. International Satellite Cloud Climatology Project (ISCCP) Documentation of New Cloud Datasets. World Meteorological Organization, 115 pp.

Roumeau, S., P. Brémaud, E. Rivière, S. Baldy, and J. L. Baray, 2000. Tropical cirrus clouds: a possible sink for ozone. Geophys. Res. Lett., vol. 27, no. 15, pp. 2233-2236.

Sherwood, S. C., 2002a. Aerosols and ice particle size in tropical cumulonimbus. J. Climate, vol. 15, no. 9, pp. 1051-1063.

Sherwood, S. C., 2002b. A microphysical connection among biomass burning, cumulus clouds, and stratospheric moisture. Science, vol. 295, pp. 1272-1275.

Sherwood, S. C., 2000. A "stratospheric drain" over the maritime continent. Geophys. Res. Lett., vol. 27, pp. 677-680.

Sherwood, S. C., and A. E. Dessler, 2003. Convective mixing near the tropical tropopause: Insights from seasonal variations. J. Atm. Sci., vol. 60, pp. 2674-2685.

Sherwood, S. C., and A. E. Dessler, 2000. On the control of stratospheric humidity. Geophys. Res. Lett., vol. 27, no. 16, pp. 2513-2516.

Skole, D., and C. Tucker, 1993. Tropical deforestation and habitat fragmentation in the Amazon: Satellite data from 1978 to 1988. Science, vol. 260, pp. 1905-1910.

Stephens, G. L., 1978. Radiation profiles in extended water clouds. II. Parameterization schemes. J. of the Atm. Sciences, vol. 35, pp. 2123-2132.

Suzuki, K., T. Nakajima, A. Numaguti, K. Kawamoto, and A. Higurashi, 2004. A study of the aerosol effect on a cloud field with simultaneous use of GCM modeling and satellite observation. J. of the Atm. Sciences, vol. 61, pp. 179-194.

Tang, Y., G. R. Carmichael, J.-H. Woo, N. Thongboonchoo, G. Kurata, I. Uno, D. G. Street, D. R. Blake, R. J. Weber, R. W. Talbot, Y. Kondo, and H. B. Singh, 2003. The influence fo biomass burning during TRACE-P experiment identified by the regional chemical transport model. J. Geophys. Res., vol. 108, no. D21, pp. 8824-8837.

Talbot, R. W., J. E. Dibb, E. M. Scheuer, D. R. Blake, N. J. Blake, G. L. Gregory, G. W. Sachse, J. D. Bradshaw, S. T. Sandholm, and H. B. Singh, 1999. Influence of biomass combustion emissions on the distribution of acidic trace gases over the southern Pacific basin during austral springtime. J. Geophys. Res., vol. 104, no. D5, pp. 5623-5634.

Trenberth, K. E., 1992: *Global Analyses from ECMWF and Atlas of 1000 to 10 mb Circulation Statistics.* TN-373+STR, National Center for Atmospheric Research, 205 pp.

Tripoli, G. J., 1992. An explicit three-dimensional nonhydrostatic numerical simulation of a tropical cyclone. Meteorol.Atmos. Phys., vol. 49, pp. 229-254.

Trosnikov, I. V., and C. A. Nobre, 1998. Estimation of aerosol transport from biomass burning areas during the SCAR-B experiment. J. Geophys. Res., vol. 103, no. D24, pp. 32129-32137.

Webster, C. R., and A. J. Heymsfield, 2003. Water isotope ratios D/H, $^{18}O/^{16}O$, $^{17}O/^{16}O$ in and out of clouds map dehydration pathways. Science, vol. 302, pp. 1742-1745.

Woodley, W. L., D. Rosenfeld, and B. A. Silverman, 2003. Results of on-top glaciogenic cloud seeding in Thailand. Part II: Exploratory analyses. J. of Applied Meteorology., vol. 42, no. 7, pp. 939-951.

Zobrist, B., C. Marcolli, T. Koop, B. P. Luo, D. M. Murphy, U. Lohmann, A. A. Zardini, U. K. Krieger, T. Corti, D. J. Cziczo, S. Fueglistaler, P. K. Hudson, D. S. Thomson, and T. Peter, 2006. Oxalic acid as a heterogeneous ice nucleus in the upper troposphere and its indirect aerosol effect. Atmos. Chem. and Physics., vol. 6, pp. 3115-3129.